Dissertation
submitted to the
Combined Faculty of Natural Sciences and Mathematics
of Heidelberg University, Germany
for the degree of
Doctor of Natural Sciences

Put forward by
Leonhard Horst
born in: Bensheim
Oral examination: 01.12.2021

Simulations of hydrodynamic phenomena in stellar interiors

Referees: Prof. Dr. Friedrich Röpke
Prof. Dr. Cornelis P. Dullemond

Zusammenfassung

In dieser Arbeit werden multidimensionale hydrodynamische Simulationen des Inneren von Sternen mit dem Seven-League Hydro (SLH) code durchgeführt. Der Fokus liegt dabei auf dynamischen Phänomenen bei niedrigen Machzahlen. Ein gutes Verständnis dieser Phänomene ist wesentlich, um die Modellierung der Evolution von Sternen zu verbessern. Es wird dargelegt, dass geeignete numerische Methoden notwendig sind, um numerische Artefakte und künstliche Dissipation zu reduzieren. Diese würden ansonsten die eigentliche physikalische Strömung dominieren. Dreidimensionale Simulationen von konvektivem Helium-Schalenbrennen werden verwendet, um die Anwachsrate der Masse der Konvektionszone zu bestimmen. Dies hilft die Parametrisierung von eindimensionalen Sternentwicklungs-Berechnungen zu verbessern. Weiterhin wird die Anregung von Wellen durch Kernkonvektion simuliert und die Resultate hinsichtlich ihrer physikalischen Plausibilität und Übereinstimmung mit Beobachtungen analysiert. Die Ergebnisse demonstrieren, dass die vom SLH code verwendeten numerischen Methoden vielversprechend sind hinsichtlich zukünftiger, realistischerer Simulationen von astrophysikalischen Strömungen.

Abstract

This thesis presents multidimensional hydrodynamic simulations of stellar interiors with a focus on dynamical phenomena at low Mach numbers using the Seven-League Hydro (SLH) code. A better understanding of these phenomena is crucial to improve the modeling of stellar evolution. It is demonstrated that suitable numerical methods are required to avoid that numerical artifacts and spurious dissipation dominate the actual physical flow. Three-dimensional simulations of convective helium shell burning are used to measure the entrainment of mass into the convective region. This aids the parametrization of entrainment in one-dimensional evolution calculations. Furthermore, the excitation of waves by core convection is simulated and the results are analyzed regarding their physical plausibility and agreement with observations. These simulations demonstrate that the current set of numerical methods used by the SLH code is promising regarding future, more realistic simulations of astrophysical flows.

Contents

CHAPTER 1

Introduction

1.1 Astrophysical context

Stars are three-dimensional (3D) objects that involve a variety of intrinsically multidimensional phenomena, such as convection, rotation, or magnetic fields. Yet, even with modern supercomputer facilities, it is not possible to resolve all relevant time and spatial scales of a star in full 3D simulations. Conventional stellar evolution simulations therefore reduce stars to spherically symmetric objects and solve the corresponding one-dimensional (1D) formulation of the underlying equations while approximating multidimensional phenomena by 1D parametrizations (e.g., Heger et al., 2000; Maeder, 2009; Kippenhahn et al., 2012; Salaris and Cassisi, 2017; Buldgen, 2019).[1] The 1D approach greatly reduces the computational costs and enables simulations to follow the full evolutionary timescales of stars which are typically at the order of millions to billions of years.

However, although the principle mechanisms that act inside stars are now known (e.g., see the books by Kippenhahn et al., 2012; Maeder, 2009; Salaris and Cassisi, 2005; Weiss et al., 2004; Prialnik, 2000) discrepancies between stellar evolution calculations and observations still exist. For example, asteroseismic data suggest that the predicted size of convective cores is generally too small (e.g., Aerts, 2021; Johnston, 2021). Current 1D prescriptions of stellar rotation can also not explain the efficient angular momentum transport needed to reproduce the rotation rates of evolved stars as inferred from asteroseismology (Aerts et al., 2019; Spada et al., 2016; Eggenberger et al., 2017; den Hartogh et al., 2020). The observation of slow rotators with large surface abundances of nitrogen and fast rotators with low abundances further challenges prescriptions of stellar rotation (Hunter et al., 2008; Morel et al., 2008; Aerts et al., 2014; Grin et al., 2017; Markova et al., 2018; Buldgen, 2019, see also the discussion by Maeder and Meynet, 2015). Another indication of the deficiency of current evolution models is the discrepancy between masses as inferred from stellar evolution calculations and masses as inferred from spectroscopy (e.g., Markova et al., 2018; Serenelli et al., 2021) or eclipsing binaries (e.g., Tkachenko et al., 2020; Serenelli et al., 2021). For massive stars, current parametrizations of convective mixing cannot fully reproduce the main-sequence (MS) width (Castro et al., 2014; Scott et al., 2021) or the surface helium abundances (Georgy et al., 2021). These examples (see also the reviews by Langer, 2012 and Maeder and Meynet, 2012) indicate that current state-of-the-art stellar evolution models are still incomplete.

The main source of uncertainty in 1D modeling is the necessity to approximate multidimensional phenomena by 1D parametrizations. The development and verification of suitable approximations is subject of ongoing research and to date, no unified prescription exists for the various multidimensional effects emerging in stars. Instead, already the specific choice

[1] There are current efforts for developing two-dimensional stellar evolution codes. However, to date, none of them is able to follow stellar evolution on long enough timescales (e.g., see the review by Lovekin, 2020).

and calibration of the respective 1D prescriptions in different stellar evolution codes leads to different evolution calculations for the same initial conditions, indicating the large uncertainties in the resulting stellar models (e.g., Meynet et al., 2013; Martins and Palacios, 2013; Jones et al., 2015; Stancliffe et al., 2016; Kaiser et al., 2020; Davis et al., 2019; Clarkson and Herwig, 2021).

Stellar evolution calculations need to consider a variety of complex phenomena. For example, convection creates large scale motions of gas which affect the chemical structure inside stars. Rotation induces large scale currents and instabilities which can have a major impact on stars, for example through the transport of angular momentum (Maeder, 2009; Maeder et al., 2013; Salaris and Cassisi, 2017). It further leads to a deformation of the star, contradicting the assumption of spherical symmetry. Therefore, the 1D equations of stellar structure need to be adapted to at least approximately include rotational effects (Meynet and Maeder, 1997). This approximation, however, is not suitable at fast rotation rates. Other phenomena are magnetic fields which interact with stellar rotation and affect angular momentum transport, binary interactions which may introduce mass transfer and change rotation and internal mixing processes by tidal interactions (e.g., Meynet et al., 2017), or mass loss at the stellar surface which is crucial especially in massive star evolution yet particularly difficult to parametrize (e.g., Smith, 2014).

In the effort for improvement, observations are essential to assess the quality of current theories and to calibrate 1D prescriptions. However, finding suitable stellar samples at sufficient accuracy is difficult. It is also not straightforward to determine properties like mass, age, rotation, or binarity of the individual stars of the sample. These properties are needed for a meaningful comparison with evolution models and observational uncertainties will propagate into the calibration of 1D parametrizations (e.g., Torres et al., 2010; Valle et al., 2017). Furthermore, the observable properties of a star are the result of the combined action of all stellar processes and it is challenging to isolate individual contributions when they are compared to 1D calculations (e.g., see discussion by Johnston, 2021).

Multidimensional hydrodynamic simulations of stellar setups are therefore important to complement observations. In such simulations, typically the Navier-Stokes equations or the Euler equations of fluid dynamics are solved numerically for stellar initial conditions. Dynamical processes may then develop self-consistently without the need of parametrization and their immediate action can be followed. These simulations further allow controlling the involved effects by considering suitable initial conditions, as for example non-rotating versus rotating, the inclusion of magnetic fields, or different energy inputs. These aspects can then be analyzed individually and the results can be used in order to calibrate already existing 1D parametrizations or to develop new prescriptions. Due to the high computational costs, multidimensional simulations are, however, restricted to timescales which are small compared to the timescales of stellar evolution, or processes at late evolutionary stages that are closer to dynamical timescales.

The focus of this thesis lies on hydrodynamic simulations of convection and associated phenomena in stellar interiors. Convection is one of the dominant processes that determines stellar evolution and is ubiquitous in stars. Convective regions occur, for example, due to increasing opacities in stellar envelopes of low-mass stars with masses smaller than about one solar mass ($M_\star \lesssim 1\,\mathrm{M}_\odot$) or in the envelope of red giants where hydrogen burning in the core has ceased, but also due to the high temperature sensitivity of nuclear burning in the cores of more massive stars ($M_\star \gtrsim 1\,\mathrm{M}_\odot$) or in shells around the core at advanced burning stages (Kippenhahn et al., 2012). The turbulent flows within these regions provide an efficient transport of material. By mixing unburnt material into burning regions, convection directly affects the evolution of the core size, the time spent on the MS, luminosity, or the

chemical composition of stars. Large convective envelopes may extend inwards to burning regions and mix the products of nuclear burning to the surface where it can be detected by observations (Maeder, 2009; Kippenhahn et al., 2012; Salaris and Cassisi, 2017). An accurate representation of convection is thus essential in order to model stellar evolution (e.g., Salaris and Cassisi, 2017; Kupka and Muthsam, 2017; Buldgen, 2019). In almost all 1D stellar evolution codes, convection is parametrized using mixing-length theory (MLT) (Böhm-Vitense, 1958) despite its known deficiencies (Kupka and Muthsam, 2017). The underlying idea of MLT and the known shortcomings of this approach are discussed in more detail in Section 1.2. In hydrodynamic simulations, basic assumptions of MLT can be verified. They further allow the identification of additional phenomena which are not included in standard MLT in order to improve current 1D models. One prominent example is the mixing of material across interfaces between convective and stable regions which naturally occurs in hydrodynamic simulations (e.g., Meakin and Arnett, 2007b) and is strongly suggested through comparison with observations (e.g., Johnston, 2021). Convection is also known to stochastically excite internal gravity waves (IGW). IGW can affect stellar evolution, for example through mixing and angular momentum transport (Alvan et al., 2015; Rogers and McElwaine, 2017; Aerts et al., 2019). Also the effects of IGW can be included into 1D calculations only by means of parametrizations (e.g., Talon, 2008; Salaris and Cassisi, 2017). Some examples for multidimensional simulations of stellar convection are simulations of the interaction with large scale currents due to rotation (e.g., Augustson et al., 2012; Brun et al., 2017), mixing in burning or surface regions (e.g., Andrassy et al., 2020; Pratt et al., 2017), or simulations of collapsing massive stars (e.g., Müller, 2020). Hydrodynamic simulations are also used to study IGW excitation, for example by convective cores (Rogers et al., 2013; Edelmann et al., 2019), by envelope convection in solar-like stars (Rogers and Glatzmaier, 2005; Alvan et al., 2014, 2015), or in simplified convective setups (Lecoanet et al., 2021).

This thesis aims at contributing to these current efforts to improve the theory of stellar evolution by performing multidimensional hydrodynamic simulations with the Seven-League Hydro (SLH) code (Miczek, 2013; Edelmann, 2014). The work focuses on simulations of stellar convection at low Mach numbers, meaning that the speed of the convective flow is small compared to the local speed of sound. This is a typical situation found in convective zones in stellar interiors of massive stars at early evolutionary phases. While understanding the action of low-Mach flows is crucial for stellar evolution, their numerical treatment is particularly challenging (e.g., Miczek et al., 2015) and therefore, Mach numbers are often artificially increased by an enhanced energy input (e.g., Cristini et al., 2019). This motivated the development of the SLH code which employs several numerical techniques to mitigate these challenges and to perform simulations at low Mach numbers with enhanced accuracy. However, as already noticed by Miczek (2013) and Edelmann (2014), these techniques are prone to instabilities in simulations which involve order of magnitude changes in density and pressure, a situation typically found in stars. The principle goal of the present thesis is therefore twofold: To assess the robustness of the numerical methods used by the SLH code in test setups and realistic astrophysical setups. But also to provide additional simulations and analysis of stellar convection and IGW that complement already published results by other groups for different stellar scenarios (e.g., Meakin and Arnett, 2007b; Cristini et al., 2019; Edelmann et al., 2019).

The thesis is structured as follows: Section 1.2 introduces the commonly used MLT of convection in 1D evolution codes along with a discussion of its well-known deficiencies and possible extensions. Section 1.3 briefly describes insights from asteroseismology related to convection. In Section 1.4, the SLH code is presented in the context of the challenges of low-Mach simulations. The chapter ends with a further motivation to improve low-Mach

simulations in Section 1.5. Chapter 2 presents results from simulations performed with the SLH code: Firstly, the importance of an accurate treatment of hydrostatic stratifications for low-Mach convection is illustrated in Section 2.1, along with possible approaches for improvements. Furthermore, entrainment rates are extracted from simulations of convective helium shell burning in Section 2.2, while demonstrating the benefits of using low-Mach techniques. It is followed by a detailed analysis of IGW excited in simulations of core convection in a massive star in Section 2.3. Chapter 3 concludes the thesis by summarizing the obtained results and discussing remaining challenges and prospects in simulations of hydrodynamic phenomena in stars.

1.2 Convection modeled in 1D stellar evolution

Conventional 1D evolution codes typically apply MLT (Böhm-Vitense, 1958) to parametrize convection. The basic principles of this approach are sketched in the following.

Convection and thermal radiation are the two main processes that transport the energy in the interior of stars, for example released by nuclear burning, to the surface.[2] Hence, in a region of the star that is not convective, energy is transported solely through the radiative flux $\mathcal{F}_{\rm rad}$, thus

$$\mathcal{F}_{\rm tot} = \mathcal{F}_{\rm rad}, \tag{1.1}$$

where $\mathcal{F}_{\rm tot}$ denotes the total energy flux in the star. Because the mean free path of photons in the deep interior of stars is short, energy transport by radiation can be described within the diffusion approximation. The radiative flux is then given by (e.g., Kippenhahn et al., 2012, Sect. 5.1.3)

$$\mathcal{F}_{\rm rad} = -\frac{4\,a\,c}{3}\,\frac{T^3}{\kappa\rho}\nabla T, \tag{1.2}$$

where ρ is the density, T the temperature, κ the Rosseland mean opacity over all frequencies, $a = 7.57 \times 10^{-15}\,\mathrm{erg\,cm^{-3}\,K^{-4}}$ the radiation constant, and c the speed of light. Rearranging Eq. (1.2) leads to an expression for the temperature gradient $\nabla_{\rm rad} \equiv \left(\frac{\mathrm{d}\ln T}{\mathrm{d}\ln P}\right)_{\rm rad}$ that is needed if the total energy flux is carried by radiation alone. One obtains

$$\nabla_{\rm rad} = -\frac{H_p}{T}\,\nabla T_{\rm rad} = \frac{3\kappa\rho H_P}{4acT^4}\frac{L_r}{4\pi r^2}, \tag{1.3}$$

where $L_r = 4\pi r^2 \mathcal{F}_{\rm tot}$ is the total luminosity of the star at radius r, P denotes the pressure, and $H_p \equiv -(\mathrm{d}r/\mathrm{d}P)\,P$ is the pressure scale height. Thus, outside of convection zones, the temperature gradient of the star $\nabla \equiv \frac{\mathrm{d}\ln T}{\mathrm{d}\ln P}$ is equal to the radiative temperature gradient, that is $\nabla = \nabla_{\rm rad}$. Within convective regions, however, the convective flux contributes to the energy transport, hence

$$\mathcal{F}_{\rm tot} = \mathcal{F}_{\rm rad} + \mathcal{F}_{\rm conv}, \tag{1.4}$$

and $\nabla \neq \nabla_{\rm rad}$. From this, three main questions arise: (i) what are the criteria to identify convective regions inside a star, (ii) how to calculate $\mathcal{F}_{\rm conv}$ and what is the resulting temperature gradient ∇ within a convection zone, (iii) how can convective mixing inside and at the boundaries of a convection zone be included in 1D stellar evolution simulations.

[2] "Neutrino cooling" by non-interacting neutrinos leaving the star is commonly thought of as an energy sink.

1.2.1 The criteria for convection

From linear perturbation theory it can be shown (e.g., see Kippenhahn et al., 2012, Sect. 6.1) that a region inside a star is convective if

$$\nabla_{\rm rad} > \nabla_{\rm ad}, \tag{1.5}$$

with the adiabatic temperature gradient (e.g., Maeder and Meynet, 2000, Sect. 3.3)

$$\nabla_{\rm ad} = \frac{P\delta}{c_p \rho T}, \tag{1.6}$$

where c_p denotes the specific heat at constant pressure and $\delta \equiv -\left(\partial \ln \rho / \partial \ln T\right)_P$ is a property given by the equation of state (EoS). If also the chemical gradient $\nabla_\mu = \frac{\partial \ln \mu}{\partial \ln P}$ is considered, a region is convective if

$$\nabla_{\rm rad} > \nabla_{\rm ad} + \frac{\varphi}{\delta}\nabla_\mu, \tag{1.7}$$

with $\varphi \equiv \left(\partial \ln \rho / \partial \ln \mu\right)_{P,T}$. Eq. (1.5) is referred to as the Schwarzschild criterion while Eq. (1.7) is called the Ledoux criterion. A stratification where

$$\nabla_{\rm ad} + \frac{\varphi}{\delta}\nabla_\mu > \nabla_{\rm rad} > \nabla_{\rm ad}$$

is called semiconvective: It is formally stable on the dynamical time scale but the oscillation amplitude of a displaced fluid element will slowly grow on the thermal time scale (e.g., see Maeder, 2009, Sect. 6.2). The increasing amplitudes eventually lead to mixing.

There is no clear consensus in the stellar evolution community which criterion is to be used to determine convective regions during 1D stellar evolution simulations. As discussed by Langer (2012), in the presence of chemical gradients the Ledoux-criterion should be taken in order to account for the stabilizing effect of $\nabla_\mu > 0$ (i.e., the molecular weight decreases toward the surface, the typical situation in single stars). This principally allows for the formation of semiconvective regions. However, it may be argued that semiconvective mixing will quickly erase the chemical gradient in these regions. The net effect is then the same as if the Schwarzschild-criterion had been used. Therefore, often the Schwarzschild-criterion is used instead of the Ledoux-criterion. But this approach is questionable if the evolutionary time scale is at the order of the time scale of semiconvective mixing. Alternatively, semiconvective mixing can be accounted for in a diffusive approach (Langer et al., 1983) while applying the Ledoux-criterion to determine convective regions. The corresponding efficiencies are, however, rather uncertain (e.g., see Kaiser et al., 2020).

For convective cores of massive stars at the MS, the difference between simulations using either of the criteria can be expected to be small as the mass of the convective core decreases during the MS evolution and hence chemical gradients lie outside the core region (Meynet et al., 2017; Martinet et al., 2021). This is, however, different for later evolutionary phases where convective shells emerge, and generally, the results can vary for the two criteria (e.g., Paxton et al., 2013, 2018, see also Kaiser et al., 2020 for a detailed discussion). The recent studies by Georgy et al. (2014, 2021) indicate that the Ledoux criterion better reproduces the observed surface abundances of chemical species in 1D models of blue supergiants. Furthermore, as pointed out by Gabriel et al. (2014), some of the numerical techniques that are commonly used to determine the boundary position using the Ledoux criterion are inaccurate if discontinuities in the chemical abundance are present. This may result in a substantial difference in the mass of convective cores. If convective boundary mixing (CBM) (see Section 1.2.3) is included in the 1D simulations, the issue seems less severe as CBM removes

possible discontinuities in the vicinity of boundaries of convection zones. It further considerably diminishes the impact of diffusive semiconvective mixing as chemical gradients are efficiently removed (Kaiser et al., 2020).

This section illustrates that already the choice of the criterion for convection and the way how it is calculated are sources of uncertainty, leading to different results for the same initial conditions.

1.2.2 The mixing-length theory of convection

Inside convective regions, the total energy is transported by both, radiation and convection (Eq. (1.4)). While for a given temperature profile, $\mathcal{F}_{\rm rad}$ is determined by Eq. (1.2), an expression for $\mathcal{F}_{\rm conv}$ is more difficult to obtain. One widely used approach is the mixing-length theory (MLT) which quantifies the efficiency of convective energy transport by means of rising "blobs" that carry a temperature excess over a mixing length $\ell_{\rm MLT}$. Different flavors of MLT exist which mainly differ in the treatment of the temporal and spatial averages that appear during the derivation of the theory. One of the mostly used formalism is the one by Böhm-Vitense (1958) which is briefly reviewed in the following on the basis of the presentations by Kippenhahn et al. (2012) and Maeder and Meynet (2000). For a comparison between different flavors see for example Tassoul et al. (1990) and Salaris and Cassisi (2008).

In MLT, the convective blobs are assumed to rise a distance $\ell_{\rm MLT}$ before they dissolve and mix with the surrounding medium. The blob is further thought to always be in pressure equilibrium with its surrounding. This is justified if convective motions are slower than the speed of sound, a reasonable assumption for the stellar interior (see, for example, figure 1 in Section 2.2). At a hypothetical spherical surface within a convective region, an average blob has moved a distance $\ell_{\rm MLT}/2$ when reaching the surface with a velocity v and a temperature excess DT compared to its surrounding. The average convective energy flux at this surface is then

$$\mathcal{F}_{\rm conv} = c_P \rho \, v \, DT. \tag{1.8}$$

The temperature excess can be expressed as

$$DT \approx \left(\frac{{\rm d}T_{\rm b}}{{\rm d}r} - \frac{{\rm d}T}{{\rm d}r} \right) \frac{\ell_{\rm MLT}}{2} = (\nabla - \nabla_b) \frac{T}{H_P} \frac{\ell_{\rm MLT}}{2}, \tag{1.9}$$

where the subscript b denotes quantities of the rising blob. Buoyancy will lead to a mean velocity v of the blob according to

$$F_g = -gD\rho, \tag{1.10}$$

where $D\rho$ denotes the density fluctuation with respect to the surrounding. The gravitational acceleration g is assumed to be constant over the considered spatial scales. If chemical gradients can be neglected, the relation between relative density and temperature fluctuations is

$$\frac{D\rho}{\rho} = \delta \frac{DT}{T}. \tag{1.11}$$

Assuming that half of the buoyancy work is dissipated during the average travel distance of $\ell_{\rm MLT}/2$, one obtains for the square of the resulting velocity

$$v^2 = \frac{g\delta}{8} \frac{\nabla - \nabla_b}{H_p} \ell_{\rm MLT}^2, \tag{1.12}$$

and finally the convective flux (Eq. (1.8)) can be approximated as

$$\mathcal{F}_{\rm conv} = \rho c_P T \sqrt{g\delta}\, \frac{\ell_{\rm MLT}^2}{4\sqrt{2}} H_p^{-3/2} (\nabla - \nabla_b)^{3/2}. \tag{1.13}$$

It remains to find an estimate for the temperature gradient ∇_b. The temperature in the blob will change because of adiabatic expansion or compression and because of energy loss by radiation. The latter is obtained with the aid of Eq. (1.2) as

$$\frac{\Delta(U_b)}{V_b} = \mathcal{F}_{\rm rad,b}\, \delta t\, \frac{A_b}{V_b} = \frac{4acT^3}{3\kappa\rho}\, \underbrace{\frac{DT}{(\ell_{\rm MLT}/2)}}_{\approx \nabla T} \underbrace{\frac{\ell_{\rm MLT}}{v}}_{\delta t}\, \frac{6}{\ell_{\rm MLT}} \tag{1.14}$$

$$= \frac{4acT^3}{3\kappa\rho}\, \frac{6\, T(\nabla - \nabla_b)}{H_p v} \tag{1.15}$$

where δt is the travel time of the blob, $\Delta(U_b)/V_b$ the energy loss of the blob per unit volume, and $\Delta(.)$ denotes the change of a quantity inside the blob compared to the initial state. A_b/V_b is the ratio of the surface to the volume of the blob. With the relation $\mathrm{d}q = c_p \mathrm{d}T - \frac{\delta}{\rho}\mathrm{d}P$ for the specific internal energy q and $\mathrm{d}T/\mathrm{d}r = (-T\,\nabla)/(H_P)$ it follows that

$$\rho\Delta(q) = \rho c_p \Delta(T) - \nabla_{\rm ad} \frac{\rho c_p T}{P}\, \frac{\mathrm{d}P}{\mathrm{d}r} \ell_{\rm MLT} \tag{1.16}$$

$$= \frac{\rho c_P T}{H_P}\, (\nabla_b - \nabla_{\rm ad})\, \ell_{\rm MLT}. \tag{1.17}$$

The energy loss given in Eq. (1.15) is associated with the change of internal energy described by Eq. (1.17) and one obtains

$$\frac{\nabla - \nabla_b}{\nabla_b - \nabla_{\rm ad}} = \frac{3\rho^2 c_P \kappa}{4acT^3}\, \frac{v \ell_{\rm MLT}}{6}. \tag{1.18}$$

With Eqs. (1.12), (1.13), and (1.18) it is now possible to solve for the unknown stellar temperature gradient ∇, see for example Maeder (2009), Sect. 5.4.3 or Kippenhahn et al. (2012), Sect. 7.2 and references therein. Different flavors of MLT result in slightly different constant pre-factors in the derived equations (see Salaris and Cassisi, 2008).

Besides the choice of the specific flavor, the result for ∇ will generally depend on the free parameter $\ell_{\rm MLT}$ which is often expressed as

$$\ell_{\rm MLT} = \alpha_{\rm MLT}\, H_P, \tag{1.19}$$

which introduces the free parameter $\alpha_{\rm MLT}$. The values for $\ell_{\rm MLT}$ or $\alpha_{\rm MLT}$ are usually obtained by calibrating 1D models to match observables of the Sun. Typical values for $\alpha_{\rm MLT}$ range between 1.7 to 1.9 for solar calibrations with different codes (e.g., Magic et al., 2010). There are also approaches to calibrate $\alpha_{\rm MLT}$ by 3D hydrodynamical simulations of convection. For example, Trampedach et al. (2014) study different types of surface layers and find $\alpha_{\rm MLT}$ ranging from 1.6 to 2.05, Magic et al. (2015) find with a similar approach $\alpha_{\rm MLT}$ ranging from 1.7 to 2.4. These studies, as well as the calibration from observables of stars with different properties (e.g., Bonaca et al., 2012; Li et al., 2018; Joyce and Chaboyer, 2018; Schootemeijer et al., 2019; Martinet et al., 2021), suggest that $\alpha_{\rm MLT}$ is not the same for all types of stars but should be varied with stellar properties. Based on asteroseismic data, Viani et al. (2018) approximate the dependence of $\alpha_{\rm MLT}$ on surface gravity, effective temperature, and metallicity of a star with a linear model. Furthermore, the calibration of $\alpha_{\rm MLT}$ itself

is not straightforward (see, e.g., Valle et al., 2019) and "[…] already for the Sun α [α_{MLT} in this thesis] is anything but constant even completely within the framework of 1D modeling." (Kupka and Muthsam, 2017, Sect. 6.1.1). As criticized by Canuto et al. (1996), the common practice to adjust the value of MLT to different astrophysical problems (different types of stars) makes it difficult to falsify MLT, see also Kupka and Muthsam (2017).

Clearly, a parametrization of the same physical process that needs individual calibration, even within the same stellar object, is not satisfactory. The derivation of MLT already indicates that MLT is based on rather crude approximations. The picture of single isolated blobs rising and then simply dissolving inside convection zones, for example, is certainly in disagreement with the turbulent flows observed in simulations and laboratory experiments. Furthermore, if MLT is to be used to approximate CBM (see Section 1.2.3) several inconsistencies arise as discussed by Renzini (1987) and reviewed in detail by Arnett et al. (2019). The precise asteroseismic measurements of pressure mode frequencies in solar-like stars further show that the prediction of the mode frequencies based on MLT generally deviates from observations (commonly referred to as "surface-effect", see also figure 1 of Ball et al., 2016). As discussed by Rosenthal et al. (1999), these differences mainly originate from the incorrect predictions of the background stratification for the stellar surface and the lacking inclusion of the impact of surface convection on the asteroseismic modes (e.g., Brown, 1984) in conventional 1D star models that apply MLT. Predictions of stellar properties based on asteroseismic measurements require accurate 1D models and are thus directly affected by the surface-effect (e.g., Aerts, 2021).

The situation can be improved when the MLT predictions for the problematic surface regions in the last time step of conventional 1D evolution simulations are replaced with mean profiles derived from radiative magnetohydrodynamic simulations (e.g., Rosenthal et al., 1999; Ball et al., 2016). Recently, it was demonstrated that coupling the results of 3D simulations directly to the 1D stellar evolution further reduces the discrepancies between predicted and observed pressure mode frequencies (Jørgensen et al., 2018, 2021; Mosumgaard et al., 2020, see also Spada et al., 2021). However, such approaches may alleviate some of the shortcomings of MLT but do not tackle the fundamental problem of finding a more appropriate 1D description of convection.

As stated by Kupka and Muthsam (2017, Sect. 3.2) the classical MLT formulation has been falsified by the discrepancies that are found when comparing to observations and hydrodynamical simulations. Yet, MLT is still the most popular approach to determine the thermal structure inside convection zones in 1D stellar models. Although there is a broad consensus that MLT needs to be replaced, Kupka and Muthsam (2017) see the following reasons why MLT is nevertheless commonly used:

- It is still the standard model of convection. Many astrophysical applications like stellar population synthesis are based on published grids of stellar evolutionary tracks which used MLT.
- It only relies on local quantities and its implementation into stellar evolution codes is rather easy.
- More sophisticated models of convection often come with additional free parameters which are harder to calibrate. Improvements have been proposed, for example, by taking the full spectrum of turbulent eddies into account instead of the free parameter ℓ_{MLT} (Canuto and Mazzitelli, 1991), or using Reynolds stress models (Canuto, 2011). However, they do not necessarily improve accuracy (Buldgen, 2019).
- Sufficiently accurate asteroseismic observations and hydrodynamic simulations that

show that even with tuning $\alpha_{\rm MLT}$, the correct pressure and temperature are not obtained, became available only recently, compared to the time MLT has already been used in 1D modeling.

1.2.3 Parametrization of convective boundary mixing

The deficiencies of MLT that have been discussed so far mainly concern the surface layers of stars. There, the density is much smaller compared to core regions which makes energy transport by convection less efficient and the full equations derived in previous sections have to be solved for ∇, meaning that all uncertainties of MLT will impact the result. The situation in the deep interior of stars is different because of the higher efficiency of convection. Only a small value of the superadiabaticity is necessary to carry the energy (e.g., see Maeder and Meynet, 2000, Sect. 5.2.1 for an order of magnitude estimate) such that within the convection zones $\nabla \approx \nabla_{\rm ad}$. For example, in the convective core of the $3\,{\rm M}_\odot$ model considered in Section 2.3, one has $(\nabla - \nabla_{\rm ad})/\nabla < 10^{-4}$. Also, velocities are in agreement with hydrodynamic simulations (e.g., see Section 2.2). Furthermore, convection will efficiently homogenize abundance gradients within the convection zone such that abundance profiles are flattened quickly.

While this means that determining the temperature gradient in the interior and mixing in the bulk of a convection zone is not a main issue, it remains that MLT is a local theory and fails for regions near the interfaces to stable zones: According to MLT, the flow has zero velocity and vanishing acceleration at the edge of a convective region. In reality, however, fluid elements approaching from within the convection zone will have a non-zero velocity. While decelerating and overturning, they reach into adjacent formally stable layers. This leads to mixing of chemical elements and possibly affects the thermal structure in the vicinity of the boundary. These effects are not captured by MLT. In principle, the inclusion of the effect of overshooting needs a non-local theory, for which many approaches have been followed, see Kupka and Muthsam (2017) for a detailed overview and discussion. However, to date, none of these are broadly applied in conventional stellar evolution codes. Instead, more commonly, prescriptions based on non-local models are applied in addition to the conventional MLT implementation and a variety of different implementations exists across different stellar evolution codes.

Step overshooting

A simple approach to model CBM is the so called "step overshooting", where the convection zone is extended by a certain fraction $\alpha_{\rm so}$ of the local pressure scale height,

$$\Delta d_{\rm ov} = \alpha_{\rm so} H_P. \tag{1.20}$$

This is motivated by the picture of penetrative convection, where CBM decreases the entropy gradient at the boundary which leads to a growth of the convective region over long enough timescales.[3] Step overshooting is, for example, the standard prescription for MLT in the Geneva stellar evolution code GENEC (Eggenberger et al., 2008).

Diffusive overshooting

Another approach is to describe the mixing across the boundaries of a convection zone (given by the local criteria Eqs. (1.5) and (1.7)) as a diffusive process. Motivated by two-dimensional

[3] It is, however, also common to only extend the mixed region by step-overshooting while keeping the temperature gradient at $\nabla = \nabla_{\rm rad}$ in the overshooting region, that is the convective region is not extended.

(2D) simulations of stellar atmospheres, the diffusion coefficient is expressed by an exponentially decreasing function in the stable zone (Freytag et al., 1996; Herwig, 2000)

$$D_{\rm ov} = D_0 \exp\left(\frac{-2z}{f_{\rm ov}\, H_P}\right), \tag{1.21}$$

where z is the distance to the edge of the convection zone and $f_{\rm ov}$ determines how far the diffusion coefficient reaches into the stable layer before it falls below a certain threshold value for which it is assumed to be zero. The value of D_0 can be estimated from $D_0 = \frac{1}{3}\ell_{\rm MLT} v_{\rm MLT}$ where $v_{\rm MLT}$ and $\ell_{\rm MLT}$ follow from MLT at a point within the convection zone near the interface to the stable zone. In the CBM region, the temperature gradient is set equal to $\nabla_{\rm rad}$ and chemical elements are mixed following a diffusion equation with the diffusion coefficient given by Eq. (1.21). This approach is, for example, used by the open-source stellar evolution code MESA (see Paxton et al., 2019 for the latest report on updates of the code). Compared to "step overshooting", the exponentially decaying diffusion approach results in smoother transitions between mixed and unmixed regions.

The values for $\alpha_{\rm so}$ and $f_{\rm ov}$ are typically calibrated, for example, by comparing the properties of the Hertzsprung-Russel diagram (HR diagram) obtained by a set of 1D stellar evolution calculations with different initial parameters to observations (e.g., Ekström et al., 2012; Martinet et al., 2021) or by means of hydrodynamic simulations (e.g., Jones et al., 2017; Korre et al., 2019; Higl et al., 2021). See Kaiser et al. (2020) for a detailed compilation of published calibrations.

By using a statistical analysis of convective overshooting events, Pratt et al. (2017, 2020) derive a diffusion coefficient from simulations of surface convection. Some first 1D evolution studies apply this prescription and find some improvements for certain observables (e.g., Baraffe et al., 2017; Jørgensen and Weiss, 2018), but it has not yet been tested in 1D calculations covering a broad parameter range.

The Bulk-Richardson entrainment law

A rather new approach to CBM in the stellar context is to describe it in terms of turbulent entrainment. It was shown by Meakin and Arnett (2007b) in 3D simulations of oxygen-shell burning that the measured entrainment of mass at the upper boundary can be described by the Bulk-Richardson entrainment law

$$\frac{v_{\rm e}}{v_{\rm rms}} = A\, {\rm Ri}_{\rm B}^{-n}, \tag{1.22}$$

where $v_{\rm e}$ is the entrainment velocity at the boundary and $v_{\rm rms}$ the root-mean square velocity inside the respective convection zone (see also Section 2.2). The Bulk-Richardson number ${\rm Ri}_{\rm B}$ measures the stiffness of a boundary and can be calculated from a given stellar profile as

$${\rm Ri}_{\rm B} = \frac{\Delta B\, l}{v_{\rm rms}^2}, \tag{1.23}$$

where l is the integral length scale of the convection and

$$\Delta B = \int_{r_c-\Delta r}^{r_c+\Delta r} N^2 \,{\rm d}r, \tag{1.24}$$

where r_c is the radius of the considered boundary and N^2 the Brunt-Väisälä frequency (BVF). The parameters n and A can be either determined by theory or extracted from hydrodynamic simulations, as for example done in Section 2.2. Recently, first applications of this prescription

of CBM to stellar evolution simulations have been published (Staritsin, 2013; Scott et al., 2021).

The various prescriptions of CBM lead to the situation that different 1D codes will predict a different evolutionary tracks for the same star, in particular for the post-MS phase. By comparing the evolutionary tracks predicted by different stellar evolution codes, Martins and Palacios (2013), Jones et al. (2015), and Stancliffe et al. (2016) demonstrate that the details of the treatment of convective mixing is one of the main sources for the uncertainty of stellar evolution models. Even if the stellar evolution calculations are done with a single 1D code, results may vary significantly due to the rather unconstrained free parameters involved in the prescriptions of CBM (e.g., Davis et al., 2019; Kaiser et al., 2020; Clarkson and Herwig, 2021). As pointed out by Kaiser et al. (2020), the calibrations of the parameters are ambiguous and a range of different values for $\alpha_{\rm so}$ and $f_{\rm ov}$ can be found in the literature.

Furthermore, typically the prescription of CBM is set at the initialization of the 1D simulations and then applied to all convection zones that emerge during the evolution, regardless of the prevailing thermodynamic conditions. However, Viallet et al. (2015) argue that the different parametrizations may be valid only for a certain range of the Péclet number Pe. The Péclet number compares the efficiency of advective heat transport to radiative heat transport and varies significantly between convection zones in the deep interior of stars ($\mathrm{Pe} \gg 1$) and convection at stellar surfaces ($\mathrm{Pe} \ll 1$). Viallet et al. (2015) therefore propose to apply different prescriptions of CBM for different regimes of the Péclet number. For example, the widely used diffusion coefficient (Eq. (1.21)) has been inferred from simulations at low Péclet numbers. Applying it to all convection zones during stellar evolution corresponds to an extrapolation over many orders of magnitude (as for example criticized by Kupka and Muthsam, 2017).

Simulations for different stellar scenarios analyzed with respect to different prescriptions will help to identify different characteristics of the mixing process. However, simulations in the stellar interior are difficult because of the involved slow flows and long timescales (see Section 1.4). The work presented in Chapter 2 will provide a further step toward such simulations.

1.3 Insights from asteroseismology

The field of asteroseismology provides guidance for developing improved prescriptions for stellar evolution codes. The constantly increasing accuracy of space telescopes has greatly improved asteroseismic observations and modeling over the past years (e.g., see the review by Bowman, 2020). Waves propagate through the stellar interior, which influences the distinct signatures they leave on the stellar surface. The interpretation of the surface signatures allows inferring information about the stellar interior and reveals discrepancies between stellar evolution calculations and observations (e.g., see Aerts et al., 2010, 2019; Aerts, 2021, for a general overview).

Convective boundary mixing

Typically, the efficient mixing in convective regions lead to gradients in the chemical compositions which in turn lead to a step-like profile of the speed of sound in this region. This causes "acoustic glitches" that generate clear signatures in the frequency spectra of pressure modes. Also the BVF will have a sharp transition in its profile, leading to "buoyancy glitches" and corresponding modulations of the period spacing of gravity waves (for a detailed discussion, see for example Aerts et al., 2010; Aerts, 2021). Studies that aim to reproduce asteroseis-

mic observables on the basis of 1D models generally agree that CBM has to be included in stellar evolution calculations as otherwise, the predicted cores are too small to explain the observed spectra (e.g., Moravveji et al., 2015, 2016; Deheuvels et al., 2016; Szewczuk and Daszyńska-Daszkiewicz, 2018). By modeling single, slowly pulsating B stars (SPB stars), some studies conclude that the exponentially diffusing approach for CBM is favored to reproduce the specific asteroseismic data (Moravveji et al., 2015, 2016). Viani and Basu (2020) find a positive correlation between the amount of CBM and the mass of stars with convective cores. However, Pedersen et al. (2021) investigated a sample of 26 SPB stars using a homogeneous modeling approach. None of the eight considered 1D mixing prescriptions (the combination of step or diffusive overshooting and four different prescriptions for envelope mixing) provides a best fit to all observed stars. They further find a wide spread for the inferred mixing efficiencies. Exceptionally small or even vanishing overshooting efficiencies are reported for two different SPB stars by Buysschaert et al. (2018) and Wu et al. (2020).

Mixing in radiative regions

Some of the aforementioned studies also demonstrate that additional mixing within radiative zones is needed to improve the comparison to observations (e.g., Moravveji et al., 2015; Pedersen et al., 2021; Dumont et al., 2021). Such mixing can, for example, be caused due to rotation or due to IGW that get excited by convective plumes hitting the interface between convective and radiative zones. In massive stars, these waves reach significant amplitudes when traveling outwards to the surface. Simulations indicate that IGW provide an efficient mechanism for chemical mixing and angular momentum transport in radiative zones (Browning et al., 2004; Rogers et al., 2013; Rogers and McElwaine, 2017). Furthermore, observations of rotating OB stars indicate a correlation between the surface nitrogen abundance and the dominant pulsation frequency, while the rotation rate seems not to be correlated (Aerts et al., 2014)[4]. It is therefore likely that the interplay between rotational effects and IGW needs to be considered in order to understand the observed mixing and angular momentum transport in rotating massive stars (Mathis et al., 2013; Rogers et al., 2013).

The low-frequency excess in massive stars

Recent studies found that the photometric spectra of massive MS and post-MS stars show nearly ubiquitous signatures of stochastic low-frequency variability, commonly referred to as the "low-frequency excess" (Bowman et al., 2019a,b, 2020; Pedersen, 2020; Dorn-Wallenstein et al., 2020). The typical signature of the excess are amplitudes above the noise level at low frequencies, that follow a flat profile toward larger frequencies, and significantly decrease for periods typically smaller than a few days. Bowman et al. (2020, 2019b) find that the observed low-frequency variabilities have a similar morphology with respect to the frequency range, the characteristic frequency where the amplitudes start to drop, and the slope of the excess over a range of masses and metallicities. In massive stars, the κ-mechanism (e.g., Aerts et al., 2010) leads to the excitation of gravity modes (g-modes) and pressure modes (p-modes). However, it only acts for stars residing in certain regions of the HR diagram (e.g., Szewczuk and Daszyńska-Daszkiewicz, 2017; Burssens et al., 2020) and can hardly explain these observations. There is therefore a current debate which mechanism is responsible for the observed low-frequency variability across the upper HR diagram (Bowman et al., 2019a; Cantiello et al., 2021).

[4]However, Maeder and Meynet (2015) note that the considered stellar sample of Aerts et al. (2014) spans a wide range of masses, ages, and metallicities and therefore may not be suitable for a definitive conclusion.

Bowman et al. (2019a,b, 2020) suggest that stochastic excitation of IGW by core convection leads to the variability at low frequencies which could explain the similar morphology along metal-rich and metal-poor stars. This is supported by simulations of IGW in hydrodynamic simulations of a $3\,M_\odot$ star (Rogers et al., 2013; Edelmann et al., 2019, see also Section 2.3). However, Lecoanet et al. (2019, 2021) predict from linear theory that peaks from coherent g-modes would be observed in addition to the low-frequency excess if the excess was due to IGW excited by core convection: Radiative damping affects low-frequency IGW the strongest. Thus, if IGW reach the surface with considerable amplitudes in the low-frequency regime, the amplitude will be even higher at larger frequencies, leading to strong peaks for coherent modes. Lecoanet et al. (2019) do not see such peaks in the spectra presented by Bowman et al. (2019a, 2020) and therefore disagree with the IGW hypothesis. While individual peaks are also not present in the spectra obtained from hydrodynamic simulations (Edelmann et al., 2019 and Section 2.3), Lecoanet et al. (2019) and Cantiello et al. (2021) argue that this may be an artifact of the artificially increased energy generation and short simulation times (see also discussion in Section 3.2). Instead, Lecoanet et al. (2019) and Cantiello et al. (2021) suggest that subsurface convection zones emerging from the iron opacity peak are responsible for the observed variability at low frequencies. Cantiello et al. (2021) show that the trend in the properties of the subsurface convection zone regarding the position in the HR diagram could explain the trend found in the observed low-frequency excess. The authors further argue that IGW by core convection would produce larger characteristic frequencies as massive stars evolve, while the opposite is observed in the spectra.

On the other hand, Pedersen (2020) investigated the spectra of 38 SPB stars which are in a mass regime where sub-surface convection zones are expected to be weak (Pedersen, 2020; Cantiello and Braithwaite, 2019; Cantiello et al., 2021). Yet, 75 % of the spectra of the SPB stars exhibit a low-frequency excess. While it seems unlikely that sub-surface convection can produce the observed spectra for these stars, IGW by core convection remains a valid explanation. Furthermore, Pedersen (2020) finds signatures of non-linear effects in the spectra of the SPB stars. This is in contradiction with the linear assumption by Lecoanet et al. (2019, 2021). The exact mechanism that drives the low-frequency excess, IGW by core convection, sub-surface convection, or a combination of both, remains to be subject of debates.

Identifying the excitation mechanism of the low-frequency excess helps to constrain simulations of IGW, the associated angular momentum transport, and its implementation into stellar evolution calculations (Aerts et al., 2019). Furthermore, an improved understanding of how IGW manifest at the stellar surface provides a possibility to infer properties of massive stars which do not exhibit standing g- and p-modes but only show spectra with a low-frequency excess (Bowman et al., 2019a). The detection of standing modes is usually required for conventional asteroseismic methods.

The asteroseismic analysis of spectra regarding CBM reveals that the current parametrization of CBM needs further refinement. A single prescription of CBM and a fixed efficiency is likely insufficient for stellar evolution modeling. Testing different stellar regimes with hydrodynamic simulations will therefore help to improve the current approaches. Furthermore, simulations of IGW provide a path toward an improved inclusion of their effect on stellar evolution. Multidimensional simulations are also an important tool to gain further insight into the excitation mechanism of IGW and the resulting surface spectra, for instance regarding the origin of the observed low-frequency excess (e.g., Edelmann et al., 2019; Ratnasingam et al., 2020, and Section 2.3).

1.4 Simulating astrophysical flows with the Seven-League Hydro code

The numerical tool to perform the simulations that are presented in Chapter 2 is the Seven-League Hydro (SLH) code. It is developed with a focus on low-Mach flows in astrophysical setups and features curvilinear grid geometries, a general EoS, a nuclear network coupled to the hydrodynamic equations, and two gravity solvers. Descriptions of the implemented methods and technical details can be found in Miczek (2013), Edelmann (2014), and Michel (2019). One of the main aspects in the development was to utilize methods that work for low-Mach flows but are also applicable to intermediate and fast flows. In this way, the SLH code is a versatile tool and can be used to address a range of different problems, involving slow and fast flows at the same time. So far, it has been applied to convective mixing in Population III stars (Edelmann, 2014), simulations of classical novae (Bolaños Rosales, 2016), simulations of dynamical shear instabilities (Edelmann et al., 2017), and silicon burning in massive stars (Michel, 2019).

The following subsections give a brief overview on the main challenges when simulating low-Mach flows and how they are addressed within the SLH code. Some of these aspects are discussed in more detail in Chapter 2.

1.4.1 The high Reynolds number in stars

The motion of the gas within stars can be described by the Navier-Stokes equations which follow from the principles of conservation of mass, momentum, and energy (e.g., Toro, 2009). A characteristic quantity for these equations is the Reynolds number Re which measures the relative importance of viscous effects and inertial forces. It is given by

$$\mathrm{Re} \equiv \frac{U\,L}{\nu}, \tag{1.25}$$

where U and L denote the characteristic velocity and length scale of the global flow and ν is the kinematic viscosity (e.g., Landau and Lifshitz, 1987). For flows at low Reynolds numbers, viscous effects dominate and the flow is laminar. If Re exceeds a critical value $\mathrm{Re}_{\mathrm{crit}}$, the flow will become turbulent. The exact value for $\mathrm{Re}_{\mathrm{crit}}$ depends on the problem at hand, but generally a flow is thought to be fully turbulent for $\mathrm{Re} \geq \mathrm{Re}_{\mathrm{crit}} \sim 10^3$ (e.g., Frisch, 1995). Using typical values for the solar envelope convection zone ($U = 10^4\,\mathrm{cm\,s^{-1}}$, $L = 0.3\,\mathrm{R}_\odot$, $\mathrm{R}_\odot = 6.96 \times 10^{10}\,\mathrm{cm}$, $\nu \approx 2\,\mathrm{cm^2\,s^{-1}}$, Hanasoge et al., 2016) one finds $\mathrm{Re}_\odot \sim 10^{14}$. The huge Reynolds number implies that the convective flow in stellar interiors is highly turbulent. Furthermore, it is orders of magnitude larger than what can be achieved in direct numerical simulations (DNS) that aim to resolve all relevant spatial scales. This is illustrated in a phenomenological picture of turbulence following the arguments given in Pope (2000), Sect. 7: The Kolmogorov length scale η_K estimates the scale below which a turbulent flow is dominated by viscous effects and is given by $\eta = (\nu^3/\epsilon)^{1/4}$, where ϵ is the mean kinetic energy transfer rate from large scales to small scales. At a specific length scale l and corresponding typical velocity $v(l)$, the rate can be estimated by $\epsilon = v^3/l$. As the transfer rate is the same on all scales it follows that $v(l) = U\,(l/L)^{1/3}$. From this, the Reynolds number can be related to the Kolmogorov scale via

$$\eta_K/L = \mathrm{Re}^{-3/4}. \tag{1.26}$$

For the Sun, $\eta_K/L \sim 10^{-11}$, meaning that one would need to resolve scales spanning more than ten orders of magnitude on the computation grid if the global flow and the physical

dissipation range is to be represented. Following similar arguments, Kupka and Muthsam (2017) estimate a total number of $\sim 10^{33}$ cells to resolve all relevant scales of the solar convection zone. Storing just a single quantity then requires about 7×10^{21} PB of memory. These numbers are representative for all types of stars. Hence, even without considering any computational costs, it is obvious that performing such simulations on conventional computers is impossible.

Instead, in typical astrophysical hydrodynamic simulations, the numerical discretization is done at scales that are orders of magnitude larger than η_K and the "numerical viscosity" that is inevitably introduced by the numerical methods to solve the equations will be orders of magnitude larger than the physical viscosity. It is therefore a common approach to abandon the explicit inclusion of viscosity that appears in the Navier-Stokes equations. This leads to the Euler equations, which describe the motion of an inviscid fluid. Because of their conservative form, common finite-volume schemes are well suited for their numerical solution. The computational domain is discretized into small volumes and the associated average states of the fluid are evolved through fluxes across the cell interfaces.

Boris (2007) discusses several arguments why simulations of turbulence still give meaningful results even though the small scales are neglected. For example, the energy content of the small scales is insignificant compared to the large, resolvable scales, as the amplitudes in spectra of kinetic energy drop toward smaller scales in turbulent flows (see for example the spectra shown in Section 2.2). Furthermore, numerical studies of turbulence show that kinetic energy is transferred exclusively between comparable scales (see references given by Boris, 2007). There is no immediate transfer from the largest to the smallest scales that would skip the intermediate scales. Thus, if the energy is properly propagated through the scales down to the grid level where it is dissipated into heat, it can be expected that the large structures are reasonably represented and are not affected by the missing small scales. It is therefore sufficient to resolve the scales that are relevant for the dynamic process under investigation, as for example mixing of species. The relevant scales can, for example, be assessed in convergence studies where the grid resolution is increased successively.

Simulations which add a sub-grid model to the Euler equations in order to mimic the transport of energy from the grid scales to the unresolved scales and eventually into heat are called large eddy simulations (LES). Sub-grid models can be complex and, in the absence of a general theory of turbulence, they involve crude approximations. Furthermore, the dissipation introduced by the sub-grid model might be of the same order as the truncation error of the applied numerical method and interference between the two mechanisms is difficult to disentangle. Also, complex models may require substantial computational resources. A more detailed discussion can be found in works by Boris (2007), Grinstein et al. (2007), or Drikakis et al. (2007). The difficulties encountered in LES motivated the concept of implicit large eddy simulations (ILES), where the numerical viscosity that is implicitly or explicitly included in the numerical scheme takes care of the dissipation, instead of a physics-based sub-grid model. As argued by Boris (2007), only a few physical requirements need to be fulfilled by the numerical scheme to ensure that the kinetic energy is transformed into heat in a physically reasonable way. The arguments in favor of the ILES approach are that it is less complex, does not require additional modeling, and its results are comparable to LES after all. For example, by studying the turbulent decay of the Taylor-Green vortex, Drikakis et al. (2007) do not find any obvious advantage of LES over ILES. The concept of ILES is also followed by the SLH code. It has been demonstrated by Berberich (2014) that the numerical methods that are used in SLH give reasonable results in the context of ILES for the decaying Taylor-Green vortex. In particular, Berberich (2014) does not find signatures of a "bottleneck effect" which emerges if the numerical scheme does not dissipate kinetic energy

quickly enough at small scales.

As indicated by the huge Reynolds number, the natural astrophysical flow is highly turbulent even on scales far below the grid scale. It is therefore desirable that a given numerical scheme has a dissipation range as narrow as possible, acting only close to the grid scale. This is particularly difficult to achieve for low-Mach flows, as demonstrated in the next section.

1.4.2 The need for low-Mach flux functions

The SLH code solves the Euler equations using the finite-volume method. Only the principle idea is sketched in the following. For a comprehensive introduction to the method see, for example, LeVeque (2002).

The 3D Euler equations can be written in a compact form as (e.g., Toro, 2009)

$$\frac{\partial \vec{U}}{\partial t} + \frac{\partial \vec{F}(\vec{U})}{\partial x} + \frac{\partial \vec{G}(\vec{U})}{\partial y} + \frac{\partial \vec{H}(\vec{U})}{\partial z} = \vec{S}(\vec{U}), \tag{1.27}$$

where

$$\vec{U} = \begin{pmatrix} \rho \\ \rho u \\ \rho v \\ \rho w \\ \rho E \\ \rho X_i \end{pmatrix}, \vec{F} = \begin{pmatrix} \rho u \\ \rho u^2 + P \\ \rho uv \\ \rho uw \\ u(\rho E + P) \\ \rho u X_i \end{pmatrix}, \vec{G} = \begin{pmatrix} \rho v \\ \rho uv \\ \rho v^2 + P \\ \rho vw \\ v(\rho E + P) \\ \rho v X_i \end{pmatrix}, \vec{H} = \begin{pmatrix} \rho w \\ \rho uw \\ \rho vw \\ \rho w^2 + P \\ w(\rho E + P) \\ \rho w X_i \end{pmatrix},$$

X_i denotes an optional set of advected scalars, and the velocity vector is given by $\vec{v} = (u, v, w)^{\mathrm{T}}$. Other variables have their usual meaning. The source term $\vec{S}$ in Eq. (1.27) may, for example, include gravity terms or the energy release from nuclear burning. In the finite-volume approach, the domain is divided into small volumes which contain the average of the state vector $\vec{U}$. By considering the average of a quantity $Q_{i,j,k}$ in cell (i, j, k) with the domain $\Omega_{i,j,k}$ and volume $V_{i,j,k}$,

$$Q_{i,j,k} = \frac{1}{V_{i,j,k}} \int_{\Omega_{i,j,k}} Q \, \mathrm{d}^3 x \,, \tag{1.28}$$

the Euler equations can be written as

$$\begin{aligned} \frac{\partial \vec{U}_{i,j,k}}{\partial t} + \frac{1}{V_{i,j,k}} \Big(& \vec{F}_{i+1/2,j,k} - \vec{F}_{i-1/2,j,k} + \\ & \vec{G}_{i,j+1/2,k} - \vec{G}_{i,j-1/2,k} + \\ & \vec{H}_{i,j,k+1/2} - \vec{H}_{i,j,k-1/2} \Big) = \vec{S}_{i,j,k}. \end{aligned} \tag{1.29}$$

Here, half-valued integers denote the interface between two neighboring cells. The form of Eq. (1.29) illustrates the conservative character of the equations. In the absence of a source term, the state vector $\vec{U}_{i,j,k}$ only changes through fluxes at the cell interfaces. Thus, the volume integral of U, for example the total energy, is conserved and can only change through fluxes across the boundary of the computational grid which are controlled by boundary conditions.

Choosing an appropriate numerical flux function is one of the key ingredients for every finite-volume code. The importance of a suitable numerical method when simulating flows

at low-Mach numbers is nicely illustrated by the work of Miczek et al. (2015). Their main results will be repeated in condensed form in the following.

The two different state vectors at the interface of two cells pose a Riemann problem. This is utilized in the well-known flux function developed by Roe (1981) which uses an approximate solution to the Riemann problem at the interfaces to construct a stabilizing upwind term. The flux is given by[5]

$$\vec{F}_{i+1/2,j,k} = \frac{1}{2}\left[\vec{F}\left(\vec{U}^L_{i+1/2,j,k}\right) + \vec{F}\left(\vec{U}^R_{i+1/2,j,k}\right)\right] - |\mathbf{A}_{\mathrm{Roe}}|\left(\vec{U}^R_{i+1/2,j,k} - \vec{U}^L_{i+1/2,j,k}\right), \quad (1.30)$$

where L, R denote the values on the left and right side of the interface. The upwind term on the right-hand side includes the matrix $\mathbf{A}_{\mathrm{Roe}}$ which depends on the left and right state vectors $\vec{U}^L, \vec{U}^R$ (for details, see for example Toro, 2009, Chap. 11). Miczek et al. (2015) conclude that the Roe flux has excessive numerical dissipation originating from the upwind matrix $\mathbf{A}_{\mathrm{roe}}$ for flows in the low-Mach regime. To demonstrate this, Miczek et al. (2015) reformulate the Euler equations in non-dimensional form such that the equations only depend on the reference Mach number $\mathrm{Ma_r}$. They are further reformulated in terms of the velocity vector $\vec{q}_n$ normal to the cell interface with the normal vector $\vec{n} = (n_x, n_y, n_z)^{\mathrm{T}}$. The general flux vector along $\vec{n}$ is then given by

$$\vec{\hat{F}}_n = \begin{pmatrix} \rho\hat{q}_n \\ \hat{\rho}\hat{u}\hat{q}_n + n_x\frac{\hat{P}}{M_r^2} \\ \hat{\rho}\hat{v}\hat{q}_n + n_y\frac{\hat{P}}{M_r^2} \\ \hat{\rho}\hat{w}\hat{q}_n + n_z\frac{\hat{P}}{M_r^2} \\ (\hat{\rho}\hat{E} + \hat{P})\hat{q}_n, \end{pmatrix}, \quad (1.31)$$

where the hats denote the non-dimensional quantities[6]. Furthermore, Eq. (1.30) can be written as

$$\vec{\hat{F}}_{i+1/2,j,k} = \frac{1}{2}\left[\widehat{\mathbf{A}}^L\vec{\hat{U}}^L_{i+1/2,j,k} + \widehat{\mathbf{A}}^R\vec{\hat{U}}^R_{i+1/2,j,k}\right] - |\widehat{\mathbf{A}}_{\mathrm{roe}}|\left(\vec{\hat{U}}^R_{i+1/2,j,k} - \vec{\hat{U}}^L_{i+1/2,j,k}\right), \quad (1.32)$$

with the flux Jacobian $\widehat{\mathbf{A}} = \partial\vec{\hat{F}}/\partial\vec{\hat{U}}$. The key finding of Miczek et al. (2015) is that the upwind matrix $\widehat{\mathbf{A}}_{\mathrm{roe}}$, which introduces a diffusion term, scales differently with $\mathrm{Ma_r}$ compared to the actual physical flux Jacobian $\widehat{\mathbf{A}}$. After transforming to the primitive variables $\vec{\hat{V}} = (\hat{\rho}, \hat{u}, \hat{v}, \hat{w}, \hat{P}, X)^{\mathrm{T}}$, they find

$$\widehat{\mathbf{A}}_{\vec{\hat{V}}} \propto \begin{pmatrix} \mathcal{O}(1) & \mathcal{O}(1) & \mathcal{O}(1) & \mathcal{O}(1) & 0 & 0 \\ 0 & \mathcal{O}(1) & 0 & 0 & \mathcal{O}\left(\frac{1}{\mathrm{Ma_r^2}}\right) & 0 \\ 0 & 0 & \mathcal{O}(1) & 0 & \mathcal{O}\left(\frac{1}{\mathrm{Ma_r^2}}\right) & 0 \\ 0 & 0 & 0 & \mathcal{O}(1) & \mathcal{O}\left(\frac{1}{\mathrm{Ma_r^2}}\right) & 0 \\ 0 & \mathcal{O}(1) & \mathcal{O}(1) & \mathcal{O}(1) & \mathcal{O}(1) & 0 \\ 0 & 0 & 0 & 0 & 0 & \mathcal{O}(1) \end{pmatrix}, \quad (1.33)$$

[5] Without loss of generality, the interface between two cells in the x-direction is considered here.

[6] For example, $\rho = \hat{\rho}\,\rho_r$ with $\hat{\rho}$ being the non-dimensional density and ρ_r being the reference density. For the non-dimensionalization as done by Miczek et al. (2015), all reference quantities cancel except for the reference Mach number.

whereas

$$\left|\widehat{\mathbf{A}}_{\mathrm{Roe},\vec{V}}\right| \propto \begin{pmatrix} \mathcal{O}(1) & \mathcal{O}(\mathrm{Ma_r}) & \mathcal{O}(\mathrm{Ma_r}) & \mathcal{O}(\mathrm{Ma_r}) & \mathcal{O}\left(\frac{1}{\mathrm{Ma_r}}\right) & 0 \\ 0 & \mathcal{O}\left(\frac{1}{\mathrm{Ma_r}}\right) & \mathcal{O}\left(\frac{1}{\mathrm{Ma_r}}\right) & \mathcal{O}\left(\frac{1}{\mathrm{Ma_r}}\right) & \mathcal{O}\left(\frac{1}{\mathrm{Ma_r}}\right) & 0 \\ 0 & \mathcal{O}\left(\frac{1}{\mathrm{Ma_r}}\right) & \mathcal{O}\left(\frac{1}{\mathrm{Ma_r}}\right) & \mathcal{O}\left(\frac{1}{\mathrm{Ma_r}}\right) & \mathcal{O}\left(\frac{1}{\mathrm{Ma_r}}\right) & 0 \\ 0 & \mathcal{O}\left(\frac{1}{\mathrm{Ma_r}}\right) & \mathcal{O}\left(\frac{1}{\mathrm{Ma_r}}\right) & \mathcal{O}\left(\frac{1}{\mathrm{Ma_r}}\right) & \mathcal{O}\left(\frac{1}{\mathrm{Ma_r}}\right) & 0 \\ 0 & \mathcal{O}(\mathrm{Ma_r}) & \mathcal{O}(\mathrm{Ma_r}) & \mathcal{O}(\mathrm{Ma_r}) & \mathcal{O}\left(\frac{1}{\mathrm{Ma_r}}\right) & 0 \\ 0 & 0 & 0 & 0 & 0 & \mathcal{O}(1) \end{pmatrix}. \tag{1.34}$$

By comparing Eq. (1.33) to Eq. (1.34) it is evident that for small Mach numbers some parts of the upwind matrix, for example the $\mathcal{O}(1/\mathrm{Ma_r})$ terms for the velocity components in Eq. (1.34), will completely dominate over the physical flux function, leading to an excessive dissipative behavior. This is clearly not desired as the artificial upwind term of the Roe scheme is meant to ensure numerical stability while the actual flux should be mainly given by the central flux $\frac{1}{2}\left[\widehat{\mathbf{A}}^L\vec{\hat{U}}^L_{i+1/2,j,k} + \widehat{\mathbf{A}}^R\vec{\hat{U}}^R_{i+1/2,j,k}\right]$ in Eq. (1.32).

To alleviate the problematic scaling, Miczek et al. (2015) propose a preconditioned Roe solver which replaces the original matrix by

$$\left(\mathbf{P}^{-1}\left|\mathbf{P}\mathbf{A}_{\mathrm{Roe}}\right|\right), \tag{1.35}$$

where $\mathbf{P}(\vec{U})$ is a preconditioning matrix that ensures the correct scaling. They demonstrate the improved properties of the preconditioned Roe solver for simulations of the Gresho vortex on a 40^2 Cartesian grid, a stationary solution to the Euler equations where the centrifugal force is balanced by a pressure gradient. The classical Roe scheme already shows significant dissipation at $\mathrm{Ma} = 10^{-2}$ and the vortex completely dissolves within one rotation for $\mathrm{Ma} \leq 10^{-3}$. In contrast, the improved scheme shows almost no dissipation, even at $\mathrm{Ma} = 10^{-4}$.

This demonstrates the importance of having a suitable numerical flux function when the typical low-Mach phenomena in stellar interiors are to be simulated. A variety of different flux functions are implemented in SLH. However, astrophysical problems require the inclusion of gravity, which was not considered in the discussion above. Indeed, gravity leads to further complications, in particular in combination with a low-Mach flux function. Numerical experiments with the SLH code revealed that many low-Mach flux functions develop strong instabilities for astrophysical setups in hydrostatic equilibrium. The instabilities may cause artificial flows at magnitudes that are stronger than the flow of interest. Such artifacts are also seen for the preconditioned Roe solver (Miczek, 2013; Edelmann, 2014). Therefore, for most of the simulations presented in Chapter 2, the AUSM$^+$−up flux is used (Liou, 2006). It splits the numerical flux into a pressure and advection part and ensures a consistent scaling in the limit of low Mach numbers. An explicit pressure-diffusion term improves the stability of the numerical scheme for low-Mach simulations. The scaling in the AUSM$^+$−up scheme is limited by a cut-off Mach number which avoids the divergence of some terms at small velocities. However, in the original version of AUSM$^+$−up, the pressure diffusion term in the advection part of the numerical flux scales with the inverse Mach number. This leads to spurious fluxes in simulations of hydrostatic atmospheres. It was therefore proposed by Miczek (2013) and Edelmann (2014) to use separate cut-off numbers for the pressure and advection term such that the strength of the pressure diffusion can be controlled separately. A more detailed description of the modified AUSM$^+$−up scheme is given in Section 2.1. Tests by Edelmann et al. (2019) and Berberich (2014) show that the results obtained with the AUSM$^+$−up

scheme are comparable with the preconditioned Roe solver. Although AUSM$^+$−up shows some improved behavior regarding stability compared to the preconditioned Roe solver, spurious flows also develop with this scheme if it is applied to astrophysical setups. This issue is discussed in detail in Section 2.1 along with strategies to suppress the arising instabilities. It is shown that the combination of the AUSM$^+$−up scheme with suitable "well-balancing" techniques that reduce the effective pressure gradient is a promising approach to simulating low-Mach flows in astrophysics.

1.4.3 Time stepping

An additional challenge of low-Mach flows is the efficiency of common time integration schemes. Eq. (1.29) can be written in compact form (this approach is called "method of lines") as

$$\frac{\partial \vec{U}_{i,j,k}}{\partial t} + \vec{R}_{i,j,k}(\vec{U}) = \vec{0}, \tag{1.36}$$

showing that the numerical formulation separates into a spatial discretization (discussed in the previous section) and a temporal discretization that will be briefly discussed here. This separation allows choosing numerical methods for time and space independently from each other which eases implementing and testing new schemes.

A common approach for the time integration is explicit time stepping where the new state of the flow is calculated from the knowledge of the current state alone. A simple example of such an explicit scheme is the forward-Euler method

$$\vec{U}^{n+1}_{i,j,k} = \vec{U}^{n}_{i,j,k} - \vec{R}_{i,j,k}(\vec{U}^n)\,\Delta t, \tag{1.37}$$

where the superscript n denotes the state of the system after n time steps. The implementation, also of even more elaborate schemes of higher order as for example multi-stage Runge-Kutta methods (e.g., Shu and Osher, 1988), does not require large coding effort. Furthermore, the efficiency of the calculation of a single explicit time step is mainly determined by the calculation of $\vec{R}_{i,j,k}$. However, the step sizes Δt of explicit time stepping are restricted by the Courant-Friedrichs-Lewy (CFL) criterion (e.g., LeVeque, 2002) which is a necessary condition for numerical stability. Thus, for low-Mach flows the maximum time step is essentially given by the sound crossing time of the smallest grid cell. This requires a huge number of time steps in order to evolve flows at low Mach numbers and explicit schemes become inefficient.

In contrast, if implicit time stepping is performed, the time step size is not restricted by stability reasons but by the desired accuracy alone. It is essentially determined by the minimum time the flow of interest, as for instance convective flows, needs to cross one grid cell. One simple example of an implicit scheme is the backward Euler method

$$\vec{U}^{n+1}_{i,j,k} = \vec{U}^{n}_{i,j,k} - \vec{R}_{i,j,k}(\vec{U}^{n+1})\,\Delta t\,. \tag{1.38}$$

Here, the calculation requires the spatial part of the equation evaluated at the unknown new state, $R_{i,j,k}(\vec{U}^{n+1})$, hence Eq. (1.38) is an implicit equation for the new state $\vec{U}^{n+1}$. Consequently, to obtain the new state, a non-linear system of equations needs to be solved. Compared to explicit schemes, this implies a considerably larger computational effort per time step. More elaborate implicit methods of higher order, for example the ESDIRK schemes (e.g., Hosea and Shampine, 1996; Kennedy and Carpenter, 2001), even require the subsequent solution of several non-linear systems. However, the increasing time step sizes that are permitted by implicit methods for decreasing flow speeds eventually overcompensate the

computational costs of one time step compared to explicit methods. The implicit method in the SLH code becomes more efficient for flows below Ma $\sim 10^{-2}$ (Miczek, 2013). This threshold, however, depends on the details of the spatial discretization (like the number of cells, reconstruction schemes, or flux function).

In SLH, the non-linear equations are solved using the Newton-Raphson method that involves solving a system of linear equations. Because of the huge number of equations[7], memory requirements prohibit a direct solution and iterative solvers are more suitable, see Miczek (2013). Some aspects of time stepping are further discussed in Sections 2.1 and 2.3.

1.5 Motivation

The previous sections illustrate that current theories and parametrizations of dynamical, multidimensional phenomena inside stars are insufficient. Classical MLT is known to capture the turbulent nature of convection inaccurately and it is not able to describe mixing of material at the boundaries of convection zones. A variety of prescriptions for CBM exists, however, each of which requires its own calibration. Asteroseismic studies reveal shortcomings of current stellar evolution models and that additional mixing in radiative envelopes of massive stars is required.

Comparisons between observations and 1D calculations are important benchmarks for current 1D models but it is difficult to develop new or improved prescriptions of complex dynamical phenomena from such comparisons alone. An example is the asteroseisimic study by Bellinger et al. (2019) which indicates that mixing processes may be still missing in current state-of-the-art 1D simulations but the origin of this process remains unclear.

Multidimensional hydrodynamic simulations are suitable to improve this situation. They are parameter-free and do not require calibration. The turbulent flow can be directly followed and simulations allow studying the action of hydrodynamic phenomena, as for instance the mixing of elements and excitation of waves. Hence, simulations can be used to identify processes not yet included in 1D simulations, as for example the angular momentum transport and mixing by IGW (Rogers et al., 2013; Rogers and McElwaine, 2017; Edelmann et al., 2019; Higl et al., 2021). Another example is the "321D" project that aims at replacing standard MLT by Reynolds-averaged Navier-Stokes equations in combination with 3D simulations (Arnett et al., 2015). In this thesis, several hydrodynamics simulations are performed to investigate CBM in different setups (see further Section 2.2) and to simulate excitation of IGW by convection (see further Section 2.3). Typically, the Mach number for such setups is expected to be very low. As discussed in Section 1.4, this leads to numerical difficulties because of long timescales, numerical dissipation, and because it is challenging to avoid spurious flows.

What can be found in the literature

Few publications specifically address simulations of low-Mach convection in astrophysical setups. Typically, a finite-volume approach is chosen and the lowest achieved Mach numbers range around 10^{-3} in more experimental simulations, but often the actual analysis is done for runs where the velocities are a factor of a few larger. Either the velocity of convection in the chosen setups is naturally at feasible Mach rumbers (e.g., Woodward et al., 2015; Jones et al., 2017), simulations are boosted (e.g., Rogers et al., 2013; Edelmann et al., 2019; Cristini

[7] For a typical simulation of 512^3 grid cells, the number of equations that need to be solved in every step is about $N_{\mathrm{var}} \times N_{\mathrm{cells}} \sim 0.7 \times 10^9$, where N_{var} is the number of conserved variables, that is ρ, $\rho\vec{u}$, and ρE.

et al., 2019), or follow only a short amount of time at nominal luminosity (e.g., Meakin and Arnett, 2007b; Cristini et al., 2019).

An exception is the simulation of convective hydrogen core burning in a $15\,M_\odot$ star by Gilet et al. (2013) who use the MAESTRO code (Almgren et al., 2007; Nonaka et al., 2010; Fan et al., 2019) which is particularly designed for low-Mach flows. Based on the data published by Gilet et al. (2013), one can infer a typical convective velocity in their simulations of $\mathrm{Ma} \sim 6 \times 10^{-4}$. This is in the regime predicted by MLT for similar stars. MAESTRO solves a modified version of the Euler equations in order to exclude sound waves from simulations and to ensure correct scaling of leading order terms in the limit of low Mach numbers. The exclusion of fast sound waves makes time stepping much more efficient as it relaxes the strict CFL criterion. However, the modified Euler equations are only strictly valid in the low-Mach limit. It is therefore difficult to simulate slow and fast flows at the same time. Because the Mach number of waves can become large in the envelope and for stability reasons, Gilet et al. (2013) need to damp the velocities in the outer parts of the computational domain and large parts of the stable envelope are excluded in the simulations. The "all-Mach" approach of the SLH code does not have these restrictions. Its capability to simultaneously evolve slow core convection and fast wave propagation is demonstrated in Section 2.3.

An approach similar to that taken in SLH is followed by the MUSIC code (Viallet et al., 2016; Goffrey et al., 2017). It solves the unmodified Euler equations and applies implicit time stepping, using a memory efficient method to solve the non-linear systems. Benchmark tests without gravity show that it is able to evolve flows at Mach numbers down to $\mathrm{Ma} \approx 10^{-6}$ (Viallet et al., 2016). However, to the author's knowledge, simulations of stellar convection for $\mathrm{Ma} \leq 10^{-3}$ have not yet been published. In the red giant simulation of Viallet et al. (2013b) the typical Mach number ranges from 10^{-1} at the top to 10^{-2} at the bottom of the convection zone. The recent series by Pratt et al. (2016, 2017, 2020) considers convection in the envelope of a young sun model. The authors do not explicitly state the Mach numbers reached in their simulation, however, in similar models the typical Mach numbers are expected to range from 10^{-3} to 10^{-2} (Viallet et al., 2013a, 2016; Popov et al., 2019).

Besides the finite-volume approach, also spectral methods are commonly used for fluid dynamic simulations. While they are not ideal for fast flows with shocks and discontinuities, flows in the intermediate- and low-Mach regime are smooth and therefore well accessible to spectral methods. Lecoanet et al. (2016) compare the simulations of 2D Kelvin-Helmholtz instabilities with the pseudo-spectral DEDALUS code (Burns et al., 2020) and the finite-volume code ATHENA (Stone et al., 2008). Their results suggest that for this particular test setup, the finite-volume approach requires a grid resolution eight times higher in each dimension to reach the same accuracy as DEDALUS. Anders and Brown (2017) use the DEDALUS code to simulate Rayleigh-Bénard convection in stratified atmospheres. In their simulations, the smallest achieved Mach numbers are $\mathrm{Ma} \sim 10^{-4}$. Spectral codes therefore appear to be a promising approach for low-Mach simulations of realistic astrophysical setups. In Section 2.3 a first comparison between the SLH code and the pseudo-spectral SPIN code (Edelmann et al., 2019) is made for the case of IGW excitation and propagation. A more comprehensive comparison, including other codes as for instance DEDALUS, would certainly be interesting, also regarding the respective computational efficiency and ability to follow CBM in stellar convection zones at low Mach numbers.

Low-Mach number simulations are needed

Because of the difficulties of high dissipation and inefficient time stepping in typical explicit non low-Mach schemes, it is common to artificially increase the velocities, for example by boosting the energy generation by orders of magnitude (e.g., Rogers et al., 2013; Edelmann

et al., 2019; Cristini et al., 2019; Käpylä, 2021a; Baraffe et al., 2021, see also Chapter 2). The results (e.g., the mixing rate) are then scaled from the boosted simulation to the nominal luminosity. Yet, it is unclear whether such a simple scaling over orders of magnitude is correct because artificial boosting changes the relation of characteristic scales of the different processes involved. For example, the Péclet number (the ratio of diffusion timescale to convection timescale) changes if the thermal diffusivity is not scaled accordingly. However, if the Péclet number is kept constant by increasing thermal diffusivity, the Prandtl number Pr (i.e., the ratio of kinematic viscosity to thermal diffusivity) will become smaller. Also, the length scales of advective processes are proportional to the timescale, while diffusive processes scale with the square root of the timescale. Thus, it is not possible to create fully equivalent simulations at different driving strengths. The effect of different characteristic numbers on the overshooting depth of convection was studied in detail by Käpylä (2019, 2021b), although the simulated flows are only mildly turbulent and probe a regime that is rather different from actual stellar conditions. Käpylä (2019, 2021b) finds only weak dependence of the overshooting depth on the Péclet number but a strong dependence on the Prandtl number. In simulations of the convective envelope of a solar-like star, Baraffe et al. (2021) find that an artificial boosting of the luminosity and thermal diffusivity may alter the mixing efficiency at the convective boundary. They argue that this may because of a changed interplay between local heating by convective penetration into the adjacent stable layers and the radiative energy transport.

Another problem of boosting is that a faster convective flow will excite IGW at higher frequencies and larger amplitudes. This also implies different spatial scales of the waves relative to other length scales of the system. This will inevitably change how they are affected by dissipative processes such as thermal diffusion and how they contribute to mixing. Larger wave amplitudes can also lead to additional non-linear effects. Artificial boosting will also change the impact of rotationally induced phenomena like meridional circulation or shear instabilities and the rotation rate would need to be scaled accordingly, leading to stronger instabilities and deformation than in the actual star. This demonstrates that the flow properties in boosted astrophysical simulations likely change compared to the unboosted cases. It is therefore desirable to perform simulations as close as possible to stellar values, in particular at the low Mach numbers that are expected inside stars. To enable such simulations is one of the main goals in the development of the SLH code. As indicated in Section 1.4 and demonstrated in the following sections, this is an ambitious project which requires a careful choice of the numerical ingredients because of the rather extreme scales of stars.

Goals of this thesis

The functionality of the SLH code has been extended and the code was applied to different astrophysical setups in the past. An analysis of results regarding their physical plausibility with a focus on low Mach numbers considerably below 10^{-2} is, however, still lacking for such setups.

One aspect of this thesis is therefore to assess the fundamental capabilities of the code by performing simulations of basic test setups that include gravity and for which a clear expectation for the results exists. Examples are tests on stable atmospheres (Section 2.1) or the evolution of linear IGW with small group velocities (Section 2.3). Some tests are inspired by the tests of Miczek (2013) and Edelmann (2014) but reinvestigated here in a more systematic way and with improved versions of the SLH code and the test setups. These basic simulations are important to identify current limitations of the code which may be less obvious in more complex simulations.

The other aspect of this thesis is to apply the SLH code to realistic but simple astrophysical

setups that involve convection for which MLT predicts low Mach numbers. The setups are realistic in the sense that they are based on 1D stellar-structure models as obtained from stellar evolution simulations but simple as these regions are chosen such that they do not involve additional complex processes (as, for instance, complicated feedback from nuclear burning, changes of the background structure, rotation, magnetic fields, and the like). For these setups, expectations from linear wave theory or basic flow properties like turbulent velocity spectra and kinetic energy dissipation are compared to the results obtained from the simulations. This provides a further, important test of the validity of the results obtained with the SLH code in slightly more complex simulations compared to plain test setups. At the same time they still provide insights to current astrophysical problems. In particular, the entrainment is measured at the boundaries of a convective burning shell in a MS star (Section 2.2). This allows the comparison with and the enlargement of the parameter space of simulations already covered by other groups. The chosen setup to study the excitation of waves by core convection (Section 2.3) is well suited to reveal the benefits of SLH simulations through comparison to simulations with codes that follow a different numerical approach. From the simulations, velocity spectra are extracted which, with some precautions, can guide the interpretation of observed stellar oscillation phenomena like the low-frequency excess observed in massive stars (Section 1.3).

CHAPTER 2

Results

In this Chapter, the main results of the thesis are presented. The content consists of three papers that have been published in the peer-reviewed journal *Astronomy & Astrophysics*[8]. The order of the sections does not follow the respective date of publication but was changed to better reflect the dependency of the content. Each section is preceded by a short introduction that describes the main context. The results are summarized in Section 3.1 and further discussed in Section 3.2.

[8] https://www.aanda.org

2.1 Publication I: Well-balancing

The publication in this section presents SLH simulations for a set of test problems while applying three different well-balancing methods in combination with the AUSM$^+$−up flux. The results are investigated regarding the improved accuracy at which small perturbations are simulated on top of strongly stratified atmospheres if well-balancing is applied.

During most of a star's evolution, self-gravity is balanced by a pressure gradient. In this hydrostatic equilibrium, pressure and density may vary over orders of magnitude from the center of a star to its surface regions. Hydrodynamic phenomena, as for example turbulent flows in convective regions, can be seen as small perturbations on top of the hydrostatic background stratification. Thus, if stellar hydrodynamics are to be simulated, it is crucial that the applied numerical tool is able to maintain the hydrostatic background to a high accuracy.

This is not trivial to achieve with finite-volume codes because typically pressure and gravity are discretized in different ways: The effect of a pressure gradient is included in the flux function while gravity is included as an additional source term. Hence, even though the initial conditions from which the numerical grid is initialized is in perfect hydrostatic equilibrium, this is not guaranteed for the discretized equations (see section 4 in the publication below for a simple example). Imperfect balancing leads to a non-zero flux across the cell interfaces and thus to spurious flows. The resulting error accumulates over the course of the simulation and is particularly problematic for simulations at low Mach numbers as the artificial flow will quickly deteriorate the physical flow.

Furthermore, as discussed in Section 1.4, the numerical flux function which calculates the flows in and out of the discrete volumes in the finite-volume approach has to be appropriate for low-Mach flows. However, in applications involving strong hydrostatic stratifications, low-Mach flux functions are prone to develop spurious, self-amplifying checkerboard-like structures in the pressure and density fields. The resulting unphysical flow then often dominates over the flow of interest (e.g., see Miczek, 2013, Edelmann, 2014, and the publication below). One possible explanation for this numerical artifact is the reduced pressure-velocity coupling of low-Mach flux functions such that the checkerboard modes are not damped efficiently enough. The excessive dissipation prevailing in conventional numerical flux functions makes them robust against checkerboard modes but inadequate for simulations of low-Mach flows.

The simulations presented in the following paper use a variant of the low-Mach AUSM$^+$−up flux which applies an explicit pressure-diffusion term to enhance pressure-velocity coupling. But this pressure-diffusion term may lead to spurious flows in the vertical direction in astrophysical setups because of the involved strong pressure gradient. The AUSM$^+$−up flux is therefore not directly applicable to astrophysical setups. However, the ability of a numerical scheme to maintain hydrostatic equilibrium and the performance of the AUSM$^+$−up flux can be significantly improved through the application of "well-balancing" techniques. Three novel methods are investigated in the publication presented in this section. These schemes utilize the prior knowledge of the hydrostatic stratification such that only perturbations of the hydrostatic background enter the flux. Thus, in the absence of perturbations, the flux is zero up to machine precision. Furthermore, applying these methods is beneficial in combination with the AUSM$^+$−up scheme: With well-balancing, the stabilizing pressure-diffusion term of AUSM$^+$−up only acts on the perturbations but not on the general background stratification. This prevents the scheme from artificially generating vertical velocities in astrophysical setups.

The presented publication first describes the three tested well-balancing schemes and the

modified AUSM$^+$−up hydro flux. Subsequently, each combination of the AUSM$^+$−up scheme with the tested well-balancing schemes is applied to four test-scenarios which involve hydrostatic stratifications and low-Mach flows similar to those expected inside real stars. The results are analyzed regarding hydrostatic stability and physical expectation. It is found that the AUSM$^+$−up flux in combination with the Deviation well-balancing method is a promising approach which is able to keep a hydrostatic atmosphere stable for long enough times and to simulate convection at Mach numbers expected in stellar interiors. While the schemes are tested with the AUSM$^+$−up flux and the SLH code, they can also be used in different codes and combined with other numerical flux functions.

Title
Well-balanced treatment of gravity in astrophysical fluid dynamics simulations at low Mach numbers

Authors
P. V. F. Edelmann, L. Horst, J. P. Berberich, R. Andrassy, J. Higl, G. Leidi, C. Klingenberg, F. K. Röpke

Publication Status
The manuscript was published on August, 2021.

DOI
10.1051/0004-6361/202140653

Author's contributions
PVFE is the principal author of this paper. The project idea was developed in a collaboration between PVFE and FR from the astrophysics group and CK from the Mathematics department of the University Würzburg. The initial implementation of the three tested well-balancing schemes was done by PVFE and JB. LH contributed through bug fixing, smaller improvements, and extensive testing. In collaboration with JB, LH implemented a framework to the SLH code that generalized the initialization of the different schemes. PFVE, RA, JH, and LH were each responsible to simulate and analyze one of the presented test simulations, as well as writing the respective section. LH designed and performed the convective box simulations which are the most complex simulations in the paper. LH further contributed parts of the introduction and theory sections and wrote the conclusion section. All authors actively contributed to discussing and interpreting the results and to the writing of the final text of the paper.

Credit

A&A 652, A53 (2021)
https://doi.org/10.1051/0004-6361/202140653

Astronomy & Astrophysics

Well-balanced treatment of gravity in astrophysical fluid dynamics simulations at low Mach numbers

P. V. F. Edelmann[1,2,3], L. Horst[2], J. P. Berberich[4], R. Andrassy[2], J. Higl[2], G. Leidi[2,5], C. Klingenberg[4], and F. K. Röpke[2,6]

[1] X Computational Physics (XCP) Division and Center for Theoretical Astrophysics (CTA), Los Alamos National Laboratory, Los Alamos, NM 87545, USA
e-mail: philipp@slh-code.org
[2] Heidelberger Institut für Theoretische Studien, Schloss-Wolfsbrunnenweg 35, 69118 Heidelberg, Germany
[3] Faculty of Physics and Astronomy, Würzburg University, Am Hubland, 97074 Würzburg, Germany
[4] Department of Mathematics, Würzburg University, Emil-Fischer-Str. 40, 97074 Würzburg, Germany
[5] Zentrum für Astronomie der Universität Heidelberg, Astronomisches Rechen-Institut, Mönchhofstr. 12-14, 69120 Heidelberg, Germany
[6] Zentrum für Astronomie der Universität Heidelberg, Institut für Theoretische Astrophysik, Philosophenweg 12, 69120 Heidelberg, Germany

Received 24 February 2021 / Accepted 29 June 2021

ABSTRACT

Context. Accurate simulations of flows in stellar interiors are crucial to improving our understanding of stellar structure and evolution. Because the typically slow flows are merely tiny perturbations on top of a close balance between gravity and the pressure gradient, such simulations place heavy demands on numerical hydrodynamics schemes.
Aims. We demonstrate how discretization errors on grids of reasonable size can lead to spurious flows orders of magnitude faster than the physical flow. Well-balanced numerical schemes can deal with this problem.
Methods. Three such schemes were applied in the implicit, finite-volume SEVEN-LEAGUE HYDRO code in combination with a low-Mach-number numerical flux function. We compare how the schemes perform in four numerical experiments addressing some of the challenges imposed by typical problems in stellar hydrodynamics.
Results. We find that the α-β and deviation well-balancing methods can accurately maintain hydrostatic solutions provided that gravitational potential energy is included in the total energy balance. They accurately conserve minuscule entropy fluctuations advected in an isentropic stratification, which enables the methods to reproduce the expected scaling of convective flow speed with the heating rate. The deviation method also substantially increases accuracy of maintaining stationary orbital motions in a Keplerian disk on long timescales. The Cargo–LeRoux method fares substantially worse in our tests, although its simplicity may still offer some merits in certain situations.
Conclusions. Overall, we find the well-balanced treatment of gravity in combination with low Mach number flux functions essential to reproducing correct physical solutions to challenging stellar slow-flow problems on affordable collocated grids.

Key words. hydrodynamics – methods: numerical – convection

1. Introduction

Astrophysical modeling often involves self-gravitating fluids. They are commonly described by the equations of fluid dynamics with a gravitational source term – viscous effects are negligible in most astrophysical systems and therefore the nonviscous Euler equations are used. Such systems can attain stationary equilibrium configurations in which a pressure gradient balances gravity, that is hydrostatic equilibrium. A prominent example are stars, modeled in classical approaches as spherically symmetric gaseous objects. Apart from this dimensional reduction, the assumption of hydrostatic equilibrium considerably simplifies the modeling of the – in reality rather complex – structure of stars. The resulting equations of stellar structure (e.g., Kippenhahn et al. 2012) enable successful qualitative modeling of the evolution of stars through different stages. The price for this success is a parametrization of multidimensional and dynamical processes that limits the predictive power of such theoretical models and requires their calibration with observations. Recent attempts to simulate inherently multidimensional and dynamical processes, such as convection in stellar interiors (e.g., Browning et al. 2004; Meakin & Arnett 2006, 2007; Woodward et al. 2015; Rogers et al. 2013; Viallet et al. 2013; Pratt et al. 2016; Müller et al. 2016; Cristini et al. 2017; Edelmann et al. 2019; Horst et al. 2020), have tried to overcome this shortcoming.

Such simulations pose a number of challenges to the underlying numerical techniques. Not only is the range of relevant spatial and temporal scales excessive, but the flows of interest arise in a configuration that is often close to hydrostatic equilibrium. This has two implications: (i) The schemes must be able to preserve hydrostatic equilibrium in stable setups over a long period of time compared to the typical timescales of the flows of interest. (ii) The flow speed v expected to arise from a small perturbation of the equilibrium configuration should be slow compared to the speed of sound c, thus the corresponding Mach number, $\mathcal{M} \equiv v/c$, is expected to be low.

If we decide to avoid approximating the equations and include all effects of compressibility, aspect (ii) above calls for special low-Mach-number solvers in numerical fluid dynamics combined with time-implicit discretization to enable time steps determined from the actual fluid velocity instead of the speed of sound as required by the CFL stability criterion (Courant et al. 1928) of time-explicit schemes. The propagation of sound waves is irrelevant for the problems at hand. Several suitable methods are implemented in the SEVEN-LEAGUE HYDRO (SLH) code. Numerical and theoretical details are discussed in Barsukow et al. (2017b,a), Edelmann & Röpke (2016), Miczek et al. (2015), Edelmann (2014), and Miczek (2013), and examples of the application to astrophysical problems can be found in Horst et al. (2020), Röpke et al. (2018), Edelmann et al. (2017), Michel (2019), and Bolaños Rosales (2016).

Aspect (i), however, also requires attention. The condition for hydrostatic equilibrium is part of the equations of stellar structure, that are discretized and numerically solved in classical stellar evolution modeling approaches. In contrast, hydrostatic equilibrium is only a special solution to the full gravo-hydrodynamic system at the level of the partial differential equations, but it is not guaranteed that discretizations of these equations can reproduce the physically correct equilibrium state. This is in particular the case because gravitational source terms are usually treated in an operator-splitting approach, resulting in different discretizations of the pressure and gravity terms. Astrophysical fluid dynamics simulations often employ finite-volume schemes, in which hydrodynamical flows are modeled with a Godunov-type flux across cell interfaces. Hydrodynamical quantities are therefore determined at these locations. The gravitational source term, in contrast, is discretized in a completely different and independent way. In a second-order code, for example, it is often calculated using cell-averaged densities assigned to cell centers. In general, this procedure does not lead to an exact cancellation of gravity and pressure gradient in hydrostatic configurations. Spurious motions are introduced that mask the delicate low-Mach-number flows arising from perturbations of this equilibrium, such as, for instance, convection driven by nuclear energy release.

To overcome the problem of aspect (i), so-called well-balancing methods have been introduced, which are numerical methods that ensure exact preservation of certain stationary states. Methods of this type have predominantly been developed for the simulation of shallow-water-type models in order to resolve stationary solutions such as the lake-at-rest solution without numerical artifacts (e.g., Brufau et al. 2002; Audusse et al. 2004; Bermudez & Vázquez 1994; LeVeque 1998; Desveaux et al. 2016a; Touma & Klingenberg 2015; Castro & Semplice 2018; Barsukow & Berberich 2020). These stationary states can be described using an algebraic relation, which favors the development of well-balanced methods. In the simulation of hydrodynamics under the influence of a gravitational field, the situation is different, since hydrostatic solutions are described by a differential equation that admits a large variety of solutions that depend on temperature and chemical composition profiles, as well as the equation of state (EoS). In practice, the concrete hydrostatic profile is determined by equations describing physical processes other than hydrodynamics and gravity, such as thermal and chemical transport and the change in energy and species abundance due to reactions.

Different approaches can be used to deal with this: The majority of well-balanced methods for the Euler equations with gravity, for example Chandrashekar & Klingenberg (2015), Desveaux et al. (2016b), Touma et al. (2016), and references therein, are designed to only balance certain classes of hydrostatic states, often isothermal, polytropic, or isentropic stratifications, under the assumption of an ideal gas EoS. However, for many astrophysical applications, in particular, cases involving late stellar evolutionary stages and massive stars, non-ideal effects of the gas may be important. In stellar interiors, the most important additions to the ideal gas EoS are radiation pressure and electron degeneracy effects. This requires a more complex – often in parts tabulated – EoS to properly describe the thermodynamical properties of the gas. We discuss an example of such an EoS in Sect. 2.2.2. Well-balanced methods which are capable of balancing hydrostatic states for general EoS have been introduced by Cargo & Le Roux (1994), Käppeli & Mishra (2014, 2016), Grosheintz-Laval & Käppeli (2019), Berberich et al. (2018, 2019, 2020, 2021), and Berberich (2021).

Most methods that have been discussed in the astrophysical context and literature (e.g., Zingale et al. 2002; Perego et al. 2016; Käppeli et al. 2011; Käppeli & Mishra 2016; Popov et al. 2019) balance a second-order approximation of the hydrostatic state rather than the hydrostatic state itself. Another recent approach is the well-balanced, all-Mach-number scheme by Padioleau et al. (2019). None of these publications tested a low-Mach-number, well-balanced method in more than one spatial dimension in a stable stratification over long timescales. As we show in this paper, long-term stability cannot be automatically inferred from one-dimensional (1D) tests, yet it is of fundamental importance for applications in stellar astrophysics.

Using a staggered grid, which in this context means storing pressure on the cell interfaces instead of the cell centers, can alleviate some of the problems of well-balancing the atmosphere, as shown, for example, in the MUSIC code (Goffrey et al. 2017, Sect. 6). For this approach, it still has to be shown that convective velocities scale correctly with the strength of the driving force at low Mach numbers, which we found very challenging in our approach, see Sect. 5.3.

The methods introduced in Berberich et al. (2018, 2019, 2021) can balance any hydrostatic stratification exactly. The only assumption is that the hydrostatic solution to be balanced is known a priori. This poses no severe restriction for many astrophysical applications where the initial condition is often constructed under the assumption of hydrostatic equilibrium. An example are simulations of stellar convection, where the initial model is commonly derived from classical stellar evolution calculations that by construction impose hydrostatic equilibrium. In this context exact well-balancing refers to preserving an initial state, which can be calculated to arbitrary precision, and not to the exactness of other input physics, such as the EoS.

Here, we discuss three possible well-balancing methods that follow rather different approaches. The first method extends the work of Cargo & Le Roux (1994) which only applied to 1D setups into the three-dimensional (3D) case and achieves well-balancing by modifying the pressure part of a general EoS. We refer to this as the Cargo–LeRoux (CL) well-balancing method. The other two methods modify how variables are extrapolated to the cell interfaces. We refer to them as the α-β well-balancing (Berberich et al. 2018, 2019) and the deviation well-balancing method (Berberich et al. 2021). For these three schemes, we describe their theoretical background and study their impact on the accuracy of solutions to a set of simplified test problems, which are designed to resemble typical situations in astrophysics.

The structure of the paper is as follows: Sect. 2 reviews the basic set of equations of fluid dynamics and their implications.

It also introduces the notation that is used in the subsequent sections. In Sect. 3 we discuss the discretization of these equations and describe the AUSM$^+$-up flux used in the later tests. The well-balancing schemes are introduced in Sects. 4.1–4.3. In Sect. 5 we test the applicability of the well-balancing methods and their performance in an extensive suite of simple application examples. Conclusions are drawn in Sect. 6.

2. Equations of compressible, ideal hydrodynamics

This section introduces the general set of equations that are solved with the SLH code in their formulation in general coordinates. The following subsections closely follow the presentation of Miczek (2013).

2.1. Compressible Euler equations

We employ *curvilinear coordinates* $\boldsymbol{x} = (x, y, z) = (x^1, x^2, x^3)$ with a smooth mapping,

$$\boldsymbol{x} : \mathbb{R}^3 \to \mathbb{R}^3, \ \boldsymbol{x} \mapsto \boldsymbol{x}(\boldsymbol{\xi}), \tag{1}$$

to Cartesian coordinates $\boldsymbol{\xi} = (\xi, \eta, \zeta) = (\xi^1, \xi^2, \xi^3)$. The reasoning here is that the coordinates $\boldsymbol{\xi}$ simplify the computations, while the coordinates $\boldsymbol{x}$ are adapted to the physical object, such as a spherical star.

The compressible Euler equations on curvilinear coordinates then read

$$J\frac{\partial \boldsymbol{u}}{\partial t} + A_\xi \frac{\partial \boldsymbol{f}_\xi}{\partial \xi} + A_\eta \frac{\partial \boldsymbol{f}_\eta}{\partial \eta} + A_\zeta \frac{\partial \boldsymbol{f}_\zeta}{\partial \zeta} = J\boldsymbol{s}, \tag{2}$$

with the vector $\boldsymbol{u}$ of conserved variables and the fluxes $\boldsymbol{f}_{\xi^l}$ given by

$$\boldsymbol{u} = \begin{pmatrix} \varrho \\ \varrho u \\ \varrho v \\ \varrho w \\ E \end{pmatrix}, \quad \boldsymbol{f}_{\xi^l} = \begin{pmatrix} \varrho\, \boldsymbol{n}_{\xi^l}^T \boldsymbol{v} \\ \varrho u\, \boldsymbol{n}_{\xi^l}^T \boldsymbol{v} + (n_{\xi^l})_x p \\ \varrho v\, \boldsymbol{n}_{\xi^l}^T \boldsymbol{v} + (n_{\xi^l})_y p \\ \varrho w\, \boldsymbol{n}_{\xi^l}^T \boldsymbol{v} + (n_{\xi^l})_z p \\ \boldsymbol{n}_{\xi^l}^T \boldsymbol{v}\,(E + p) \end{pmatrix}, \tag{3}$$

for $l = 1, 2, 3$. Here, density and pressure are denoted by ϱ and p, respectively. The velocity vector, expressed through its curvilinear components, reads $\boldsymbol{v} = (u, v, w)$ and enters the equation for the total energy density $E = \varrho\epsilon + \frac{1}{2}\varrho|\boldsymbol{v}|^2 + \varrho\phi$ with the specific energy ϵ and the gravitational potential ϕ. The inclusion of the potential in the total energy does not lead to numerical difficulties here because it is similar in magnitude to the internal energy in a stellar context in general and in all the test problems presented in Sect. 5 in particular. This is possibly different in other situations, where one of the energies is much larger and cancellation errors can become a problem.

The Euler Eq. (2) in their curvilinear form in depend on the derivatives of the coordinate transformation. Its Jacobi determinant is

$$J = \left|\frac{\partial \boldsymbol{x}}{\partial \boldsymbol{\xi}}\right| = \sum_{l,m,n=1}^{3} \epsilon_{lmn} \frac{\partial x^l}{\partial \xi} \frac{\partial x^m}{\partial \eta} \frac{\partial x^n}{\partial \zeta}, \tag{4}$$

where ϵ_{lmn} is the three-dimensional Levi-Civita symbol. The normal vector $\boldsymbol{n}_{\xi^l}$ and interface area A_{ξ^l} in ξ^l-direction are

$$\boldsymbol{n}_{\xi^l} = \frac{J}{A_{\xi^l}} \begin{pmatrix} \frac{\partial \xi^l}{\partial x} \\ \frac{\partial \xi^l}{\partial y} \\ \frac{\partial \xi^l}{\partial z} \end{pmatrix}, \quad A_{\xi^l} = \sqrt{\left(J\frac{\partial \xi^l}{\partial x}\right)^2 + \left(J\frac{\partial \xi^l}{\partial y}\right)^2 + \left(J\frac{\partial \xi^l}{\partial z}\right)^2}. \tag{5}$$

External forces that enter Eq. (2) are – with an exception discussed below – collectively denoted by the source term $\boldsymbol{s}$. While there are different possible contributions, for example energy generation due to nuclear burning, gravity inevitably appears in any astrophysical setup. At the same time it might pose difficulties for hydrodynamical codes to maintain hydrostatic solutions to Eq. (2) (see Sect. 2.3) if it includes a strong gravitational source term as is common in the interior of stars. When gravity is the only source term, the expression for $\boldsymbol{s}$ reads

$$\boldsymbol{s} = \begin{pmatrix} 0 \\ -\varrho\frac{\partial \phi}{\partial x} \\ -\varrho\frac{\partial \phi}{\partial y} \\ -\varrho\frac{\partial \phi}{\partial z} \\ 0 \end{pmatrix}. \tag{6}$$

This adds gravitational forces to the momentum part of Eq. (2). The presence of a gravitational field also affects the evolution of total energy. We include this effect in the definition of the total energy rather than the source term, since this treatment significantly improved our accuracy in numerical experiments. We found this to be crucial in simulations of low Mach number convection.

The source term adds gravitational force to the momentum equations. For our current treatment and test setups, the gravitational potential ϕ is fixed in time and changes the mass distribution during the simulation is excluded, meaning self-gravity is neglected. It is a reasonable simplification if the setup is very close to hydrostatic equilibrium and the change in the mass distribution is negligible. Such an approximation, however, fails for stellar core simulations at later evolutionary stages, where asymmetries in the mass distribution may arise due to violent convective motions. However, these setups are not the typical use cases of the well-balancing techniques presented in this paper as deviations from hydrostatic equilibrium are nonnegligible. In our notation lower indices do not indicate partial derivatives to avoid confusion.

2.2. Equation of state

The common choice to close the Euler system Eq. (2) is using an EoS. There are few physically relevant EoS which can be given in a short, explicit analytical form. Two of these are discussed in the following. We assume that all components of the gas are in local thermodynamic equilibrium, that is they can all be described with a common temperature.

2.2.1. Ideal gas

The ideal gas is one of the simplest EoS, yet with a wide range of applications. It describes an ensemble of randomly moving, noninteracting particles in thermodynamic equilibrium. It is an acceptable model for terrestrial gases, such as air, for which the interactions between the particles are small. It serves well in the case of a fully ionized plasma, such as in the interior of stars, as long as the effects of degeneracy and radiation pressure are small.

The ideal gas pressure is given by

$$p(\varrho, \epsilon) = p(\varrho, T(\varrho, \epsilon)) = \frac{R}{\mu}\varrho T(\varrho, \epsilon), \tag{7}$$

with the temperature

$$T(\varrho, \epsilon) = \frac{(\gamma - 1)\mu}{R} \cdot \frac{\epsilon}{\varrho}. \tag{8}$$

The gas constant R for the ideal gas is $8.31446261815324 \times 10^7$ erg K^{-1} mol^{-1}. The specific heat ratio γ depends on the internal degrees of freedom in the underlying gas mixture, typical values are 5/3 for monatomic gases and 7/5 for diatomic gases. For our treatment, it is convenient to write the ideal gas EoS in the form of Eq. (7) depending on the temperature T instead of the explicit dependence of ϵ. We use this form of the EoS to formulate hydrostatic equilibria with certain temperature profiles.

2.2.2. Helmholtz equation of state

While the ideal gas is a useful approximation of the EoS of stellar interiors, it does not capture the effect of partially or fully degenerate electrons or of radiation pressure. A commonly used EoS that includes these effects to great precision is the Helmholtz EoS (Timmes & Swesty 2000). It relies on a interpolation of the Helmholtz free energy from tabulated values using biquintic Hermite polynomials. All other quantities are then derived from expressions involving derivatives of the Helmholtz free energy. This approach ensures that all thermodynamic consistency relations are fulfilled automatically. This EoS has a wide range of applicability and serves as a typical example of a general tabulated EoS, contrasting our approaches to some well-balanced methods relying on using a specific EoS, such as the ideal gas.

2.3. Hydrostatic solutions

Except for the very late stages of stellar evolution, stars can be considered as gaseous spheres, which change only over very long timescales, much longer that those of the fluid motions. Dynamical processes acting in the interiors, as for example convective motions, however, evolve on much shorter timescales. Thus, in hydrodynamical simulations that aim to follow such fast processes, a star can, to first order, be described as a static stratification with pressure and density profiles constant in time, that is

$$\boldsymbol{v} \equiv \boldsymbol{0},\ \varrho(t, \boldsymbol{x}) = \varrho(\boldsymbol{x}),\ \text{and}\ p(t, \boldsymbol{x}) = p(\boldsymbol{x}). \tag{9}$$

These conditions reduce the first and the last part of Eq. (2) to the trivial relations

$$\partial_t \varrho = 0 \qquad \text{and} \qquad \partial_t(\varrho E) = 0. \tag{10}$$

The momentum equations lead to the *hydrostatic equation*

$$\nabla p(\varrho, T) = -\varrho \nabla \phi. \tag{11}$$

This equation is invariant under transformations between different sets of curvilinear coordinates. A pair of constant-in-time functions ϱ and p, which satisfy Eq. (11) together with the chosen EoS is called hydrostatic solution or hydrostatic equilibrium. Since the EoS usually depends on temperature, there is in many cases a whole continuum of hydrostatic solutions rather than uniqueness.

Convective stability

Depending on the stratification, perturbations to the hydrostatic solution may lead to dynamical phenomena. One important example is convection, where hydrostatic equilibrium is not perfectly fulfilled anymore but deviations are small.

The criterion for stability against convection is typically derived by considering the behavior of a small fluid element being perturbed from the surrounding stratification. The frequency at which the element oscillates around its equilibrium position χ_0 is called the Brunt–Väisälä frequency N. Its square is given by

$$N^2 = \frac{\partial \phi}{\partial \chi} \frac{1}{\varrho_{\text{ext}}} \left(\frac{\partial \varrho_{\text{int}}}{\partial \chi} - \frac{\partial \varrho_{\text{ext}}}{\partial \chi} \right) \Bigg|_{\chi_0}, \tag{12}$$

where χ denotes the vertical coordinate[1], ϱ_{int} is the density of the small fluid element, and ϱ_{ext} is the density of the background stratification. It is assumed that the fluid element changes its state adiabatically, that is without exchanging heat with its surrounding, and the derivative $\partial \varrho_{\text{int}}/\partial \chi$ is interpreted as the adiabatic change of density while maintaining pressure equilibrium with the background stratification at height χ. For the full derivation of Eq. (12) we refer the reader to any textbook on stellar astrophysics (e.g., Maeder 2009; Kippenhahn et al. 2012).

It is common to express the gradients in Eq. (12) in terms of different variables. In the case of homogeneous composition ($\mu(\boldsymbol{x}) = \text{const.}$) Eq. (12) is equivalent to

$$N^2 = -\frac{\partial \phi}{\partial \chi} \frac{\partial}{\partial \chi} \left(\frac{s}{c_{\text{p}}} \right) = -\frac{\partial \phi}{\partial \chi} \frac{\delta}{T} \left[\frac{\partial T}{\partial \chi} - \left(\frac{\partial T}{\partial \chi} \right)_{\text{ad}} \right], \tag{13}$$

with specific entropy s and specific heat at constant pressure c_{p} and the equation of state derivative,

$$\delta = -\frac{\partial \ln \varrho}{\partial \ln T}, \tag{14}$$

which is 1 in the ideal gas case. The subscript "ad" denotes the adiabatic derivative as mentioned above.

Another common form of this equation is using a variant of the temperature gradients expressed using pressure as a coordinate,

$$\nabla = \frac{\partial \ln T}{\partial \ln p}. \tag{15}$$

Using this definition Eq. (12) is equivalent to

$$N^2 = -\frac{\partial \phi}{\partial \chi} \frac{\delta}{H_{\text{p}}} (\nabla - \nabla_{\text{ad}}), \tag{16}$$

with the pressure scale height,

$$H_{\text{p}} = -\frac{\partial \chi}{\partial \ln p} = -p \frac{\partial \chi}{\partial p}. \tag{17}$$

We call a hydrostatic equilibrium stable with respect to convection or convectively stable, if $N^2 \geq 0$. Otherwise we call it unstable with respect to convection or convectively unstable. This is a local definition, which means that a hydrostatic solution can be convectively stable in one region and convectively unstable in another. A suitable reference time for convectively stable setups is the minimal Brunt–Väisälä time

$$t_{\text{BV}} = \min_{\boldsymbol{x} \in \Omega} t_{\text{BV}}^{\text{loc}}(\boldsymbol{x}) = \frac{2\pi}{\max_{\boldsymbol{x} \in \Omega} N(\boldsymbol{x})}. \tag{18}$$

It seems to be a natural timescale for the evolution of small perturbations as explained for example in Berberich et al. (2019). For any hydrostatic solution, the value of N^2 can be either calculated analytically (for simple EoS, like the ideal gas EoS) or numerically for more complex EoS.

[1] That is the direction opposing the vector of gravitational acceleration.

Another useful timescale is the sound crossing time $t_{\rm SC}$ through the domain. Similar to Käppeli & Mishra (2016), we define $t_{\rm SC}$ in the direction of coordinate ξ^l as

$$t_{\rm SC} = 2 \min_{\xi^i, i\neq l} \int_{\xi^l_L}^{\xi^l_U} \mathrm{d}\xi^l \frac{1}{c\left(\xi^1, \xi^2, \xi^3\right)}, \tag{19}$$

with ξ^l_L and ξ^l_R being the lower and upper boundaries of the domain in that direction. The speed of sound c is calculated using the equation of state. An expression for the sound speed using a general equation of state is given by

$$c(\varrho, \epsilon) = \sqrt{\frac{\partial p(\varrho,\epsilon)}{\partial \varrho} + \frac{\partial p(\varrho,\epsilon)}{\partial \epsilon} \cdot \frac{\epsilon + p(\varrho,\epsilon)}{\varrho}}, \tag{20}$$

where the function for the pressure p comes from an equation of state (see Sect. 2.2).

3. Discretization

Analytic solutions to Eq. (2) as for example given by the hydrostatic solution of Sect. 2.3 are exceptions and require special initial conditions. To obtain more general solutions, which also allow for more complex dynamics such as turbulent convection developed from perturbations in a hydrostatic stratification, Eq. (2) needs to be solved numerically. While there are several different numerical approaches, this section focuses on the methods that are employed by the SLH code. For a more general introduction on this topic, see Toro (2009).

3.1. Finite-volume scheme

For the numerical solution, the underlying equations have to be discretized on a, possibly curvilinear, mesh that resembles the physical spatial domain. This grid is then mapped to Cartesian coordinates on which the computations are conducted. A set of integers $(i,\ j,\ k)$ denotes the center of the $(i,\ j,\ k)$-th cell while, for example, $(i+1/2,\ j,\ k)$ denotes the interface between cell $(i,\ j,\ k)$ and $(i+1,\ j,\ k)$. The semi-discrete finite-volume scheme is obtained by integrating Eq. (2) over the cell volume in computational space, leading to

$$\begin{aligned} V_{ijk}\frac{\partial \boldsymbol{U}_{ijk}}{\partial t} = &- A_{i+\frac{1}{2},j,k}(\hat{\boldsymbol{F}}_\xi)_{i+\frac{1}{2},j,k} + A_{i-\frac{1}{2},j,k}(\hat{\boldsymbol{F}}_\xi)_{i-\frac{1}{2},j,k} \\ &- A_{i,j+\frac{1}{2},k}(\hat{\boldsymbol{F}}_\eta)_{i,j+\frac{1}{2},k} + A_{i,j-\frac{1}{2},k}(\hat{\boldsymbol{F}}_\eta)_{i,j-\frac{1}{2},k} \\ &- A_{i,j,k+\frac{1}{2}}(\hat{\boldsymbol{F}}_\zeta)_{i,j,k+\frac{1}{2}} + A_{i,j,k-\frac{1}{2}}(\hat{\boldsymbol{F}}_\zeta)_{i,j,k-\frac{1}{2}} + V_{ijk}\hat{\boldsymbol{S}}_{ijk}, \end{aligned} \tag{21}$$

where V_{ijk} is the volume of the corresponding cell in physical space and $A_{i+\frac{1}{2},j,k}$, $A_{i,j+\frac{1}{2},k}$, and $A_{i,j,k+\frac{1}{2}}$ are the interface areas of the interfaces in ξ, η, and ζ-direction respectively. Details on the computation of cell volumes and interface areas are computed to second order following Kifonidis & Müller (2012). The cell-averaged source term is approximated to second order by

$$\hat{\boldsymbol{S}}_{ijk} = \varrho_{ijk} \begin{pmatrix} 0 \\ (g_x)_{ijk} \\ (g_y)_{ijk} \\ (g_z)_{ijk} \\ 0 \end{pmatrix}, \tag{22}$$

where ϱ_{ijk} is the cell-averaged value of density and the cell-centered gravitational acceleration $(g_\chi)_{ijk} = -\left.\frac{\partial \phi}{\partial \chi}\right|_{\boldsymbol{x}_{ijk}}$ is computed analytically from the given gravitational potential ϕ.

In Eq. (21), $\hat{\boldsymbol{F}}_{\xi^l}$ is an approximation of the interface flux for $l = 1, 2, 3$. There is some freedom in constructing the approximate flux function that calculates $\hat{\boldsymbol{F}}_{\xi^l}$ and many approaches can be found in the literature. However, the specific choice is crucial for the accuracy of the numerical solution. This is further discussed in Sect. 3.2 in the context of flows at low Mach numbers

$$M = \frac{|\boldsymbol{v}|}{c}, \tag{23}$$

where c is the speed of sound given by Eq. (20).

The values that enter the approximate flux function need to be reconstructed from the center of the cells to the corresponding interfaces. The reconstruction and the evaluation of the flux is done for each coordinate direction separately, before the resulting fluxes over the surfaces are added for each cell.

The semi-discrete scheme is then evolved in time using an ODE solver, such as a Runge–Kutta method. With an at least linear reconstruction and a sufficiently accurate ODE solver this discretization yields a second-order accurate scheme as has been numerically verified by Berberich et al. (2019). For the tests in this article we mainly use the implicit second-order accurate three step Runge–Kutta method ESDIRK23 of Hosea & Shampine (1996).

We chose an advective CFL time step (CFL_u), not strictly for reasons of stability, but as a good compromise between accuracy and efficiency. In curvilinear coordinates it takes the form

$$\Delta t_{\mathrm{CFL}_u} = c_{\mathrm{CFL}} \min_{ijkl} \frac{(\Delta\xi^l)_{ijk}}{|\boldsymbol{n}_{\xi^l} \cdot \boldsymbol{v}|_{ijk}}, \tag{24}$$

with a constant c_{CFL} of order unity and an estimate of the cell length in direction ξ^l given by

$$(\Delta\xi^1)_{ijk} = \frac{V_{ijk}}{\frac{1}{2}\left(A_{i-\frac{1}{2},j,k} + A_{i+\frac{1}{2},j,k}\right)}, \tag{25}$$

and accordingly for $(\Delta\xi^2)_{ijk}$ and $(\Delta\xi^3)_{ijk}$.

This time step criterion generally works well when the flow is fully developed, but it has problems when the Mach numbers on the grid are very small (e.g., in the beginning of a simulation with zero initial velocities), because this yields very large or infinite time steps. As a way to prevent this, Miczek (2013) suggests to include the free-fall signal velocity in the time step calculation. The so-called CFL_{ug} time step is then given by

$$\Delta t_{\mathrm{CFL}_{ug}} = c_{\mathrm{CFL}} \min_{ijkl} \frac{(\Delta\xi^l)_{ijk}}{s_{ijkl}}, \tag{26}$$

with the signal velocity

$$s_{ijkl} = \frac{1}{2}\left(a^l |\boldsymbol{n}_{\xi^l} \cdot \boldsymbol{v}| + \sqrt{|\boldsymbol{n}_{\xi^l} \cdot \boldsymbol{v}|^2 + 4a^l c_{\mathrm{CFL}} (\Delta\xi^l) \boldsymbol{n}_{\xi^l} \cdot \boldsymbol{g}}\right)_{ijk}. \tag{27}$$

The parameter a^l selects the right branch of the quadratic solution and is given in Table 1.

For Mach numbers close to $M = 1$, however, it is usually more efficient to use explicit time stepping. For this we use the third-order accurate RK3 scheme of Shu & Osher (1988) with a CFL_{uc} time step controlled by the fluid velocity and sound speed. It is given by

$$\Delta t_{\mathrm{CFL}_{uc}} = \frac{c_{\mathrm{CFL}}}{N_{\mathrm{dim}}} \min_{ijkl} \frac{(\Delta\xi^l)_{ijk}}{|\boldsymbol{n}_{\xi^l} \cdot \boldsymbol{v}|_{ijk} + c_{ijk}}, \tag{28}$$

Table 1. Parameter a^l used in the computation of the signal velocity in Eq. (27).

Condition	a^l
$\boldsymbol{n}_{\xi^l} \cdot \boldsymbol{v} > 0, \boldsymbol{n}_{\xi^l} \cdot \boldsymbol{g} > 0$	$+1$
$\boldsymbol{n}_{\xi^l} \cdot \boldsymbol{v} \leq 0, \boldsymbol{n}_{\xi^l} \cdot \boldsymbol{g} \leq 0$	-1
$\boldsymbol{n}_{\xi^l} \cdot \boldsymbol{v} > 0, \boldsymbol{n}_{\xi^l} \cdot \boldsymbol{g} \leq 0, \frac{\left(\boldsymbol{n}_{\xi^l} \cdot \boldsymbol{v}\right)^2}{4\boldsymbol{n}_{\xi^l} \cdot \boldsymbol{g}} + c_{\mathrm{CFL}}(\Delta\xi^l) \leq 0$	$+1$
$\boldsymbol{n}_{\xi^l} \cdot \boldsymbol{v} > 0, \boldsymbol{n}_{\xi^l} \cdot \boldsymbol{g} \leq 0, \frac{\left(\boldsymbol{n}_{\xi^l} \cdot \boldsymbol{v}\right)^2}{4\boldsymbol{n}_{\xi^l} \cdot \boldsymbol{g}} + c_{\mathrm{CFL}}(\Delta\xi^l) > 0$	-1
$\boldsymbol{n}_{\xi^l} \cdot \boldsymbol{v} \leq 0, \boldsymbol{n}_{\xi^l} \cdot \boldsymbol{g} > 0, \frac{\left(\boldsymbol{n}_{\xi^l} \cdot \boldsymbol{v}\right)^2}{4\boldsymbol{n}_{\xi^l} \cdot \boldsymbol{g}} + c_{\mathrm{CFL}}(\Delta\xi^l) > 0$	-1
$\boldsymbol{n}_{\xi^l} \cdot \boldsymbol{v} \leq 0, \boldsymbol{n}_{\xi^l} \cdot \boldsymbol{g} > 0, \frac{\left(\boldsymbol{n}_{\xi^l} \cdot \boldsymbol{v}\right)^2}{4\boldsymbol{n}_{\xi^l} \cdot \boldsymbol{g}} + c_{\mathrm{CFL}}(\Delta\xi^l) \leq 0$	$+1$

where N_{dim} denotes the spatial dimensionality of the equations. In contrast to the previous criteria, this is a strict stability criterion for the explicit time stepping. We note that the use of a third-order scheme is not strictly necessary for the presented results. A second-order time integration scheme, such as RK2 (Shu & Osher 1988), yields virtually identical results in combination with second-order spatial reconstruction.

3.2. Numerical flux functions

A fundamental part of the discretization is the choice of a numerical two-state flux. These fluxes give approximate solutions of the two-state Riemann problem at the cell interfaces. Choosing different numerical fluxes yields different properties for the scheme. Many of the typically used Riemann solvers or other flux functions suffer from excessive Mach number dependent diffusion. In the case of the Roe solver (Roe 1981) the origin of this is an upwind term in the schemes that is needed for numerical stability (e.g., Turkel 1987; Guillard & Viozat 1999; Miczek et al. 2015). Other Godunov-type schemes are subject to similar issues (Guillard & Murrone 2004). To correct this behavior, a number of low Mach number fixes have been proposed that aim on reducing the excessive diffusion and make it independent of the Mach number (e.g., Turkel 1987; Li & Gu 2008; Rieper 2011; Oßwald et al. 2015; Miczek et al. 2015; Barsukow et al. 2017a; Berberich & Klingenberg 2020).

One peculiarity of astrophysical setups compared to, for example, setups in the engineering community is the presence of strong stratifications where pressure and density may change by orders of magnitudes within the computational domain. In such setups, the reduction of diffusion comes with the risk of reducing stability and many of the schemes found in the literature develop instabilities. The SLH code is designed in a modular fashion that facilitates the implementation and testing of different types of flux functions. In numerical tests we find the so-called AUSM$^+$-up method to yield appropriate results in the low-Mach regime in combination with the well-balancing method discussed here. The basic construction and a modification for improved low-Mach behavior is discussed here.

An approach to numerical flux functions that can easily be extended to flows at low Mach numbers is followed in the class of Advective Upstream Splitting Methods (AUSM), which have been first introduced by Liou & Steffen (1993). In Liou (1996) the AUSM scheme was extended to AUSM$^+$, the idea of which we briefly describe in the following. To be consistent with the original publication, we use dimensionalized quantities.

The central idea is to split the analytical flux function $\boldsymbol{f}_\chi$ of Eq. (2) into a pressure and a mass flux via

$$\boldsymbol{f}_{x_i} = p\,\boldsymbol{e}_{i+1} + \dot{m}_i \psi, \tag{29}$$

with

$$\dot{m}_i = \varrho v_i, \qquad \psi = \begin{pmatrix} 1 \\ u \\ v \\ w \\ E + \frac{p}{\varrho} \end{pmatrix}, \qquad i \in [1,2,3] \tag{30}$$

and the i-th canonical basis vector in the five-dimensional flux vector space $\boldsymbol{e}_i$. This formulation is given for Cartesian coordinates, a transformation to curvilinear coordinates is possible.

The pressure and mass flux of Eq. (29) are discretized separately which results in the numerical flux function

$$\hat{\boldsymbol{F}}_{x_i}(\boldsymbol{U}_L, \boldsymbol{U}_R) = p_{1/2}(\boldsymbol{U}_L, \boldsymbol{U}_R)\,\boldsymbol{e}_{i+1} + \dot{m}_{1/2}(\boldsymbol{U}_L, \boldsymbol{U}_R)\psi_{\mathrm{up}}(\boldsymbol{U}_L, \boldsymbol{U}_R), \tag{31}$$

where the upwind term ψ_{up} is given by

$$\psi_{\mathrm{up}}(\boldsymbol{U}_L, \boldsymbol{U}_R) = \begin{cases} \psi(\boldsymbol{U}_L) & \text{if } \dot{m}_{1/2}(\boldsymbol{U}_L, \boldsymbol{U}_R) \geq 0, \\ \psi(\boldsymbol{U}_R) & \text{otherwise.} \end{cases} \tag{32}$$

The core properties of this numerical flux function are determined by the definition of the interface values $p_{1/2}$ and $\dot{m}_{1/2}$ of the pressure p and the mass flux $\dot{m}_i$. With the initially proposed definitions of Liou (1996), this flux function is not capable of resolving low Mach number flows. However, Liou (2006) extended the AUSM$^+$ scheme to AUSM$^+$-up with enhanced low Mach number capability.

For AUSM$^+$-up, the interface pressure is defined as

$$\begin{aligned} p_{1/2} = {} & \mathcal{P}^+_{(5)}(M_L)p_L + \mathcal{P}^-_{(5)}(M_R)p_R \\ & - K_u \mathcal{P}^+_{(5)}(M_L)\mathcal{P}^+_{(5)}(M_R)(\varrho_L + \varrho_R)(f_a\, c_{1/2})(u_R - u_L), \end{aligned} \tag{33}$$

where $\mathcal{P}^\pm_{(5)}$ are fifth degree polynomial functions, $c_{1/2}$ is an approximation for the interface speed of sound, and K_u is a constant that can be set to a value between zero and unity. We refer the reader to Liou (2006) for the detailed definitions of the terms. The third term on the right hand side of Eq. (33) that includes velocity-diffusion is called u-term and is designed to reduce the numerical dissipation at low Mach numbers. It involves a scaling factor f_a defined as

$$f_a = M_{\mathrm{o}}(2 - M_{\mathrm{o}}), \tag{34}$$

with

$$M_{\mathrm{o}} = \min\left[1, \max\left(\mathrm{Ma}, M_{\mathrm{cut}}\right)\right], \tag{35}$$

where M_{cut} is a cut-off Mach number that ensures that f_a does not approach 0 in the limit of very small Mach numbers. This is necessary to prevent singularities as the inverse of f_a enters into the mass-flux part (see Eq. (36)) in the original definition of AUSM$^+$-up. However, as described below, the SLH code sets the scaling in these two parts independently such that M_{cut} can be theoretically set to zero. In SLH, for implementation reasons the value is set to a small value, typically to 10^{-13}, to avoid divergence at smaller Mach numbers. This could easily be changed, but does not have a practical influence on our calculations. The mass flux in AUSM$^+$-up is given by

$$\dot{m}_{1/2} = c_{1/2} M_{1/2} \begin{cases} \varrho_L & \text{if } M_{1/2} > 0, \\ \varrho_R & \text{otherwise,} \end{cases} \tag{36}$$

with the interface Mach number

$$M_{1/2} = \mathcal{M}^{+}_{(4)}(M_L) + \mathcal{M}^{-}_{(4)}(M_R) - \frac{K_p}{f_a^p}\max\left(1-\sigma\bar{M}^2, 0\right)\frac{p_R - p_L}{\varrho_{1/2}c_{1/2}^2}. \tag{37}$$

Here, $\mathcal{M}^{\pm}_{(4)}$ are fourth degree polynomial functions and $\bar{M} = (u_L^2+u_R^2)/(2c_{1/2}^2)$. K_p and σ are constants between zero and unity. The last term is called the p-term and is a pressure diffusion term that was introduced to ensure pressure–velocity coupling at low speeds (Edwards & Liou 1998). In the original AUSM$^+$-up scheme the Mach number dependent scaling of the p-term, f_a^p, was chosen identical to that of the u-term, f_a. Similar to Miczek (2013) we chose independent cut-off values for f_a and

$$f_a^p = M_o^p(2 - M_o^p), \quad M_o^p = \min\left[1, \max\left(M, M^p_{\mathrm{cut}}\right)\right]. \tag{38}$$

This way, f_a^p can be defined with a significantly higher cut-off Mach number (typically around 10^{-1}) compared to f_a. This prevents stability issues, which can occur at locally very low Mach numbers when $1/f_a^p$ becomes exceedingly large. We use this modified scheme in the presented tests and refer to it as AUSM$^+$-up. Still even this scheme is struggling with maintaining a simple hydrostatic stratification as shown in Sect. 5.1.

It is important to note that the role of the effect of the pressure diffusion is altered by combining AUSM$^+$-up with any of the well-balancing methods described in the following: well-balancing techniques lead to an exact reconstruction of the hydrostatic pressure. Only the nonhydrostatic pressure deviations are captured by the reconstruction and given to the numerical flux. Hence, when well-balancing is applied, the pressure diffusion acts on the nonhydrostatic pressure only.

We define a corresponding basic scheme called AUSM$^+_{\mathrm{B}}$-up by setting $M_{\mathrm{cut}} = M^p_{\mathrm{cut}} = 1$. This scheme does have high dissipation at low Mach numbers and we just use it to assess the interaction of the various well-balanced schemes with low Mach number flux functions.

4. Well-balancing methods

To illustrate the issue with configurations close to hydrostatic equilibrium in finite-volume codes we consider the effect of one time step on an initial configuration in perfect hydrostatic equilibrium. For simplicity we discretize the time derivative using the forward Euler method and only consider the one-dimensional Euler equations. From the analytic result we expect that this step will not alter the states and any subsequent steps will also keep the hydrostatic equilibrium intact. To this end we associate a discrete stationary solution that provides a good approximation to the hydrostatic equilibrium. If starting from a discrete hydrostatic equilibrium, the solution of the time evolutionary problem does not change for a numerical scheme, we call it well-balanced.

The density, momentum, and total energy after one time step of length Δt (denoted by the superscript "1") are calculated from the previous values (denoted by the superscript "0"), the interface fluxes $\hat{\boldsymbol{F}}$, and the cell-centered source term $\hat{\boldsymbol{S}}$. The result for cell i is

$$\varrho_i^1 = \varrho_i^0 - \frac{\Delta t}{\Delta x}\left[\left(\hat{\boldsymbol{F}}^0_{i+\frac{1}{2}}\right)_1 - \left(\hat{\boldsymbol{F}}^0_{i-\frac{1}{2}}\right)_1\right], \tag{39}$$

$$(\varrho u)_i^1 = (\varrho u)_i^0 - \frac{\Delta t}{\Delta x}\left[\left(\hat{\boldsymbol{F}}^0_{i+\frac{1}{2}}\right)_2 - \left(\hat{\boldsymbol{F}}^0_{i-\frac{1}{2}}\right)_2\right] + \Delta t\left(\hat{\boldsymbol{S}}_i\right)_2, \tag{40}$$

$$E_i^1 = E_i^0 - \frac{\Delta t}{\Delta x}\left[\left(\hat{\boldsymbol{F}}^0_{i+\frac{1}{2}}\right)_3 - \left(\hat{\boldsymbol{F}}^0_{i-\frac{1}{2}}\right)_3\right], \tag{41}$$

where the indexes outside the parentheses stand for the vector component of the flux or source term. To be well-balanced, a scheme needs to guarantee that the step leaves the state unchanged, which leads to the conditions

$$0 = \left(\hat{\boldsymbol{F}}^0_{i+\frac{1}{2}}\right)_1 - \left(\hat{\boldsymbol{F}}^0_{i-\frac{1}{2}}\right)_1, \tag{42}$$

$$0 = \left(\hat{\boldsymbol{F}}^0_{i+\frac{1}{2}}\right)_2 - \left(\hat{\boldsymbol{F}}^0_{i-\frac{1}{2}}\right)_2 - \Delta x\left(\hat{\boldsymbol{S}}_i\right)_2, \tag{43}$$

$$0 = \left(\hat{\boldsymbol{F}}^0_{i+\frac{1}{2}}\right)_3 - \left(\hat{\boldsymbol{F}}^0_{i-\frac{1}{2}}\right)_3. \tag{44}$$

As the fluxes are evaluated at different states, none of these conditions is fulfilled automatically. A consistent numerical flux will automatically satisfy Eqs. (42) and (44) because the 1- and 3-components of the fluxes are zero for $u = 0$. The case of Eq. (43) is less straightforward. Here, the discretization of the source term must be constructed to match the flux difference in the hydrostatic case. The methods described in the following subsections achieve this in different ways.

4.1. Cargo–LeRoux method

4.1.1. The one-dimensional Cargo–LeRoux method

One method to turn almost any hydrodynamics scheme into a well-balanced scheme was suggested by Cargo & Le Roux (1994) (see also Le Roux 1999). The only prerequisites it needs are support for a general equation of state and flux functions that resolve contact discontinuities. For completeness we describe the original method, which is only applicable in the one-dimensional case, and turn to the multidimensional extension in Sect. 4.1.2. The one-dimensional Euler equations with gravity read

$$\frac{\partial}{\partial t}\begin{pmatrix}\varrho\\ \varrho u\\ E'\end{pmatrix} + \frac{\partial}{\partial x}\begin{pmatrix}\varrho u\\ \varrho u^2 + p\\ u(E'+p)\end{pmatrix} = \begin{pmatrix}0\\ \varrho g\\ \varrho g u\end{pmatrix}, \tag{45}$$

with g being the, possibly negative, gravitational acceleration in the x-direction. The 1D method presented here relies on gravity being constant in space and time. Furthermore, $E' = \varrho\epsilon + \frac{1}{2}\varrho|\boldsymbol{v}|^2$ is the total energy excluding potential energy. It is only used in the one-dimensional method in this subsection. The multidimensional extension in Sect. 4.1.2 follows a slightly different principle using the total energy E including the potential as defined in Sect. 2.

Cargo & Le Roux (1994) suggest the introduction of a potential q defined by its spatial and temporal derivatives

$$\frac{\partial q}{\partial x} = \varrho g, \quad \frac{\partial q}{\partial t} = -\varrho u g. \tag{46}$$

Numerically, this potential is treated like a composition variable, meaning that its time evolution is determined by the advection equation,

$$\frac{\partial(\varrho q)}{\partial t} + \frac{\partial(\varrho q u)}{\partial x} = 0. \tag{47}$$

This ensures that the conditions of Eq. (46) are fulfilled at all times if they are satisfied initially.

Expressing the right side of Eq. (45) using q yields

$$\frac{\partial}{\partial t}\begin{pmatrix}\varrho\\ \varrho u\\ E'\end{pmatrix} + \frac{\partial}{\partial x}\begin{pmatrix}\varrho u\\ \varrho u^2 + p\\ u(E'+p)\end{pmatrix} = \begin{pmatrix}0\\ \frac{\partial q}{\partial x}\\ -\frac{\partial q}{\partial t}\end{pmatrix}. \tag{48}$$

Collecting derivatives with respect to the same variable and inserting $0 = q - q$ results in

$$\frac{\partial}{\partial t}\begin{pmatrix}\varrho\\ \varrho u\\ E'+q\end{pmatrix}+\frac{\partial}{\partial x}\begin{pmatrix}\varrho u\\ \varrho u^2+p-q\\ u(E'+q+p-q)\end{pmatrix}=\begin{pmatrix}0\\0\\0\end{pmatrix}. \tag{49}$$

At this point we introduce a modified EoS based on an arbitrary original EoS by defining a new pressure, Π, and total energy per volume, F, as

$$\Pi = p - q, \quad F' = E' + q. \tag{50}$$

With this definition Eq. (49) takes the form of the homogeneous Euler equations for a modified EoS,

$$\frac{\partial}{\partial t}\begin{pmatrix}\varrho\\ \varrho u\\ F'\end{pmatrix}+\frac{\partial}{\partial x}\begin{pmatrix}\varrho u\\ \varrho u^2+\Pi\\ u(F'+\Pi)\end{pmatrix}=\begin{pmatrix}0\\0\\0\end{pmatrix}. \tag{51}$$

The physical meaning of q is that of hydrostatic pressure, except for an arbitrary constant offset. This means that the modified pressure Π of an atmosphere in perfect hydrostatic equilibrium is spatially constant, making the solution of the Euler equations trivial.

This new EoS does not change the speed of sound. This can easily be seen from rewriting the expression for the speed of sound for a general EoS (20) in terms of Π and F'. Because q does not depend on any other thermodynamic variables, the rewritten expression takes the same form as the original.

4.1.2. A multidimensional extension

An obvious multidimensional extension of the aforementioned method would be introduce a potential q with the defining properties

$$\nabla q = \varrho \boldsymbol{g}, \quad \frac{\partial}{\partial t} q = -\varrho \boldsymbol{g} \cdot \boldsymbol{u}. \tag{52}$$

While the algebra shown in Eqs. (48)–(51) is still valid for this new potential, the problem with this definition is the mere existence of this potential q. From Eq. (52) follows that

$$\nabla \times (\nabla q) = \nabla \times \varrho \boldsymbol{g} = \boldsymbol{0}, \tag{53}$$

and using the fact that $\nabla \times \boldsymbol{g} = 0$, due to $\boldsymbol{g}$ being derived from a gravitational potential, we can simplify this equation to

$$\nabla \times \varrho \boldsymbol{g} = \varrho \nabla \times \boldsymbol{g} - \boldsymbol{g} \times \nabla \varrho = -\boldsymbol{g} \times \nabla \varrho = \boldsymbol{0}. \tag{54}$$

This means that a potential only exists if the cross product $\boldsymbol{g} \times \nabla \varrho$ vanishes. This only happens for any of the following three conditions: the trivial case of gravity being globally zero, the case of constant density, and the case where the gradient of density has the same equilibrium with its surroundings. Thus, the approach of Eq. (52) is not suitable.

In order to construct a general, but approximate, multidimensional extension of the well-balanced method from Sect. 4.1.1, we restrict ourselves to problems in which ϱ does not vary strongly on equipotential surfaces of the gravitational potential ϕ. We denote an average on these equipotential surfaces, which we call horizontal average, with the operator $\langle\cdot\rangle$, so we can define an averaged density

$$\varrho_0 = \langle \varrho \rangle. \tag{55}$$

By definition of the horizontal average, the gradient of ϱ_0 is parallel to $\boldsymbol{g}$. This allows us to define the potential by

$$\nabla q = \varrho_0 \boldsymbol{g}, \quad \frac{\partial}{\partial t} q = 0, \tag{56}$$

for which Eq. (54) is fulfilled automatically.

The fluxes (Eq. (3)) and the source term (Eq. (6)) in the compressible Euler equations (Eq. (2)) can then be rewritten as

$$\boldsymbol{f}_{\xi^l} = \begin{pmatrix}\varrho\, \boldsymbol{n}_{\xi^l}^T \boldsymbol{v}\\ \varrho u\, \boldsymbol{n}_{\xi^l}^T \boldsymbol{v} + (n_{\xi^l})_x \Pi\\ \varrho v\, \boldsymbol{n}_{\xi^l}^T \boldsymbol{v} + (n_{\xi^l})_y \Pi\\ \varrho w\, \boldsymbol{n}_{\xi^l}^T \boldsymbol{v} + (n_{\xi^l})_z \Pi\\ \boldsymbol{n}_{\xi^l}^T \boldsymbol{v}\,(F+\Pi)\end{pmatrix}, \quad \boldsymbol{s} = \begin{pmatrix}0\\ -(\varrho-\varrho_0)\frac{\partial \phi}{\partial x}\\ -(\varrho-\varrho_0)\frac{\partial \phi}{\partial y}\\ -(\varrho-\varrho_0)\frac{\partial \phi}{\partial z}\\ 0\end{pmatrix}. \tag{57}$$

There are two fundamental differences between this form and Eq. (51). First, $F = E + q$ is defined including the potential energy. This is different from the one-dimensional case in Eq. (50). q is now temporally constant, but because of the different definition of the total energy, the source term in the energy equation still vanishes. Second, the source term in the momentum equation does not completely vanish anymore. It is now proportional to the local deviation of density from its horizontal average. Even though this scheme loses some of the advantageous properties of the one-dimensional version, it is still a significant improvement for multidimensional simulations of stratified atmospheres.

A positive side effect of q being temporally constant is that, in contrast to the original Cargo–LeRoux method, the gravitational acceleration, g, is now allowed to vary spatially. A temporal variation of g is also possible, for example through self-gravity, but that necessitates a recomputation of q to keep the well-balanced property.

Because it only requires to a slight modification of the EoS, it is expected that the Cargo–LeRoux well-balancing method can be implemented into an existing hydrodynamic code rather easily, provided it supports a general EoS. Cargo–LeRoux well-balancing generally only works with flux functions that preserve contact discontinuities. It works well with the AUSM$^+$-up family of fluxes used in this paper.

4.2. The α-β method

Another approach to balance any hydrostatic solution is the α-β well-balancing method presented by Berberich et al. (2018). Similar to the Cargo–LeRoux method, the hydrostatic solution needs to be known a priori. An advantage of the α-β well-balancing however is, that it permits an arbitrary, even multidimensional, structure of the hydrostatic target solution. Hence, the α-β method is able to deal with the example of a low-density bubble in pressure-equilibrium with its surrounding of Sect. 4.1 that could not be balanced with the Cargo–LeRoux method.

The key idea of this method is to replace the physical values of ϱ and p by their respective relative deviation prior to the reconstruction at the cell interfaces. The reconstructed values are then multiplied by the known hydrostatic solution at the interfaces. The second-order approximation of gravity is constructed such that the source term exactly cancels the flux over the interface and hence that the initial hydrostatic stratification is maintained to machine precision.

For convenience, the working principle of the α-β well-balancing method is demonstrated for the one-dimensional Euler equations in Cartesian coordinates. The extension to higher

dimensional curvilinear grids follows the same principle and can be found in Berberich et al. (2019) together with a mathematically more rigorous formulation of the method.

For a given gravitational potential $\phi(x)$, we denote $\tilde{\varrho}$ and $\tilde{p}$ as the solution to the hydrostatic equation (Eq. (11)) in one dimension, that is

$$\frac{\partial \tilde{p}}{\partial x} = -\tilde{\varrho}\frac{\partial \phi(x)}{\partial x}. \tag{58}$$

The solutions are written as

$$\tilde{\varrho} = \varrho_0\,\alpha(x), \quad \tilde{p} = p_0\,\beta(x), \tag{59}$$

where $\alpha(x)$, $\beta(x)$ are dimensionless profiles and ϱ_0, p_0 carry the physical dimension of density and pressure, respectively. It is assumed that the profiles in Eq. (59) are known at least at coordinates that coincide with cell centers and interfaces.

The numerical solution of the one-dimensional Euler equation in the finite volume approach requires the reconstruction of the quantities from each cell center i of the computational domain to the respective cell interfaces $i+\frac{1}{2}$. In general, there is some freedom in choosing the set of quantities that is reconstructed in addition to the velocities. This is exploited by the α-β well-balancing method, which considers the relative deviation from the hydrostatic solution. The set of quantities at cell i that are reconstructed is hence chosen to be

$$\boldsymbol{W}_i = \left(W_i^{\varrho}, W_i^{u}, W_i^{p}\right) = \left(\frac{\varrho_i}{\alpha(x_i)}, u_i, \frac{p_i}{\beta(x_i)}\right). \tag{60}$$

There is no restriction on the specific choice of the reconstruction scheme that calculates the value of W_i at the interface, that is $W_{i\pm\frac{1}{2}}$. After reconstruction, the variables are transformed back to their physical counterpart by multiplication with the known hydrostatic solution at the interfaces,

$$\begin{aligned} \varrho_{i+\frac{1}{2}}^{L/R} &= \alpha\left(x_{i+\frac{1}{2}}\right)\left(W_{i+\frac{1}{2}}^{\varrho}\right)^{L/R}, \qquad & u_{i+\frac{1}{2}}^{L/R} &= \left(W_{i+\frac{1}{2}}^{u}\right)^{L/R}, \\ p_{i+\frac{1}{2}}^{L/R} &= \beta\left(x_{i+\frac{1}{2}}\right)\left(W_{i+\frac{1}{2}}^{p}\right)^{L/R}. \end{aligned} \tag{61}$$

Here, L/R denotes the value at the interface when reconstructing from the left or right side, respectively. The values given by Eq. (61) enter into the numerical flux function (see Sect. 3.2).

If density ϱ and pressure p on the computational grid correspond to the hydrostatic solution Eq. (59) and $u \equiv 0$, it follows that the quantities reconstructed from the left and right side are equal for all cell interfaces and hence

$$\boldsymbol{U}_{i+\frac{1}{2}}^{L} = \boldsymbol{U}_{i+\frac{1}{2}}^{R} = \boldsymbol{U}_{i+\frac{1}{2}}. \tag{62}$$

If the left and right interface state are the same, any numerical flux function has to equal the analytical flux function to ensure the consistency of the method. Thus,

$$\hat{\boldsymbol{F}}_x\left(\boldsymbol{U}_{i+\frac{1}{2}}^{L}, \boldsymbol{U}_{i+\frac{1}{2}}^{R}\right) = \boldsymbol{f}_x\left(\boldsymbol{U}_{i+\frac{1}{2}}\right) = \begin{pmatrix} 0 \\ \tilde{p}(x_{i+\frac{1}{2}}) \\ 0 \end{pmatrix}, \tag{63}$$

which immediately follows from Eq. (3) for vanishing velocities.

In order to maintain hydrostatic equilibrium, the residual flux of Eq. (63) has to be balanced exactly by the source term $\boldsymbol{s}$ in Eq. (2). To achieve this, the α-β method expresses the gravitational potential in Eq. (6) with the aid of the hydrostatic equation Eq. (58) as

$$-\frac{\partial \phi}{\partial x} = \frac{p_0}{\varrho_0\,\alpha(x)}\frac{\partial \beta(x)}{\partial x}. \tag{64}$$

The one-dimensional source term for gravity (see Eq. (22)) is then given by

$$\hat{\boldsymbol{S}}_i = \begin{pmatrix} 0 \\ s_i \\ 0 \end{pmatrix}, \quad s_i = \frac{p_0}{\varrho_0}\frac{\beta_{i+\frac{1}{2}} - \beta_{i-\frac{1}{2}}}{\Delta x}\frac{\varrho_i}{\alpha_i}, \tag{65}$$

which is a second-order accurate discretization. If the states on the computational grid correspond to the hydrostatic solution, then Eq. (65) reduces to

$$\begin{aligned} \boldsymbol{s}_i &= \begin{pmatrix} 0 \\ \tilde{p}\left(x_{i+\frac{1}{2}}\right) - \tilde{p}\left(x_{i-\frac{1}{2}}\right) \\ 0 \end{pmatrix} \\ &= \hat{\boldsymbol{F}}_x\left(\boldsymbol{U}_{i+\frac{1}{2}}^{L}, \boldsymbol{U}_{i+\frac{1}{2}}^{R}\right) - \hat{\boldsymbol{F}}_x\left(\boldsymbol{U}_{i-\frac{1}{2}}^{L}, \boldsymbol{U}_{i-\frac{1}{2}}^{R}\right) \end{aligned} \tag{66}$$

and the discretized source term exactly cancels the interface fluxes. This leads to zero residual and thus to a well-balanced scheme. The well-balanced property for the one-dimensional α-β method is formally shown in Berberich et al. (2018).

4.3. The deviation method

In the following we give a short description of the simple and general well-balanced method introduced in Berberich et al. (2021). For more details we refer the reader to this reference. The core of the method is the target solution $\tilde{\boldsymbol{u}}$, which must be known a priori. It has to be a stationary solution to the Euler equations (2), that is it has to satisfy the relation

$$A_\xi\frac{\partial \boldsymbol{f}_\xi(\tilde{\boldsymbol{u}})}{\partial \xi} + A_\eta\frac{\partial \boldsymbol{f}_\eta(\tilde{\boldsymbol{u}})}{\partial \eta} + A_\zeta\frac{\partial \boldsymbol{f}_\zeta(\tilde{\boldsymbol{u}})}{\partial \zeta} = J\boldsymbol{s}(\tilde{\boldsymbol{u}}). \tag{67}$$

It is noteworthy that, in contrast to other well-balancing methods, it can include a nonzero velocity. In the numerical applications in Sect. 5 we are going to store the hydrostatic or stationary solution which shall be well-balanced in $\tilde{\boldsymbol{u}}$. Subtracting Eq. (67) from Eq. (2) yields the evolution equation

$$\begin{aligned} J\frac{\partial(\Delta \boldsymbol{u})}{\partial t} &+ A_\xi\left(\frac{\partial \boldsymbol{f}_\xi(\tilde{\boldsymbol{u}}+\Delta\boldsymbol{u})}{\partial \xi} - \frac{\partial \boldsymbol{f}_\xi(\tilde{\boldsymbol{u}})}{\partial \xi}\right) \\ &+ A_\eta\left(\frac{\partial \boldsymbol{f}_\eta(\tilde{\boldsymbol{u}}+\Delta\boldsymbol{u})}{\partial \eta} - \frac{\partial \boldsymbol{f}_\eta(\tilde{\boldsymbol{u}})}{\partial \eta}\right) \\ &+ A_\zeta\left(\frac{\partial \boldsymbol{f}_\zeta(\tilde{\boldsymbol{u}}+\Delta\boldsymbol{u})}{\partial \zeta} - \frac{\partial \boldsymbol{f}_\zeta(\tilde{\boldsymbol{u}})}{\partial \zeta}\right) = J\left(\boldsymbol{s}(\tilde{\boldsymbol{u}}+\Delta\boldsymbol{u}) - \boldsymbol{s}(\tilde{\boldsymbol{u}})\right) \end{aligned} \tag{68}$$

for the deviations $\Delta\boldsymbol{u} = \boldsymbol{u} - \tilde{\boldsymbol{u}}$ from the target solution $\tilde{\boldsymbol{u}}$. In order to obtain a well-balanced scheme which exactly maintains the stationary target solution $\tilde{\boldsymbol{u}}$, we discretize Eq. (68) instead of Eq. (2). This yields

$$\begin{aligned} V_{ijk}\frac{\partial(\Delta \boldsymbol{U})_{ijk}}{\partial t} = &- A_{i+\frac{1}{2},j,k}(\hat{\boldsymbol{F}}_\xi^{\mathrm{dev}})_{i+\frac{1}{2},j,k} + A_{i-\frac{1}{2},j,k}(\hat{\boldsymbol{F}}_\xi^{\mathrm{dev}})_{i-\frac{1}{2},j,k} \\ &- A_{i,j+\frac{1}{2},k}(\hat{\boldsymbol{F}}_\eta^{\mathrm{dev}})_{i,j+\frac{1}{2},k} + A_{i,j-\frac{1}{2},k}(\hat{\boldsymbol{F}}_\eta^{\mathrm{dev}})_{i,j-\frac{1}{2},k} \\ &- A_{i,j,k+\frac{1}{2}}(\hat{\boldsymbol{F}}_\zeta^{\mathrm{dev}})_{i,j,k+\frac{1}{2}} + A_{i,j,k-\frac{1}{2}}(\hat{\boldsymbol{F}}_\zeta^{\mathrm{dev}})_{i,j,k-\frac{1}{2}} \\ &+ V_{ijk}\hat{\boldsymbol{S}}_{ijk}^{\mathrm{dev}}, \end{aligned} \tag{69}$$

where the numerical flux differences

$$\left(\hat{\boldsymbol{F}}_{\xi}^{\mathrm{dev}}\right)_{i+\frac{1}{2},j,k} = \left(\hat{\boldsymbol{F}}_{\xi}\right)_{i+\frac{1}{2},j,k} - \boldsymbol{f}_{\xi}\left[\tilde{\boldsymbol{u}}\left(\boldsymbol{x}_{i+\frac{1}{2},j,k}\right)\right],$$
$$\left(\hat{\boldsymbol{F}}_{\eta}^{\mathrm{dev}}\right)_{i,j+\frac{1}{2},k} = \left(\hat{\boldsymbol{F}}_{\eta}\right)_{i,j+\frac{1}{2},k} - \boldsymbol{f}_{\eta}\left[\tilde{\boldsymbol{u}}\left(\boldsymbol{x}_{i,j+\frac{1}{2},k}\right)\right],$$
$$\left(\hat{\boldsymbol{F}}_{\zeta}^{\mathrm{dev}}\right)_{i,j,k+\frac{1}{2}} = \left(\hat{\boldsymbol{F}}_{\zeta}\right)_{i,j,k+\frac{1}{2}} - \boldsymbol{f}_{\zeta}\left[\tilde{\boldsymbol{u}}\left(\boldsymbol{x}_{i,j,k+\frac{1}{2}}\right)\right]$$

are the differences between the numerical fluxes evaluated at the states $\tilde{\boldsymbol{u}} + \Delta\boldsymbol{U}^{L/R}$ and the exact fluxes evaluated at the values of the target solution at the interface centers. The interface values $\Delta\boldsymbol{U}^{L/R}$ are obtained via reconstruction. To reconstruct in the set of variables $\boldsymbol{u}^{\mathrm{other}} = \mathcal{T}(\boldsymbol{u})$ that is different from conserved variables $\boldsymbol{u}$, the reconstruction is applied to the transformed deviations

$$\Delta\boldsymbol{U}_{ijk}^{\mathrm{other}} = \mathcal{T}\left(\tilde{\boldsymbol{u}}\left(\boldsymbol{x}_{ijk}\right) + \Delta\boldsymbol{U}_{ijk}\right) - \mathcal{T}\left(\tilde{\boldsymbol{u}}\left(\boldsymbol{x}_{ijk}\right)\right). \tag{70}$$

After reconstruction, the interface values are transformed back. For the left interface values, this reads

$$\boldsymbol{U}_{i+\frac{1}{2},j,k}^{L} = \mathcal{T}^{-1}\left(\mathcal{T}\left(\tilde{\boldsymbol{u}}\left(\boldsymbol{x}_{i+\frac{1}{2},j,k}\right)\right) + \Delta\boldsymbol{U}_{i+\frac{1}{2},j,k}^{\mathrm{other}}\right), \tag{71}$$

and right interface values are calculated likewise. The source term difference discretization in Eq. (69) is

$$\hat{\boldsymbol{S}}_{ijk}^{\mathrm{dev}} = \hat{\boldsymbol{S}}\left(\tilde{\boldsymbol{u}}\left(\boldsymbol{x}_{ijk}\right) + \Delta\boldsymbol{U}_{ijk}\right) - \hat{\boldsymbol{S}}\left(\tilde{\boldsymbol{u}}\left(\boldsymbol{x}_{ijk}\right)\right), \tag{72}$$

where $\hat{\boldsymbol{S}}(\boldsymbol{U})$ means that the source term discretization Eq. (22) is evaluated at the state $\boldsymbol{U}$. It has been shown in Berberich et al. (2021) that this modification of the scheme (21) renders it well-balanced in the sense that the residual vanishes if $\boldsymbol{u} = \tilde{\boldsymbol{u}}$ and that the method can be applied in arbitrarily high order finite-volume codes.

This method follows ideas already published elsewhere in the literature. Veiga et al. (2019) introduce a similar well-balanced scheme in the context of finite element methods. The method introduced in Dedner et al. (2001) for stratified MHD flows with gravity also shares many features with the deviation method. The key difference is that the Dedner et al. (2001) method subtracts the residual of the initial state of the simulation, while the deviation method subtracts a known background state during the spatial reconstruction step, which is at an earlier stage. While we have not quantified this in tests, it is expected that the deviation method will produce a more accurate reconstruction close to equilibrium because it is essentially reconstructing a constant function.

5. Numerical tests and application examples

This section presents simple test simulations that verify that the presented well-balancing methods in combination with a low-Mach flux function are stable and do enable correct representation of slow flows in stellar-type stratifications. This is done for steady-state and dynamical test problems. Unless stated otherwise, time integration is performed with the implicit ESDIRK23 scheme in combination with the CFL_{ug} time step criterion (Eq. (26)). The corresponding value of c_{CFL} is stated for each of the simulations individually. For the numerical flux, the AUSM$^+$-up scheme (Sect. 3.2) is used with $f_a^p = 0.1$ and $f_a = 10^{-13}$. Interface values are calculated from cell averages by applying linear reconstruction without any slope or flux limiters. The set of reconstructed quantities is either ϱ-P or ϱ-T, depending of the well-balancing method, and will be stated explicitly for the respective simulations. The choice of appropriate boundary conditions depends on the specific setup, hence they are given for each setup individually. All of our test cases are two-dimensional for computational reasons, although the methods are equally valid in three spatial dimensions. Qualitatively different results for the 3D case are not expected.

5.1. Simple stratified atmospheres

A useful test problem for the quality of a well-balanced scheme is a stably stratified atmosphere. A zero-velocity initial condition should be maintained perfectly, at least down to rounding errors. However, in a not well-balanced scheme the pressure-gradient force and gravity do not cancel exactly and the systems ends up in a state with small, but nonzero, acceleration. Depending on the details of the numerical flux, this acceleration may prevent the simulation of flows at very low Mach numbers or it may cause unphysical convection in formally stable stratifications. In any case, keeping a hydrostatic stratification stable is a necessary, but not a sufficient condition for a well-balanced scheme to be useful for the simulation of stratified atmospheres.

We start with the one-dimensional (1D), isothermal test case of Käppeli & Mishra (2016) on the domain $[0, 2\,\mathrm{cm}]$. Gravity is points into negative x-direction and the gravitational potential is given by

$$\phi = s_0 x, \tag{73}$$

with a steepness s_0 of $1\,\mathrm{cm\,s^{-2}}$. The constant temperature profile is convectively stable for any equation of state with a positive value of δ (Eq. (14)). The density and pressure profiles fulfilling Eq. (11) are given by,

$$\varrho = \varrho_0 \exp\left(-\frac{\varrho_0}{p_0}\phi\right), \quad p = p_0 \exp\left(-\frac{\varrho_0}{p_0}\phi\right). \tag{74}$$

This expression holds for any form of the gravitational potential, not just Eq. (73). The reference density and pressure are set to $\varrho_0 = 1\,\mathrm{g\,cm^{-3}}$ and $p_0 = 1\,\mathrm{Ba}$, respectively. We use Dirichlet boundary conditions, which are initialized with the hydrostatic profile and then left unchanged throughout the simulation. The equation of state is that of an ideal gas with an adiabatic exponent $\gamma = 5/3$.

Figure 1 shows the time evolution of the maximum Mach number for this isothermal configuration in 1D simulations with 64 grid cells using a variety of well-balancing methods and two different flux functions. The simulations use linear reconstruction in ϱ-P variables, $c_{\mathrm{CFL}} = 0.9$ for the time step size, and they were run until $t = 5000\,t_{\mathrm{BV}}$. The figure shows that runs without well-balancing immediately reach Mach numbers between 10^{-6} and 10^{-5}, while all of the tested well-balancing methods manage to keep the Mach number below 10^{-12}. The choice of flux function does not qualitatively affect the results here, in particular it does not play a role if we use a low Mach number flux, such as AUSM$^+$-up, or a standard flux, such as AUSM$_{\mathrm{B}}^+$-up (see Sect. 3.2).

Certain phenomena, such as convection, are inherently multidimensional and cannot develop in 1D geometry. Therefore we repeat this test using a two-dimensional (2D) atmosphere. For simplicity we keep gravity pointing in the negative x-direction. The horizontal boundaries are periodic. Figure 2 shows the evolution of the maximum Mach number and horizontal density

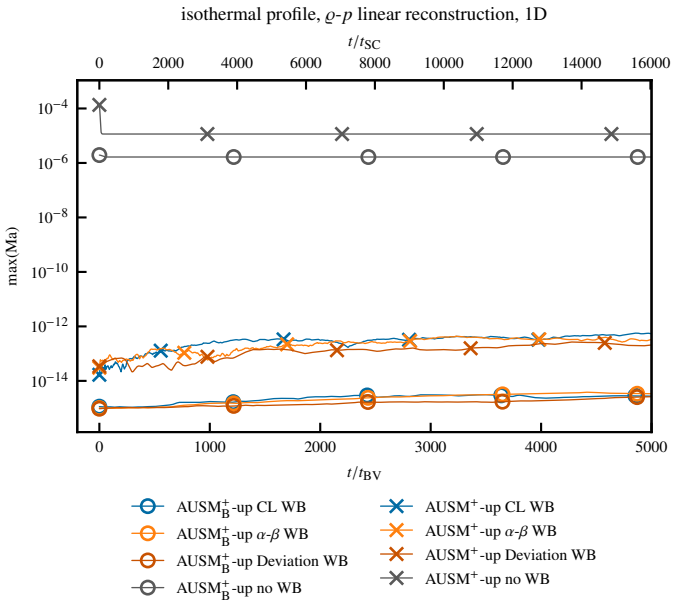

Fig. 1. Time evolution of the maximum Mach number in a 1D atmosphere with an isothermal temperature profile (Eq. (74)) and a linear gravitational potential (Eq. (73)). The colors indicate different well-balancing (WB) methods, the markers different flux functions. CL stands for Cargo–LeRoux. Time is given in units of the Brunt–Väisälä time $t_{BV} = 9.93\,\mathrm{s}$ (Eq. (18)) and sound-crossing time $t_{SC} = 3.10\,\mathrm{s}$ (Eq. (19)). The curves have been slightly smoothed for better visibility.

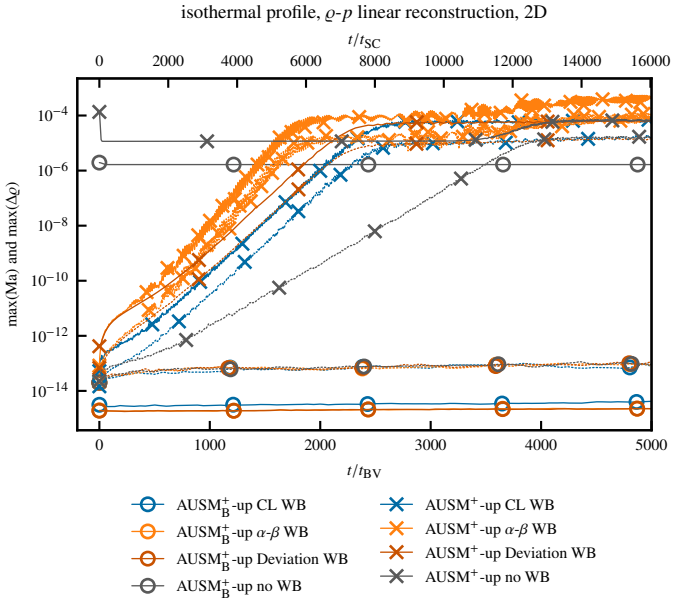

Fig. 2. Same as Fig. 1, but for a 2D atmosphere. The solid lines represent the maximum Mach numbers on the grid and the dotted lines the horizontal density fluctuations according to Eq. (75). The curves have been slightly smoothed for better visibility.

fluctuation $\Delta\varrho$ over time. The latter is defined as

$$\Delta\varrho = \varrho - \langle\varrho\rangle_y, \tag{75}$$

with $\langle\cdot\rangle_y$ denoting an average over the y direction.

Similar to the 1D case, we see that the simulations without well-balancing immediately reach Mach numbers around 10^{-5}. All simulations using any well-balanced method start from very low Mach numbers ($\approx 10^{-13}$), but the ones using the low Mach number AUSM$^+$-up flux show an exponential growth over the next few thousand t_{BV}. The growth of the Mach number is linked to that of $\Delta\varrho$. This growth even affects the Mach numbers in the simulation without well-balancing, where the Mach number increases further after about $4000\,t_{BV}$. The well-balanced simulations using the AUSM^+_B-up flux do not show this behavior and retain the very low Mach numbers. We found that other low Mach number fluxes, such as the one by Miczek et al. (2015) and Li & Gu (2008), show a growth similar to AUSM$^+$-up, although the rate varies between the different schemes. These spurious velocities are likely due to pressure–velocity decoupling, which is a common issue with compressible low Mach number methods. In combination with a gravity source term this can lead to an instability very similar to convection, but in stable stratifications. The reason is that pressure does not immediately return to its horizontal equilibrium. A common way to partially alleviate this effect is to introduce a form of pressure diffusion, such as the one suggested by Edwards & Liou (1998), which is also used in the AUSM$^+$-up solver.

While the standard flux seems to perform better in this static test case, it is ultimately not suited for the simulation of dynamic phenomena at low Mach numbers, such as convection or waves, due to its high numerical dissipation.

Figure 3 shows the typical pattern of the exponentially growing perturbation in both Mach number and $\Delta\varrho$. In both quantities we see a resolved pattern in the horizontal direction, but a grid-level oscillation in the vertical direction. One hypothesis for this behavior is that it is due to unresolved internal gravity waves in combination with pressure–velocity decoupling, see Sect. 5.3.

We run the same tests for polytropic stratifications. Here the profiles of density, pressure, and temperature are

$$\varrho = \varrho_0\theta^{\frac{1}{\nu-1}}, \quad p = p_0\theta^{\frac{\nu}{\nu-1}}, \quad T = \frac{p_0\mu}{\varrho_0 R}\theta = T_0\theta, \tag{76}$$

with

$$\theta = 1 - \frac{\nu-1}{\nu}\frac{\varrho_0}{p_0}\phi. \tag{77}$$

We set $\mu = 1\,\mathrm{g\,mol^{-1}}$. The polytropic index ν determines the slopes of the profiles. If ν is less than the adiabatic exponent γ, the atmosphere is stable. If $\nu > \gamma$, it is unstable. If both are equal the atmosphere is isentropic and therefore marginally stable.

Figure 4 shows the maximum Mach number and $\Delta\varrho$ for an isentropic atmosphere. Here the Brunt–Väisälä time t_{BV} is not well defined because $N = 0$. Instead we use the sound-crossing time $t_{SC} = 4.28\,\mathrm{s}$ for reference. α-β and deviation well-balancing stay at very low Mach numbers below 10^{-7}, independently of the choice of flux function. This result suggests that the issue with the exponential growth of perturbations in combination with low Mach number flux functions is more severe in more stable stratifications. In contrast to the isothermal test we see that Cargo–LeRoux well-balancing behaves quite similarly to the not well-balanced case. Both quickly reach Mach numbers of about 10^{-1} with flow patterns that resemble 2D convection. It is likely that this marginally unstable stratification experiences the growth of convection due to the less than ideal well-balancing properties of the Cargo–LeRoux method.

As a last test we run a polytropic stratification with $\nu = 1.6 < \gamma = 5/3$, which is stably stratified, but less so than the isothermal case. The relevant timescales here are $t_{BV} = 20.1\,\mathrm{s}$ and $t_{SC} = 4.13\,\mathrm{s}$. The results are shown in Fig. 5. Here we see that the cases without well-balancing and with Cargo–LeRoux

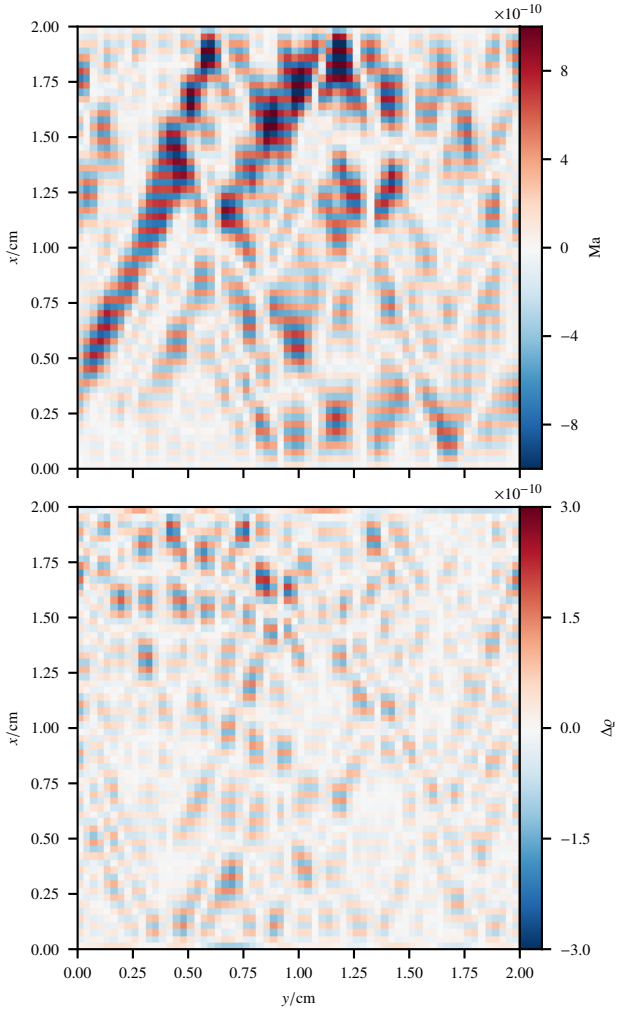

Fig. 3. Mach number (*top panel*) and horizontal density fluctuation $\Delta\varrho$ (*bottom panel*) of the 2D isothermal simulation using the AUSM$^+$-up flux and deviation well-balancing at time $t = 1000\,t_{\mathrm{BV}}$. Gravity is directed in negative x-direction.

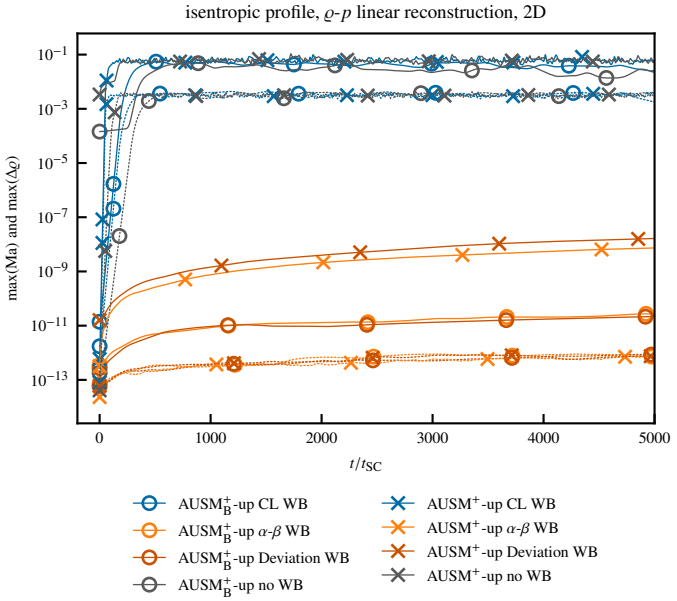

Fig. 4. Same as Fig. 2, but for an isentropic stratification. The solid lines represent the maximum Mach numbers on the grid and dotted lines the horizontal density fluctuations according to Eq. (75). Time is given in units of the sound-crossing time $t_{\mathrm{SC}} = 4.28\,\mathrm{s}$. The curves have been slightly smoothed for better visibility.

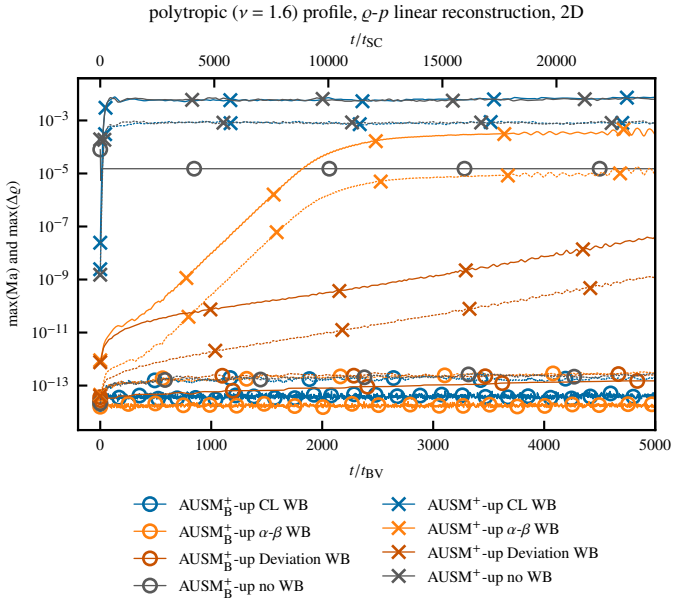

Fig. 5. Same as Fig. 2, but for a polytropic stratification with $\nu = 1.6$. The adiabatic exponent is $\gamma = 5/3$. The solid lines represent the maximum Mach numbers on the grid and dotted lines the horizontal density fluctuations according to Eq. (75). Time is given in units of Brunt–Väisälä time $t_{\mathrm{BV}} = 20.1\,\mathrm{s}$ and sound-crossing time $t_{\mathrm{SC}} = 4.13\,\mathrm{s}$. The curves have been slightly smoothed for better visibility.

well-balancing fail to preserve the hydrostatic equilibrium in combination with the low Mach number flux. For the other two well-balancing methods there is a much clearer difference in the growth rate of the perturbation with deviation well-balancing growing significantly more slowly, reaching only Mach numbers of 10^{-7} after $5000\,t_{\mathrm{BV}}$. Any of the well-balancing methods manages to keep the Mach numbers below 10^{-11} when combined with the AUSM$_{\mathrm{B}}^+$-up flux, which does not have low Mach number properties. This is in agreement with the findings in the isothermal case.

Appendix A shows the same isentropic and polytropic tests as in Figs. 4 and 5, but in the 1D case. In contrast to the 2D cases, the Mach numbers stay at low values for the runs using well-balancing also when using the AUSM$^+$-up solver. This is consistent with the hypothesis that these velocities are a form of unphysical convection caused by pressure–velocity decoupling, which is obviously not possible in only one spatial dimension.

The spurious growth we found in combination with low-Mach-number fluxes is likely not a problem particular to the well-balanced methods we presented. We considered very long timescales of thousands of sound-crossing and Brunt–Väisälä times. This is much longer than the timescales typically used to test well-balancing methods. Käppeli & Mishra (2016), for example, ran their hydrostatic setup only for $2\,t_{\mathrm{SC}}$[2]. While this would definitely show any major issues with the basic

[2] Käppeli & Mishra (2016) show another test of a 3D simulation that covers several convective turnover times and contains a stable layer. The simulation shows strong, unphysical flows in the stable layer when run without a well-balanced method, but these disappear when their well-balanced method is used. Considering they did not use a low Mach number method, this is consistent with our results.

well-balanced property of the scheme, it does not reveal the long-term growth of instabilities in the stable region. This is something to bear in mind when applying such methods to partly convectively stable configurations, such as stars. Whether the described phenomenon is an issue for real-world applications depends on many factors, such as how well the stratification is resolved and what timescales are of relevance. In particular for applications with large stable regions and long simulation times, such as in asteroseismological hydrodynamics simulations, this has to be carefully considered. The most promising method in this test is the deviation well-balancing method in combination with the AUSM$^+$-up flux.

5.2. Hot bubble

Convection in the stellar interior is usually slow and almost adiabatic. A typical convection zone is nearly isentropic, although the stratification in the star's gravitational field can span orders of magnitude in pressure and density. The buoyant acceleration of a fluid parcel is given by its entropy fluctuation with respect to the mean entropy at any given radius. Entropy fluctuations are constantly created by sources of heating or cooling. However, once the fluid parcel has left the heating or cooling layer and travels through the rest of the convection zone, the parcel's entropy must be preserved except for those parts that have mixed with their surroundings. If the flow is slow, all entropy fluctuations inside the convection zone are also small and it becomes numerically challenging to preserve their exact values when density and pressure change by large factors as the fluctuations are advected along the gravity vector.

We test the numerical schemes' entropy-preservation properties under the conditions described above by simulating the buoyant rise of a "bubble" with an adjustable initial entropy fluctuation embedded in a layer of constant entropy. The layer is strongly stratified in pressure and density due to the presence of gravity. We call this setup "hot bubble", because we use positive initial entropy fluctuations. Negative initial entropy fluctuations would make the bubble fall, but everything else would work in the same way. Our setup is similar to that used by Almgren et al. (2006) to test their MAESTRO code, although their equation of state and stratification differ from our setup. We also test our methods down to much lower Mach numbers.

We construct the stratification in a two-dimensional box 10^6 cm wide and spanning the vertical range from $y = 0$ to $y = y_{\max} = 1.5 \times 10^6$ cm. To avoid any influence of boundary conditions, we use periodic boundaries and a periodic profile of gravitational acceleration

$$g_y = g_0 \sin(k_y y), \tag{78}$$

where g_0 is a constant to be specified later and $k_y = 2\pi/y_{\max}$. The box is filled with an ideal gas with the ratio of specific heats $\gamma = 5/3$ and mean molecular weight $\mu = 1\,\mathrm{g\,mol^{-1}}$. At $y = 0$, we set the pressure to $p_0 = 10^6$ Ba and the temperature to $T_0 = 300$ K. The stratification is isentropic, that is

$$\varrho(y) = \left(\frac{p(y)}{A}\right)^{1/\gamma}, \tag{79}$$

where $A = A_0 = \text{const.}$ everywhere outside of the bubble. Inside the bubble, we perturb the entropy via

$$A = A_0 \left[1 + \left(\frac{\Delta A}{A}\right)_{t=0} \cos\left(\frac{\pi}{2}\frac{r}{r_0}\right)^2\right], \tag{80}$$

where $(\Delta A/A)_{t=0}$ is the bubble's amplitude and $r = \left[(x - x_0)^2 + (y - y_0)^2\right]^{1/2}$ is the distance from the bubble's center with $x_0 = 5 \times 10^5$ cm and $y_0 = 1.875 \times 10^5$ cm. The bubble has a radius of $r_0 = 1.25 \times 10^5$ cm. We do not perturb the hydrostatic pressure stratification, which is given by the expression

$$p(y) = \left\{p_0^{1-\frac{1}{\gamma}} + \left(1 - \frac{1}{\gamma}\right)\frac{g_0}{A_0^{\frac{1}{\gamma}} k_y}\left[1 - \cos(k_y y)\right]\right\}^{\frac{\gamma}{\gamma-1}}. \tag{81}$$

The amplitude g_0 of the gravity profile sets the ratio of the maximum to the minimum pressure in the periodic pressure profile. To make the problem numerically challenging, we use a pressure ratio of 100, which is achieved with $g_0 = -1.09904373 \times 10^5\,\mathrm{cm\,s^{-2}}$. This stratification is stronger than that in the convective core of a typical massive main-sequence star, in which the pressure changes by a factor of a few. On the other hand, the relative pressure drop from the bottom of the solar convective envelope to the photosphere is $\approx 10^9$.

We start with a moderate initial entropy perturbation of $(\Delta A/A)_{t=0} = 10^{-3}$, which makes the bubble rise at moderately low Mach numbers of a few times 10^{-2}. This allows us to perform simulations with all three well-balancing methods as well as simulations without any well-balancing at modest grid resolution of 128×192, see Fig. 6. We run this series of simulations with fixed time steps of 0.2 s. With the exception of the Cargo–LeRoux and α-β methods, which require ϱ-P reconstruction, we test both ϱ-P and ϱ-T reconstruction. The central, most buoyant, part of the bubble accelerates fastest. The bubble gets deformed into a mushroom-like shape with two trailing vortices and it expands as it rises into layers of lower pressure. Ideally, the initially positive entropy fluctuations $\Delta A/A$ should mix with the isentropic ($\Delta A/A = 0$) background stratification, creating smaller but still positive entropy fluctuations. The entropy fluctuations may locally increase a bit as kinetic energy is slowly dissipated into heat, but there is no physical way for them to become negative. Any negative entropy fluctuations in the numerical solution result from numerical errors.

Figure 6 shows that both the absence of well-balancing and the Cargo–LeRoux method generate large areas of negative entropy fluctuations comparable to or even larger in absolute value than the bubble's initial amplitude. Large-scale positive entropy fluctuations also occur far from the bubble and they clearly do not result from hydrodynamic mixing. They rather seem to be caused by entropy nonconservation as the bubble pushes the surrounding stratification upwards and downwards. In the no-well-balancing case, errors in $\Delta A/A$ are smaller when ϱ-T reconstruction is employed as compared with ϱ-p reconstruction. This may be due to the fact that the pressure changes by a factor of 100 in the computational domain whereas the temperature only changes by a factor of 6.3. In any case, α-β and deviation well-balancing clearly provide far superior results with only a mild and highly localized undershoot in $\Delta A/A$ above the bubble. With the deviation method, this success is independent of the choice of reconstruction.

All of the methods tested converge upon grid refinement, although not in the same way, see the series of runs shown in Fig. 7. In this series, we keep the 0.2 s time steps for all runs except those on the finest (256×384) grid, for which we use 0.1 s. When there is no well-balancing or the Cargo–LeRoux method is used, the amplitude of the large-scale entropy-conservation errors around the bubble decreases upon grid refinement and the bubble's shape slowly approaches that obtained with the α-β and deviation methods. The errors are still substantial even

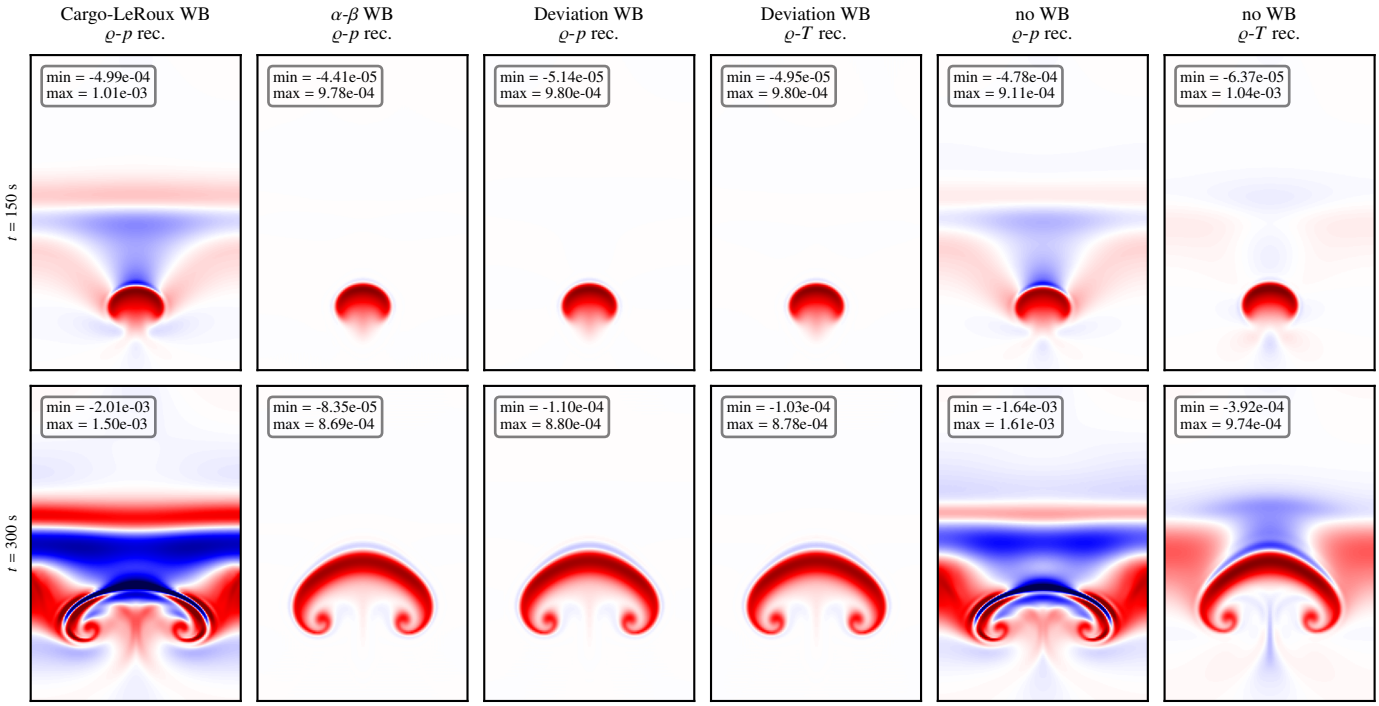

Fig. 6. Time evolution (*top to bottom*) of the hot-bubble problem when solved using different well-balancing and reconstruction schemes (*left to right*) on a 128 × 192 grid. In all of the cases, entropy fluctuations $\Delta A/A$ are shown on the same color scale ranging from -10^{-3} (dark blue) through 0 (white) to 10^{-3} (dark red). The minimum and maximum values of $\Delta A/A$ in the whole simulation box are given in each panel's inset. The amplitude of the initial entropy perturbation is $(\Delta A/A)_{t=0} = 10^{-3}$.

on the finest (256 × 384) grid tested. The slight entropy undershoot produced by the α-β and deviation methods does not decrease in amplitude but it does decrease in spatial extent as the grid is refined. Surprisingly, we do not observe any significant entropy fluctuations far from the bubble even on the coarsest grid (64 × 96) with these two methods.

As the bubble's initial amplitude $(\Delta A/A)_{t=0}$ is decreased, the typical Mach number in the flow field decreases as

$$\mathrm{Ma} \propto \left(\frac{\Delta A}{A}\right)^{1/2}_{t=0}. \tag{82}$$

This scaling results from the fact that the bubble's acceleration is proportional to $\Delta\varrho/\varrho \propto \Delta A/A$ and the velocity an object in uniformly accelerated motion reaches over a fixed distance (i.e., until the bubble has reached the same evolutionary stage) is proportional to the square root of the acceleration. Although the bubble's acceleration is not constant, the bubble always evolves in the same way, just slower, when its initial amplitude is decreased and the scaling still holds.

The scaling is also demonstrated in Fig. 8, which shows a series of runs performed on a 128 × 192 grid with $(\Delta A/A)_{t=0}$ ranging from 10^{-3} down to 10^{-11}. As $(\Delta A/A)_{t=0}$ decreases, we increase time steps in this order: 0.2 s, 1 s, 10 s, 25 s, 25 s. The solver's convergence worsens as all fluctuations become smaller, limiting the maximum time step size. We only include the α-β and deviation well-balancing methods in this experiment, because entropy-conservation errors quickly dominate the solution when the initial amplitude is decreased and the Cargo–LeRoux or no well-balancing method is used. Because the Mach number is expected to scale according to Eq. (82), we scale the time when the simulation is stopped with $(\Delta A/A)^{-1/2}_{t=0}$. This way, we compare the results when the bubble has reached approximately the same height and evolutionary stage as the previously discussed case with $(\Delta A/A)_{t=0} = 10^{-3}$ at $t = 300$ s (Fig. 6). Both the α-β and deviation well-balancing methods provide essentially the same solutions, reproducing the expected Mach-number scaling down to Ma $\sim 10^{-6}$. The amplitude of the entropy undershoot above the bubble is 24% lower when the α-β method is used as compared with the deviation method. The most extreme run with $(\Delta A/A)_{t=0} = 10^{-11}$ reaches the limits of our current implementation and we can see numerical noise developing in the stratification, see Figs. B.1 and B.2. Figure 8 also shows that the minimum and maximum entropy fluctuations in the evolved flow scale in proportion to the initial amplitude of the bubble.

5.3. Simple convection setup

The previous section demonstrated the capabilities of the α-β and deviation well-balancing schemes to evolve the rise of a bubble with an entropy excess in an isentropic stratification at low Mach numbers. This can be interpreted as a test for the fundamental mechanism of convection. The purpose of this section is to also assess the benefit from well-balancing techniques for fully developed convection in a realistic stellar scenario.

The prototype of a convective region in stellar interiors includes a steady heating source in the form of nuclear burning that injects energy over a long period in time. If radiative transport of energy is not efficient enough, the temperature gradient will steepen until it reaches the adiabatic temperature gradient. According to Eq. (16), this region will become unstable and convection will set in. As convection is very efficient in transporting energy, a common assumption is that the stratification settles to an nearly adiabatic temperature gradient in the steady state.

In stars, a convective region is typically adjacent to convectively stable regions. The mixing processes across the interfaces of convectively stable and unstable regions have a profound

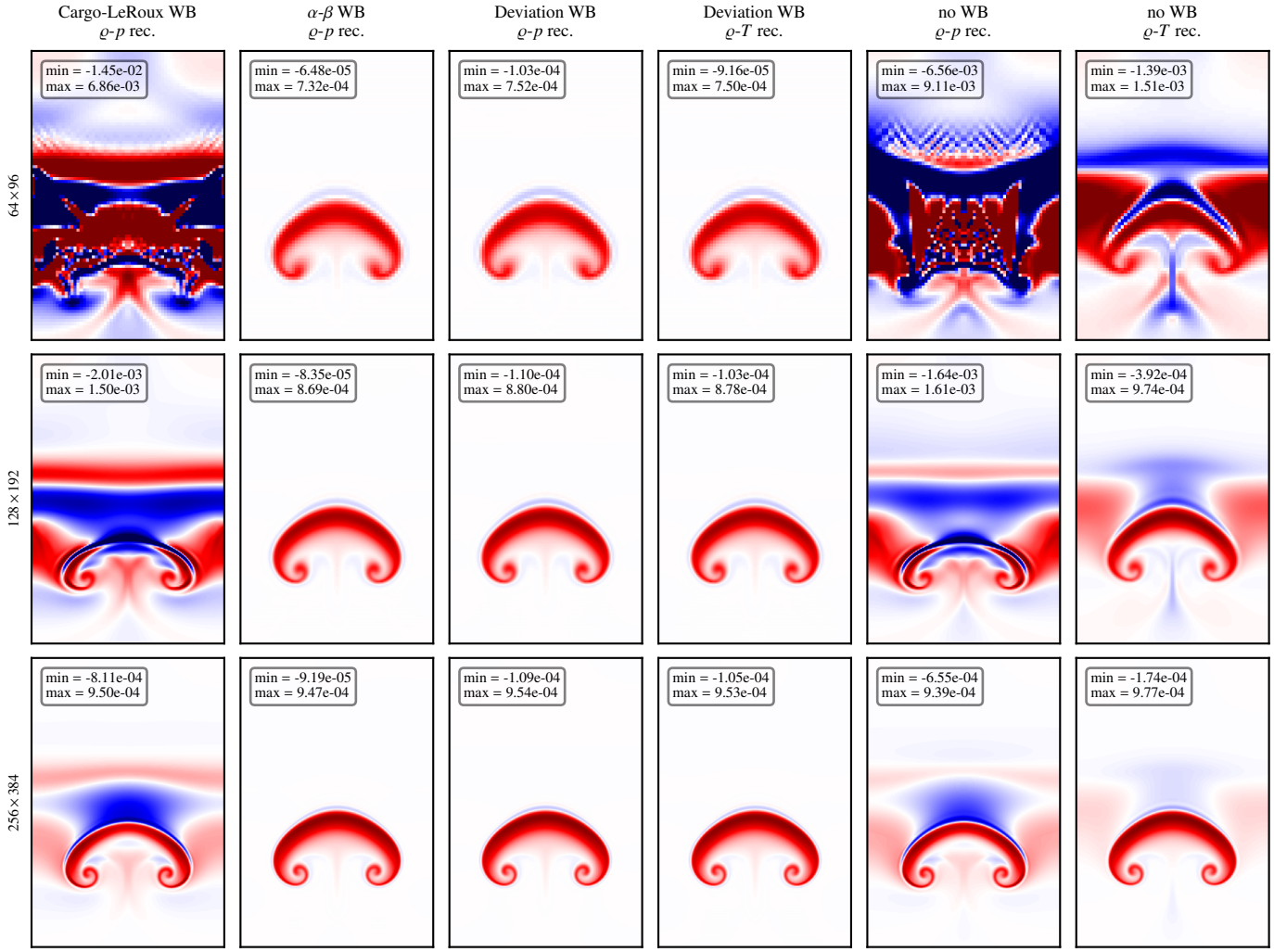

Fig. 7. Same as Fig. 6, but showing the solutions' resolution dependence (*top to bottom*) at $t = 300\,\mathrm{s}$.

impact on stellar evolution, yet it is particularly difficult to parametrize these processes in one-dimensional stellar evolution codes. A common strategy for improving the current 1D description is to investigate the dynamics at the interfaces of convection zones by means of multidimensional hydrodynamical simulations (Jones et al. 2017; Cristini et al. 2019; Pratt et al. 2020; Higl et al. 2021; Horst et al. 2021).

The Mach number of convection deep in the stellar interior is estimated to be on the order of 10^{-4} in early stages of stellar evolution. Accurate modeling of the early phases is, however, crucial as it determines the whole subsequent evolution of the star and inaccuracies will propagate to later stages. Thus, numerical experiments that address convection in stellar interiors rely on schemes that accurately maintain hydrostatic stratifications and that are able to follow convection at low Mach numbers for a sufficient amount of time.

The initial stratification for the test series presented in this section consists of a convective region with a stable layer on top. One possibility to set up this configuration would be to use realistic initial conditions from a 1D stellar evolution code. However, such 1D profiles usually require some extra treatment before they can be used for hydrodynamical simulations, for example a smoothing of sharp composition gradients or to properly impose a flat entropy profile in the convection zone. Instead, we use analytical initial conditions to be able to test the numerical methods under well-defined but realistic conditions. This way, any numerical artifacts that may arise can solely be attributed to the methods applied rather than to inadequate initial conditions.

To construct the initial hydrostatic stratification, we follow the procedure described by Edelmann et al. (2017). It imposes the profile of the superadiabaticity $\Delta\nabla = \nabla - \nabla_{\mathrm{ad}}$ while integrating the equation of hydrostatic equilibrium (Eq. (11)). According to Eq. (16), $\Delta\nabla$ determines the sign of the Brunt–Väisälä frequency. It is therefore possible to precisely control which regions are convectively stable ($\Delta\nabla < 0$) and unstable ($\Delta\nabla > 0$) as well as the respective transitions between these regions. A marginally stable stratification is imposed inside the convection zone by setting $\Delta\nabla_{\mathrm{CZ}} = 0$. In the stable region, we impose $\Delta\nabla_{\mathrm{SZ}} = -\nabla_{\mathrm{ad}}$, which corresponds to an isothermal stratification.

To connect the two regions, we use a sinusoidal transition, which ensures that the transition between the two $\Delta\nabla$-values is well-defined and can be resolved numerically. The profile with a transition between the convection and stable zones then takes the form

$$\Delta\nabla(y) = \Delta\nabla_{\mathrm{CZ}} + \frac{1}{2}\left[1 + \sin\left(\frac{\pi}{2}\,\eta(y, K, y_{\mathrm{CZ,SZ}})\right)\right](\Delta\nabla_{\mathrm{SZ}} - \Delta\nabla_{\mathrm{CZ}})\,, \tag{83}$$

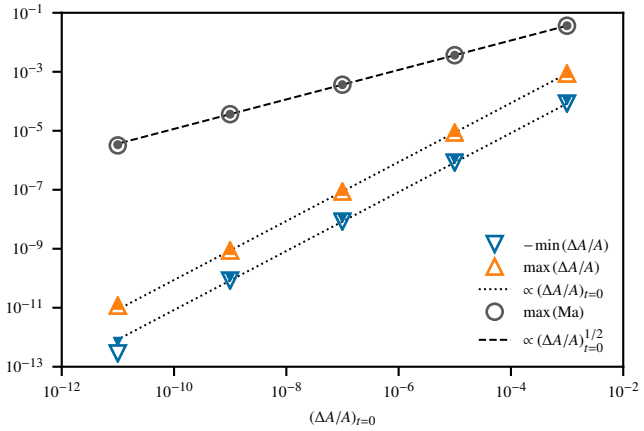

Fig. 8. Dependence of the maximum Mach number Ma and minimum and maximum entropy fluctuations $\Delta A/A$ on the bubble's initial amplitude $(\Delta A/A)_{t=0}$. All measurements are taken when the bubble has evolved to a stage comparable to that shown in the bottom row of Fig. 6. Open and filled symbols correspond to runs with α-β and deviation well-balancing, respectively. The lines show that the Mach number scales according to Eq. (82) and the minimum and maximum entropy fluctuations scale in proportion to the bubble's initial amplitude.

with

$$\eta(y, K, y_i) = \begin{cases} -1 & \text{if } K(y - y_i) < -1, \\ 1 & \text{if } K(y - y_i) > 1, \\ K(y - y_i) & \text{otherwise,} \end{cases} \tag{84}$$

where the constant K determines the steepness of the transition. It is set such that the transition is resolved by at least 20 grid cells. The coordinate $y_{\mathrm{CZ,SZ}}$ denotes the middle of the transition starting at $y_{\mathrm{CZ,SZ}} - 1/K$ and ending at $y_{\mathrm{CZ,SZ}} + 1/K$. The value of $y_{\mathrm{CZ,SZ}}$ is given in Table 2. The computational domain spans $2y_{\mathrm{CZ,SZ}}$ in the horizontal direction. The profiles of temperature T, pressure p and density ϱ then follow from integrating the equation of hydrostatic equilibrium Eq. (11) as described by Edelmann et al. (2017) with a spatially constant gravitational acceleration of $|\boldsymbol{g}| = 6.6 \times 10^4\,\mathrm{cm\,s^{-2}}$. The initial values required for the integration are listed in Table 2. They are representative of the conditions expected in the convective core of a 25 $M_\odot$ main sequence star with a mean atomic weight of $\overline{A} = 1.3$ and a mean charge of $\overline{Z} = 1.1$.

Figure 9 shows the resulting profiles of $\Delta\nabla$, T, and ϱ as well as the fact that the transition between the convective and stable zone is well resolved even on the coarsest SLH grid. Because cores of massive stars are hot, a considerable fraction of the total pressure is contributed by the radiation field. The relative importance of radiation pressure is given in the lower panel of Fig. 9. It ranges from roughly 20% in the bottom region to about 60% in the top region where the density is low. This test setup is therefore also an example where the ideal gas EoS is not sufficient to describe the thermodynamic behavior of the gas and which requires well-balancing methods that can handle general EoS.

To trigger convection in the initially marginally stable convection zone, a heat source is placed at the bottom of the convection zone that continuously injects energy into the system with a sinusoidal profile peaking at the bottom of the domain. The heating profile is given by

$$\dot{e}_h(y) = \dot{e}_0\, a\, \sin\left(\frac{\pi}{2}\left[1 + \eta(y, K, 0)\right]\right)\,\mathrm{erg\,s^{-1}\,cm^{-3}}, \tag{85}$$

Table 2. Parameters of the convection test setup.

Quantity	Value
T_0	3.7×10^7 K
p_0	$2.4 \times 10^{16}\,\mathrm{g\,cm^{-1}\,s^{-2}}$
$\lvert\boldsymbol{g}\rvert$	$6.6 \times 10^4\,\mathrm{cm\,s^{-2}}$
y_{bot}, y_{top}	0, 2.6×10^{11} cm
$y_{\mathrm{CZ,SZ}}$	$0.66\, y_{\mathrm{top}}$
$x_{\mathrm{right}} - x_{\mathrm{left}}$	$2\, y_{\mathrm{CZ,SZ}}$
$\Delta\nabla_{\mathrm{CZ}}$, $\Delta\nabla_{\mathrm{SZ}}$	0, $-\nabla_{\mathrm{ad}}$
$\overline{A}$, $\overline{Z}$	1.3, 1.1

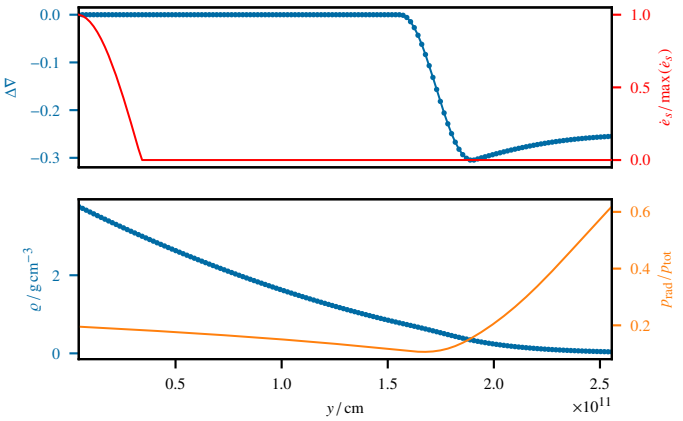

Fig. 9. Initial stratification of the convection setup. The red curve illustrates the position and shape of the energy injection which has nonzero values only at the bottom of the convection zone. Its actual amplitude is set for the different simulations individually. Dots denote the positions of cell centers on a grid with 144 vertical cells, the lowest resolution used in the SLH simulations presented in this section.

with

$$a = \frac{4\sin(\pi K \Delta y/4)}{\pi K \Delta y},\; K = \frac{1}{0.2\, y_{\mathrm{CZ,SZ}}}, \tag{86}$$

where Δy denotes the grid spacing in the vertical direction. As introduced here, $\dot{e}_0$ is dimensionless. The factor a ensures that the total heating rate is independent of grid resolution. In a stationary state, the convective velocity is expected to scale with the heating rate,

$$\mathrm{Ma_{rms}} \propto \dot{e}_0{}^{1/3}. \tag{87}$$

This scaling can be motivated using dimensional arguments (e.g., see Jones et al. 2017) or the mixing-length theory (Kippenhahn et al. 2012) and has been confirmed in numerical experiments (e.g., Cristini et al. 2019; Edelmann et al. 2019; Andrassy et al. 2020).

To test the low-Mach capabilities of the methods that are presented in this paper, the amplitude of the heating factor $\dot{e}_0$ is decreased successively while the root mean square (rms) Mach number measured from the simulation is compared to the expected scaling Eq. (87). The upper limit of $\dot{e}_0$ is chosen such that the resulting Mach number is in a regime where also simulations without well-balancing follow the scaling. A deviation from the expected scaling at lower values of $\dot{e}_0$ and correspondingly lower Mach number then indicates that numerical errors have become significant and the method has reached its limit of

applicability. The scaling test is performed for all available well-balancing methods and also in the absence of well-balancing. The domain is discretized by 72×144 cells. This rather coarse resolution is chosen to assess the ability of the well-balancing method to balance hydrostatic stratifications even with a moderate number of cells. While any consistent method will ultimately be able to follow low-Mach-number flows given a sufficiently fine grid, this is computationally not feasible, especially in 3D. The simulations use periodic boundary conditions in the horizontal direction. At the top and bottom of the domain solid-wall boundaries are employed that do not allow mass to enter or leave the domain. For the time stepping, we set $c_{\mathrm{CFL}} = 0.5$. The initial stratification is perturbed by random density fluctuations at the $O\left(10^{-14}\right)$ level to facilitate the growth of the convective instability. Additionally, the heating profile Eq. (85) is modulated by a sinusoidal function along the horizontal direction to break the initial horizontal symmetry. The wavelength is one fourth of the horizontal extent and the amplitude is set to $0.01\, \dot{e}_h(y)$. The modulation is switched off after the flow has reached a substantial fraction of its final speed.

For all simulations, a grid file is saved every 200 time steps. For each saved grid, the mass-weighted rms Mach number $\mathrm{Ma}_{\mathrm{rms}}$ is calculated. To this end, only the fixed region from y_{bot} to $y_{\mathrm{CZ,SZ}}$ is considered, although the position of the boundary between convective and stable zone is dynamical and may change over time. However, for the simulation presented in this section, this effect is negligible and a fixed region is chosen for convenience. For all simulations, $\mathrm{Ma}_{\mathrm{rms}}$ is then averaged over the same time span in terms of the convective turnover time τ_{conv}, which we define as

$$\tau_{\mathrm{conv}} = \frac{2\, y_{\mathrm{CZ,SZ}}}{v_{\mathrm{rms}}}, \tag{88}$$

where v_{rms} is the rms velocity. This ensures that the stochastic fluctuations, which have different typical timescales for different flow speeds, are accounted for in a similar way for all simulations. Due to the steady heat injection and the small amount of numerical dissipation in 2D simulations, the value of τ_{conv} slightly decreases over time as velocities slightly increase. Thus, the average of τ_{conv} depends on the time interval considered and is not clear how to chose the proper time interval for the different simulations. Instead, the number of turnover times N_τ as a function of physical time t,

$$N_\tau(t) = \int_0^t \frac{1}{\tau_{\mathrm{conv}}(t')}\, \mathrm{d}t', \tag{89}$$

is used to determine the respective time intervals and the averaging is done in the time interval $t \in [t(N_\tau = 5),\, t(N_\tau = 10)]$. The resulting $\mathrm{Ma}_{\mathrm{rms}}$ as functions of the heating rate are depicted in Fig. 10. For the two highest values of $\dot{e}_0$, that is at $\mathrm{Ma}_{\mathrm{rms}}$ around 9×10^{-3} and 4×10^{-3}, all methods agree and $\mathrm{Ma}_{\mathrm{rms}}$ follows the scaling given by Eq. (87). This is not the case at lower heating rates. For $\dot{e}_0 \lesssim 10^5$, the simulation using the Cargo–LeRoux well-balancing method considerably deviates from the expected scaling by giving a value of $\mathrm{Ma}_{\mathrm{rms}}$ that does not correlate with the energy input anymore but stays rather constantly slightly below 4×10^{-3}. Almost identical results are found when no well-balancing is applied in combination with ϱ-p as reconstruction variables. At this point, it seems that Cargo–LeRoux well-balancing is not able to improve the behavior at lower Mach numbers. The results slightly improve if ϱ-T are used for reconstruction and no well-balancing is used. In this case, the Mach number settles slightly below $\mathrm{Ma}_{\mathrm{rms}} = 2 \times 10^{-3}$ for an energy

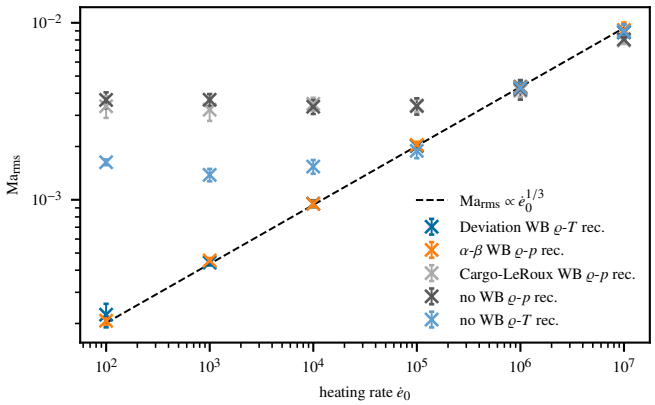

Fig. 10. Root mean square Mach number $\mathrm{Ma}_{\mathrm{rms}}$ as a function of the heating rate $\dot{e}_0$. The dashed line represents the expected scaling according to Eq. (87). All values correspond to time averages over $t \in [t(N_\tau = 5),\, t(N_\tau = 10)]$ (see text). The vertical error bars denote one standard deviation of the temporal average of $\mathrm{Ma}_{\mathrm{rms}}$.

input rate lower than $\dot{e}_0 = 10^5$. The reason for this could be the nonnegligible contribution of radiation-pressure to total pressure. As $p_{\mathrm{rad}} \propto T^4$, a more accurate reconstruction of T could lead to an interface pressure that is closer to the hydrostatic solution and hence artifacts from imperfect balancing are reduced.

By definition, α-β well-balancing requires ϱ-p to be reconstructed while the variables can be chosen freely for deviation well-balancing. Hence we have chosen ϱ-T for the deviation runs for comparison. However, no major differences can be seen between α-β and deviation in Fig. 10. Both $\mathrm{Ma}_{\mathrm{rms}}$ profiles closely follow the scaling down to the smallest value of $\dot{e}_0$. Due to the hydrostatic solution's being stored at cell interfaces in these two methods, the particular choice of variables for reconstruction seem to be less important. In contrast, the Cargo–LeRoux method reconstructs the potential q at the interfaces using values at the cell centers, which can introduce an error in the total energy over many time steps. A possible fix for this would be to store q at the cell interfaces, however this is currently not implemented in our code.

It is not obvious how to assess the accuracy at which hydrostatic equilibrium is maintained within the convective region. Convection will inevitably introduce ram pressure, p_{ram}. Its ratio with thermal pressure, p_{thermal}, is expected to scale as $p_{\mathrm{ram}}/p_{\mathrm{thermal}} \sim \mathrm{Ma}_{\mathrm{rms}}{}^2$. This gives an order-of-magnitude estimate for the expected minimal deviation from the initial hydrostatic pressure stratification caused by convective motion alone, independent of the choice of well-balanced method. We have verified that the respective relative deviation from the hydrostatic pressure at $t(N_\tau = 7.5)$ scales as $\mathrm{Ma}_{\mathrm{rms}}{}^2$ for all sets of simulations. The only exception is the simulation with deviation well-balancing at the lowest heating rate, which may be a result of sound waves excited by the strong flow field in the stable zone (see Fig. 11 and the next paragraph). Table C.1 lists the ratio exemplarily for the simulations using α-β well-balancing. There, the relative deviation ranges from about 10^{-7} at the smallest heating rate to roughly 10^{-4} at the largest rate. At $t = 0$ we measure a mean relative deviation of 2.7×10^{-8}, which originates entirely in the discretization error of the pressure gradient. The fact that the relative deviations from hydrostatic equilibrium are of the same order of magnitude as the ram pressure implies that they are not an artifact of the well-balancing method, but physically caused by the convective motions.

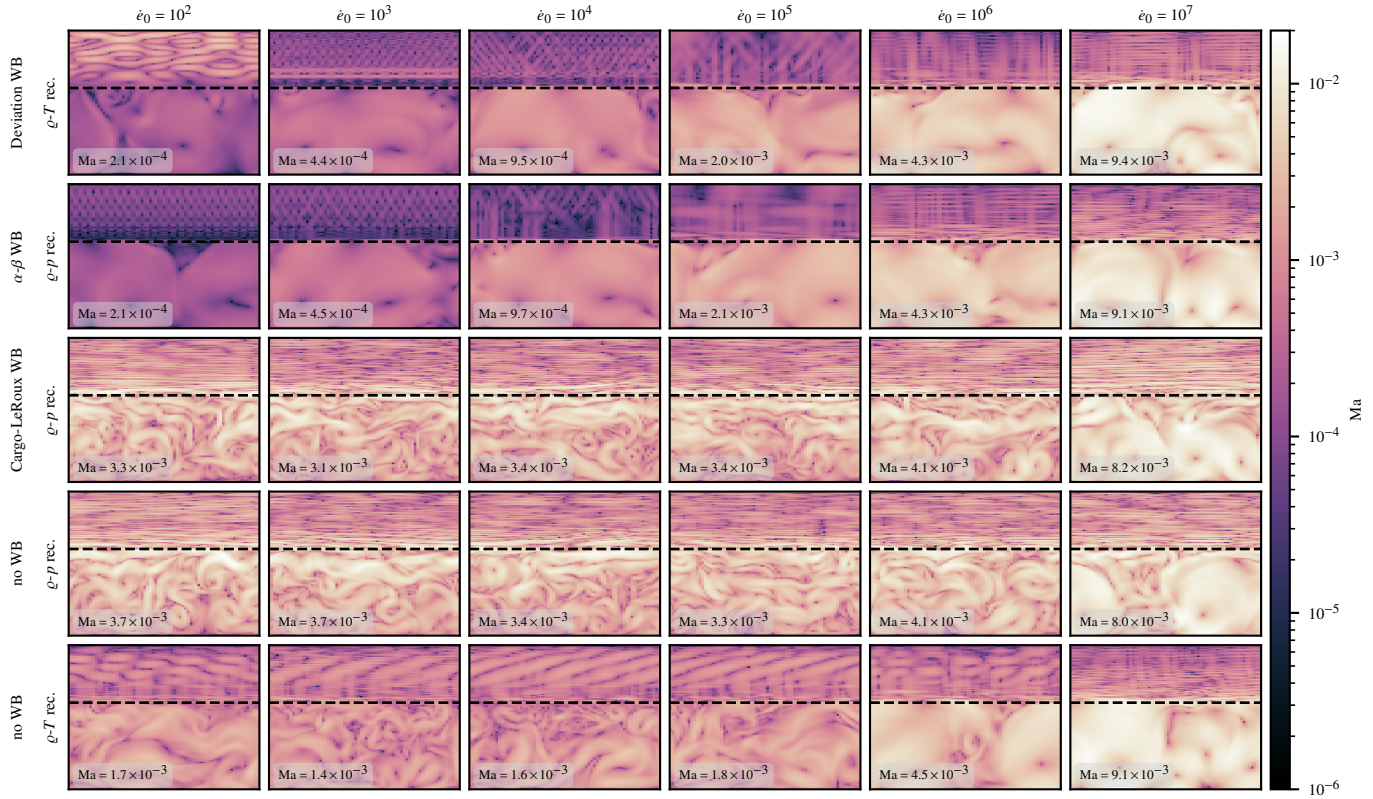

Fig. 11. Mach number of the flow for different values of the heating rate $\dot{e}_0$ (*left to right*) and different well-balancing methods (*top to bottom*). The dashed black lines denote the boundaries of the convection zone at $y = y_{\rm top}$, see Table 2 for an overview of simulation parameters. The insets displays the rms Mach number $\mathrm{Ma}_{\rm rms}$ within the convection zone for the snapshot shown. All snapshots are taken at $t(N_\tau = 7.5)$.

To also add a qualitative visual verification of the arising convection, the flow patterns are shown in Fig. 11 in the middle of the time frame considered. For the highest heating rate, all simulations show the typical flow morphology of two-dimensional convection: A pair of large eddies form with a size that is determined by the vertical extent of the convection zone. At lower heating rates, the flow pattern remains basically the same for deviation and α-β well-balancing, which strengthens our confidence in these solutions. In contrast, the flow patterns obtained with Cargo–LeRoux well-balancing or without any well-balancing are dominated by incoherent, small-scale structures. While for the "no WB" run with ϱ-T reconstruction, the Mach numbers achieved are somewhat smaller, the general flow pattern is similar. We assume that these motions are caused by the imperfect hydrostatic equilibrium.

Convective regions are known to excite internal gravity waves (IGW) in adjacent stable layers (see e.g., Rogers et al. 2013; Edelmann et al. 2019; Horst et al. 2020). Assuming that IGW are predominantly generated at periods close to the convective turnover time $\tau_{\rm conv}$ (cf. Edelmann et al. 2019), we can estimate their vertical wavelength $\lambda_{\rm v}$ using the dispersion relation of IGW in the Boussinesq approximation (see, e.g., Sutherland 2010),

$$\lambda_{\rm v} = \frac{\lambda_{\rm h}}{\sqrt{[N\tau_{\rm conv}/(2\pi)]^2 - 1}}, \tag{90}$$

where $\lambda_{\rm h}$ is the horizontal wavelength. It follows that the vertical wavelength decreases with increasing $\tau_{\rm conv}$ for $\lambda_{\rm h}$ = const. and the waves will become unresolved when the heating rate is decreased on the same computational grid.

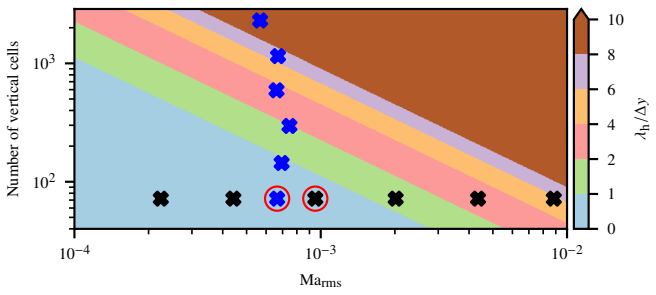

Fig. 12. Expected typical vertical wavelength (Eq. (90)) in grid cells of internal gravity waves as a function of $\mathrm{Ma}_{\rm rms}$ in two series of simulations with the deviation well-balancing method. Black crosses correspond to simulations at fixed resolution but increasing heating rate. Blue crosses correspond to simulations at a fixed heating rate but different resolution. The two encircled data points result from the same simulation but $\mathrm{Ma}_{\rm rms}$ has been determined at a different time.

We estimate the vertical wavelengths according to Eq. (90) exemplarily for the simulations with deviation well-balancing shown in Figs. 10 and 11. To calculate $\lambda_{\rm v}$, the value of the Brunt–Väisälä frequency is taken at the top of the box domain and $\lambda_{\rm h} = 2\,y_{\rm CZ,SZ}$, which corresponds to the maximal horizontal wavelength that fits into the computational domain. The ratio of $\lambda_{\rm v}$ to the vertical grid spacing is shown in Fig. 12 as black crosses. At all but the two highest heating rates, the vertical wavelength is less than two cells and it follows from the Nyquist sampling criterion that such waves cannot be represented on our coarse grid. Indeed, for these runs strange patterns appear in the stable zone as can be seen in Fig. 11. A peculiar pattern is visible in the stable zone for deviation well-balancing at the lowest

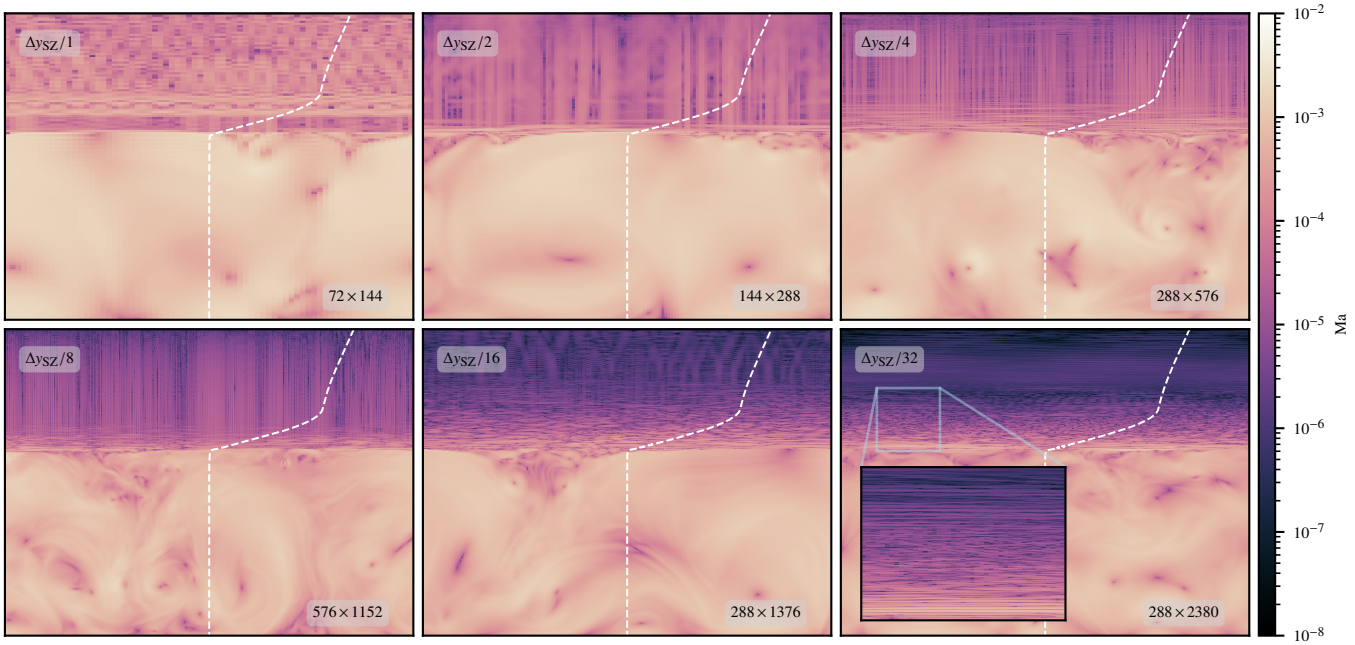

Fig. 13. Mach number for a heating rate of $\dot{e}_0 = 10^4$ and deviation well-balancing at different resolutions. The upper left box in each panel indicates the change in the vertical resolution relative to the resolution used for the Mach number scaling. The lower right box gives the total number of cells of the particular simulation. All snapshots are taken as soon as convection has fully developed. The dashed white line illustrates the profile of the Brunt–Väisälä frequency as a function of height with arbitrary units on the x-axis.

heating rate. While its origin is not completely understood, we have verified that the results look similar to the other runs when ϱ-p reconstruction or a higher grid resolution is applied. Our estimate gives typical wavelengths of two to six cells in the two simulations with the highest heating rates. Hence, the flow patterns in Fig. 11 for these two simulation probably include some real internal gravity waves, but they are still dominated by artifacts.

To confirm that our interpretation is correct, we run another series of simulations with increasing vertical resolution at $\dot{e}_0 = 10^4$. Deviation well-balancing is used in this experiment. Because of the higher computational costs, there is not enough data to perform meaningful averages and $\mathrm{Ma}_{\mathrm{rms}}$ is extracted for a single snapshot as soon as convection has developed in the whole convective zone. The results are shown as blue crosses in Fig. 12. Because $\mathrm{Ma}_{\mathrm{rms}}$ is measured at earlier times compared with the corresponding simulation in the heating series, the $\mathrm{Ma}_{\mathrm{rms}}$ of the lowest-resolution run does not coincide with the (red circled) black cross corresponding to the same simulation. We see that the expected typical vertical wavelength is resolved by more than eight cells on the finest grid. Figure 13 shows the flow pattern for the different grid resolutions. In the center and right panel of the lower row, the resolution in the convective zone corresponds to the resolution of the upper right panel (288×576). Close to the transition to the stable zone, the vertical spacing is smoothly reduced to 1/32 of the starting resolution. This saves computing resources and also illustrates that the patterns do not depend on the resolution in the convective zone. The transition is shown in Fig. C.1.

Our resolution study indicates that with increasing vertical resolution in the stable zone artifacts are diminished. For the highest resolution fine wave patterns are observed. As grid resolution increases, nearly horizontal wave patterns first appear close to the convective boundary, where N gradually increases from zero to relatively large values higher up in the stable zone.

While our findings can be explained by unresolved IGW, we cannot exclude that at least to some extent also numerical artifacts contribute to the flows in the stable zone. Nevertheless, our tests with the simple convective box show that, as soon as we resolve the IGW sufficiently, artifacts tend to disappear and any instabilities possibly still present do not visibly dominate the flow. At the same time, this illustrates that, depending on the actual stellar profile, rather high grid resolution is needed to properly resolve the waves.

5.4. Keplerian disk

Some astrophysical problems involve stationary solutions that are not at rest, for example a rotating star that is partially stabilized by the centrifugal force (e.g., Tassoul 2000; Maeder 2009). Another case is the Keplerian motion around a central gravitational mass m in its gravitational potential $\phi(r) = -\frac{Gm}{r}$. Gaburro et al. (2018) describe a nondimensional test setup of a circular disk with $\varrho_0 = p_0 = 1$ around a massive object. Neglecting its own gravitational field, such a disk can be stabilized by a flow velocity of

$$u(x, y) = -\sin\left[\mathrm{atan2}\,(y, x)\right]\sqrt{\frac{Gm}{r(x, y)}} \tag{91}$$

$$v(x, y) = \cos\left[\mathrm{atan2}\,(y, x)\right]\sqrt{\frac{Gm}{r(x, y)}}, \tag{92}$$

where $r = \sqrt{x^2 + y^2}$ and $\mathrm{atan2}\,(y, x)$ is the typical shortcut for choosing the quadrant of $\arctan(y/x)$ correctly. For convenience we set $G = m = 1$. We simulate the Keplerian disk from radius $r = 1$ to 2 on a polar grid with 20 radial and 70 angular cells as well as on a finer grid with 100 radial and 350 angular cells. Polar coordinates are the appropriate choice for the problem's geometry and should therefore lead to the least amount

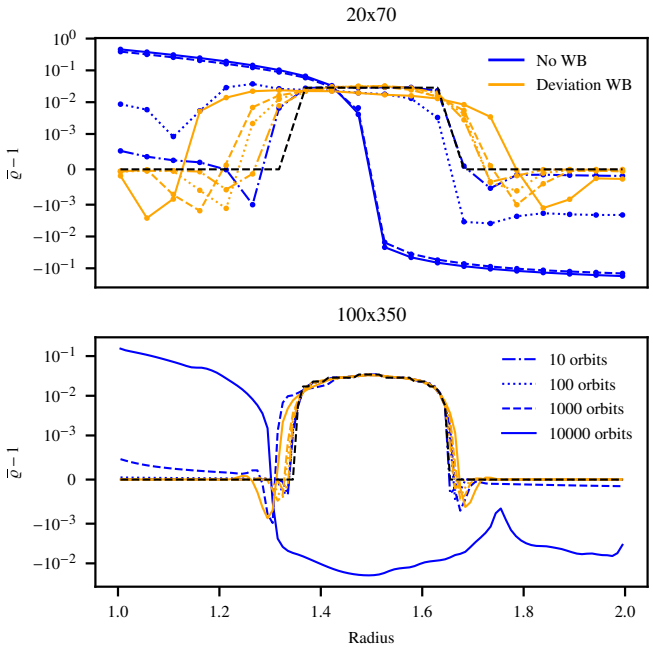

Fig. 14. Time evolution of the angle-averaged density profiles $\overline{\varrho} - 1$ in the Keplerian disk setup. *Top panel*: results with a grid resolution of 20×70 cells, where the dots on top of the lines represent corresponding results computed with implicit time stepping. *Bottom panel*: same quantity computed on a much finer grid of 100×350 cells. The black dashed lines in each panel show the respective initial density profiles.

of numerical errors. We use periodic and solid-wall boundaries in the angular and radial directions, respectively. The flow has a maximum Mach number of 1 at the inner domain boundary dropping to ≈0.6 at the outer boundary. We perform most of our simulations with the explicit RK3 scheme (see Sect. 3) because it is more efficient in this Mach number range. The time step of explicit runs is set by the CFL_{uc} criterion (Eq. (28)) with $c_{\mathrm{CFL}} = 0.4$. For the lower-resolution setup we also perform simulations with implicit time stepping and the CFL_{ug} time step criterion (Eq. (26)) with $c_{\mathrm{CFL}} = 0.4$. We find that the results of the implicit runs are identical to the explicit time stepping (see dots in upper panel of Fig. 14). Tests with the explicit, second-order RK2 scheme also give almost identical results.

Since the disk is isobaric, we use ϱ-p reconstruction for this test case. Here we only compare simulations without well-balancing to runs with deviation well-balancing, since the other methods presented in this work are not capable of stabilizing a target solution with a nonzero velocity field (see Sect. 4.3).

In order to asses the stability of the setup we add a density perturbation with $\varrho = 2$ in the circular region $(x + 1.5)^2 + y^2 < 0.15^2$ and follow its evolution up to 10 000 orbital periods, where the orbital period is taken at the central point of the perturbation. A perfect solution will maintain the initial radial density distribution of the perturbation at all times. However, due to its radial extent there will be a phase shift between the innermost and outermost regions of the perturbation. Furthermore, numerical diffusion will spread the perturbation predominantly in the direction of its movement. Therefore the perturbation evolves into a homogeneous ring orbiting the central object with a density that corresponds to the initial angle-averaged density $\overline{\varrho}$.

In Fig. 14 we show how the profile of $\overline{\varrho} - 1$ evolves with time. The target solution is given as a black dashed line. For a grid resolution of 20×70 cells the run without well-balancing only shows small deviations from the target solution after 10 orbital periods. However, we already see that mass starts to accumulate in the center. The mass can not leave the domain and accrete onto the central object due to our wall boundaries. Over time, more and more mass flows to the inner boundary. After 100 orbits the center has approximately the same density as the initial perturbation, and after 1000 orbits the profile has completely shifted toward the inner boundary. This is also clearly visible in the two-dimensional density distribution shown in Fig. D.1. With deviation well-balancing the profile remains mostly stable up to 1000 orbits. The perturbation is slowly diffusing symmetrically around the initial peak, maintaining the general shape of the initial density profile. After 10 000 orbits we see that also the run with deviation well-balancing has become noticeably asymmetric toward the center. The regions where the density falls bellow the initial density profile are most likely related to the fact that we do not use flux limiters for these runs. Undershoots at steep gradients are a common consequence of this omission.

Increasing the resolution improves the stability of the runs without well-balancing (see bottom panel in Fig. 14). At a resolution of 100×350 cells the distribution is still almost identical to the initial perturbation even after 100 orbits. Only after 1000 orbits we start to notice the accumulation of mass at the inner boundary similar to the low-resolution case. After 10 000 orbits, however, the distribution has again completely shifted towards the center and the initial perturbation is not recognizable any longer. The high-resolution run with deviation well-balancing, on the other hand, is almost identical to the target solution even after 1000 orbits. The increased radial resolution has reduced the radial diffusion observed in the low-resolution runs. The density undershoots become more noticeable at the 10 000 orbit mark. There we again identify a tendency for a slow drift towards the center. However, thanks to the use of well-balancing the shape of the initial perturbation is still retained approximately.

This test shows that the flexibility of the deviation well-balancing method also allows to maintain stable configurations other than hydrostatic equilibrium. This is particularly important for the long-term evolution of such systems. Without well-balancing stability can only be achieved by increasing grid resolution, which leads to substantially higher computational cost.

6. Summary and conclusions

We have presented the deviation, the α-β, and the Cargo–LeRoux well-balancing methods that aim to improve the ability of finite-volume codes to maintain hydrostatic stratifications even at moderate grid resolution. The performance of these methods were assessed in a set of test simulations of static and dynamical setups. Special emphasis was given to flows at low Mach numbers. They are particularly challenging to evolve because they require special low-Mach hydrodynamic flux solvers, which in turn come with reduced dissipation and hence are prone to numerical instabilities. Also, it seems natural that slight deviations from hydrostatic equilibrium lead to low-Mach flows, as is the case, for example, in stellar convection. All simulations were performed with the time-implicit SLH code that solves the fully compressible Euler equations using a modified version of the low-Mach AUSM$^+$-up hydrodynamic flux solver. Our experience shows that the inclusion of gravitational potential energy in the total energy is essential to correctly representing slow flows in stratified atmospheres in the cell-centered discretization of gravity implemented in SLH; see Mullen et al. (2021) for an alternative approach. To the best of our knowledge, the present study is the first to reach Mach numbers as low as

2×10^{-4} in stratified convection using the fully compressible Euler equations.

The first test of the well-balancing schemes is to evolve a 1D hydrostatic atmosphere in time at low resolution for an isothermal, an isentropic, and a polytropic stratification. In all cases, the absence of a well-balancing scheme quickly led to spurious velocities at significant amplitudes. The application of any of the considered well-balancing methods removed this problem and managed to keep the flow below Mach numbers of 10^{-12} for very long times. Repeating the same test in 2D revealed that low Mach number flux functions, such as AUSM$^+$-up, are subject to an exponential growth of the Mach number and horizontal density fluctuations, which is not physically expected in a stably stratified atmosphere. This effect became less pronounced the closer the stratification was to the marginally stable, isentropic profile. In the isentropic case α-β and deviation well-balancing in combination with the low-Mach flux remained stable (Ma $\lesssim 10^{-8}$) for long times, while with Cargo–LeRoux well-balancing the setup developed a flow at Mach numbers of about 10^{-1}. These examples showed that it is important to test well-balanced schemes in more than one spatial dimension and for more than just a few sound-crossing times, as only then slowly growing instabilities become noticeable, especially in very stable stratifications.

While it is a necessary condition to maintain an initially static setup, only dynamical setups are of actual interest in multidimensional simulations. In a second test, we considered the rise of a hot bubble in a periodic background stratification spanning two orders of magnitude in pressure at constant entropy. We tuned the bubble's entropy excess to reach different rising speeds. With Cargo–LeRoux well-balancing and without any well-balancing, unphysical entropy fluctuations appeared in large parts of the atmosphere and a relatively fine grid (256×384) was required to make their amplitude smaller than that of even the hottest bubble considered. The corresponding Mach number of Ma $\sim 3 \times 10^{-2}$ seemed to be close to a limit of practical applicability of these two methods in such a strong stratification. The α-β and deviation methods fared much better with no entropy changes far from the bubble and only a slight entropy undershoot right above the bubble even on a coarse (64×96) grid. Equally good results were obtained with the initial amplitude decreased by a factor of 10^6, leading to Ma $\sim 3 \times 10^{-5}$. Numerical effects started to dominate only at Ma $\sim 3 \times 10^{-6}$ after the amplitude was decreased by another factor of 10^2.

We proceeded with a setup involving a convection zone with a stable zone on top. The stratification was chosen to be representative of core convection in a 25 $M_\odot$ main-sequence star. Radiation pressure was a substantial fraction of the total pressure, testing the methods' capability to deal with a general EoS. We used volume heating of adjustable amplitude to drive the convection. With Cargo–LeRoux well-balancing and without well-balancing, the rms Mach number of the convective flow ceased to correlate with the heating rate at $\mathrm{Ma}_{\mathrm{rms}} \sim 4 \times 10^{-3}$ and the flow became dominated by small-scale structures of numerical origin. The lowest reachable value of $\mathrm{Ma}_{\mathrm{rms}}$ dropped by about a factor of two when switching from ϱ-p to ϱ-T reconstruction in the absence of well-balancing. Only the α-β and deviation methods were able to reproduce the expected scaling of $\mathrm{Ma}_{\mathrm{rms}}$ with the heating rate (Eq. (87)) down to the slowest flows tested ($\mathrm{Ma}_{\mathrm{rms}} \sim 2 \times 10^{-4}$). We observed spurious patterns in the stable layer and demonstrated that they were caused by unresolved internal gravity waves, whose vertical wavelength becomes extremely short with increasing period. The patterns disappeared when the typical vertical wavelengths of waves with periods close to the convective turnover frequency became resolved by 8 to 10 cells (grid of 288×2380 cells).

The deviation method, unlike the other methods presented in this work, can deal with arbitrary stationary states. We illustrated this capability in our last test, in which we followed many orbits of a density perturbation in a Keplerian disk around a point mass. The angle-averaged density profile should ideally remain constant in this model. Without any well-balancing, imperfect balance between the centrifugal force and gravity led to mass redistribution towards inner parts of the disk after many orbits. Deviation well-balancing much improved the solutions with only slight radial broadening of the initial perturbation even after 10^4 orbits with a moderate resolution of 100×350 cells.

In summary, our results show that well-balancing can substantially reduce the grid resolution needed to correctly follow tiny perturbations in situations in which the stationary background state involves the balance of two large opposing forces. We obtained comparable results with the α-β and deviation methods, both far surpassing the Cargo–LeRoux method in accuracy in the low-Mach-number regime. The α-β and deviation methods are also expected to be more accurate than the majority of other well-balanced methods present in astrophysical literature (e.g., Zingale et al. 2002; Perego et al. 2016; Käppeli et al. 2011; Käppeli & Mishra 2016; Padioleau et al. 2019), because they exactly balance the stationary solution rather than an approximation to it. Although an analytical prescription is often not available, the stationary solution can be computed to an arbitrary degree of accuracy in many astrophysical applications. This statement only holds in the case that the hydrostatic background state does not change in time. In this case an update is necessary, which we do not discuss in this paper. This step would likely involve a local approximation to hydrostatic equilibrium, similar to the ones suggested in the other aforementioned methods. It should be noted, however, that such an update is unnecessary in the case of very slow flows, such as in earlier phases of stellar evolution, because the background state hardly changes over time, even after hundreds of convective turnover times.

We prefer to use the deviation method, because it is more general and does not impose any restrictions on reconstruction variables. The method can be applied both to nearly hydrostatic cases and to cases in which rotation becomes important. The latter can have strong impact on stellar evolution (Maeder & Meynet 2000) as well as on the propagation of IGW in stars (Rogers et al. 2013).

The Cargo–LeRoux method still has its place, though. Horst et al. (2021) show for the case of convective helium-shell burning that this method considerably reduces numerical diffusion of the hydrostatic background stratification as compared to the unbalanced case if the gravitational energy is not included in the total energy. Therefore we consider the Cargo–LeRoux method as a valid method that leads to improvements already with little development effort.

This paper focuses on setups with simple grid geometries, but the SLH code can use general curvilinear grids. This allows us to adapt grid geometry to the problem at hand. Standard spherical grids adapt to the geometry of slowly or nonrotating stars, but they suffer from singularities at the center and at the poles. A star can be inscribed in a simple Cartesian grid (e.g., Woodward et al. 2015), but this requires to also impose a spherical boundary condition on the grid. When done on the cell level, the sphere is rough on small scales and can generate spurious vorticity. We have implemented the cubed-sphere grid proposed by Calhoun et al. (2008) in our SLH code. The grid is logically rectangular but geometrically spherical with a

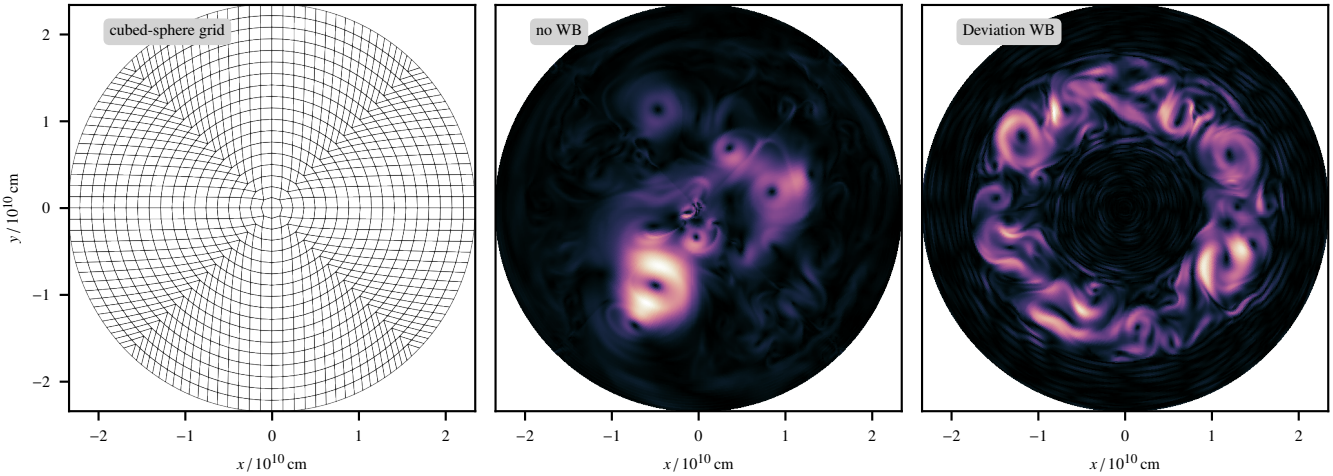

Fig. 15. *Left panel*: geometry of the cubed-sphere grid. The number of cells has been reduced compared to grids used in the other two panels to ease the identification of individual cells and their shapes. *Middle and right panel*: shell convection in a setup comparable to that in Sect. 5.3 but with a shallower stratification and ideal gas EoS. *Middle panel*: color coded Mach number in a run without well-balancing. Numerical discretization errors quickly lead to spurious flows in the central region and the maximum Mach number reaches 3×10^{-2}. In the run with deviation well-balancing shown in the *right panel* the convective shell is clearly maintained. The maximum Mach number is 2×10^{-3}.

smooth outer boundary, see Fig. 15 for a 2D version. Discretization errors along the grid's strongly deformed diagonals make it almost impossible to follow nearly hydrostatic flows without any well-balancing method. Figure 15 shows an SLH simulation with a convective shell embedded between two stably stratified zones. With deviation well-balancing, we obtain the expected convective shell with convection-generated IGW propagating in the stable zones. If we turn the well-balancing off, a convection-like flow of numerical origin appears and mixes the convection zone with the whole inner stable zone. This result is promising, but limits of applicability of the deviation method on the cubed-sphere grid are still to be investigated.

Acknowledgements. PVFE was supported by the U.S. Department of Energy through the Los Alamos National Laboratory (LANL). LANL is operated by Triad National Security, LLC, for the National Nuclear Security Administration of the U.S. Department of Energy (Contract No. 89233218CNA000001). PVFE, LH, JPB, RA, JH, GL, and FKR acknowledge support by the Klaus Tschira Foundation. The work of FKR and PVFE was supported by the German Research Foundation (DFG) through the graduate school on "Theoretical Astrophysics and Particle Physics" (GRK 1147). The work of CK and FKR is supported by DFG through grants KL 566/22-1 and RO 3676/3-1, respectively. JPB acknowledges the grants HITS 21.03.2018, HITS 18.12.2018 and HITS 26.08.2020. This work has been assigned a document release number LA-UR-21-21056.

References

Almgren, A. S., Bell, J. B., Rendleman, C. A., & Zingale, M. 2006, ApJ, 637, 922
Andrassy, R., Herwig, F., Woodward, P., & Ritter, C. 2020, MNRAS, 491, 972
Audusse, E., Bouchut, F., Bristeau, M.-O., Klein, R., & Perthame, B. 2004, SIAM J. Sci. Comput., 25, 2050
Barsukow, W., & Berberich, J. P. 2020, J. Sci. Comput., submitted
Barsukow, W., Edelmann, P. V. F., Klingenberg, C., Miczek, F., & Röpke, F. K. 2017a, J. Sci. Comput., 72, 623
Barsukow, W., Edelmann, P. V. F., Klingenberg, C., & Röpke, F. K. 2017b, in ESAIM: Proceedings and Surveys, Vol. 58, Workshop on low velocity flows, Paris, 5–6 November 2015, ed. S. Dellacherie, 27
Berberich, J. P. 2021, Doctoral Thesis, Universität Würzburg, Germany
Berberich, J. P., & Klingenberg, C. 2020, SEMA SIMAI Series: Numerical Methods for Hyperbolic Problems Numhyp 2019, submitted
Berberich, J. P., Chandrashekar, P., & Klingenberg, C. 2018, Theory, Numerics and Applications of Hyperbolic Problems I, Springer Proceedings in Mathematics & Statistics, ed. C. Klingenberg, & M. Westdickenberg, 236
Berberich, J. P., Chandrashekar, P., Klingenberg, C., & Röpke, F. K. 2019, Commun. Comput. Phys., 26, 599
Berberich, J. P., Käppeli, R., Chandrashekar, P., & Klingenberg, C. 2020, Commun. Comput. Phys., submitted [arXiv:2005.01811]
Berberich, J. P., Chandrashekar, P., & Klingenberg, C. 2021, Comput. Fluids, 219, 104858
Bermudez, A., & Vázquez, M. E. 1994, Comput. Fluids, 23, 1049
Bolaños Rosales, A. 2016, Dissertation, Julius-Maximilians-Universität Würzburg, Germany
Browning, M. K., Brun, A. S., & Toomre, J. 2004, ApJ, 601, 512
Brufau, P., Vázquez-Cendón, M., & García-Navarro, P. 2002, Int. J. Numer. Methods Fluids, 39, 247
Calhoun, D. A., Helzel, C., & Leveque, R. J. 2008, SIAM Rev., 50, 723
Cargo, P., & Le Roux, A. 1994, Comptes rendus de l'Académie des sciences Série 1, Mathématique, 318, 73
Castro, M. J., & Semplice, M. 2018, Int. J. Numer. Methods Fluids, 89, 304
Chandrashekar, P., & Klingenberg, C. 2015, SIAM J. Sci. Comput., 37, B382
Courant, R., Friedrichs, K. O., & Lewy, H. 1928, Math. Ann., 100, 32
Cristini, A., Meakin, C., Hirschi, R., et al. 2017, MNRAS, 471, 279
Cristini, A., Hirschi, R., Meakin, C., et al. 2019, MNRAS, 484, 4645
Dedner, A., Kröner, D., Sofronov, I. L., & Wesenberg, M. 2001, J. Comput. Phys., 171, 448
Desveaux, V., Zenk, M., Berthon, C., & Klingenberg, C. 2016a, Math. Comput., 85, 1571
Desveaux, V., Zenk, M., Berthon, C., & Klingenberg, C. 2016b, Int. J. Numer. Methods Fluids, 81, 104
Edelmann, P. V. F. 2014, Dissertation, Technische Universität München, Germany
Edelmann, P. V. F., & Röpke, F. K. 2016, in JUQUEEN Extreme Scaling Workshop 2016, eds. D. Brömmel, W. Frings, & B. J. N. Wylie, JSC Internal Report No. FZJ-JSC-IB-2016-01, 63
Edelmann, P. V. F., Röpke, F. K., Hirschi, R., Georgy, C., & Jones, S. 2017, A&A, 604, A25
Edelmann, P. V. F., Ratnasingam, R. P., Pedersen, M. G., et al. 2019, ApJ, 876, 4
Edwards, J. R., & Liou, M.-S. 1998, AIAA J., 36, 1610
Gaburro, E., Castro, M. J., & Dumbser, M. 2018, MNRAS, 477, 2251
Goffrey, T., Pratt, J., Viallet, M., et al. 2017, A&A, 600, A7
Grosheintz-Laval, L., & Käppeli, R. 2019, J. Comput. Phys., 378, 324
Guillard, H., & Murrone, A. 2004, Comput. Fluids, 33, 655
Guillard, H., & Viozat, C. 1999, Comput. Fluids, 28, 63
Higl, J., Müller, E., & Weiss, A. 2021, A&A, 646, A133
Horst, L., Edelmann, P. V. F., Andrássy, R., et al. 2020, A&A, 641, A18
Horst, L., Hirschi, R., Edelmann, P. V. F., Andrassy, R., & Roepke, F. K. 2021, A&A, in press, https://doi.org/10.1051/0004-6361/202140825
Hosea, M., & Shampine, L. 1996, Appl. Numer. Math., 20, 21, Method of Lines for Time-Dependent Problems
Jones, S., Andrassy, R., Sandalski, S., et al. 2017, MNRAS, 465, 2991
Käppeli, R., & Mishra, S. 2014, J. Comput. Phys., 259, 199
Käppeli, R., & Mishra, S. 2016, A&A, 587, A94
Käppeli, R., Whitehouse, S. C., Scheidegger, S., Pen, U. L., & Liebendörfer, M. 2011, ApJS, 195, 20

Kifonidis, K., & Müller, E. 2012, A&A, 544, A47
Kippenhahn, R., Weigert, A., & Weiss, A. 2012, Stellar Structure and Evolution (Berlin, Heidelberg: Springer-Verlag)
Le Roux, A. Y. 1999, ESAIM: Proc., 6, 75
LeVeque, R. J. 1998, J. Comput. Phys., 146, 346
Li, X.-S., & Gu, C.-W. 2008, J. Comput. Phys., 227, 5144
Liou, M.-S. 1996, J. Comput. Phys., 129, 364
Liou, M.-S. 2006, J. Comput. Phys., 214, 137
Liou, M.-S., & Steffen, C. J. J. 1993, J. Comput. Phys., 107, 23
Maeder, A. 2009, Physics, Formation and Evolution of Rotating Stars, Astronomy and Astrophysics Library (Berlin Heidelberg: Springer)
Maeder, A., & Meynet, G. 2000, ARA&A, 38, 143
Meakin, C. A., & Arnett, D. 2006, ApJ, 637, L53
Meakin, C. A., & Arnett, D. 2007, ApJ, 667, 448
Michel, A. 2019, Dissertation, Ruprecht-Karls-Universität Heidelberg, Germany
Miczek, F. 2013, Dissertation, Technische Universität München, Germany
Miczek, F., Röpke, F. K., & Edelmann, P. V. F. 2015, A&A, 576, A50
Mullen, P. D., Hanawa, T., & Gammie, C. F. 2021, ApJS, 252, 30
Müller, B., Viallet, M., Heger, A., & Janka, H.-T. 2016, ApJ, 833, 124
Oßwald, K., Siegmund, A., Birken, P., Hannemann, V., & Meister, A. 2015, Int. J. Numer. Methods Fluids, 81, 71
Padioleau, T., Tremblin, P., Audit, E., Kestener, P., & Kokh, S. 2019, ApJ, 875, 128
Perego, A., Cabezón, R. M., & Käppeli, R. 2016, ApJS, 223, 22
Popov, M. V., Walder, R., Folini, D., et al. 2019, A&A, 630, A129
Pratt, J., Baraffe, I., Goffrey, T., et al. 2016, A&A, 593, A121
Pratt, J., Baraffe, I., Goffrey, T., et al. 2020, A&A, 638, A15
Rieper, F. 2011, J. Comput. Phys., 230, 5263
Roe, P. L. 1981, J. Comput. Phys., 43, 357
Rogers, T. M., Lin, D. N. C., McElwaine, J. N., & Lau, H. H. B. 2013, ApJ, 772, 21
Röpke, F. K., Berberich, J., Edelmann, P. F. V., et al. 2018, NIC Series, NIC Symposium 2018, Jülich (Germany), 22 Feb 2018–23 Feb 2018 (Jülich: Forschungszentrum Jülich GmbH, Zentralbibliothek), 49, 115
Shu, C.-W., & Osher, S. 1988, J. Comput. Phys., 77, 439
Sutherland, B. 2010, Internal Gravity Waves (Cambridge University Press)
Tassoul, J. L. 2000, Stellar Rotation
Timmes, F. X., & Swesty, F. D. 2000, ApJS, 126, 501
Toro, E. F. 2009, Riemann Solvers and Numerical Methods for Fluid Dynamics: A Practical Introduction (Berlin, Heidelberg: Springer)
Touma, R., & Klingenberg, C. 2015, Appl. Numer. Math., 97, 42
Touma, R., Koley, U., & Klingenberg, C. 2016, SIAM J. Sci. Comput., 38, B773
Turkel, E. 1987, J. Comput. Phys., 72, 277
Veiga, M. H., Romero Velasco, D. A., Abgrall, R., & Teyssier, R. 2019, Commun. Comput. Phys., 26, 1
Viallet, M., Meakin, C., Arnett, D., & Mocák, M. 2013, ApJ, 769, 1
Woodward, P. R., Herwig, F., & Lin, P.-H. 2015, ApJ, 798, 49
Zingale, M., Dursi, L. J., ZuHone, J., et al. 2002, ApJS, 143, 539

Appendix A: Simple stratified atmospheres

These are the 1D counterparts of the isentropic and polytropic tests in Sect. 5.1.

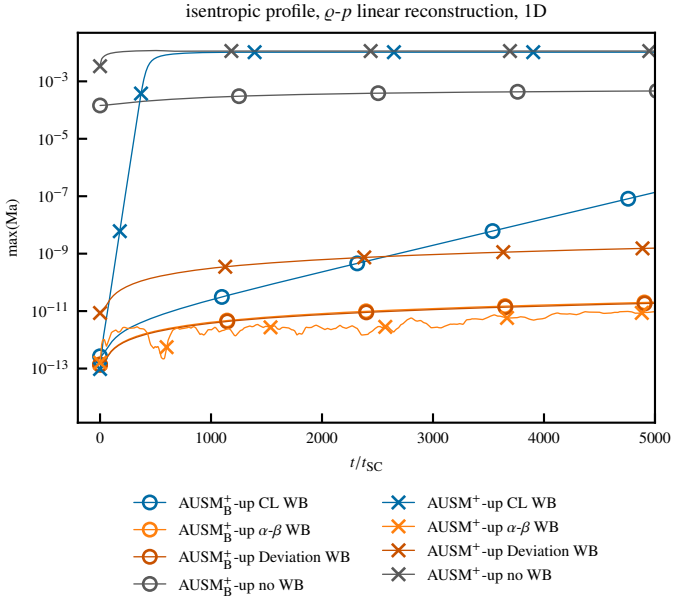

Fig. A.1. Same as Fig. 4, but as a 1D simulation. The adiabatic exponent is $\gamma = 5/3$. The solid lines represent the maximum Mach numbers on the grid. Time is given in units of the sound-crossing time $t_{SC} = 4.28$ s. The curves have been slightly smoothed for better visibility.

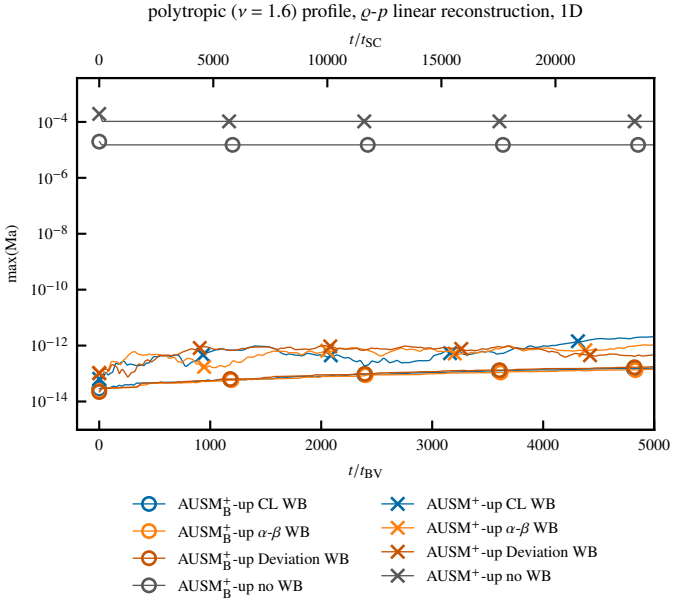

Fig. A.2. Same as Fig. 5, but as a 1D simulation. The adiabatic exponent is $\gamma = 5/3$. The solid lines represent the maximum Mach numbers on the grid. Time is given in units of Brunt–Väisälä time $t_{BV} = 20.1$ s and sound-crossing time $t_{SC} = 4.13$ s. The curves have been slightly smoothed for better visibility.

Appendix B: Hot bubble

This appendix explores the amplitude dependence of the hot bubble test from Sect. 5.2.

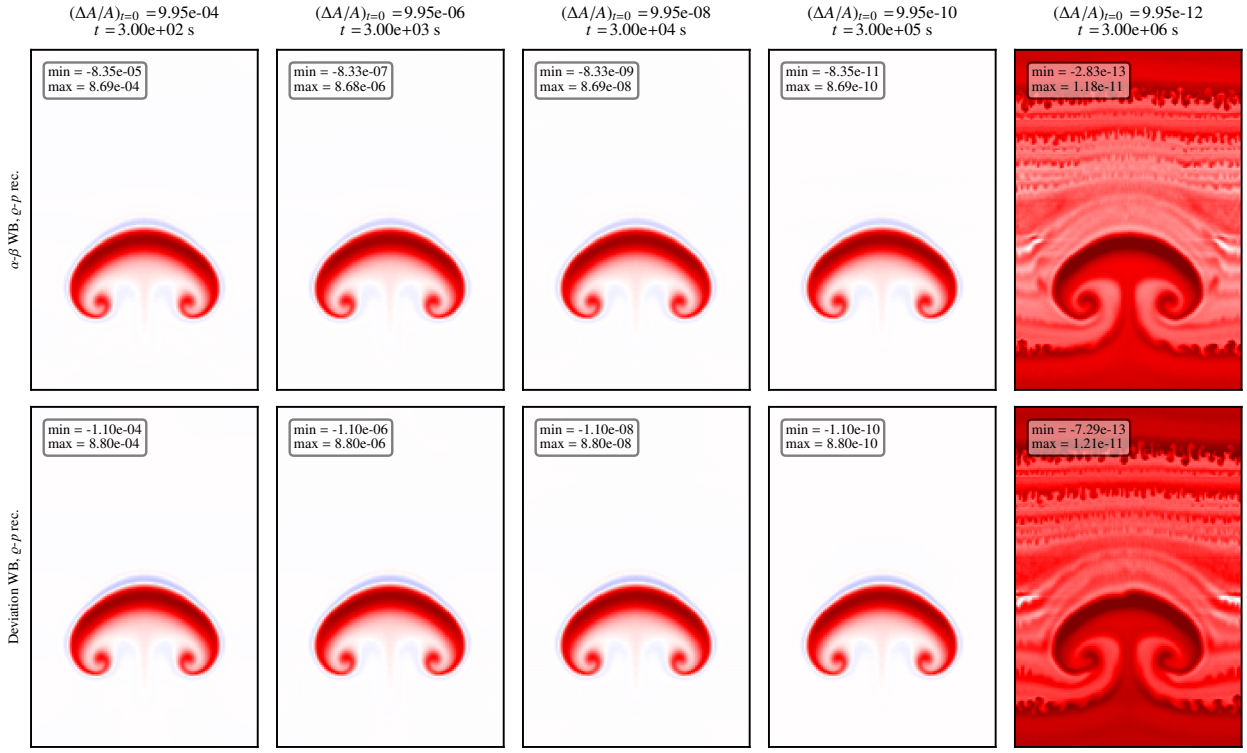

Fig. B.1. Same as Fig. 6, but showing the dependence of the solution on the initial amplitude $(\Delta A/A)_{t=0}$ (left to right) on the 128 × 192 grid for the two best well-balancing methods (rows). The final time of the simulations is scaled with $(\Delta A/A)^{1/2}_{t=0}$ allowing the bubbles to reach the same evolutionary stage, see Sect. 5.2.

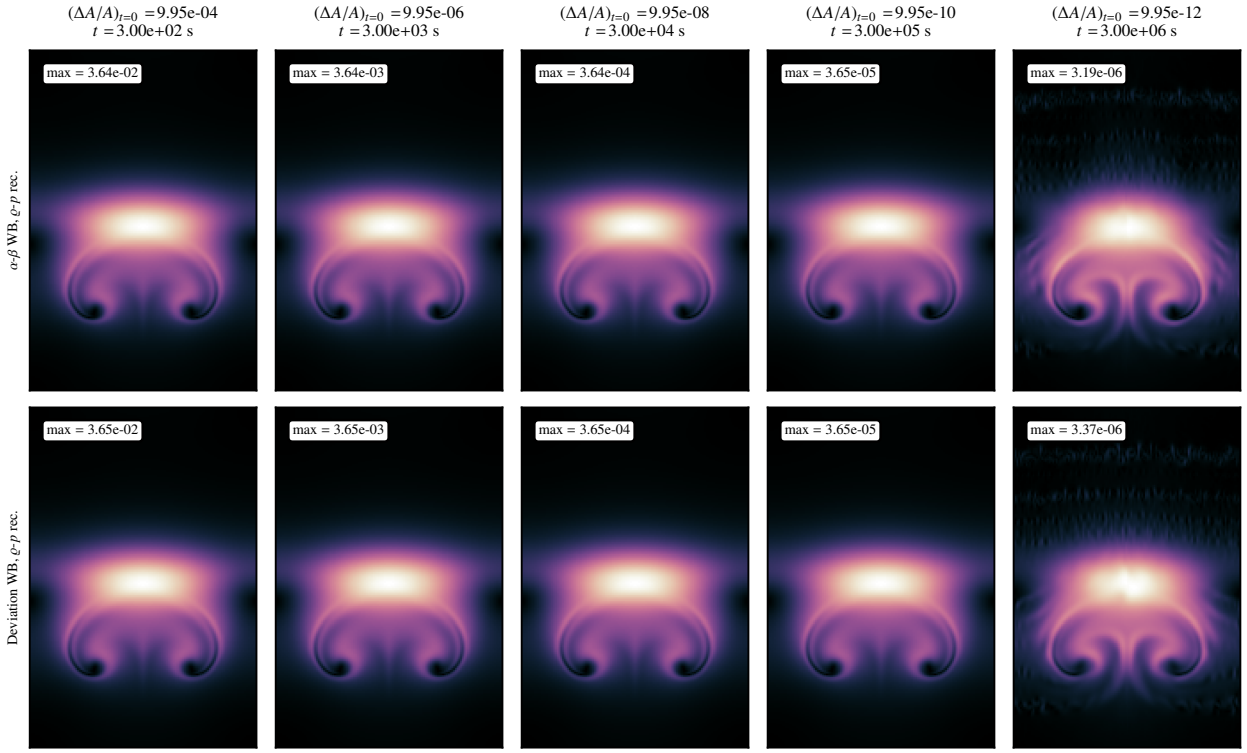

Fig. B.2. Mach-number distributions in the solutions shown in Fig. B.1. The color scheme ranges from 0 (black) to the maximum value (white) reached in the simulation box, which is also indicated at the top of the panels.

Appendix C: Simple convective box setup

Table C.1 shows that the relative deviation from hydrostatic equilibrium in the convective box test from Sect. 5.3 scales with the square of the rms Mach number in the convection zone.

Table C.1. Relative deviation from hydrostatic equilibrium, rms Mach number, and ratio of the squared Mach number to the deviation at different heating rates.

$\dot{e}_0$	$\frac{(\partial p/\partial y)-\varrho\, g}{(\partial p/\partial y)}$	$\mathrm{Ma}_{\mathrm{rms}}$	$\mathrm{Ma}_{\mathrm{rms}}{}^2 \left[\frac{(\partial p/\partial y)-\varrho\, g}{(\partial p/\partial y)}\right]^{-1}$
10^{02}	2.03×10^{-07}	2.07×10^{-04}	0.21
10^{03}	1.10×10^{-06}	4.54×10^{-04}	0.19
10^{04}	3.71×10^{-06}	9.50×10^{-04}	0.24
10^{05}	1.45×10^{-05}	2.04×10^{-03}	0.29
10^{06}	3.79×10^{-05}	4.33×10^{-03}	0.49
10^{07}	1.88×10^{-04}	9.21×10^{-03}	0.45

Notes. The data is derived from the simulations using the α-β well-balancing method, spatially averaged over the convection zone, and averaged over a time frame spanning $5\,\tau_{\mathrm{conv}}$. The results confirm the expected scaling of the relative deviation from hydrostatic equilibrium with $\sim \mathrm{Ma}_{\mathrm{rms}}{}^2$ (see text) within the accuracy of our order-of-magnitude estimate.

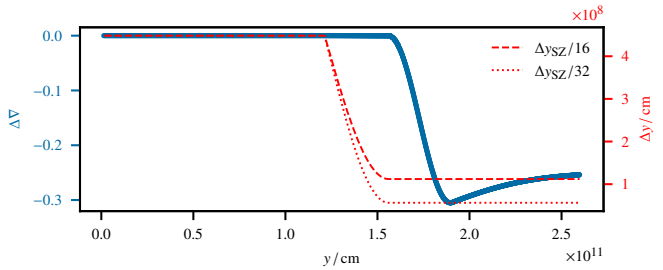

Fig. C.1. Varying vertical grid spacing as a function of the vertical coordinate y for the simulations shown in the center and right panels of the lower row in Fig. 13. The superadiabaticity is shown as a blue line, a negative value indicates a convectively stable stratification. The spacing changes smoothly to a finer resolution slightly before the transition to the stable zone starts.

Appendix D: Keplerian disk

Figure D.1 shows the time evolution of density in the Keplerian disk problem from Sect. 5.4.

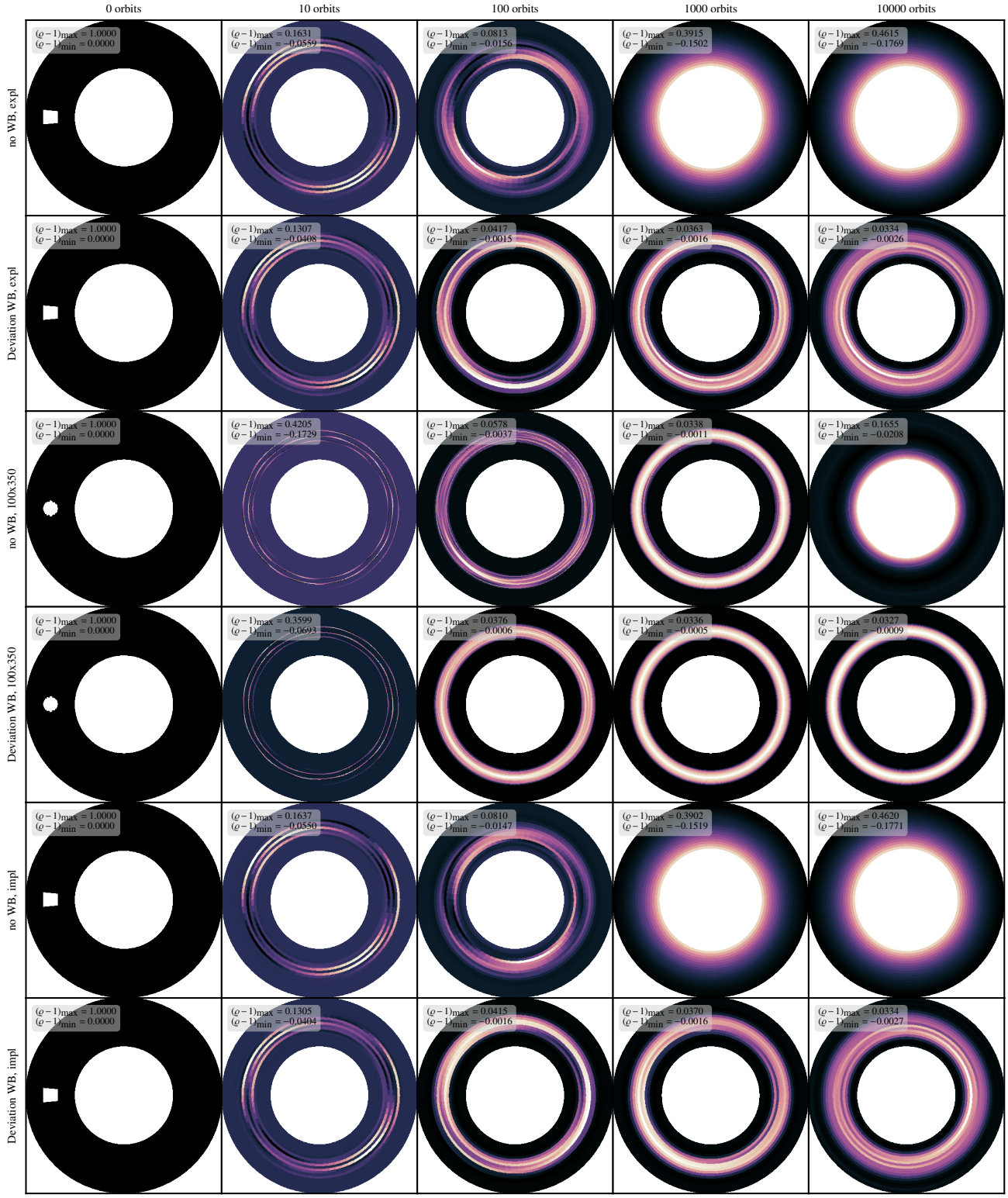

Fig. D.1. Snapshots of the density distribution during the evolution of the Keplerian disk. Shown are runs with deviation well-balancing and without well-balancing using explicit time stepping and resolutions of 20×70 cells as well as 100×350 grid cells. The bottom two rows show the same setup evolved with implicit time stepping at a resolution of 20×70 cells. To emphasize the deviation from the initial background density of $\varrho_0 = 1$ we show here $\varrho - 1$ and give the maximum and minimum of this quantity in an inset for each snapshot.

2.2 Publication II: Helium shell burning

The publication in this section reports on 3D SLH simulations of convection in a $25\,M_\odot$ star. It assesses the performance of the AUSM$^+$−up flux compared to non low-Mach flux functions and quantifies the amount of CBM.

In the previous section, the SLH code was applied to 1D and 2D test scenarios in order to validate the benefits of using well-balancing techniques. In this section, 3D simulations of convection in a $25\,M_\odot$ star are performed. The initial conditions are based on a realistic model obtained from stellar evolution calculations. The model is taken at a time when core helium burning has ceased in the center of the star but continues in a shell around the core (see figure 1 of the publication below). A shellular convection zone has the advantage that two interfaces between a convective and radiative zone can be investigated in a single setup. This increases the covered parameter space at the same computational costs compared to a setup of core convection.

As discussed in Section 1.2, convective mixing is crucial for stellar evolution but difficult to parametrize in 1D evolution codes. Therefore, multidimensional hydrodynamic simulations can help to test, calibrate, and develop descriptions like the ones presented in Section 1.2.3. Recent studies of entrainment consider convective-radiative boundaries for carbon shell burning (Cristini et al., 2017, 2019), oxygen shell burning (Meakin and Arnett, 2007b; Jones et al., 2017; Andrassy et al., 2020), core hydrogen burning (Meakin and Arnett, 2007b; Gilet et al., 2013; Higl et al., 2021), or mixing at the bottom of the surface convection zone in a pre-MS star (Pratt et al., 2016, 2020). Extending these studies to other evolutionary stages will help to find possible dependencies of mixing on stellar parameters.

In the publication presented in this section, the case of convective helium shell burning is simulated for the first time in the context of CBM. For the chosen setup, MLT predicts convection at a Mach number of about 10^{-4} which seems to be accessible according to the results obtained in the previous Section 2.1. However, at the time when the simulations of helium shell burning were performed, only the Cargo-LeRoux well-balancing method was fully available in SLH. The tests presented in Section 2.1 indicate that results with Cargo-LeRoux are only reliable for Mach numbers above 10^{-3}. Therefore, the Mach number was increased by artificially boosting the energy generation by factors of about 10^4. This is a common method in order to shift the velocities into regimes that are more feasible for the respective numerical methods (e.g., Rogers et al., 2013; Edelmann et al., 2019; Cristini et al., 2019) but might change the relative importance of different processes compared to the actual star as discussed in Section 1.5.

While the presented simulations do not yet overcome the common problem of boosting, the Cargo-LeRoux well-balancing method allows the application of the low-Mach AUSM$^+$−up flux and to carefully analyze its performance in a realistic stellar setup. This is an important step since low-Mach fluxes are required for the ultimate goal to simulate low-Mach convection, but, as demonstrated in Section 2.1, they are not guaranteed to work in astrophysical setups in general. Furthermore, the study presented below contributes to the current effort to cover a wide range of different convective setups within stars.

In the publication, after a description of the general setup, the resulting convective flow is analyzed regarding properties of the turbulent velocity spectrum and the kinetic energy in the context of Reynolds-averaged implicit large eddy simulations (RA-ILES) (Mocák et al., 2014, 2018; Arnett et al., 2019). The key idea of RA-ILES is to close higher order terms in the spatially and time averaged Euler equations (in the limit of vanishing viscosity) with the results from ILES. This allows, for example, identifying the different terms that contribute

to the evolution of kinetic energy and to quantify the amount of numerical dissipation. In this way, it is also a diagnostic for potential unphysical behavior of the applied numerical scheme. Furthermore, the entrainment rate of material in the convective region is measured for different boosting strengths and corresponding different convective velocities. Because $\mathrm{Ri_B}$ depends on the velocity, the measured entrainment rate at different values of $\mathrm{Ri_B}$ can be used to obtain best fitting values for (A, n) in Eq. (1.22).

It is found that the low-Mach AUSM$^+$−up flux can be successfully applied to astrophysical setups and that its results are superior compared to a non low-Mach scheme already at intermediate Mach numbers. The extracted mass entrainment rates are in a similar regime as the rates reported by other studies. Furthermore, also the extracted rates in this simulation indicate an unrealistic fast growth of the convection zone if it is applied over evolutionary timescales.

Title
Multidimensional low-Mach number time-implicit hyrodynamic simulations of convective helium shell burning in a massive star

Authors
L. Horst, R. Hirschi, P. V. F. Edelmann, R. Andrassy, F. K. Röpke

Publication Status
The manuscript was published on September, 2021.

DOI
10.1051/0004-6361/202140825

Author's contributions
LH is the principal author of this paper. The initial setup for the simulations was suggested by RH who also contributed the corresponding MESA model and provided figure 1. RH further provided parts of the computing resources. LH performed all hydrodynamic simulations, analyzed the results, produced all remaining figures and wrote the manuscript. LH also included the changes suggested by the referee. The current status of the project and next steps were discussed in frequent meetings with all authors who also actively contributed to the manuscript by suggesting content, improvements, and corrections.

A&A 653, A55 (2021)
https://doi.org/10.1051/0004-6361/202140825

Astronomy & Astrophysics

Multidimensional low-Mach number time-implicit hydrodynamic simulations of convective helium shell burning in a massive star

L. Horst[1], R. Hirschi[2,3], P. V. F. Edelmann[4], R. Andrássy[1], and F. K. Röpke[1,5]

[1] Heidelberger Institut für Theoretische Studien, Schloss-Wolfsbrunnenweg 35, 69118 Heidelberg, Germany
e-mail: leonhard.horst@posteo.de
[2] Astrophysics Group, Keele University, Keele, Staffordshire ST5 5BG, UK
[3] Kavli Institute for the Physics and Mathematics of the Universe (WPI), University of Tokyo, 5-1-5 Kashiwanoha, Kashiwa 277-8583, Japan
[4] X Computational Physics (XCP) Division and Center for Theoretical Astrophysics (CTA), Los Alamos National Laboratory, Los Alamos, NM 87545, USA
[5] Zentrum für Astronomie der Universität Heidelberg, Institut für Theoretische Astrophysik, Philosophenweg 12, 69120 Heidelberg, Germany

Received 17 March 2021 / Accepted 30 June 2021

ABSTRACT

Context. A realistic parametrization of convection and convective boundary mixing in conventional stellar evolution codes is still the subject of ongoing research. To improve the current situation, multidimensional hydrodynamic simulations are used to study convection in stellar interiors. Such simulations are numerically challenging, especially for flows at low Mach numbers which are typical for convection during early evolutionary stages.

Aims. We explore the benefits of using a low-Mach hydrodynamic flux solver and demonstrate its usability for simulations in the astrophysical context. Simulations of convection for a realistic stellar profile are analyzed regarding the properties of convective boundary mixing.

Methods. The time-implicit Seven-League Hydro (SLH) code was used to perform multidimensional simulations of convective helium shell burning based on a 25 $M_\odot$ star model. The results obtained with the low-Mach AUSM$^+$-up solver were compared to results when using its non low-Mach variant AUSM$^+_{\rm B}$-up. We applied well-balancing of the gravitational source term to maintain the initial hydrostatic background stratification. The computational grids have resolutions ranging from 180×90^2 to 810×540^2 cells and the nuclear energy release was boosted by factors of 3×10^3, 1×10^4, and 3×10^4 to study the dependence of the results on these parameters.

Results. The boosted energy input results in convection at Mach numbers in the range of 10^{-3}–10^{-2}. Standard mixing-length theory predicts convective velocities of about 1.6×10^{-4} if no boosting is applied. The simulations with AUSM$^+$-up show a Kolmogorov-like inertial range in the kinetic energy spectrum that extends further toward smaller scales compared with its non low-Mach variant. The kinetic energy dissipation of the AUSM$^+$-up solver already converges at a lower resolution compared to AUSM$^+_{\rm B}$-up. The extracted entrainment rates at the boundaries of the convection zone are well represented by the bulk Richardson entrainment law and the corresponding fitting parameters are in agreement with published results for carbon shell burning. However, our study needs to be validated by simulations at higher resolution. Further, we find that a general increase in the entropy in the convection zone may significantly contribute to the measured entrainment of the top boundary.

Conclusion. This study demonstrates the successful application of the AUSM$^+$-up solver to a realistic astrophysical setup. Compressible simulations of convection in early phases at nominal stellar luminosity will benefit from its low-Mach capabilities. Similar to other studies, our extrapolated entrainment rate for the helium-burning shell would lead to an unrealistic growth of the convection zone if it is applied over the lifetime of the zone. Studies at nominal stellar luminosities and different phases of the same convection zone are needed to detect a possible evolution of the entrainment rate and the impact of radiation on convective boundary mixing.

Key words. stars: massive – stars: interiors – convection – methods: numerical – hydrodynamics

1. Introduction

Mixing induced by convection in the stellar interior plays an essential role in the evolution of stars. Parametrizing its complex multidimensional nature in one-dimensional (1D) stellar evolution codes is, however, particularly difficult. A reliable prescription of convective effects in 1D codes is still lacking today and the resulting stellar evolution models depend on the specific choice of the employed paramterization and the particular parameter values. This is, for example, demonstrated in recent studies by Kaiser et al. (2020) and Davis et al. (2019) on uncertainties in core properties and nucleosynthesis for massive stars.

With asteroseismic data of observed stars, it is possible to determine properties of the stellar interiors (see Aerts 2021 for a detailed review). They can be utilized to narrow down the range of possible parameters. It is now possible to determine that some convective boundary mixing models provide a better fit to certain asteroseismic observations than others (e.g., Viani & Basu 2020; Angelou et al. 2020; Michielsen et al. 2019; Pedersen et al. 2018, 2021), but probing the small-scale physics of the mixing is beyond the reach of even state-of-the-art asteroseismology.

A complimentary approach to improve the current situation is to perform multidimensional simulations by numerically

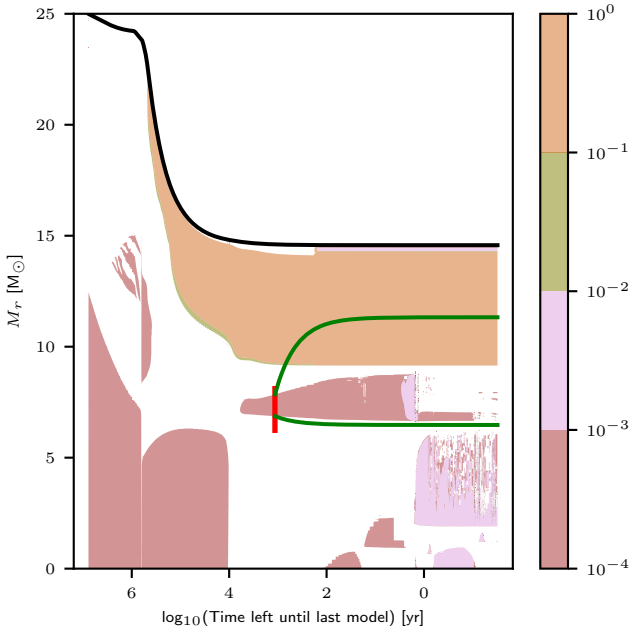

Fig. 1. Convective regions during the evolution of an 1D 25 $M_\odot$ star model simulated with the MESA code. Shaded regions correspond to convection zones. The color-shading represents the mixing-length theory (MLT)-predicted Mach number. The black solid line denotes the total mass of the model. The red vertical line indicates the point in the evolution at which the SLH simulations start and the mass extent of the initial model. The green lines indicate the mass entrainment at the upper and lower boundaries as extracted from the 3D hydrodynamic simulations. See discussion in Sect. 5.4.

solving the equations of fluid dynamics for realistic stellar models. In such simulations, convection develops self-consistently and their detailed analysis provides insights into the fundamental processes at play. This way, currently used parametrizations of convection in 1D codes can be constrained or discarded and new prescriptions may be developed.

The complex problem of convection and associated mixing of material across the interfaces into stable zones in the stellar context is subject of active, ongoing research. Numerical simulations become particularly challenging when the flow of interest is slow compared to the speed of sound, that is for small values of the Mach number

$$\mathrm{Ma} = \frac{v}{c_{\mathrm{sound}}}, \tag{1}$$

where v is the flow velocity and c_{sound} is the local speed of sound. One challenge is the restricted step size of conventional explicit time stepping schemes which must be smaller than the sound crossing time of a single grid cell for numerical stability. Thus, at low Mach numbers, an excessively large number of time steps is needed to evolve the slow flow and explicit schemes become inefficient. Additionally, artifacts of the numerical discretization must be kept at a very low level because inaccuracies can quickly lead to spurious velocities at the same order as the flow of interest. Hence, appropriate numerical techniques must be chosen carefully.

For massive stars, low-Mach number flows typically arise in convection during the early phases of stellar evolution, see for example the evolution of the 25 $M_\odot$ star depicted in Fig. 1. Inaccuracies in the 1D prescription of convection in these phases propagate to all subsequent evolutionary phases and also enter predictions for the final stages of stars and observables. We therefore believe that successful simulations of these challenging settings are crucial to further improve the agreement between stellar modeling and observations.

One approach to meet the challenges of low-Mach flows is to modify the underlying hydrodynamic equations. This is, for example, done in the MAESTRO code (Almgren et al. 2007; Nonaka et al. 2010; Fan et al. 2019), where the Euler equations are modified to exclude the physics of sound waves and to ensure the correct scaling of leading-order terms in the low-Mach limit. This permits larger time steps and increases the efficiency for slow flows. An example for low-Mach simulations with the MAESTRO code are the three-dimensional (3D) simulations of core hydrogen burning by Gilet et al. (2013). Another approach is to perform implicit time stepping while solving the unmodified Euler equations, including sound waves. The time step size is then only restricted by the desired accuracy at which the flow is to be followed. This is for example employed by the MUSIC code in combination with a staggered spatial grid. Benchmark tests have shown that the code is able to evolve flows at Mach numbers down to Ma $\approx 10^{-6}$ (Viallet et al. 2016) and that a hydrostatic atmosphere remains stable (Goffrey et al. 2017).

The Seven-League (SLH) hydro code, which is used for the simulation presented here, is designed to tackle the numerical difficulties of low-Mach flows. It uses implicit time stepping and solves the fully compressible Euler equations. Furthermore, it applies special numerical flux functions with enhanced low-Mach capabilities in combination with well-balancing techniques to improve the representation of slow flows. This way, the SLH code is able to capture flows at low and moderate Mach numbers on the same grid.

The work we present in this paper aims at contributing to the recent effort to improve the understanding of the complex behavior of convection by means of hydrodynamic simulations. We demonstrate the benefits from using the low-Mach-number flux AUSM$^+$-up even at moderate Mach numbers. For this, 3D simulations of convective He-shell burning in a 25 $M_\odot$ star are presented and analyzed regarding general properties of the turbulent convection. In addition, we complement recent efforts to characterize convective boundary mixing by means of multidimensional simulations (e.g., Meakin & Arnett 2007; Woodward et al. 2015; Jones et al. 2017; Cristini et al. 2017, 2019; Pratt et al. 2017, 2020; Higl et al. 2021).

The paper is structured as follows: In Sect. 2 we briefly describe the basic properties of the SLH code. In Sect. 3 the initial conditions for the simulations are presented along with a detailed description of mapping the 1D model to the SLH grid and the applied energy boosting. In the 1D and two-dimensional (2D) test simulations presented in Sect. 4 we assess the hydrostatic stability of the initial profile using the Cargo–LeRoux well-balancing method and determine the required amount of artificial energy boosting. The corresponding 3D simulations are analyzed in Sect. 5 regarding properties of the turbulent convective flow and boundary mixing. Section 6 summarizes the results.

2. The Seven-League Hydro (SLH) code

The hydrodynamic simulations presented in this paper are performed with the SLH code (Miczek 2013; Edelmann 2014). It solves the fully compressible Euler equations in a finite volume approach. The underlying equations are formulated in general, curvilinear coordinates and mapped onto a logically rectangular computational grid, following the method of Kifonidis & Müller (2012). This allows one to construct almost arbitrary grid geometries that can be adapted to the physical setup that is

investigated (Miczek 2013). The Helmholtz equation of state (EoS) (Timmes & Swesty 2000) is implemented and accounts for radiation pressure and degeneracy effects. The hydrodynamic equations are coupled to a nuclear reaction network (Edelmann 2014).

The SLH code is designed to simulate hydrodynamic phenomena in the context of stellar astrophysics for flows at low and intermediate Mach numbers. The following discussion briefly summarizes how the numerical challenges, especially for low-Mach flows, are approached in SLH. For a more in-depth description of the applied methods we refer the reader to Edelmann et al. (2021), Edelmann (2014), and Miczek (2013).

2.1. Flux Solver

Miczek et al. (2015) and Barsukow et al. (2017) demonstrated that low-Mach flows require special numerical flux functions because common schemes, as for example the popular Roe solver (Roe 1981), suffer from excessive numerical dissipation. A variety of flux functions with improved low-Mach capabilities can be found in the literature. One promising method that seems to be applicable to problems in stellar astrophysics is the AUSM$^+$-up scheme (Liou 2006) which is implemented into SLH with a slight modification. As described in Edelmann et al. (2021), the SLH implementation uses two independent parameters to control the velocity diffusion (f_a) and pressure diffusion (f_a^{p}), respectively. The original AUSM$^+$-up scheme only uses a single parameter. It has been demonstrated by Horst et al. (2020) that compared to the classical Roe scheme the AUSM$^+$-up solver significantly improves the accuracy at which internal gravity waves can be followed for group velocities at low Mach numbers. For all simulations with the AUSM$^+$-up solver presented in this paper, we set the parameters to the values $f_a^{\mathrm{p}} = 0.1$ and $f_a = 10^{-10}$, which has proven to yield robust results in previous test simulations.

In Sect. 5 we compare simulations with the AUSM$^+$-up solver with its basic variant AUSM$_{\mathrm{B}}^+$-up in order to demonstrate the improved results when using AUSM$^+$-up. The AUSM$_{\mathrm{B}}^+$-up scheme is a subclass of the AUSM$^+$-up scheme and is obtained by disabling the scaling of the incorporated velocity and pressure diffusion with Mach number. This scaling ensures the correct behavior of leading terms of the pressure field in the limit of $\mathrm{Ma} \to 0$ (see Liou 2006, Sec. 3.2 for details). Hence, AUSM$_{\mathrm{B}}^+$-up does not have enhanced low-Mach capabilities. In SLH, the AUSM$_{\mathrm{B}}^+$-up solver option is obtained by setting $f_a^{\mathrm{p}} = f_a = 1$.

2.2. Well-balancing

Maintaining hydrostatic equilibrium is not trivial in finite volume codes because commonly gravity is discretized differently than the conserved variables and enters the equations in an operator-split approach. Hence, even if the initial data on the computational grid is formally in perfect hydrostatic equilibrium, a residual source term in the momentum and energy parts of the Euler-equations will remain (see, e.g., Käppeli & Mishra 2016; Popov et al. 2019; Berberich et al. 2021; Edelmann et al. 2021). For the SLH code, Edelmann et al. (2021) demonstrate that proper well-balancing techniques allow to simulate convection at $\mathrm{Ma} \sim 10^{-4}$. However, this requires methods that have become available only after the simulations of helium shell burning were carried out. In the simulations presented here, we use the multidimensional extension (Edelmann et al. 2021) of the 1D Cargo–LeRoux well-balancing scheme (Cargo & Le Roux 1994). Edelmann et al. (2021) show that it is not possible to perform simulations at Mach numbers considerably smaller than $\mathrm{Ma} \sim 10^{-3}$. At Mach numbers below this threshold the flow is deteriorated by discretization errors. Thus, for our study, the energy generation from helium burning that drives the convection has to be boosted by three orders of magnitude to increase the convective velocities, see Sects. 3.2 and 4.2. Still, Cargo–LeRoux well-balancing is crucial to maintain the background stratification, as demonstrated in Sect. 4.1.

2.3. Time stepping

To circumvent the small time step sizes of explicit time marching schemes, the SLH code applies implicit time stepping. Here, the time step size is not restricted by numerical stability requirements but only by the desired accuracy at which the flow is to be followed. At low Mach numbers, the large time steps and hence smaller number of total steps overcompensates the higher computational costs of a single step compared with explicit schemes. For the simulations presented in this paper the ESDIRK23 scheme (Hosea & Shampine 1996) is used, which is second order accurate in time. The resulting system of nonlinear equations is solved with the Newton-Raphson method.

For all simulations presented here, linear reconstruction is used. Slope limiter are usually required to diminish oscillations at steep gradients. However, the partially discontinuous spatial derivatives of common limiters deteriorate the convergence rate of the Newton-Raphson method. Further tests are needed to explore their possible applications in implicit SLH simulations.

3. Model setup

3.1. Construction of the initial model

The initial conditions for the hydrodynamic SLH simulation are based on an 1D model obtained with the open-source stellar evolution code MESA (Paxton et al. 2011, 2013, 2015, 2019),

The model corresponds to a $25\,M_\odot$ star at solar metallicity ($Z = 0.014$) evolved until the exhaustion of core oxygen burning. The model develops a convective helium burning shell (at $\log_{10}(\text{time left}) \lesssim 4$ in Fig. 1) following core helium burning. The numerical settings are similar to Kaiser et al. (2020) (see their Sect. 3) and briefly summarized here. Convective zones are determined using the Schwarzschild criterion, which neglects chemical gradients. It states that regions are convective if the superadiabaticity $\Delta\nabla$ is positive, that is

$$\Delta\nabla := \nabla - \nabla_{\mathrm{ad}} > 0, \tag{2}$$

where ∇_{ad} denotes the adiabatic temperature gradient while the actual temperature gradient of the gas is given by $\nabla = \mathrm{d}\ln T/\mathrm{d}\ln P$.

Convection is parametrized using MLT and a mixing length of $\ell_{\mathrm{MLT}} = 1.6\,H_{\mathrm{P}}$, where H_{P} denotes the pressure scale height

$$H_{\mathrm{P}} = -\frac{\mathrm{d}r}{\mathrm{d}P}P. \tag{3}$$

To model convective boundary mixing (CBM), the exponentially-decaying diffusion approach of Freytag et al. (1996) and Herwig et al. (1997) is used. The corresponding diffusion coefficient is (Herwig et al. 1997):

$$D_{\mathrm{CBM}} = D_0(f_0)\,\exp\left(\frac{-2\,[r - r_0(f_0)]}{f_{\mathrm{CBM}}\,H_{\mathrm{P}}^{\mathrm{CB}}}\right), \tag{4}$$

where the free parameter $f_{\rm CBM}$ determines the extent of the CBM in terms of the pressure scale height at the boundary of the convection zone $H_{\rm P}^{\rm CB}$. For the top boundary of convective regions, $D_0(f_0)$ is the MLT diffusion coefficient evaluated at $r_0(f_0) = r_{\rm CB} - (f_0\, H_p)$ where $r_{\rm CB}$ is the radius of the boundary as given by Eq. (2). The free parameter f_0 ensures that the diffusion coefficient is calculated inside the convection zone to avoid the sharp drop in D in the immediate vicinity of the boundary. The diffusion coefficient $D_{\rm CBM}$ is applied for radii larger than $r_0(f_0)$ until it drops below 10^2 cm s^{-1}. For the bottom boundary of convective regions, the scheme is adapted to apply CBM below the convective boundary. The initial 1D model was obtained with the parameters $f_{\rm CBM} = 0.022$ and 0.0044 for the top and bottom boundaries, respectively. At both boundaries, $f_0 = 0.025$ was used. We refer to Kaiser et al. (2020) for a discussion of these parameters and the related uncertainties.

Our simulations focus on convection in the helium-burning shell. The red vertical line in Fig. 1 indicates the evolutionary point at which the SLH simulations start and the extent in mass coordinates of the simulation domain. It corresponds to the early phase of helium-shell burning when the radial extent of the shell is still relatively small. Compared with later phases, this enables a better resolution at convective boundaries for a fixed computing budget. Choosing the convective shell also allows us to study two boundaries rather than only one for convective cores.

Models from stellar evolution codes typically exhibit step-like transitions in the 1D profiles, for example in the profiles of species abundances or thermodynamic quantities such as entropy. Even with moderate CBM parameters, such as used in the 1D input models, convective boundaries are very narrow. This is problematic for conventional hydrodynamic simulations because, if possible at all, a high number of grid cells is necessary to spatially resolve such transitions. Furthermore, we found in preliminary 2D test simulation that the steep gradients lead to strong initial flows in the convection zone. This effect was diminished, yet not fully resolved, for low resolution runs by applying rather strong smoothing to the initial profiles.

SLH simulations require the initial conditions to accurately fulfill the equation of hydrostatic equilibrium. This is not guaranteed for the 1D input profiles after they have been smoothed. Therefore, the equation of hydrostatic equilibrium needs to be integrated again while prescribing the profile of one thermodynamic quantity from the 1D MESA profiles. It is important that in this process the convection zone, characterized by a negative Brunt-Väisälä frequency (BVF), is maintained. For a nonrotating star, the BVF is given by (e.g., see Maeder 2009, Sect. 6.4.1)

$$N^2 = \frac{g\delta}{H_{\rm P}}\left(\nabla_{\rm ad} - \nabla + \frac{\varphi}{\delta}\nabla_\mu\right), \tag{5}$$

where g is the magnitude of the gravitational acceleration, $\delta = -(\partial \ln\rho/\partial \ln T)_{P,\mu}$, $\varphi = (\partial \ln\rho/\partial \ln\mu)_{P,T}$, and the gradient in mean molecular weight μ reads $\nabla_\mu = {\rm d}\ln\mu/{\rm d}\ln P$. These quantities are determined by the EoS. For the simulations presented here, we follow the approach of Edelmann et al. (2017) to reproduce a given 1D profile of the superadiabaticity $\Delta\nabla$. This allows one to directly control the extent of the convective region in the initial condition if the chemical gradient can be neglected in the convection zone, as is the case for our model. It also ensures that the value of $\Delta\nabla$ is reasonably close to zero and does not lead to an initial convective flow that is mainly driven by an excess in superadiabaticity. We construct the initial model on a radial grid that is much finer than the actual computational grid in SLH. For the computational grid, the initial state is obtained by interpolating from the fine grid to the positions of the respective cell centers. Because of the fine input grid, interpolation errors are negligibly small.

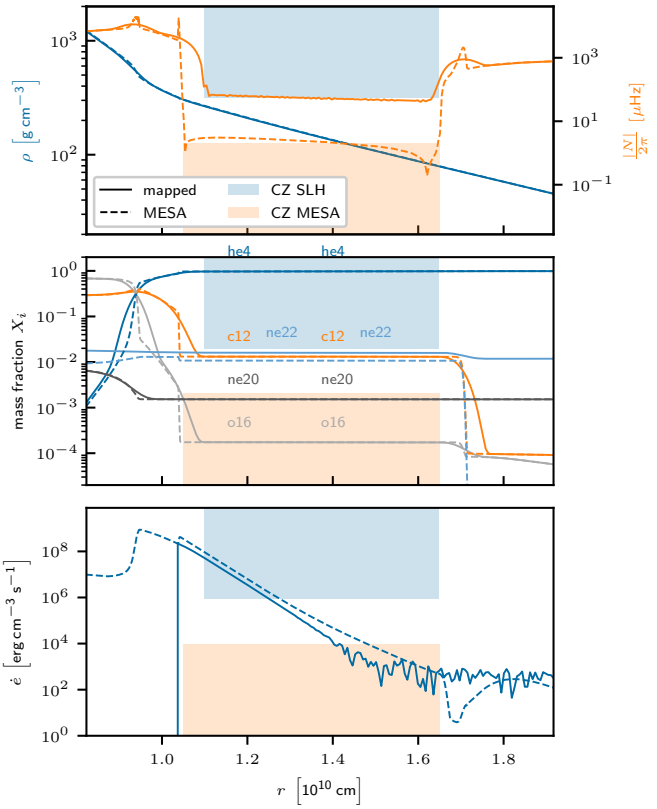

Fig. 2. Initial profiles for the underlying 1D MESA model (dashed) and the mapped SLH model (solid lines). The shaded areas mark the convection zone for mapped profiles (blue) and MESA profiles (orange). The oscillatory behavior of the energy generation is a numerical artifact at negligible amplitudes.

Preliminary SLH simulations revealed that setting the superadiabaticity on the SLH grid to a value of -1.5×10^{-5} whenever $\Delta\nabla_{\rm MESA} > -10^{-3}$ leads to a gentle transition from the initial hydrostatic stratification to fully developed convection and avoids a large initial peak in kinetic energy at the onset of convection. The slightly stable stratification would considerably hinder convection if the nominal luminosity was used. Because we have to increase the energy input anyway, this is not an issue for the simulations presented here.

In addition to the convective shell, parts of the radiative zones which lie above and below the convection zone are included in the computational domain. Their respective radial extent is chosen to be one half of the extent of the convection zone itself. This way, the impact of the top and bottom boundary conditions will be reduced while keeping the computational cost at a moderate level.

The resulting profiles after smoothing and mapping the region of interest from the 1D stellar model to the computational grid are shown in Fig. 2. The density closely follows the profiles as given by the 1D MESA input model. However, smoothing changes the profile of the BVF and alters the size of the convection zone (shaded areas in Fig. 2). Especially the position of the bottom boundary changes and the convection zone starts at a somewhat larger radius in the mapped model.

In Sect. 5.4 we measure the mass entrainment across the boundaries of the convective zone. An often employed quantity to characterize the resistance to such a mixing (also called

stiffness) is the bulk Richardson number $\mathrm{Ri_B}$. For comparability, we follow the notation of Cristini et al. (2017, 2019) (C+17 and C+19 hereafter) and write

$$\mathrm{Ri_B} = \frac{\Delta B\, l}{v_{\mathrm{rms}}^2}, \tag{6}$$

where v_{rms} is the rms velocity of the convection and the integral length scale l of the convection is set to one half of the pressure scale height at the boundary. The buoyancy jump ΔB is given by

$$\Delta B = \int_{r_c-\Delta r}^{r_c+\Delta r} N^2 \,\mathrm{d}r, \tag{7}$$

where r_c is the radial position of the respective boundary. The integration width Δr is a somewhat arbitrary parameter but should be chosen such that it includes the full region of the evanescent convective flow at the boundaries. Following C+19, we set Δr to a quarter of the local pressure scale height. Compared to our measurements of the boundary widths given in Sect. 5.6 (see Table 5), this seems to be an appropriate value for the top boundary but might overestimate the bottom boundary.

The definition of C+17 for l and Δr is not applicable for convection zones that are thinner than a pressure scale height and some form of correlation function of the turbulent flow field might be more appropriate. This, however, is not easily obtained in 1D stellar evolution codes. Generally, the definition of l and Δr is ambiguous in the astrophysical literature which makes it difficult to directly compare the values of the bulk Richardson number in simulations carried out by different groups (see for example Meakin & Arnett 2007; Arnett et al. 2009; Salaris & Cassisi 2017; Cristini et al. 2017; Collins et al. 2018; Higl et al. 2021).

To assess the impact of the applied smoothing on the stiffness, we compare the numerator of Eq. (6) for the original 1D MESA input model and the mapped SLH model at the respective top and bottom boundary. We find

$$\left.\frac{(\Delta B\, l)_{\mathrm{MESA}}}{(\Delta B\, l)_{\mathrm{SLH}}}\right|_{\mathrm{bot}} \approx 2.9, \qquad \left.\frac{(\Delta B\, l)_{\mathrm{MESA}}}{(\Delta B\, l)_{\mathrm{SLH}}}\right|_{\mathrm{top}} \approx 1.6, \tag{8}$$

which indicates that the mapping only has a moderate impact on the stiffness of the boundary.

Due to the computational costs involved, not all nuclear species of the MESA nuclear network can be included to the SLH simulation. Instead, we only account for ^{4}He, ^{12}C, ^{16}O, ^{20}Ne, and ^{22}Ne. The abundance profile of each species, except for ^{22}Ne, is taken directly from the MESA model and smoothed in the same way as the other input profiles. The abundance of ^{22}Ne follows from the condition $\sum_i X_i = 1$ in every cell, where X_i is the mass fraction of species i. The resulting profiles are shown in the middle panel of Fig. 2.

Although the smoothing procedure causes the SLH model to slightly deviate from the original 1D MESA model, the MESA model involves uncertainties of its own. Therefore, we still consider the SLH model to be representative of typical conditions expected in He-burning shells of massive stars.

3.2. Energy generation and boosting

The energy release is calculated using the JINA REACLIB reaction files (Cyburt et al. 2010) and displayed in the lowest panel of Fig. 2. From the profile of the energy generation rate as given directly by the MESA model (dashed line) it is apparent that the peak of nuclear burning does not coincide with the convection zone (orange shade) but instead is located somewhat beneath. This is common for burning shells, which develop convection above the energy peak where the temperature gradient becomes steeper than the adiabatic one.

To ensure that convection is driven by the actual energy input and not by numerical artifacts, the nominal energy input must be boosted. The strength of the required boosting is determined in Sect. 4.2. We couple the boosting of the energy generation to the abundance of ^{4}He such that only regions are boosted where the mass fraction of ^{4}He is higher than 90% of the initial abundance in the convection zone, that is for abundances higher than 0.87. The energy input is turned off everywhere else.

3.3. Thermal diffusion

Thermal radiation is treated in the diffusion limit in SLH. This is justified by the high optical depth in the interior regions of stars. While the 1D input profile from the MESA code is in thermal balance, that is the energy flux equals the integrated energy generation, this is not true anymore within the convection zone of the SLH simulations with boosted energy generation. Radiative effects certainly are crucial over the long timescales covered in simulations of stellar evolution. However, for the much shorter dynamical timescales we expect the imbalance to be of minor importance: Following the same arguments as Horst et al. (2020), we calculate the thermal adjustment timescale (e.g., Maeder 2009, Sect. 3.2.) via

$$\tau_{\mathrm{diff}}(\Delta x_{\mathrm{diff}}) \sim \frac{(\Delta x_{\mathrm{diff}})^2}{K}, \qquad K = \frac{4\, a\, c_{\mathrm{light}}\, T^3}{3\, \kappa \rho^2\, C_{\mathrm{P}}}, \tag{9}$$

where Δx_{diff} is a typical diffusion length scale, the radiation constant $a = 7.57 \times 10^{15}\,\mathrm{erg\,cm^{-3}\,K^{-4}}$ and C_{P} denotes the specific heat of the gas at constant pressure. All other values have their usual meanings. The opacity κ that enters the thermal diffusivity K is taken from the 1D MESA profile. Because advective and diffusive processes have a different temporal and spatial scaling, it is not clear how to scale the opacity with our energy boosting. Therefore, we keep the opacity at its stellar value in this study.

Assuming as typical length scale the radial grid spacing of the finest resolution that will be used (810 radial cells, see Sect. 5), we find a mean adjustment timescale of $\overline{\tau_{\mathrm{diff}}}(\delta r_{810}) = 5{\times}10^2$ h. The timescale is shortest at the outermost regions where the opacity is the smallest, but is always larger than 10^2 h (see Fig. B.1). This is at the order of our longest runs, which, however, have lower radial resolution than what is assumed in this estimate. Taking the convection zone as typical length scale we obtain $\overline{\tau_{\mathrm{diff}}}(\delta r_{\mathrm{CZ}}) \approx 4 \times 10^7$ h $\approx 4.5 \times 10^3$ yr which is orders of magnitude longer than all of our simulations. We therefore conclude that for the particular simulations presented here the effect of thermal diffusion is negligible and that the thermal imbalance due to our increased energy input does not impact the global structure of the star over the duration of our simulations.

3.4. Discretizing the computational domain

To reduce the computational costs, we have to use a spherical-wedge grid geometry, although this choice eliminates the large-scale flows seen in comparable 4π simulations of Woodward et al. (2015), Jones et al. (2017), Andrassy et al. (2020), and Gilet et al. (2013). The chosen wedge geometry reduces the computational cost by a factor of 32 compared to a full 4π simulation at the same vertical and horizontal resolution.

For the 4π simulations mentioned above, we calculate the aspect ratios (we adopt here the formulation of Jones et al. 2017)

as $(r_{\rm top} - r_{\rm bot})/r_{\rm top}$, where $r_{\rm top}$, $r_{\rm bot}$ denote the radial position of the bottom and top boundary of the convection zone. The aspect ratio for the He-flash simulation of Woodward et al. (2015) is about 0.67, for the O-shell simulation of Jones et al. (2017), Andrassy et al. (2020) it is about 0.5 and for the H-core burning of Gilet et al. (2013) it is 1. With decreasing aspect ratio, the maximum possible size of convection cells decreases and so does the impact of restricting the flow to a spherical wedge. The He-shell simulation presented here has an aspect ratio of only 0.32. Furthermore, the study by Gilet et al. (2013) indicates that, while the flow morphology differs distinctly between their hydrogen core simulations for full 4π and single octant domains, basic turbulent properties and mixing rates are in a reasonable agreement. From this, we expect that the imprint of the restricted geometry on our results is sufficiently small. However, the influence of the domain size should be assessed in more detail in future studies.

We set the horizontal extent of the computational domain to be as twice as large as the vertical extent of the convection zone. This enables the formation of two large vortices, a typical phenomenon we observe in 2D and 3D simulations. The corresponding opening angle is about 45°. The constant grid spacing giving cell aspect ratios ranging from roughly unity at the bottom to one half at the top of the domain.

The lowest resolution that will be used in this study has 180 vertical cells and 90 horizontal cells. This ensures that the pressure scale height is resolved by at least 25 cells and that the initial transitions from radiative to convective regions as given by the profile of the BVF are resolved by at least 20 cells.

Periodic boundary conditions are employed in horizontal direction. In both radial directions, layers of two cells are added (ghost cells). They are initialized with the mapped hydrostatic state but are not evolved in time.

4. 1D and 2D test simulations

While proper turbulent behavior of convection can only be followed in 3D simulations, much cheaper 1D and 2D simulations are well suited to test stability and basic properties of the initial hydrostatic stratification. Such low-dimensional simulations are utilized in this section to demonstrate that applying the Cargo–LeRoux well-balancing method successfully stabilizes the hydrostatic stratification described in Sect. 3, even at low resolution. Furthermore, a series of 2D simulations is presented to estimate the required strength of the artificial boost of the nuclear energy release.

4.1. Testing the impact of the Cargo–LeRoux well-balancing in 1D and 2D

To demonstrate the capabilities of well-balancing, we performed 1D simulations with and without the Cargo–LeRoux method. For these simulations, the energy input was switched off.

In Fig. 3, the change in the BVF and the pressure are shown after simulating 10 h of physical time (about 500 sound crossing times) in 1D. If the hydrostatic stratification was perfectly maintained, the initial profiles would stay constant in time. However, for a grid with 180 radial cells, it is obvious that the formally static setup changes considerably if no well-balancing is applied. The BVF has increased its value in the convection zone and the top boundary of the convection zone has moved inward. The relative pressure change is on the order of 10^{-3} throughout the domain. In contrast, the BVF profile does not visibly change in the run with Cargo–LeRoux well-balancing. The

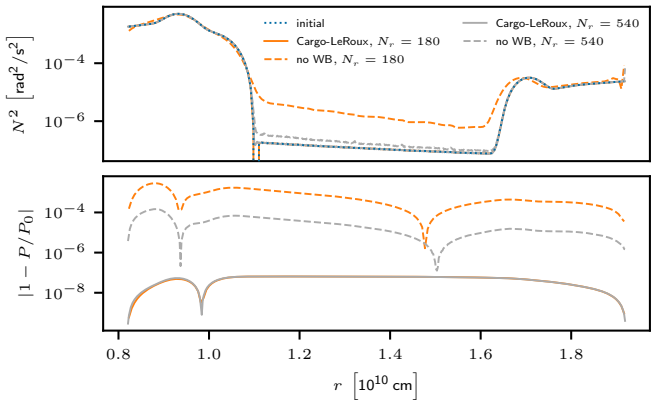

Fig. 3. Profiles of the BVF (*upper panel*) and relative change in pressure (*lower panel*) after simulating 10 h of physical time with and without well-balancing. N_r denotes the number of radial cells that are used for the discretization.

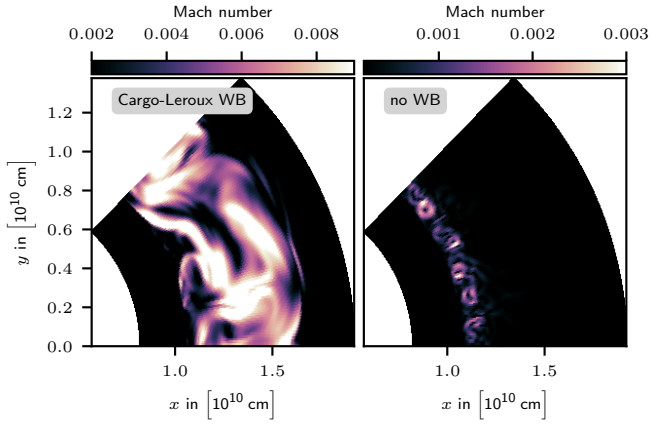

Fig. 4. Flow morphology in terms of Mach number in a 2D wedge after simulating 10 h of physical time. The nuclear energy release has been boosted by a factor of 1×10^4. The *left panel* corresponds to a simulation that applies Cargo–LeRoux well-balancing while well-balancing is absent in the simulation shown on the *right*. The domain is discretized by 180×90 cells.

relative pressure changes are about 10^{-8} which is 4 orders of magnitude smaller. The simulations shown in Fig. 3 apply the lowest radial resolution that is used for the 3D simulations in Sect. 5. The spurious change of the background stratification is expected to decrease at higher resolutions even if no well-balancing is applied. Indeed, for 540 radial cells, the overall changes decrease considerably. Yet, deviations from the initial stratification are still visible and the change in pressure is significant.

Hence, the 1D simulations indicate that, especially at low resolution, well-balancing is necessary to maintain hydrostatic equilibrium at a sufficient accuracy. This is further confirmed in the heated 2D counterparts of the 1D simulations. For a moderate energy input the setup is evolved for 10 h of physical time in 2D wedge geometry. The resulting flow is depicted in Fig. 4. The simulation with Cargo–LeRoux well-balancing has developed the typical large coherent convective eddies inside the convection zone that are driven by the energy input. This is clearly different from the flow that develops if no well-balancing is applied. Because of the changing background, the BVF has become too large, such that the energy input is not sufficient to establish convection. Instead, only at the base of the convection zone where

the heating has its maximum a narrow band of small-scale eddies emerges.

4.2. Testing artificial boosting of nuclear burning in 2D simulations

Boosting the physical energy generation from nuclear burning is a common technique in multidimensional simulations of steady convection, especially in early stellar evolutionary phases. As predicted by mixing-length theory and confirmed in numerical studies (see, e.g., C+19 or Andrassy et al. 2020) the convective velocity $v_{\rm conv}$ scales as

$$v_{\rm conv} \propto L^{1/3}, \tag{10}$$

where L is the luminosity in the convection zone. Thus, increasing the energy input leads to larger velocities.

Higher velocities can be beneficial for several reasons. As discussed in Sect. 2, convectional finite-volume schemes based on Riemann solvers have difficulties to resolve flows at low Mach numbers. Therefore, artificial boosting can be used to move the flow-velocities to regimes that are more suitable for the applied numerical scheme. Furthermore, if explicit time stepping is used, higher velocities improve the ratio of permitted time step size to the timescale of the flow. This reduces the computational costs.

Another purpose of applying energy boosting is to run simulations with the same setup but different boosting strengths. This allows one to investigate the properties of mixing at the boundaries and the entrainment rate as functions of convective velocities for a single stratification. This has been done in later phases of stellar evolution for example by C+19 or Andrassy et al. (2020) and is also utilized in Sect. 5.

The obvious downside of the artificial energy boosting is that the simulations do not represent the physical situation in the original stellar model anymore. In 1D stellar evolution codes, the structure of a star critically depends on the balance between energy generation (e.g., by nuclear burning), cooling processes (e.g., by escaping neutrinos) and energy transport within the star (e.g., by radiation or convection). This balance is disturbed if the energy input is changed. While we think it is still possible with such simulations to assess the effect of dynamical phenomena such as turbulent mixing and excitation of waves, they are probably not suitable to study the long-term behavior of convection where the interplay between turbulence and thermal diffusion might become important.

Apart from the reasons mentioned above, a sufficient energy boosting is also necessary to increase the velocity above the numerical threshold at about Ma $\approx 10^{-3}$ for SLH simulations with the Cargo–LeRoux well-balancing method. To assess by how much the energy generation has to be increased for the 3D simulations, a set of 2D wedge simulations is performed with varying strengths of the energy boosting. The resolution is set to 180×90 cells (lowest resolution in the 3D runs) and the simulations are performed for boosting factors ranging from 1 (no boosting) to 3×10^4. The resulting temporal mean of the root-mean square (rms) Mach number $\mathrm{Ma}_{\rm rms}$ as a function of energy input is then compared to the scaling law in Eq. (10). In order to determine the region for which the rms value of the Mach number is calculated, the convection zone is identified by means of the gradient of the advected passive scalar, as will be explained in Sect. 5.1. For the size of the time frame, we consider the convective turnover time

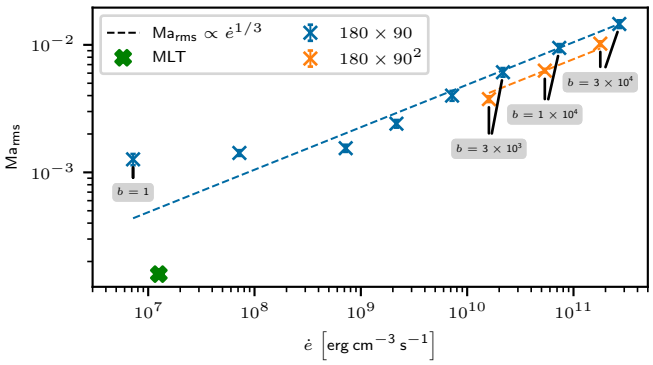

Fig. 5. Measured rms Mach number as function of the input energy rate $\dot{e}$ in 2D (blue) and 3D simulations (orange). Vertical error bars correspond to the standard deviation of the average over the time frame of $\Delta N_{\tau_{\rm conv}} = 10$. The dashed lines reflect the scaling law in Eq. (10). Numbers given in the boxes correspond to energy boosting factors for the lowest and the three highest boostings. The green cross marks the Mach number of Ma $\approx 1.6 \times 10^{-4}$ as predicted by MLT at the nominal energy generation rate in the original MESA model.

$$\tau_{\rm conv} = \frac{2\Delta_{\rm CZ}}{v_{\rm rms}}, \tag{11}$$

where $\Delta_{\rm CZ}$ is the radial extent of the convection zone and $v_{\rm rms}$ the rms velocity within the area spanned by $\Delta_{\rm CZ}$ and the horizontal extent of the domain. By taking $\tau_{\rm conv}$ as the underlying unit of time, we account for the different speed at which the hydrodynamical processes evolve for different driving strengths. To finally determine the time frame for which $v_{\rm rms}$ is determined, we calculate the number of covered turnover times $N_{\tau_{\rm conv}}$ as

$$N_{\tau_{\rm conv}}(t) = \int_{t_0}^{t} \frac{1}{\tau_{\rm conv}(t')}\,\mathrm{d}t'. \tag{12}$$

Using Eq. (12) automatically accounts for different lengths and characteristics that may arise for initial transients for different luminosity boosting and resolutions. Therefore, we find it more convenient to define a time frame in terms of $N_{\tau_{\rm conv}}$ instead of finding a suitable physical time interval by hand.

To account for the fact that the boosted region may change during a simulation, the energy release is integrated over the domain and averaged for the considered time frame of $t \in [t(N_{\tau_{\rm conv}} = 10),\ t(N_{\tau_{\rm conv}} = 20)]$.

As shown in Fig. 5, the data points of the three highest boostings (3×10^3, 1×10^4, and 3×10^4) closely follow the expectation of Eq. (10). For lower energy boosting, we find deviations from the scaling. The corresponding flow patterns along with the detected boundaries are shown in Fig. B.2. The flow of the 2D simulation with the lowest boosting clearly differs from the other 2D simulations. The appearance of incoherent, small-scale patterns in SLH simulations of convection is likely an indication that the flow is driven by numerical artifacts (see also Edelmann et al. 2021). Based on these results, we conclude that the set of boosting factors $b \in \left[3 \times 10^3, 1 \times 10^4, 3 \times 10^4\right]$ is suitable for the subsequent 3D simulations.

5. 3D SLH results

After the basic properties of the stellar model have been tested in 1D and 2D hydrodynamic simulations, this section presents

Table 1. Properties of the 3D simulations with a boosting factor of 3×10^4.

Resolutions	180×90^2		360×180^2		540×360^2		810×540^2	
num. flux	AUSM$^+$-up	AUSM^+_B-up	AUSM$^+$-up	AUSM^+_B-up	AUSM$^+$-up	AUSM^+_B-up	AUSM$^+$-up	AUSM^+_B-up
Δt_{tot} [h]	128.45	65.70	18.27	18.41	10.87	14.53	3.32	2.38
ΔN_{conv}	44.88	21.87	6.24	5.51	3.16	4.62	1.32	0.87
$\overline{\tau}_{conv}$ [h]	3.04	2.93	2.25	2.42	2.68	2.63	2.35	2.84
Ma_{rms} $\left[10^{-2}\right]$	1.07	1.01	1.08	0.98	0.86	0.88	1.00	0.81

Notes. Simulations with 810×540^2 cells are restarted from the corresponding 540×360^2 simulations at $N_{\tau_{conv}} = 3.1$ (AUSM$^+$-up) and $N_{\tau_{conv}} = 3.6$ (AUSM^+_B-up). Legend: Δt_{tot}: total covered stellar time. $\Delta N_{\tau_{conv}}$: total number of turnover times. $\overline{\tau}_{conv}$: mean convective turnover time averaged for the last available $0.5 N_{\tau_{conv}}$, respectively. Ma_{rms}: rms Mach number corresponding to $\overline{\tau}_{conv}$.

Table 2. Properties of the 3D simulations with a grid size of 180×90^2 cells.

Boosting	3×10^3		1×10^4		3×10^4	
num. flux	AUSM$^+$-up	AUSM^+_B-up	AUSM$^+$-up	AUSM^+_B-up	AUSM$^+$-up	AUSM^+_B-up
Δt_{tot} [h]	199.92	183.11	139.68	97.45	128.45	65.70
ΔN_{conv}	30.61	22.61	34.00	20.70	44.88	21.87
$\overline{\tau}_{conv}$ [h]	6.13	7.24	4.27	4.61	3.04	2.93
Ma_{rms} $\left[10^{-2}\right]$	0.40	0.33	0.65	0.56	1.07	1.01

Notes. Quantities have the same meaning as in Table 1.

Table 3. Properties of the 3D simulations with a grid size of 360×240^2 cells.

Boosting	3×10^3	1×10^4	3×10^4
num. flux	AUSM$^+$-up	AUSM$^+$-up	AUSM$^+$-up
Δt_{tot} [h]	9.48	15.86	10.20
ΔN_{conv}	1.40	4.05	4.06
$\overline{\tau}_{conv}$ [h]	6.86	3.85	2.39
Ma_{rms} $\left[10^{-2}\right]$	0.33	0.61	1.09

Notes. Quantities have the same meaning as in Table 1.

the results regarding turbulent flow properties and entrainment obtained from 3D simulations. We analyze the results for varying resolution and convective driving. To demonstrate that the low-Mach AUSM$^+$-up flux scheme is beneficial even for moderate Mach numbers, the respective results are compared to its basic version AUSM^+_B-up that is not expected to show enhanced low-Mach capabilities. A comparison to more commonly used flux functions, such as the Roe solver, would have been a more obvious choice. This was not possible as the applied Cargo–LeRoux well-balancing method is not fully compatible with the Roe scheme. However, in Sect. 5.2, we show for a reduced domain that the numerical diffusivity is similar for AUSM^+_B-up and the Roe scheme.

A major restriction for our 3D simulations is posed by the available computational resources. While a higher resolution is certainly desirable, it considerably reduces the physical time for which we could follow convection. However, convection has to be covered for several turnover times τ_{conv} in order to analyze mixing processes at the boundaries of the convection zone. We therefore can only investigate the effect of boundary mixing at the lowest resolution of 180×90^2. At higher resolution, our simulations only cover a few multiples of τ_{conv} which is too short to track mixing at the boundaries but is sufficient to extract properties of turbulence. In this section we present simulations with resolutions ranging from 180×90^2 to 810×540^2. The basic properties of the simulations are summarized in Tablea 1–3. We note that the radial resolution from 360×180^2 to 540×360^2 cells changes by a factor of 1.5, while the corresponding number of horizontal cells changes by a factor of 2. This was done inadvertently, but we are confident that it does not prevent the comparison of the results between the different resolutions. The simulations at a resolution of 810×540^2 cells are restarted from the corresponding simulations at 540×360^2 at a stage of fully developed convection. This avoids the slow initial transients and hence reduces computational costs.

To conclude the 2D scaling test of the previous section, the scaling relation Eq. (10) is shown for the lowest resolution and the AUSM$^+$-up solver in Fig. 5 (orange crosses). The 3D data is in good agreement with the expected scaling. The corresponding flow patterns are found in Fig. B.2 at a resolution of 180×90^2. From MLT, a convective velocity of $Ma_{MLT} \approx 1.6 \times 10^{-4}$ is predicted. If we extrapolate from the 3D results to stellar luminosity we find a value of $Ma_{ext} \approx 4.0 \times 10^{-4}$. The ratio $Ma_{ext}/Ma_{MLT} \approx 2.5$ is similar to what has been obtained by Jones et al. (2017). This ratio indicates a reasonable agreement, taking into account that MLT only provides an order-of-magnitude estimate and that the results from our simulations need to be extrapolated to nominal luminosity.

5.1. Tracing the boundaries of the convection zone

For the analysis that is presented in the subsequent sections, the top and bottom radii of the convection zone, $r_{CZ,0}$ and $r_{CZ,1}$, have to be extracted from the simulations. This can be done in different ways, for example by considering the radii where the decline in the horizontal velocity is steepest (Jones et al. 2017), where the species abundance gradient is steepest (Meakin & Arnett 2007), or where the mean atomic weight is equal to its averaged value within the convective and adjacent stable zone (C+17).

Furthermore, to avoid the use of averages which might underestimate the effect of strong but rare mixing events, extreme value statistics could be used (Pratt et al. 2017) or the standard deviation of a dynamical quantity like the kinetic energy (Higl et al. 2021).

Our approach is to advect ρX with the fluid flow where X is a passive scalar. Its initial distribution increases at a constant slope from -1 at the bottom boundary of the computational domain to 1 at the top (dashed line in Fig. 6). The passive scalar will quickly be mixed within the convection zone while forming a transition between the initially linear decrease and a flat region. The position of the boundaries is then defined as the radius where the spatial gradient of the horizontally averaged passive scalar is largest. We find that after an initial redistribution of the scalar by the onset of convection our method gives robust results.

This definition of the boundary position is similar to using the abundance gradient. However, it does not depend on the initial 1D structure in terms of strength and position of the gradients. Furthermore, the abundance and passive scalar profiles are immediate measurements of the mixing compared to measuring for example overshooting events or standard deviations, which are linked to mixing only indirectly.

For an exemplary simulation, Fig. 6 shows the profile of the advected passive scalar at the start of the simulation and around $t\,(N_{\tau_{\rm conv}} = 10)$. The efficient mixing by convection has homogenized the passive scalar within the convection zone. At the top and bottom boundary of the computational domain, the profile of the passive scalar is almost not distinguishable from the initial distribution. The orange shaded area denotes the convection zone according to the criterion $N^2 < 0$ and it is clearly visible that this definition underestimates the extent of the convection zone. The bottom and top boundaries of the convection zone as given by the maximum absolute value of the radial gradient of the passive scalar are shown as blue dots. There are small amounts of numerical under- and overshoots in the profile of the passive scalar. This is due to a lack of slope-limiter for reconstruction for the implicit time stepping.

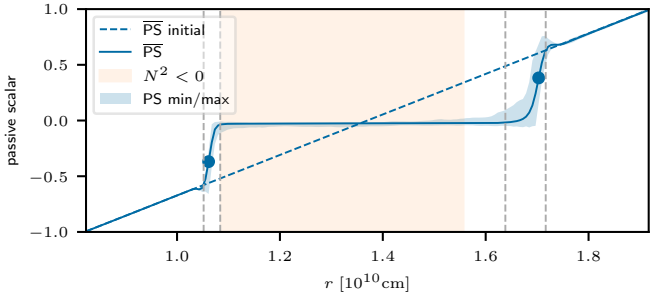

Fig. 6. Horizontal mean of the advected passive scalar for a simulation with a resolution of 180×90^2. The initial distribution of the scalar is shown as dashed line, the solid line represents the time-averaged profile for $t \in [t\,(N_{\tau_{\rm conv}} = 9.9), t\,(N_{\tau_{\rm conv}} = 10.1)]$. The blue shaded area corresponds to the minimal and maximal value of the passive scalar at the corresponding radius for the latest considered snapshot. The radii at which the absolute value of the radial derivative is largest are indicated by dots. They define the position of the top and bottom boundaries. The shaded orange area marks the convective region according to the stability criterion $N^2 < 0$. Vertical dashed lines denote the respective boundary widths which are defined in Sect. 5.6.

5.2. Kinetic energy spectra and comparison with turbulence theory

Kolmogorov (1941) (see also Landau & Lifshitz 1987) predicts that the spectrum of kinetic energy $\varepsilon_{\rm kin}$ in 3D isotropic turbulence follows

$$\varepsilon_{\rm kin}(\ell) \propto \hat{v}^2(\ell) \propto \ell^{-5/3}, \tag{13}$$

where ℓ is the angular order. Although stellar convection is not isotropic on large scales, many numerical experiments reveal spectra similar to this prediction on sufficiently small scales (Porter & Woodward 2000; Gilet et al. 2013; Verma et al. 2017, C+17). The spectra of turbulent convection in 3D typically divide into three regions (see Arnett et al. 2015 for a more detailed discussion): At large spatial scales, that is at small values of the angular order ℓ, the energy from heating is injected into the flow, forming the integral range. At somewhat smaller scales, or equivalently for larger ℓ, the inertial range forms that follows the scaling of Eq. (13). The inertial range extends down to the small scales where dissipating effects such as viscosity become relevant and turbulent kinetic energy is transformed into internal energy. This leads to a steeper drop in $\varepsilon_{\rm kin}(\ell)$ for larger ℓ and marks the dissipation range. In the stellar context, it is impossible to resolve the spatial scales where physical viscosity takes place. Thus, in implicit large eddy simulations (ILES), the effect of viscosity is not modeled explicitly but follows from the numerical viscosity inherent in the applied numerical scheme at small scales (see, e.g., Arnett et al. 2015, 2018). This is the case for the SLH code that solves the Euler equations which follow from the Navier-Stokes equations for vanishing viscosity but does not apply any subgrid scale model for turbulent dissipation. It therefore is desirable to resolve the scaling Eq. (13) to the smallest scales possible while still having a numerically stable scheme. Hence, one way to compare the quality of numerical schemes is to compare their respective range in ℓ for which they reproduce an inertial range with a scaling according to Eq. (13).

In the following, we present the spectra for the 3D SLH simulations and compare the low-Mach AUSM$^+$-up solver to the AUSM$^+_{\rm B}$-up scheme. In setups with an approximate spherical symmetry, the spatial spectra of turbulent flows are typically given in terms of power spectra for spherical harmonics. This makes use of the fact that a given function $F(\vartheta, \varphi)$ on the spherical surface can be decomposed into spherical harmonics as

$$F(\vartheta, \varphi) = \sum_{\ell=0}^{\infty} \sum_{m=-\ell}^{\ell} f_{\ell m} Y_{\ell m}(\vartheta, \varphi), \tag{14}$$

where $f_{\ell m}$ is the amplitude for the corresponding spherical harmonic Y_{lm} of angular degree ℓ and angular order m. For our analysis we apply the open-source shtools[1] (Wieczorek & Meschede 2018), a collection of Fortran90 and Python libraries for spherical harmonics data analysis. To decompose the velocity fields that result from our simulations, we proceed as follows:

The shtools assume that the input data is provided for the whole spherical surface. The computational domain in our simulations, however, is a spherical wedge. We therefore expand the $\varphi - \vartheta$ plane covered by our simulations to the full spherical surface. For this, the data from our simulation is repeated periodically to fill the regions that are not covered by the computational domain, see Fig. 7. This gives slightly weaker artifacts than zero-padding.

To further reduce the artifacts introduced by our limited domain, we make use of the ability of shtools to apply an arbitrary window function to extract localized spectra. The shtools construct the windows automatically and provide the user the

[1] https://shtools.oca.eu

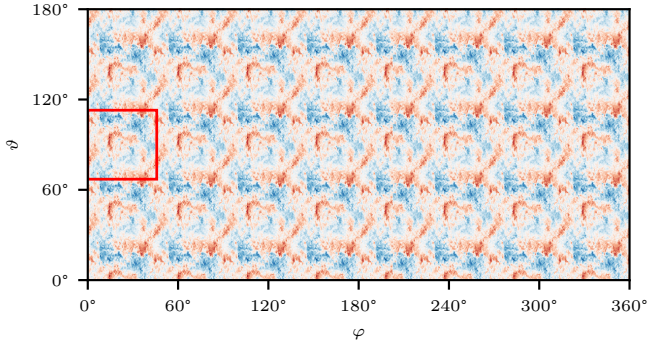

Fig. 7. Expansion of the velocity data for one exemplary 3D wedge simulation. Color coded is the velocity component in φ-direction. The red square marks the actual computational domain. The rest of the plane is filled by periodically repeating the simulation data in ϑ and φ direction.

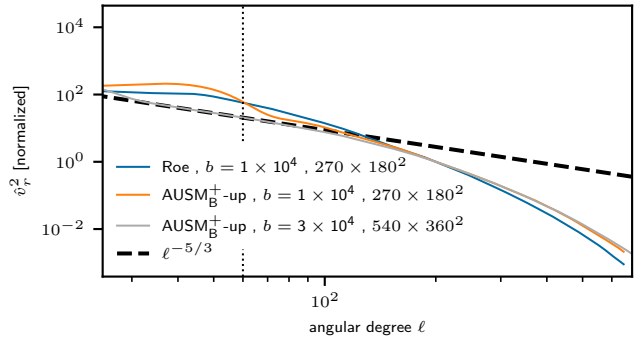

Fig. 8. Spectra of the radial kinetic energy component. The blue and orange line correspond to simulations with the Roe and AUSM$_B^+$-up schemes of a reduced domain that only contains a fraction of the convection zone. The gray line shows the spectrum for a simulation of the full domain with the AUSM$_B^+$-up solver, the same grid spacing, but a different energy boosting. The amplitudes have been normalized such that they are unity at $\ell = 200$ to ease the comparison. The dashed line marks the Kolmogorov-scaling according to Eq. (13). The vertical dotted line at $\ell_{\max} = 60$ denotes the spectral width of the applied window functions for the runs with 270×180^2 cells. For $\ell \leq \ell_{\max}$, their spectra are dominated by the convolution with the window function and do not reflect real data. The horizontal axis is truncated at the spectral width of the window function for the 540×360^2 run which corresponds to $\ell_{\max} = 25$.

option to restrict the bandwidth of the created windows by an upper limit $\ell_{\max}$. The necessary bandwidth of the window function increases with smaller localized areas. The shtools then calculate different realizations of window functions that have their power concentrated in the considered region within the $\vartheta - \varphi$ plane. The spectra of all windows are averaged (multitaper, see also Wieczorek & Simons 2005). For the input of the multitaper spectrum, we set $\ell_{\max}$ to a sufficiently high value to obtain at least 10 window realizations from shtools which have 99% of their power localized in the computational domain.

The spectra that are presented in the following are taken at a constant radius in the middle of the convection zone. This is justified if the flow is isotropic, which is not the case at large scales (small ℓ) but a reasonable assumption at small scales. Isotropy is also a necessary condition for the Kolmogorov-scaling Eq. (13) to form. The extracted spectra are averaged over roughly one convective turnover time.

In order to demonstrate the improved performance of the low-Mach AUSM$^+$-up solver, we compare it to its basic variant AUSM$_B^+$-up. The AUSM solver family is not yet widely used

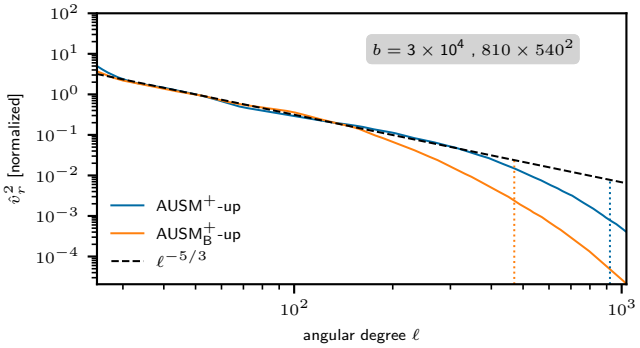

Fig. 9. Spectra of the radial kinetic energy component for the AUSM$_B^+$-up and AUSM$^+$-up solver at a resolution of 810×540^2 cells and an energy boosting of $b = 3 \times 10^4$. The amplitudes are normalized to unity at $\ell = 50$ for better comparability. Dotted vertical lines mark the angular degree ℓ at which the relative deviation from the Kolmogorov-law is one decade. For the AUSM$_B^+$-up solver this happens at $\ell \approx 470$, for the AUSM$^+$-up solver at $\ell \approx 920$. The horizontal axis is truncated at the spectral width of the applied window function ($\ell_{\max} = 25$).

in the astrophysical community. To get an idea how AUSM$_B^+$-up compares to the well-known Roe scheme, we compare their spectra for a reduced domain, which only contains a subset of the convection zone. This is necessary because we find numerical artifacts for Roe in combination with Cargo–LeRoux well-balancing that lead to spurious flows in the stable regions at radii where abundances change.

Their spatial resolutions are the same as for the 540×360^2 simulations of the full domain. The result is shown in Fig. 8. The spectra demonstrate that, at least within the convection zone, the AUSM$_B^+$-up and the Roe solver are both dissipative and do not show an inertial range. For comparison, the spectrum of a simulation which has the same spatial resolution but using the AUSM$_B^+$-up scheme is added to the figure along with the Kolmogorov-law Eq. (13). The similarity between the Roe and AUSM$_B^+$-up solver is also evident in the flow pattern, Fig. B.3.

The spectra for the highest available resolution and the full domain are shown in Fig. 9. We find that the AUSM$_B^+$-up and AUSM$^+$-up solver both show a well-defined inertial range where the slope closely follows the prediction of a Kolmogorov spectrum. The vertical dotted lines in Fig. 9 mark the scale at which there is a significant deviation from the Kolmogorov-law. From this measure we find that the inertial range of the AUSM$^+$-up solver extends toward scales that are about a factor two smaller compared to the AUSM$_B^+$-up solver.

In Fig. 10 the turbulent convective velocity field is depicted for a slice through the three-dimensional domain for a single snapshot. The AUSM$^+$-up scheme clearly shows smaller structures in the flow field as compared with AUSM$_B^+$-up on the same computational grid. This is also apparent in Fig. 11 which shows the magnitude of vorticity $|\nabla \times \boldsymbol{u}|$, where $\boldsymbol{u}$ is the velocity vector. To further illustrate the advantages of the low-Mach flux AUSM$^+$-up over AUSM$_B^+$-up, we compare in Fig. 12 the spectra at different resolutions. We find that for the AUSM$^+$-up solver, a grid resolution of 360×180^2 gives an inertial range that is comparable to the 810×540^2 resolution of simulations with AUSM$_B^+$-up.

5.3. Comparing numerical dissipation from RA-ILES results

The comparison of the kinetic energy spectra is complemented by analyzing the different simulations in the terms of

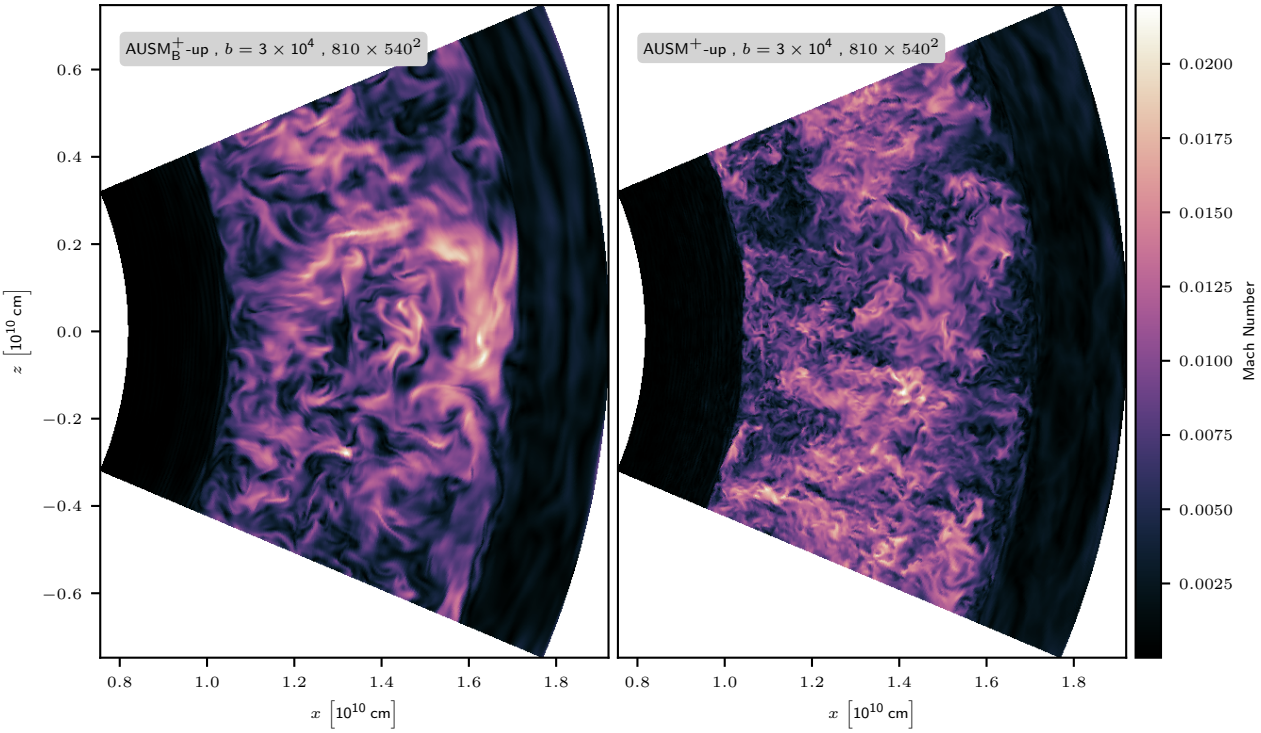

Fig. 10. Mach number for a slice through the domain for simulations at a resolution of 810×540^2 cells with the AUSM$_B^+$-up solver (*left*) and AUSM$^+$-up solver (*right*). The data is taken from the latest available snapshot, respectively.

Reynolds averaged implicit large eddy simulations (RA-ILES) (Mocák et al. 2014; Arnett et al. 2019). The fundamental idea is to separate the different components of the Navier-Stokes equations into mean and fluctuating parts and to determine them by analyzing numerical simulations. The physical interpretation of these parts then gives useful insight into the complex interplay between different processes that act in turbulent convection and at the boundaries of the convection zone.

While the RA-ILES framework provides a wealth of equations (see Mocák et al. 2014 for an extensive overview), we focus on analyzing the equation for turbulent kinetic energy. It allows one to quantify the effect of implicit numerical dissipation of kinetic energy that is inherent in all ILES. This equation has been used in several publications in the past (see, e.g., Arnett et al. 2009; Mocák et al. 2014, 2018), and aided the analysis of the effects of resolution and convective driving (C+17, C+19) or different strengths of stratification (Viallet et al. 2013). Following the formulation of Mocák et al. (2014), the time evolution for the kinetic energy of an inviscid fluid can be written as

$$\partial_t(\bar{\rho}\tilde{\epsilon}_k) + \nabla_r(\bar{\rho}\,\tilde{v}_r\tilde{\epsilon}_k) = -\nabla_r\,(f_\mathrm{P} + f_k) + W_b + W_\mathrm{P}, \qquad (15)$$

where ϵ_k is the specific kinetic energy, $f_\mathrm{P} = \overline{P'v_r'}$ the acoustic flux, $f_k = \overline{\rho v_r'' \epsilon_k''}$ the turbulent kinetic energy flux, $W_b = \overline{\rho}\,\overline{v_r''}\,\tilde{g}_r$ the buoyancy work, $W_\mathrm{P} = \overline{P'd''}$ the turbulent pressure dilatation, and $d = \nabla \cdot \boldsymbol{v}$. The radial component of the gravitational acceleration is denoted by g_r. The definition of the Reynolds average $\overline{q}$, Favre average $\tilde{q}$, and the corresponding fluctuations q', q'' for a quantity q are given in Appendix A. For a more detailed discussion of the individual terms, see for example Meakin & Arnett (2007), Viallet et al. (2013), or Mocák et al. (2014).

Because numerical solutions are only approximations to the true solution, Eq. (15) will in general not be fulfilled exactly in hydrodynamic simulations. Instead, there will be a residual $\mathcal{N}_{\epsilon_k}$ between the left-hand and right-hand side. In energy conserving methods like finite volume schemes, $\mathcal{N}_{\epsilon_k}$ then measures the numerical dissipation of kinetic energy into internal energy, the fundamental property of ILES. The exact value of $\mathcal{N}_{\epsilon_k}$ depends on the details of the numerical scheme, the resolution, but also on the specific physical problem at hand. Generally, the value of $\mathcal{N}_{\epsilon_k}$ cannot be controlled in ILES. However, extracting the terms in Eq. (15) from a hydrodynamic simulation, the strength of numerical dissipation that acted for the considered time in a specific simulation can be determined from the average value of $\mathcal{N}_{\epsilon_k}$.

We calculate all the terms in Eq. (15) for the AUSM$_B^+$-up and AUSM$^+$-up solver at different resolutions. Third-order central differences are used to evaluate the gradients. Except for the highest resolution, the results are averaged over the time interval of $t \in [t\,(N_{\tau_\mathrm{conv}} = 2)\,, t\,(N_{\tau_\mathrm{conv}} = 3)]$ which is the maximum overlapping time frame. For the highest resolution, the simulations are averaged over only $\Delta N_{\tau_\mathrm{conv}} = 0.6$. Ideally, the averages would be performed over several turnover times to improve the statistics. While our short time frames probably make a quantitative comparison of the components less robust, we think that a qualitative comparison is still meaningful and that the main characteristics of Eq. (15) are captured.

In Fig. 13 the profiles of the individual terms of Eq. (15) are depicted for successively increasing resolutions[2]. We find

[2] In the RA-ILES analysis framework of SLH, all required fluctuations are calculated and stored already during the simulation, such that we have data for every single time step. However, there was a flaw in the calculation of the velocity divergence for the simulations presented here. Therefore, the velocity divergence had to be re-calculated in a post-processing step, for which the 3D velocity data is only available for the stored grid files but not for every time step. Fortunately, only the value of W_P is affected which is, however, small in general and the impact of the post-processing is negligible.

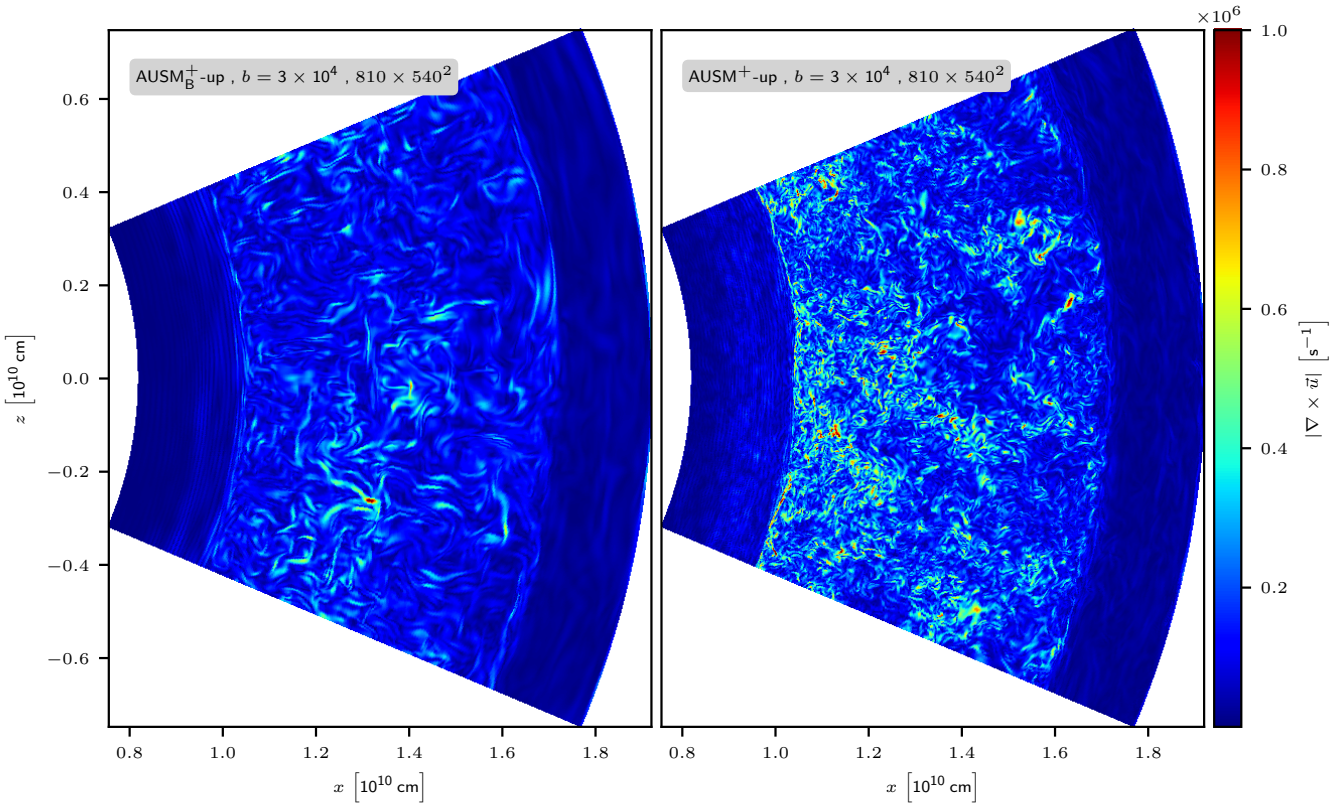

Fig. 11. Similar to Fig. 10, but for the magnitude of the vorticity.

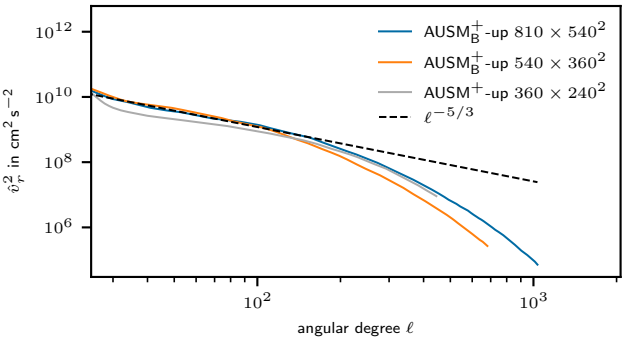

Fig. 12. Spectra of the radial kinetic energy component for the AUSM^+_B-up and AUSM$^+$-up solver at different resolutions and an energy boosting of $b = 3 \times 10^4$.

our results in qualitative agreement with simulations of oxygen burning (Viallet et al. 2013, Fig. 8) and carbon burning (Fig. 9 of C+17, see also C+19). The small but noticeable nonzero values for the left-hand side of Eq. (15) (dashed lines in Fig. 13) are due to the short time interval considered. For comparison, we recalculated in Fig. 14 the results for the lowest resolution but a time interval that covers $\Delta N_{\tau_{\rm conv}} = 10$. Here, the time evolution of the kinetic energy is close to zero.

The dominant part on the right-hand side is the buoyancy work W_b that is positive in the convection zone and changes sign at the boundaries to the stable layers. The acoustic and turbulent kinetic energy fluxes show a more complex behavior and change signs several times in the convection zone. The pressure dilatation term $W_{\rm P}$ takes a rather low value for all simulations owing to the fact that the density stratification within the convection zone is small. As shown by Viallet et al. (2013), the situation can be different in other setups. They find that in the convective envelope of a 5 $M_\odot$ red giant star, pressure dilatation contributes a significant part to the overall budget of Eq. (15) as the convection zone spans several pressure scale-heights. In general, we do not find significant qualitative differences between different resolutions and between the AUSM^+_B-up and AUSM$^+$-up solver. At the lowest resolution with AUSM$^+$-up, small oscillations on the grid level are visible for the acoustic flux $f_{\rm P}$ within the convection zone. However, they vanish for increasing resolution. At high resolution, we find oscillations in $f_{\rm P}$ at the domain boundaries, the origin of which is not completely clear. We suspect an interplay of better resolved internal gravity waves with the constant ghost cell boundaries. This inevitably leads to shear because velocities are set to zero in the boundary cells.

The dotted lines in Fig. 13 correspond to the numerical dissipation of kinetic energy $\mathcal{N}_{\epsilon_k}$ acting in the respective simulation. In general, the dissipation is distributed over the whole convection zone and vanishes in the stable layers. For the AUSM$^+$-up solver, some smaller oscillations are visible near the boundaries which stem from the oscillations in $f_{\rm P}$. Comparing the results of the AUSM^+_B-up and AUSM$^+$-up solver at each resolution, the profiles of $\mathcal{N}_{\epsilon_k}$ have similar amplitudes in the main part of the convection zone. However, for the simulations using the AUSM^+_B-up solver, the numerical dissipation shows a distinct peak at the bottom boundary. The peak height and width decreases with increasing resolution. The same behavior was found by C+17 for carbon-shell burning and by Viallet et al. (2013) for oxygen-shell burning. However, this peak is absent in the simulations using the AUSM$^+$-up solver. From the shape and position of the peak of $\mathcal{N}_{\epsilon_k}$ in the plots for the AUSM^+_B-up solver it seems that the peak is due to an imbalance between the

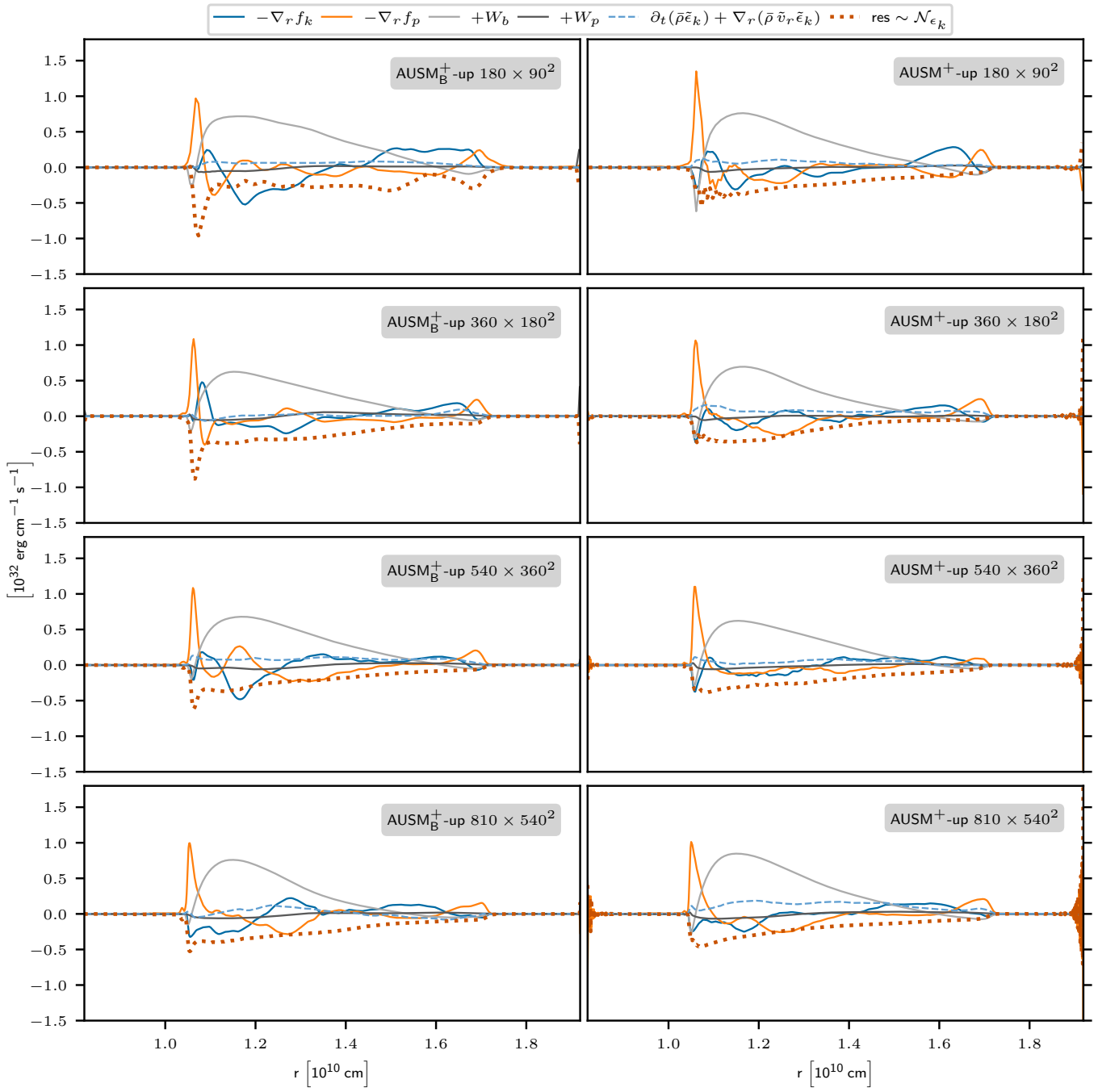

Fig. 13. Profiles of the different components of kinetic energy equation in the RA-ILES framework, Eq. (15). The resolution increases from top to bottom. The left column corresponds to results using the AUSM^+_B-up solver and the right column to results using the AUSM$^+$-up solver. All simulations boost the nuclear energy generation by a factor of 3×10^4. The profiles are averaged for roughly one convective turnover time. Similar to Viallet et al. (2013), the components are multiplied by the geometrical factor $4\pi r^2$.

acoustic flux f_p and W_b. Although the peak in f_p appears to be similar in shape and amplitude for the two solvers, a more pronounced opposed peak in W_b seems to counteract the gradient of f_p in the AUSM$^+$-up runs.

We directly compare the numerical dissipation $\mathcal{N}_{\epsilon_k}$ for the different simulations in Fig. 15. For AUSM$^+$-up, the amplitudes seem to be converged already for the lowest resolution, although low-resolution runs show oscillations in the numerical dissipation. Also for the AUSM^+_B-up solver, the dissipation in the bulk of the convection zone seems not to depend strongly on the resolution. This is consistent with the expected independence of the turbulent dissipation rate from the effective viscosity, which is set by the grid scale. However, at the bottom boundary, the peak decreases with increasing resolution and seems to converge toward a value that is similar to the dissipation of the AUSM$^+$-up solver. These results are fully in line with the simulations shown in Figs. 1 and 2 of Arnett et al. (2018) which summarize the numerical dissipation in oxygen- and carbon-shell burning simulations with the PROMPI code. For their highest-resolution run, they find that the peak at the bottom boundary seems to merge with the bulk dissipation. This indicates that the low-Mach AUSM$^+$-up solver improves the behavior at the

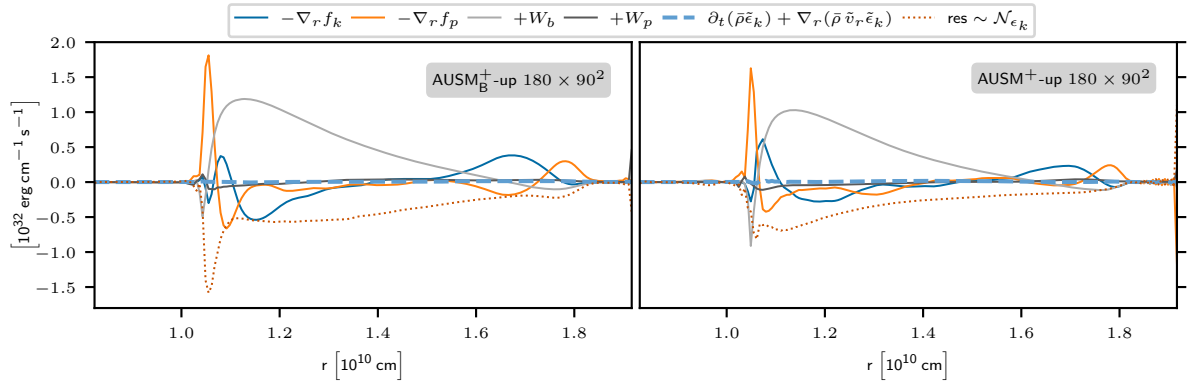

Fig. 14. Same quantities as in Fig. 13, but for a time interval of $t \in [t\,(N_{\tau_{\rm conv}} = 10)\,, t\,(N_{\tau_{\rm conv}} = 20)]$.

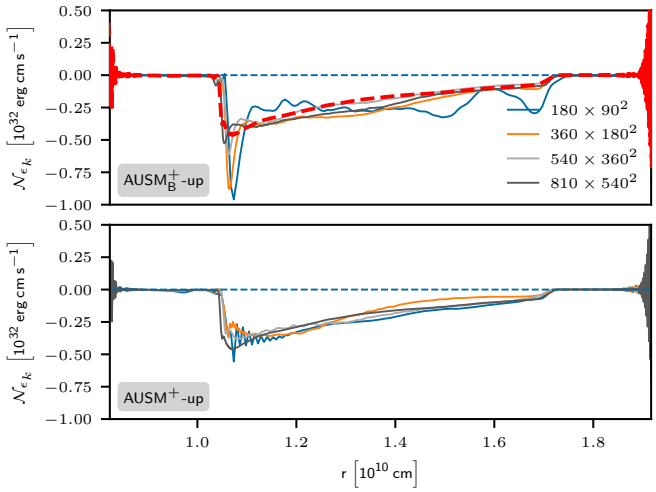

Fig. 15. Residual $\mathcal{N}_{\epsilon_k}$ for the runs shown in Fig. 13. For comparison, the profile of $\mathcal{N}_{\epsilon_k}$ for the 810×540^2 AUSM$^+$-up simulation is included as a red dashed line in the upper panel.

bottom boundary, even at moderate Mach numbers and moderate resolution.

5.4. Convective boundary mixing

An important process in stellar interiors is the entrainment of material from stable layers at the boundaries of a convection zone into the convective region. This has implications for the star's further evolution because the entrained material serves as fuel for the burning region. Despite its importance, it needs to be parametrized in conventional 1D stellar evolution simulations due to its inherently multidimensional nature. For the various types of convection, for example in shallow zones in the stellar interior or extended regions in the envelope of solar-like stars, different physical mechanisms are dominant. It is therefore of interest to develop and validate different possible parametrizations with the help of multidimensional simulations.

Viallet et al. (2015) suggest to use the local Péclet number, the ratio of advective and diffusive timescales, in the boundary region to distinguish between different types of convective boundary mixing. Estimating the typical velocity v and length scale l of convection through MLT, we find a minimum Péclet-number within the convection zone of

$$\mathrm{Pe} = \frac{ul}{K} = \frac{3D_{\rm mlt}}{K} \approx 5 \times 10^4 \gg 1, \tag{16}$$

where K is the thermal diffusivity (see Eq. (9)) and $D_{\rm MLT} = 1/3\, u_{\rm MLT}\, l_{\rm MLT}$ is the diffusion coefficient obtained from MLT. The large Péclet number implies minor importance of radiation for the mixing, in accordance with our estimates in Sect. 3.3. The artificial boosting will increase the Péclet number even further in the hydrodynamic simulations. Following Viallet et al. (2015), at Pe $\gg 1$ mixing can be thought to occur via turbulent entrainment, where small-scale instabilities are caused by the shear created by overturning convective cells at the boundaries (see Viallet et al. 2013 for a detailed description). As demonstrated by Meakin & Arnett (2007) for stellar convection, turbulent entrainment can be characterized in terms of the bulk Richardson entrainment law

$$\frac{v_{\rm e}}{v_{\rm rms}} = A\,\mathrm{Ri}_{\rm B}^{-n}, \tag{17}$$

where $v_{\rm e}$ is the entrainment velocity of the top or bottom convective boundary, $v_{\rm rms}$ the rms velocity in the convection zone, and $\mathrm{Ri}_{\rm B}$ the bulk Richardson number (see Eq. (6)). For the results presented in the following, we have checked by visually inspecting the time evolution of the density and boundary profiles that $v_{\rm e}$ is dominated by mass entrainment and the impact of thermal expansion is negligible. The analysis with respect to Eq. (17) is reported in various other studies which generally find an agreement with the measured entrainment (e.g., Gilet et al. 2013, Müller et al. 2016, C+17, C+19, Higl et al. 2021). In the following, we extend these studies for the case of helium shell burning.

By fitting Eq. (17) to simulations of mixing across boundaries at different $\mathrm{Ri}_{\rm B}$, the value of A and n can be determined. In shell simulations, this is possible either by measuring the entrainment at the bottom and top boundary in a single simulation (different $\mathrm{Ri}_{\rm B}$ because of different BVF profiles, e.g., C+17), by measuring entrainment in simulations with different convective driving (different $\mathrm{Ri}_{\rm B}$ because of varying $v_{\rm rms}$), or both (e.g., C+19).

To extract meaningful results, such simulations need to be run for multiple convective turnover times. Furthermore, as pointed out by Woodward et al. (2015), the resolution must be sufficiently high for obtaining converged entrainment rates across the boundaries. To relate the different grid sizes that have been used in the aforementioned studies, we compare the number of vertical grid cells ($\#_{\rm CZ}$) that are located within the convection zones. Only grids that have been used to derive an entrainment rate are considered here. This simple comparison neglects the impact of restricted domains and does not consider the different stiffness of transitions from stable to convection

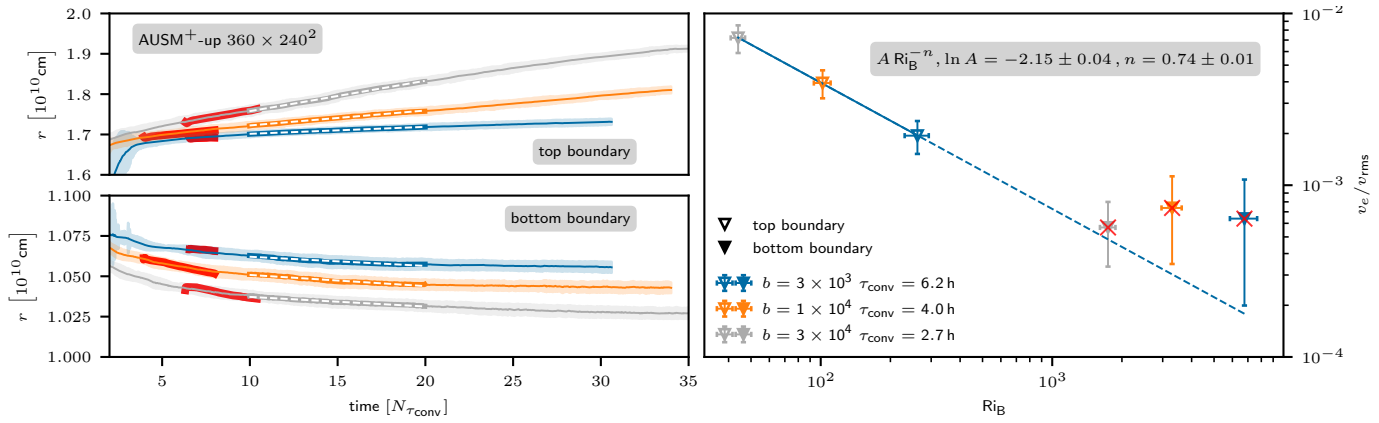

Fig. 16. *Left plots:* radial positions of the top and bottom boundaries as functions of multiples of the respective convective turnover times. The radial position is the average position over all angles, the shading marks the corresponding spatial standard deviation of the boundary position. The white dashed lines indicate the time frame considered to obtain the data for the right column. Thick red lines show the evolution of simulations with a grid size of 360×240^2 cells for comparison. The scales of the y-axis for the top and bottom boundary have been adapted for better visibility. All simulations apply the AUSM$^+$-up scheme while the nuclear energy release is boosted by factors of 3×10^3, 1×10^4, and 3×10^4. *Right plot:* ratio of entrainment velocity v_e and rms velocity v_{rms} as a function of the bulk Richardson number Ri_B for the simulations shown in the left column. The horizontal error bars indicate the standard deviations of the temporal means of Ri_B. Vertical error bars correspond to the standard deviations of the entrainment velocities for a sliding window of size $\Delta N_{\tau_{conv}} = 1$. The time frame is large enough to filter out sound waves but it is somewhat arbitrary. However, the error bars give an idea of the spread in the entrainment velocity. Markers that are crossed are not considered for fitting Eq. (17) to the data. The fit is shown as solid blue line. The dashed line at high Ri_B marks the regime of extrapolation.

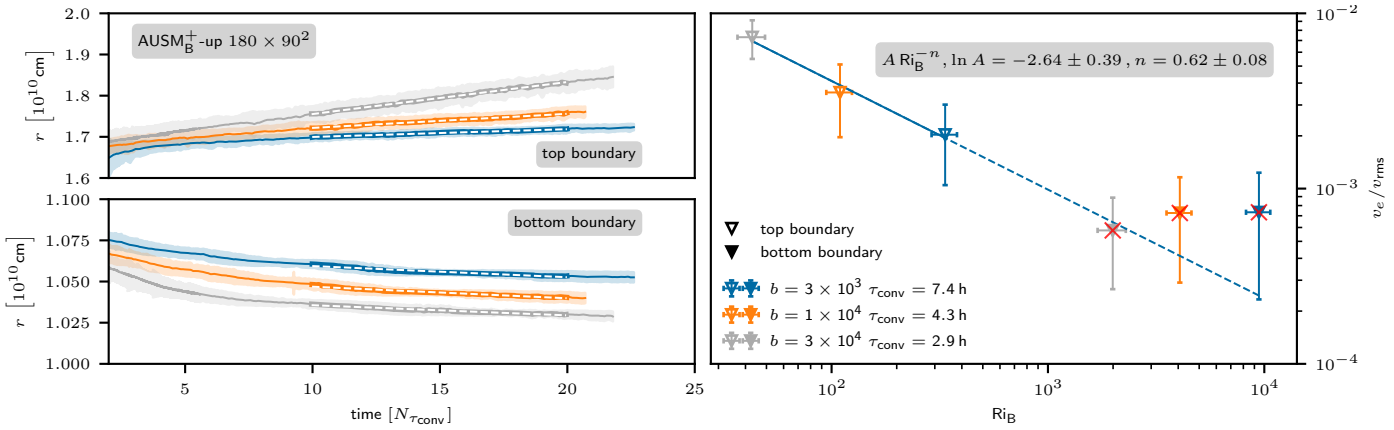

Fig. 17. Same as Fig. 16 but for simulations using the AUSM^+_B-up solver.

zones. However, it still gives an estimate of the scales that are resolved by the grid compared to the global scale of the convection zone. Woodward et al. (2015) find entrainment rates that are in reasonable agreement for simulations with $\#_{CZ} = 219$ (grid sizes of 768^3) and more cells. Most of the simulations presented by Jones et al. (2017) have $\#_{CZ} = 170$, while they show for one particular case that entrainment agrees with the results of a simulation with $\#_{CZ} = 341$ (grid sizes of 768^3 and 1536^3, respectively). The highest resolution used by C+17 to determine the entrainment rate has $\#_{CZ} = 256$ (for a grid of 512^3). Our computational resources only allow to run simulations long enough on grids with 180×90^2 cells which corresponds to $\#_{CZ} = 105$. This resolution might not be sufficient and we cannot test whether the results presented in this section are converged. However, our analysis still provides a first glimpse on what coefficients might be expected for the He-shell burning. Moreover, we are able to compare the results from the low-Mach AUSM$^+$-up solver to AUSM^+_B-up and assess whether the bulk Richardson scaling can be reproduced even at low resolution.

We determine the entrainment rate v_e in Eq. (17) from the mean radial position over time of the top and bottom boundary, respectively. The positions of the boundaries are extracted as described in Sect. 5.1, the values for v_{rms} consider the entire convection zone.

The plots on the left of Fig. 16 show the evolution of the boundary positions for the boosting factors 3×10^3, 1×10^4, and 3×10^4 when using the AUSM$^+$-up solver. Qualitatively, the behavior is as expected: A higher boosting factor leads to stronger convection, faster entrainment of the passive scalar, and thus to a faster moving boundary. The entrainment velocity at the bottom boundary is considerably smaller than at the top boundary. According to Eq. (17) this is expected for a larger value of Ri_B which is indeed confirmed in the right panel, where the data for the bottom boundary reside at $Ri_B > 10^3$. A similar situation is observed for simulations with the AUSM^+_B-up solver, shown in Fig. 17.

In order to fit Eq. (17) to the data, we consider the time frame of $t \in [t(N_{\tau_{conv}} = 10), t(N_{\tau_{conv}} = 20)]$. The lower limit is given by the end of the initial transient in the evolution of the

Table 4. Summary of the basic properties of the simulations shown in Figs. 16 and 17.

Boosting factors	3×10^4		1×10^4		3×10^3	
num. flux function	AUSM$^+$-up	AUSM^+_B-up	AUSM$^+$-up	AUSM^+_B-up	AUSM$^+$-up	AUSM^+_B-up
$\tau_{\rm conv}$ [h]	2.69	2.86	3.96	4.32	6.21	7.40
$v_{\rm e}^B$ $\left[10^2\,{\rm cm\,s^{-1}}\right]$	−6.14	−6.05	−4.86	−4.52	−2.54	−2.55
$v_{\rm e}^T$ $\left[10^3\,{\rm cm\,s^{-1}}\right]$	7.80	7.60	2.60	2.20	0.77	0.71
$v_{\rm e}^T/v_{\Delta s}$	0.45	0.54	0.39	0.52	0.34	0.41
$u_{\rm cell}^B$ $\left[{\rm cell}\,\tau_{\rm conv}^{-1}\right]$	−0.10	−0.10	−0.11	−0.12	−0.09	−0.11
$u_{\rm cell}^T$ $\left[{\rm cell}\,\tau_{\rm conv}^{-1}\right]$	1.23	1.28	0.61	0.56	0.28	0.31
$v_{\rm rms}$ $\left[10^6\,{\rm cm\,s^{-1}}\right]$	1.08	1.04	0.66	0.62	0.40	0.35
${\rm Ri}_{\rm B}^B$ $\left[10^3\right]$	1.74	1.99	3.29	4.07	6.76	9.44
${\rm Ri}_{\rm B}^T$ $\left[10^2\right]$	0.44	0.43	1.02	1.09	2.62	3.35

Notes. All data is obtained by considering a time interval of $\Delta N_{\tau_{\rm conv}} = 10$. Legend: $\tau_{\rm conv}$: mean convective turnover time. $v_{\rm e}^B$, $v_{\rm e}^T$: entrainment velocities at the bottom and top boundary. $v_{\rm e}^T/v_{\Delta s}$: Ratio of the entrainment velocity at the top boundary to the velocity estimated by a general entropy increase within the convection zone, see text and Eq. (21). $u_{\rm cell}^B$, $u_{\rm cell}^T$: number of vertical grid cells crossed by the bottom (top) boundary over the period of one $\tau_{\rm conv}$. $v_{\rm rms}$: rms velocity in the convection zone. ${\rm Ri}_{\rm B}^B$, ${\rm Ri}_{\rm B}^T$: bulk Richardson number at the bottom and top boundary.

passive scalar. The length of the shortest simulations constitutes the upper limit, such that the same time frame can be used for both sets of simulations. The extracted values listed in Table 4 reveal that the bottom boundaries move only by about one cell during the entire considered time frame of $\Delta N_{\tau_{\rm conv}} = 10.0$. This indicates that our grid is not fine enough to properly track this subtle shift, which is also suggested from the thin boundary widths measured for the bottom boundary, see Sect. 5.6. An additional complication arises by the profile of energy generation (Fig. 2) which has its peak beneath the convection zone. Because we do not increase the efficiency of radiative diffusion in accordance with the artificial boosting, internal energy will accumulate below the convection zone. This leads to a local increase in the BVF and the boundary gets stiffer. Hence, the entrainment velocity decreases when the bottom boundary approaches the peak of the energy generation. Because of this artificial phenomenon and the unresolved boundary motion we exclude the data points of the bottom boundaries from the analysis.

Using a least-square fit of Eq. (17) to the extracted data, we find

$$\begin{aligned} \ln A_{\rm A^+\text{-up}} &= -2.15 \pm 0.04, & n_{\rm A^+\text{-up}} &= 0.74 \pm 0.01, \\ \ln A_{\rm A^+_B\text{-up}} &= -2.64 \pm 0.39, & n_{\rm A^+_B\text{-up}} &= 0.62 \pm 0.08, \end{aligned} \tag{18}$$

where the errors correspond to the standard deviation of the fitting parameters. We note that the errors are obtained without taking the individual error bars shown in Figs. 16 and 17 into account. The standard deviation in ${\rm Ri_B}$ and the spread in the entrainment velocity are likely correlated between some of the data points and subject to systematic shifts. Therefore, we think a treatment in terms of proper error propagation could be misleading. The error bars are shown nonetheless in the figures to give an idea of the general variability of the data points. The small uncertainties given in Eq. (18) thus indicate only that our data is well represented by Eq. (17) but should not be taken as a measure of the overall accuracy of our analysis.

The results with the AUSM$^+$-up and AUSM^+_B-up schemes are similar, but the dependence of the entrainment on the bulk Richardson number is somewhat steeper for AUSM$^+$-up. As a rough test for convergence, the set of simulations with the AUSM$^+$-up solver has been restarted after the initial transient on grids with a resolution of 360×240^2. The flow state is interpolated to the finer grids using constant interpolation. The corresponding tracks of the radial boundary positions are shown as thick red lines in Fig. 16. For the top boundary, the entrainment rate is similar to the low resolution runs. At the bottom boundaries, entrainment appears to be slightly faster. Generally, the better resolved simulations follow a similar trend as the low resolution runs. However, more data is needed for a stronger statement on convergence and to extract meaningful estimates for A and n also from the better resolved simulations. Another parameter that impacts the results is the considered time interval. Using the full data of the AUSM$^+$-up runs shown in Fig. 16, we extract the parameters A and n for a fixed length of $\Delta N_{\tau_{\rm conv}} = 5$ but for a changing central time (Fig. 18). We find that the value of the exponent n increases from $n \approx 0.4$ and settles to a value of $n \approx 0.75$ for central times later than $t\,(N_{\tau_{\rm conv}} = 20)$. The value of $\ln A$ changes in a very similar way from $\ln A \approx -3.5$ to $\ln A \approx -2.5$. Figure 18 reveals that the values settle after central $N_{\tau_{\rm conv}} \approx 20$. Therefore, it seems more appropriate to consider the time interval of $t \in [t\,(N_{\tau_{\rm conv}} = 17.5)\,, t\,(N_{\tau_{\rm conv}} = 25)]$ to determine best-fitting values of A and n. The upper limit is given by the time the top boundary reaches the top of the computational domain and boundary conditions will start to affect the results. We obtain

$$\ln A_{\rm A^+\text{-up}} = -2.24 \pm 0.45, \qquad n_{\rm A^+\text{-up}} = 0.76 \pm 0.10, \tag{19}$$

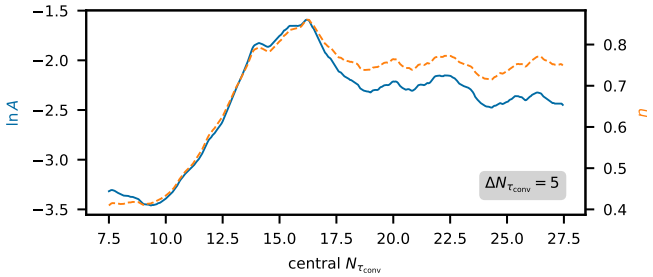

Fig. 18. Time evolution of the fit parameters A (blue solid line) and n (orange dashed line) for a fixed time frame of $\Delta N_{\tau_{\rm conv}} = 5$ and moving central time.

see also Fig. B.4. These values are similar to the previous result. However, considering the peak in the evolution in Fig. 18 between $N_{\tau_{\rm conv}} = 10$ and $N_{\tau_{\rm conv}} = 20$, this might be a coincidence. There is not sufficient data for the simulations with the AUSM$^+_{\rm B}$-up solver to repeat this calculation but we expect it to show a similar trend.

The results given in Eqs. (18) and (19) are within the regime $0.5 \leq n \leq 1$, which is compatible with values reported in laboratory and numerical experiments (see, e.g., Meakin & Arnett 2007 and C+17 for a discussion and corresponding references). Our fitting parameters are similar to the findings of C+19 for the carbon shell. They obtain parameters[3] of $\ln A_{\rm C19} = -2.98 \pm 0.13$ and $n_{\rm C19} = 0.74 \pm 0.04$. In contrast, Meakin & Arnett (2007) report $\ln A_{\rm M07} = 0.062 \pm 0.87$ and $n_{\rm M07} = 1.05 \pm 0.21$ and also the results of Jones et al. (2017) and Andrassy et al. (2020) agree with an exponent of $n \approx 1$, as pointed out by Müller (2020). Further simulations are needed to scrutinize the values of A and n, also keeping in mind that different values may exist for different stellar convection zones.

Combining the results of Eq. (19) with the MLT prediction of $\mathrm{Ma}_{\rm MLT} \approx 10^{-4}$ and $\mathrm{Ri}_{\rm B} = 7 \times 10^4$ for the 1D MESA model, we find a mass entrainment rate of

$$\dot{m}_e = 4\pi r^2 \rho \, \mathrm{Ma}_{\rm MLT} \, c_{\rm sound} \, A \mathrm{Ri}_{\rm B}^{-n} = 9.6 \times 10^{-11} \, M_\odot \, \mathrm{s}^{-1}, \quad (20)$$

for the top boundary. The value for the bottom boundary is about a factor ten smaller. This confirms the finding of previous 3D hydro simulations (e.g., C+17) that lower boundaries of convective shells are stiffer and thus have less entrainment than the top boundaries. The associated growth of the convective region at the upper and lower boundaries using these rates until the end of the evolution is indicated by green lines in Fig. 1. This illustrates that, while the much stiffer lower boundary only slightly changes, the upper boundary considerably moves outward. At the rate of the mass entrainment of Eq. (20), the total mass of the initial convection zone of 1.1 $M_\odot$ is doubled within 350 yr. However, a substantial growth of the convection zone leads to different bulk Richardson numbers at the boundaries and thus change the mass entrainment rate. Moreover, as seen in Fig. 1, the convection zone is growing also in the 1D evolution calculation. The mass entrainment rate given in Eq. (20) is therefore only representative for a short fraction of the shell's lifetime at the evolutionary time the simulation was calculated. It is also a warning that one cannot simply use numerical values like entrainment rates extracted from single 3D simulations and apply them at different phases of stellar evolution. Instead, it is best to use theoretical prescriptions like the entrainment law. Recently, 1D stellar evolution models using the entrainment law on the main-sequence have been computed by Scott et al. (2021) and better reproduce the mass dependence of the main-sequence width. New 1D models during other phases of stellar evolution will be needed to assess the ability of the entrainment law to represent convective boundary mixing in 1D models throughout stellar evolution.

The expansion of the convection zone seen in the 1D evolution is part of a global restructuring of the star after core helium burning. Turbulent entrainment does not contribute as it is not included in our 1D calculation. However, the growth may be attributed to a process that is likely also present in our hydrodynamic simulations: In a simplified picture, the heating through nuclear burning successively increases the entropy within the convection zone. This leads to a small region at the top boundary where it exceeds the entropy at the immediate beginning of the radiation zone. This region is unstable and will merge with the convection zone. We estimate the speed $v_{\Delta s}$ at which this process would move the outer boundary by

$$v_{\Delta s} = \left(\frac{\Delta s_{\rm CZ}}{\Delta t}\right) \Big/ \left(\frac{\Delta s_{\rm RZ}}{\Delta r}\right), \quad (21)$$

where $\Delta s_{\rm CZ}/\Delta t$ is the ratio of the mean temporal increase in entropy inside the convection zone and $s_{\rm RZ}/\Delta r$ corresponds to the mean entropy gradient at $t = 0$ for a region above the top boundary. For the simulation with the highest boosting that was used to obtain the results in Eq. (19) we find a ratio of

$$\frac{v_{\Delta s}}{v_{\rm e}^T} \approx 60\%, \quad (22)$$

where $v_{\rm e}^T$ is the entrainment velocity at the top boundary as measured from the advected passive scalar. The considered profiles to calculate $v_{\Delta s}$ are plotted in Fig. 19, the spatial entropy gradient is calculated considering the initial model. The ratios of our other simulations range between 30% to 50% and are listed in Table 4. This is similar to the value of 49% found by Andrassy et al. (2020) for carbon-shell burning while Meakin & Arnett (2007) find a maximum ratio of 17% for oxygen shell burning[4]. These values suggest that a considerable fraction of the entrainment speed could be contributed through increasing entropy. Consequently, this process needs to be disentangled from the growth through turbulent entrainment before the entrainment according to Eq. (17) is used in stellar evolution codes or compared between simulations of different convection zones.

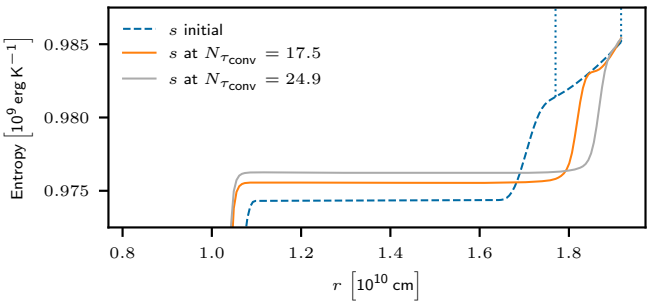

Fig. 19. Initial entropy profile and profiles after 17.5 and 25 convective turnover times for the 3D simulation with a grid of 180×90^2 cells, the AUSM$^+$-up solver, and an energy boosting of $b = 3 \times 10^4$. Vertical dotted lines mark the region that is considered to calculate the mean entropy gradient in the radiation zone $\Delta s_{\rm RZ}/\Delta r$ from the initial entropy profile.

5.5. Characterizing the mixing

It is not trivial to determine the details of the – possibly small-scale – events that lead to turbulent mixing. In their PPMstar

[3] We note that the value and error of A given in their Fig. 14 mix linear (for A value) and logarithmic (for the uncertainty) scales. The values presented here are recalculated from the same data set in terms of the natural logarithm.

[4] It is not clear to us whether Meakin & Arnett (2007) calculated the spatial entropy gradient in the radiation zone or at the transition from convection to radiation zone. In the latter case, the gradient is much steeper, the estimated velocity will be smaller, and we would obtain a ratio similar to that of Meakin & Arnett (2007). However, we think that only the gradient above the boundary transition is relevant.

simulations, Woodward et al. (2015), Jones et al. (2017), and Andrassy et al. (2020) find that trains of small Kelvin-Helmholtz rolls emerge at the boundary. However, they do not appear in regions of largest shear but rather at the point where two convective cells turn and move back into the convection zone.

From our 2D visualizations we are not able to easily find large scale, coherent modes. In order to identify possible correlations between the strength of shear and the amount of mixing in our simulations, we use a simple analysis of the velocity field at the top boundary: For a narrow region below the top boundary, we measure along radial rays the volume-weighted deviation of the passive scalar from its mean in the convection zone

$$\widetilde{\mathrm{PS}}(\vartheta,\varphi) = \frac{\sum_{r\in[r_{\mathrm{PS}},r_{\mathrm{P}}]} V(r,\vartheta,\varphi)\left[\mathrm{PS}(r,\vartheta,\varphi) - \overline{\mathrm{PS}}(\vartheta,\varphi)\right]}{\sum_{r\in[r_{\mathrm{PS}},r_{\mathrm{P}}]} V(r,\vartheta,\varphi)}, \tag{23}$$

where PS denotes the value of the passive scalar, $\overline{\mathrm{PS}}(\varphi,\vartheta)$ is the average over the middle third of the convection zone, and V the volume of the grid cell. The radii r_{PS}, r_{P} define the considered radial domain, where r_{P} corresponds to the beginning of the transition to the stable zone at the top of the convection zone, as defined in Sect. 5.6 and $r_{\mathrm{PS}} = 0.95\, r_{\mathrm{P}}$. The value of the passive scalar is larger above the top boundary compared to its mean (see Fig. 6). Hence, a positive deviation from the mean corresponds to an entrainment event. The considered domain does not include mixing directly at the boundary because there, deviations are usually large but do not necessarily descend into the convection zone.

In addition, we estimate the strength of shear by

$$S_h(\vartheta,\varphi) = \int_{r_{\mathrm{PS}}}^{r_{\mathrm{S}}} \sqrt{\left(\partial_r v_\varphi\right)^2 + \left(\partial_r v_\vartheta\right)^2}\,\mathrm{d}r, \tag{24}$$

where v_ϑ, v_φ denotes the ϑ,φ-velocity components. Because the shear at the boundary matters here, we extend the considered zone to r_{S} which coincides with the end of the transition to the radiation zone as defined in Sect. 5.6. The different regions are indicated in Fig. 20. With the described procedure we obtain data pairs that correlate shear strength to mixing strength. Our simple approach does not consider that the mixing events will also depend on the history of the velocity field and its gradient along the individual downflows. However, it still gives some measure of the correlation between shear and mixing: The characteristic time scale for global changes of the flow field is given by the turn over time. The animated versions[5] of Fig. 20 illustrate that the mixing events detected between the dashed-dotted line and the dashed line happen on time scales which are much shorter. If the mixing were caused by Kelvin-Helmholz instabilities overturning the whole boundary layer one may assume that they grow fastest in regions of strongest shear. We then would expect the rapidly-growing Kelvin-Helmholz rolls to become detectable in the layer where we measure $\widetilde{\mathrm{PS}}$ after a fraction of the global turnover time scale. However, the shear layers caused by the overturning of the large scale flows at the convective boundary should be present for as long as the global turnover time scale. The extracted data pairs can therefore be used to investigate a possible correlation between shear strength and mixing.

The result for the AUSM$^+$-up solver at a resolution of 180×90^2 is shown in Fig. 21 for increasing energy boostings. In all simulations, the counts of positive passive scalar fluctuations cluster at the lower end of the measured shear strength range. At slightly negative deviations, a narrow band with a

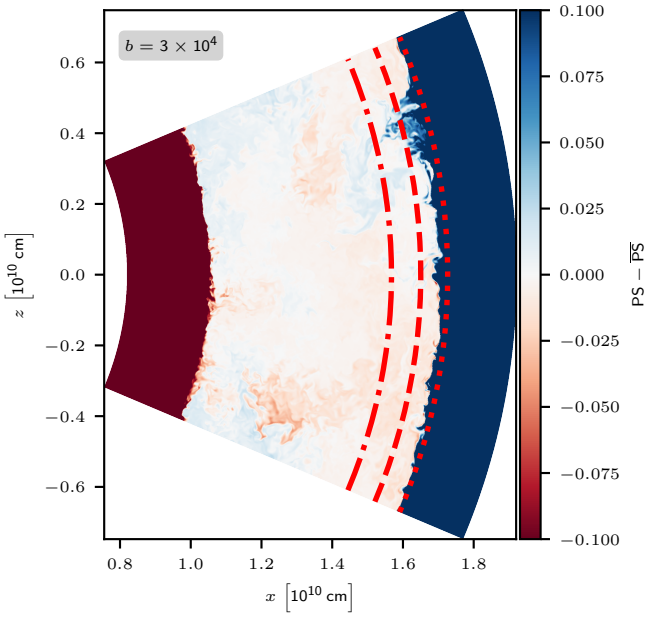

Fig. 20. Fluctuations of the passive scalar PS from its mean value $\overline{\mathrm{PS}}$ for a snapshot of the 3D simulation at a resolution of 810×540^2 cells and a boosting factor of 3×10^4. The mean $\overline{\mathrm{PS}}$ is taken over the inner third of the convection zone. The dashed-dotted line corresponds to r_{PS}, the dashed line to r_{P} and the dotted line to r_{S}. Their meanings are explained in the main text.

high number of counts forms which stretches over a larger range of shear strengths. As indicated by the blue lines, at smaller shear strengths mixing events dominate over "no mixing" events. The noisy profile at the strongest shear can be attributed to the small number of total counts (thin line) and corresponding poor statistics.

The evidence of mixing at the lower end of the range is in line with the fact that the horizontal velocity naturally has to decrease where strong downflows form because the velocity is redirected inward there. The narrow band corresponds to rays with no mixing events such that the contained passive scalar is slightly below but very close to the average within the convection zone. If the energy boosting is increased, convection gets more vigorous and hence the narrow band extends toward larger shear strengths. Mixing follows this trend, but still dominantly appears at lower shear strengths. By visually inspecting the flow morphology of their 3D simulations, Woodward et al. (2015) find that mixing predominately occurs in regions where two large convective cells meet and overturn. The premixed material that accumulates in the wedge between two cells somewhat beneath the boundary has a sufficiently small buoyancy force with respect to the bulk of the convection zone such that the downflows are strong enough to bring the material inward. Because of the decreasing horizontal velocity of the turning cells, this premixed region will necessarily have weaker shear (as measured by Eq. (24)) compared to the region where the fluid moves almost horizontally. The results of our analysis seem to support this picture.

In Fig. 22 we compare in a similar histogram the results of the AUSM$^+$-up and AUSM$^+_{\mathrm{B}}$-up solver at the runs with highest resolution. The direct comparison shows that shear values spread over a larger range for the AUSM$^+$-up solver, which can be attributed to its better-resolved turbulent flow (see Figs. 9 and 10). The AUSM$^+_{\mathrm{B}}$-up solver shows slightly stronger mixing events. The apparent return toward positive deviations at large

[5] https://zenodo.org/record/4776452

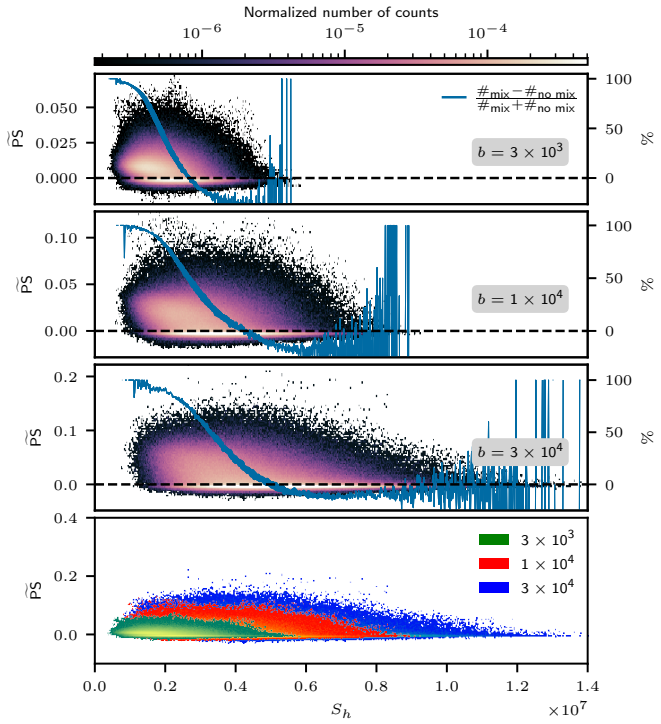

Fig. 21. Histogram of fluctuations of the passive scalar $\widetilde{PS}$ (Eq. (23)) as a function of shear strength for simulations with the AUSM$^+$-up solver and a resolution of 180×90^2. The boosting strength increases from top to bottom. The *lowest panel* combines all three histograms to ease the direct comparison. The values of fluctuations and shear strengths are extracted in a narrow band below the top boundary of the convection zone, as illustrated in Fig. 20. The histograms are normalized by the total number of counts, that is the number of horizontal grid cells multiplied by the number of considered grid files. The blue lines indicate the relative excess of mixing events (positive passive scalar fluctuation) or "no mixing" events (negative passive scalar fluctuation) relative to the total number of events for the respective shear strength. The width of the lines is scaled linearly with the relative contribution of the counts at the respective shear strength to the global number of counts. A thick line therefore indicates a significant contribution while the thin lines at very small and large shear strengths indicate a negligible contribution to the total amount of events. The considered time frame is $t \in [t\,(N_{\tau_{\text{conv}}} = 17.5)\,,\, t\,(N_{\tau_{\text{conv}}} = 25)]$.

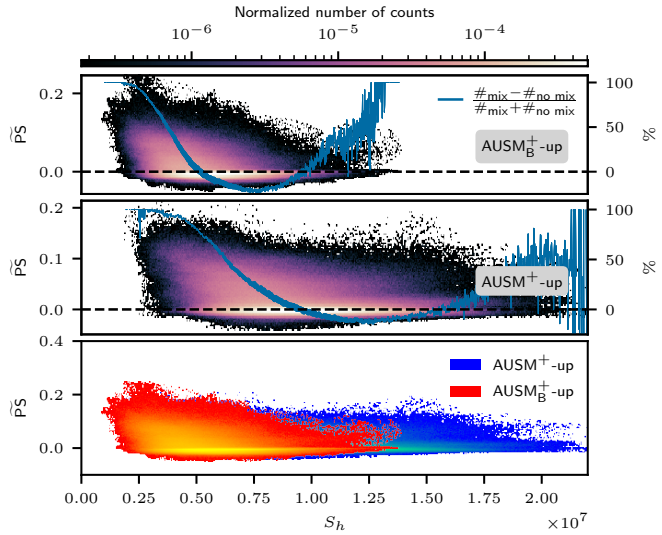

Fig. 22. Same as Fig. 21, but here for the AUSM$_{\text{B}}^{+}$-up (*top panel*) and AUSM$^+$-up (*bottom panel*) solver at a resolution of 810×540^2 and an energy boosting of 3×10^4. The considered time frame spans over $\Delta N_{\tau_{\text{conv}}} = 0.5$, including the respective latest snapshot of each run.

shear is insignificant due to the small number of total counts at larger shear, as indicated by the thin line.

5.6. Boundary width

Another characteristic of convection is the shape of the boundary layers between the convection zone and the convectively stable zones. While the boundary width has to be parametrized in 1D stellar evolution codes, it develops self-consistently in hydrodynamic simulations. As can be seen in Fig. 6, the transition that forms during the simulation is not sharp but rather changes gradually across a certain vertical width. This is due to at least two processes. The first, and most important, is partial mixing across the boundary layer by turbulent entrainment. The second, which is less important in the simulations presented in this study, is the deformation of the boundary layer producing an undulated surface rather than a perfectly spherical surface. Neither of these processes exist in most 1D models, which generally assume a sharp step-like boundary. The exception is 1D models using partial mixing beyond the convective boundary such as the prescriptions of exponentially decaying mixing by Freytag et al. (1996) and Herwig et al. (1997).

Comparisons to asteroseismology (e.g., Moravveji et al. 2016; Arnett & Moravveji 2017; Michielsen et al. 2019; Pedersen et al. 2021) also support smoother over step-like boundaries. More work is needed to better understand the shape boundaries since they can have a decisive impact on the evolution and nucleosynthesis (e.g., Battino et al. 2016).

In this section we compare the transition layer widths for simulations with different resolutions, flux solvers and boostings. Our approach to extract the widths is similar to the procedure described by C+17 but instead of abundance profiles we use the passive scalar as tracer. We define the inner radii of the transitions at the bottom (top) of the convection zone as the radii at which the horizontal mean of the passive scalar is larger than its initial value at this radius plus (minus) 0.05. The outer radius of the transitions at the bottom (top) is taken to be the radius at which the horizontal mean of the passive scalar is below (above) the spatial mean over the inner third by 0.05. To determine the corresponding radii, the profile of the passive scalar is interpolated. The resulting widths are shown exemplarily in Fig. 6, marked by vertical dashed lines. The absolute value of the width depends on the particular choice of the thresholds for the deviations from the initial profile. However, it still gives a measure for the relative dependence on resolution, boosting strength and numerical flux solver. We have verified that the trends found for the boundary widths do not depend on the specific choice of the threshold value.

In Table 5 the resulting widths are listed for simulations applying the AUSM$_{\text{B}}^{+}$-up and AUSM$^+$-up solver at a fixed resolution of 180×90^2 for varying boosting strength. We find that generally the top boundary width is larger than the bottom boundary. This is in line with the much higher bulk Richardson number at the bottom boundary (Table 4). The top boundary broadens with increasing energy input because stronger driving leads to stronger convection and eventually to enhanced mixing that reaches further into the stable zone. In addition, the interface gets more deformed. This is in accordance with the results reported by C+17. Also the transition of the bottom boundary widens with increasing driving and is generally narrower for runs

Table 5. Boundary widths of the bottom and top boundaries for different energy boosting factors at a resolution of 180×90^2 cells.

Boost	AUSM^+_B-up		AUSM$^+$-up	
	$\delta_{r,\mathrm{bot}}$	$\delta_{r,\mathrm{top}}$	$\delta_{r,\mathrm{bot}}$	$\delta_{r,\mathrm{top}}$
	$[10^8\ \mathrm{cm}]$		$[10^8\ \mathrm{cm}]$	
3.0×10^3	1.57 ± 0.07	5.27 ± 0.22	2.11 ± 0.11	3.70 ± 0.05
1.0×10^4	1.72 ± 0.07	6.51 ± 0.37	2.25 ± 0.08	4.51 ± 0.12
3.0×10^4	1.93 ± 0.06	8.88 ± 0.37	2.30 ± 0.09	5.71 ± 0.33
	$\delta_{r,\mathrm{bot}}$	$\delta_{r,\mathrm{top}}$	$\delta_{r,\mathrm{bot}}$	$\delta_{r,\mathrm{top}}$
	$[10^{-2}\ \mathrm{H_p}]$		$[10^{-2}\ \mathrm{H_p}]$	
3.0×10^3	5.58 ± 0.25	15.41 ± 0.63	7.52 ± 0.40	10.81 ± 0.15
1.0×10^4	6.17 ± 0.24	18.94 ± 1.07	8.11 ± 0.29	13.13 ± 0.36
3.0×10^4	7.01 ± 0.23	25.63 ± 1.08	8.40 ± 0.31	16.48 ± 0.96

Notes. The upper set shows the widths in units of cm while the lower set shows the widths in terms of the mean pressure scale height over the boundary width. The values are averages taken over a time interval of $\Delta N_{\tau_{\mathrm{conv}}} = 10$, starting at $t\,(N_{\tau_{\mathrm{conv}}} = 10)$. Errors correspond to the standard deviation of the temporal averages.

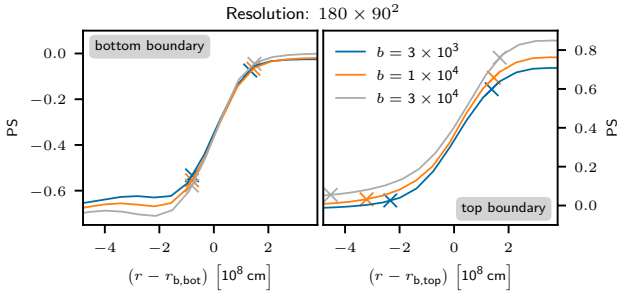

Fig. 23. Profiles of the advected passive scalar for different energy input boostings. All simulations use the AUSM$^+$-up solver. The profiles are taken at $t\,(N_{\tau_{\mathrm{conv}}} = 15)$, crosses denote the beginning and end of the boundary transition zone, as defined in the text. Following the approach of C+17, the profiles are shifted by the radial position of the bottom ($r_{b,\mathrm{bot}}$) and top ($r_{b,\mathrm{top}}$) boundary, respectively. The different amplitudes of the passive scalar below the bottom and above the top boundary are due to the fact that the initial profile is linear, see Fig. 6. Larger boosting leads to faster entrainment and the top boundary will have already moved toward larger radii, that is larger values of the passive scalar, for the snapshot shown in Fig. 23.

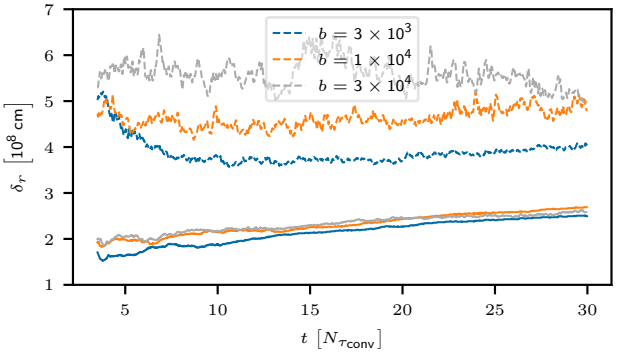

Fig. 24. Widths of the upper (dashed lines) and lower (solid lines) boundary for different strengths of the energy generation boosting as a function of convective turnover times τ_{conv}. All simulations use the AUSM$^+$-up flux.

with the AUSM^+_B-up solver. However, because of the stiffness of the bottom boundary, changes are only subtle. With a radial grid spacing of about $0.6{\times}10^8$ cm, the bottom boundaries are resolved by a few cells only. The relative changes are even on the subgrid level and can only be followed by interpolation. Hence, the robustness of these results is difficult to assess.

Figure 23 illustrates the boundary widths for one particular point in time. This is similar to Fig. 12 of C+17 for the carbon-burning shell simulations: For the top boundary, the broadening with increasing energy input is clearly visible but it is less obvious at the bottom boundary.

The time evolution of the boundary widths is shown in Fig. 24. The upper transition exhibits some variability over time with an amplitude that increases with the driving strength. Almost no fluctuations are visible for the bottom boundary. A slight trend toward shallower transitions is noticeable. These results confirm the general dependence of the boundary width on the stiffness and driving strength.

To assess the impact of resolution, we compare the widths at a boosting factor of 3×10^4 for simulations on successively finer grids in Table 6. Because the finer resolved simulations cover less convective turn over times, the averages are taken at earlier times compared to the data listed in Table 5.

For both flux functions we find that the widths of the upper boundary noticeably decrease when the grid is refined from a resolution of 180×90^2 to 360×180^2. For even finer grids, the width changes only slightly, which is confirmed in the boundary profiles shown in Fig. 25. While the results seem to be converged for the respective flux functions, there is still a discrepancy between the solvers at the bottom boundary which persists even for the highest resolution. This offset is much larger than the small fluctuations of the width for the lower boundary (Fig. 26). However, we note that the boundaries for the highest resolution runs need some time to adapt to the increased grid resolution and that boundary widths at early times may still change, as indicated in Fig. 24. Therefore, larger time intervals are needed for a stronger statement on the convergence.

6. Conclusion

Our study complements the exploration of convective boundary mixing in stellar interiors with multidimensional hydrodynamic simulations of convective helium-shell burning. The initial stratification is based on an 1D MESA model of a $25\,M_\odot$ star. Gilkis & Soker (2016) use the MAESTRO code to perform hydrodynamic simulations of convective helium-shell burning

Table 6. Boundary widths of the bottom and top boundaries for different resolutions and a boosting factor of 3×10^4.

Resolution	AUSM^+_B-up		AUSM$^+$-up	
	$\delta_{r,\mathrm{bot}}$	$\delta_{r,\mathrm{top}}$	$\delta_{r,\mathrm{bot}}$	$\delta_{r,\mathrm{top}}$
	$[10^8$ cm$]$		$[10^8$ cm$]$	
180×90^2	2.10 ± 0.03	7.22 ± 0.12	1.94 ± 0.04	5.65 ± 0.12
360×180^2	1.93 ± 0.08	5.35 ± 0.19	1.38 ± 0.03	4.41 ± 0.09
540×360^2	1.73 ± 0.04	4.88 ± 0.16	1.26 ± 0.04	4.76 ± 0.20
810×540^2	1.49 ± 0.04	4.60 ± 0.13	1.07 ± 0.03	4.61 ± 0.10
	$\delta_{r,\mathrm{bot}}$	$\delta_{r,\mathrm{top}}$	$\delta_{r,\mathrm{bot}}$	$\delta_{\mathrm{r,top}}$
	$[10^{-2}$ H$_\mathrm{p}]$		$[10^{-2}$ H$_\mathrm{p}]$	
180×90^2	7.52 ± 0.12	21.10 ± 0.34	6.96 ± 0.16	16.53 ± 0.35
360×180^2	6.90 ± 0.30	15.64 ± 0.55	4.94 ± 0.09	12.87 ± 0.27
540×360^2	6.17 ± 0.14	14.26 ± 0.47	4.48 ± 0.16	13.96 ± 0.57
810×540^2	5.30 ± 0.15	13.44 ± 0.39	3.83 ± 0.11	13.47 ± 0.29

Notes. Quantities have the same meaning as in Table 5. The values are averages over a time range of $\Delta N_{\tau_\mathrm{conv}} = 0.5$, the central time is $t\,(N_{\tau_\mathrm{conv}} = 4.2)$. Due to insufficient data, the central time is set to $t\,(N_{\tau_\mathrm{conv}} = 2.9)$ for the run with the AUSM$^+$-up solver at a resolution of 540×360^2 cells.

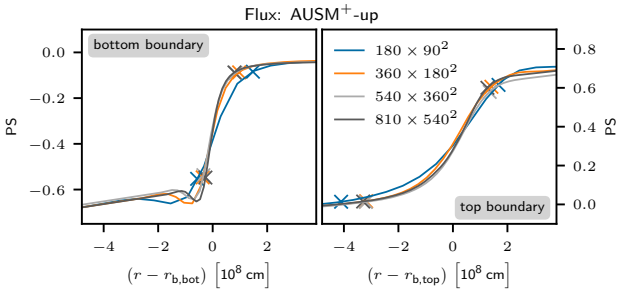

Fig. 25. Similar to Fig. 23 but for a fixed energy boosting factor of 3×10^4 and varying resolution. All simulations use the AUSM$^+$-up solver. The profiles are taken at $N_{\tau_\mathrm{conv}} = 4.5$, except for the run with a grid of 540×360^2 cells. Here, the profile is taken at $N_{\tau_\mathrm{conv}} = 3.1$, the latest available snapshot.

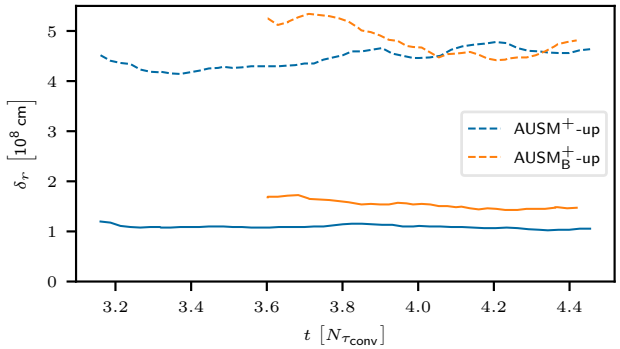

Fig. 26. Same as Fig. 24 but for a resolution of 810×540^2 and a fixed energy boosting of 3×10^4.

in a 15 $M_\odot$ star. Their study, however, focuses on the angular momentum distribution within the convection zone and the boundaries to stable layers above and below the convective shell are not analyzed in detail.

Our 2D and 3D hydrodynamic simulations in spherical-wedge geometry are performed with the time-implicit, finite-volume Seven-League Hydro (SLH) code. We calculate the hydrodynamic fluxes with the low-Mach AUSM$^+$-up scheme in combination with Cargo–LeRoux well-balancing. Because previous SLH simulations with this combination had shown that convection is represented properly only for Mach numbers above 10^{-3}, the energy input had to be boosted to increase the velocities. We applied boosting factors ranging from 3×10^3 to 3×10^4. This results in Mach numbers ranging from $\sim 5 \times 10^{-3}$ to $\sim 1 \times 10^{-2}$. The employed grid resolutions range from 180×90^2 cells up to 810×540^2 cells.

In order to assess the performance of the AUSM$^+$-up solver, we compare different diagnostic values to a variant of this scheme, denoted as AUSM^+_B-up, that does not employ the improved low-Mach capabilities. The flow morphology of fully developed convection at a resolution of 810×540^2 reveals that AUSM$^+$-up reproduces significantly more small-scale structures than the AUSM^+_B-up scheme (Fig. 10). This is confirmed by the corresponding kinetic energy spectrum (Fig. 9). The spectrum obtained with the AUSM$^+$-up scheme has an inertial range that reaches down to scales a factor of two smaller than in the spectrum for the AUSM^+_B-up scheme. The numerical dissipation as obtained from the RA-ILES kinetic energy equation shows an improved behavior at the bottom boundary and indicates that the dissipation is converged already at rather low resolution (Fig. 13). For the AUSM^+_B-up solver, convergence is found only at the highest resolution of 810×540^2 cells. These results indicate that a low-Mach method is beneficial already at moderate Mach numbers. In a future study, simulations of convection with the AUSM$^+$-up solver will be compared in detail to more widely used approaches, as, for example, to the PPM method.

We analyzed the entrainment rate at the boundaries of the convection zone in terms of the bulk Richardson number (Eq. (6)). For this, a series of simulations with varying boosting strength has been carried out on grids with 180×90^2 cells. We found an exponent of $n = 0.76$ (Fig. 16) which is compatible with C+17 and C+19 but smaller than results reported for example by Meakin & Arnett (2007) or Andrassy et al. (2020) who find $n \approx 1$. Furthermore, in our simulations a considerable fraction of the measured entrainment velocity may be attributed to entropy increase in the convection zone due to the energy release. This is an important aspect if the results of entrainment studies from hydrodynamic simulations are to be used in 1D calculations. Recently, the Bulk-Richardson entrainment scaling was applied to stellar evolution calculations (Staritsin 2013; Scott et al. 2021). Scott et al. (2021) show that it naturally leads to a mass-dependent

efficiency of CBM, which is suggested by observations. However, their study indicates that values of $n < 1$ result in a too efficient mixing and that the values for A that are commonly found in hydrodynamic simulations are too large. Future simulations, especially at nominal luminosity, may help to identify the origins of this discrepancy, also regarding the question whether it is applicable only to a subset of convection zones during stellar evolution as suggested by Viallet et al. (2015).

Measuring the widths of the transitions from the convection zone to the adjacent stable zones showed that the transition is wider for the 180×90^2 resolution compared with simulations on finer grids. This indicates that our results may not be numerically converged and that our higher-resolution simulations need to be continued to verify the robustness of our result for the entrainment rate. We further assessed the relation between shear strength and mixing events in our simulations and found that mixing occurs not in the regions of strongest shear but rather at lower values in the range of measured shear strengths (Fig. 21). This is consistent with the findings of Woodward et al. (2015).

Our study has demonstrated that the low-Mach AUSM$^+$-up solver is suitable to address setups that base on realistic stellar models if well-balancing is used. Recently, the Deviation well-balancing scheme of Berberich et al. (2021) was added to the SLH code. In simplified convective test simulations presented by Edelmann et al. (2021), the achieved Mach numbers reach Ma $\approx 10^{-4}$. These velocities are in the regime of convective velocities predicted by MLT in early evolutionary phases of stars. The combination of the new Deviation well-balancing method and the AUSM$^+$-up solver is a promising approach for future SLH simulations of stellar convection in the low-Mach regime without the need of artificially boosted energy generation.

Acknowledgements. L. H., F. K. R., and R. A. acknowledge support by the Klaus Tschira Foundation. The work of F. K. R. is supported by the German Research Foundation (DFG) through grants KL 566/22-1 and RO 3676/3-1, respectively. PVFE was supported by the US Department of Energy through the Los Alamos National Laboratory (LANL). LANL is operated by Triad National Security, LLC, for the National Nuclear Security Administration of the US Department of Energy (Contract No. 89233218CNA000001). The authors gratefully acknowledge the Gauss Centre for Supercomputing e.V. (www.gauss-centre.eu) for funding this project by providing computing time through the John von Neumann Institute for Computing (NIC) on the GCS Supercomputers JUQUEEN (Jülich Supercomputing Centre 2015) and JUWELS (Jülich Supercomputing Centre 2019) at Jülich Supercomputing Centre (JSC). This work also used the DiRAC@Durham facility managed by the Institute for Computational Cosmology on behalf of the STFC DiRAC HPC Facility (www.dirac.ac.uk). The equipment was funded by BEIS capital funding via STFC capital grants ST/P002293/1, ST/R002371/1 and ST/S002502/1, Durham University and STFC operations grant ST/R000832/1. DiRAC is part of the National e-Infrastructure. Furthermore, this article is based upon work from the "ChETEC" COST Action (CA16117), supported by COST (European Cooperation in Science and Technology). R. H. acknowledges support from the IReNA AccelNet Network of Networks, supported by the National Science Foundation under Grant No. OISE-1927130 and from the World Premier International Research Centre Initiative (WPI Initiative), MEXT, Japan. This work has been assigned a document release number LA-UR-21-22119. The authors thank Cyril Georgy for useful discussion in the early stages of this project and in particular for organizing the ISSI Team 367 meeting in 2018.

References

Aerts, C. 2021, Rev. Mod. Phys., 93, 015001
Almgren, A. S., Bell, J. B., & Zingale, M. 2007, J. Phys. Conf. Ser., 78, 012085
Andrassy, R., Herwig, F., Woodward, P., & Ritter, C. 2020, MNRAS, 491, 972
Angelou, G. C., Bellinger, E. P., Hekker, S., et al. 2020, MNRAS, 493, 4987
Arnett, W. D., & Moravveji, E. 2017, ApJ, 836, L19
Arnett, D., Meakin, C., & Young, P. A. 2009, ApJ, 690, 1715
Arnett, W. D., Meakin, C., Viallet, M., et al. 2015, ApJ, 809, 30
Arnett, W. D., Meakin, C., Hirschi, R., et al. 2018, ArXiv e-prints [arXiv:1810.04659]
Arnett, W. D., Meakin, C., Hirschi, R., et al. 2019, ApJ, 882, 18
Barsukow, W., Edelmann, P. V. F., Klingenberg, C., Miczek, F., & Röpke, F. K. 2017, J. Sci. Comput., 72, 623
Battino, U., Pignatari, M., Ritter, C., et al. 2016, ApJ, 827, 30
Berberich, J. P., Chandrashekar, P., & Klingenberg, C. 2021, Comput. Fluids, 104858
Cargo, P., & Le Roux, A. 1994, C.R. Acad. Sci., Ser 1, Math., 318, 73
Collins, C., Müller, B., & Heger, A. 2018, MNRAS, 473, 1695
Cristini, A., Meakin, C., Hirschi, R., et al. 2017, MNRAS, 471, 279
Cristini, A., Hirschi, R., Meakin, C., et al. 2019, MNRAS, 484, 4645
Cyburt, R. H., Amthor, A. M., Ferguson, R., et al. 2010, ApJS, 189, 240
Davis, A., Jones, S., & Herwig, F. 2019, MNRAS, 484, 3921
Edelmann, P. V. F. 2014, Dissertation (Technische Universität München)
Edelmann, P. V. F., Röpke, F. K., Hirschi, R., Georgy, C., & Jones, S. 2017, A&A, 604, A25
Edelmann, P. V. F., Horst, L., Berberich, J. P., et al. 2021, A&A, 652, A53
Fan, D., Nonaka, A., Almgren, A. S., Harpole, A., & Zingale, M. 2019, ApJ, 887, 212
Freytag, B., Ludwig, H. G., & Steffen, M. 1996, A&A, 313, 497
Gilet, C., Almgren, A. S., Bell, J. B., et al. 2013, ApJ, 773, 137
Gilkis, A., & Soker, N. 2016, ApJ, 827, 40
Goffrey, T., Pratt, J., Viallet, M., et al. 2017, A&A, 600, A7
Herwig, F., Bloecker, T., Schoenberner, D., & El Eid, M. 1997, A&A, 324, L81
Higl, J., Müller, E., & Weiss, A. 2021, A&A, 646, A133
Horst, L., Edelmann, P. V. F., Andrássy, R., et al. 2020, A&A, 641, A18
Hosea, M., & Shampine, L. 1996, Appl. Numer. Math., 20, 21
Jones, S., Andrassy, R., Sandalski, S., et al. 2017, MNRAS, 465, 2991
Jülich Supercomputing Centre, 2015, J. Large-scale Res. Facil., 1
Jülich Supercomputing Centre, 2019, J. Large-scale Res. Facil., 5
Kaiser, E. A., Hirschi, R., Arnett, W. D., et al. 2020, MNRAS, 496, 1967
Käppeli, R., & Mishra, S. 2016, A&A, 587, A94
Kifonidis, K., & Müller, E. 2012, A&A, 544, A47
Kolmogorov, A. N. 1941, Dokl. Akad. Nauk SSSR, 30, 299. in Russian
Landau, L. D., & Lifshitz, E. M. 1987, Fluid Mechanics (Course of Theoretical Physics: Volume 6), 2nd edn. (Oxford: Butterworth-Heinemann)
Liou, M.-S. 2006, J. Comput. Phys., 214, 137
Maeder, A. 2009, Physics, Formation and Evolution of Rotating Stars, Astronomy and Astrophysics Library (Berlin Heidelberg: Springer)
Meakin, C. A., & Arnett, D. 2007, ApJ, 667, 448
Michielsen, M., Pedersen, M. G., Augustson, K. C., Mathis, S., & Aerts, C. 2019, A&A, 628, A76
Miczek, F. 2013, Dissertation, Technische Universität München, Germany
Miczek, F., Röpke, F. K., & Edelmann, P. V. F. 2015, A&A, 576, A50
Mocák, M., Meakin, C., Viallet, M., & Arnett, D. 2014, ArXiv e-prints [arXiv:1401.5176]
Mocák, M., Meakin, C., Campbell, S. W., & Arnett, W. D. 2018, MNRAS, 481, 2918
Moravveji, E., Townsend, R. H. D., Aerts, C., & Mathis, S. 2016, ApJ, 823, 130
Müller, B. 2020, Liv. Rev. Comput. Astrophys., 6, 3
Müller, B., Viallet, M., Heger, A., & Janka, H.-T. 2016, ApJ, 833, 124
Nonaka, A., Almgren, A. S., Bell, J. B., et al. 2010, ApJS, 188, 358
Paxton, B., Bildsten, L., Dotter, A., et al. 2011, ApJS, 192, 3
Paxton, B., Cantiello, M., Arras, P., et al. 2013, ApJS, 208, 4
Paxton, B., Marchant, P., Schwab, J., et al. 2015, ApJS, 220, 15
Paxton, B., Smolec, R., Schwab, J., et al. 2019, ApJS, 243, 10
Pedersen, M. G., Aerts, C., Pápics, P. I., & Rogers, T. M. 2018, A&A, 614, A128
Pedersen, M.G., Aerts, C., Pápics, P.I., et al. 2021, Nat. Astron., 5, 715
Popov, M. V., Walder, R., Folini, D., et al. 2019, A&A, 630, A129
Porter, D. H., & Woodward, P. R. 2000, ApJS, 127, 159
Pratt, J., Baraffe, I., Goffrey, T., et al. 2017, A&A, 604, A125
Pratt, J., Baraffe, I., Goffrey, T., et al. 2020, A&A, 638, A15
Roe, P. L. 1981, J. Comput. Phys., 43, 357
Salaris, M., & Cassisi, S. 2017, Roy. Soc. Open Sci., 4, 170192
Scott, L. J. A., Hirschi, R., Georgy, C., et al. 2021, MNRAS, 503, 4208
Staritsin, E. I. 2013, Astron. Rep., 57, 380
Timmes, F. X., & Swesty, F. D. 2000, ApJS, 126, 501
Verma, M. K., Kumar, A., & Pandey, A. 2017, New J. Phys., 19, 025012
Viallet, M., Baraffe, I., & Walder, R. 2013, A&A, 555, A81
Viallet, M., Meakin, C., Prat, V., & Arnett, D. 2015, A&A, 580, A61
Viallet, M., Goffrey, T., Baraffe, I., et al. 2016, A&A, 586, A153
Viani, L. S., & Basu, S. 2020, ApJ, 904, 22
Wieczorek, M. A., & Meschede, M. 2018, Geochem. Geophys. Geosyst., 19, 2574
Wieczorek, M. A., & Simons, F. J. 2005, Geophys. J. Int., 162, 655
Woodward, P. R., Herwig, F., & Lin, P.-H. 2015, ApJ, 798, 49

Appendix A: Reynolds and Favre decomposition

The Reynolds decomposition splits a quantity $q(r, \vartheta, \varphi, t)$ in its mean value $\overline{q}(r)$ averaged over space and time

$$\overline{q}(r) = \frac{1}{\Delta t \Delta\Omega} \int_{\Delta t} \int_{\Delta\Omega} q(r, \vartheta, \varphi, t)\, \mathrm{d}\Omega\, \mathrm{d}t, \tag{A.1}$$

where $\mathrm{d}\Omega = \sin\vartheta\, \mathrm{d}\varphi\, \mathrm{d}\vartheta$ and the fluctuation q' is defined as

$$q'(r, \vartheta, \varphi, t) = q(r, \vartheta, \varphi, t) - \overline{q}(r). \tag{A.2}$$

The Favre decomposition separates a quantity q into the density-weighted average

$$\tilde{q}(r) = \frac{\overline{\rho q}}{\overline{\rho}} \tag{A.3}$$

and the corresponding fluctuation q'' defined via

$$q''(r, \vartheta, \varphi, t) = q(r, \vartheta, \varphi, t) - \tilde{q}(r). \tag{A.4}$$

Appendix B: Supplementary plots

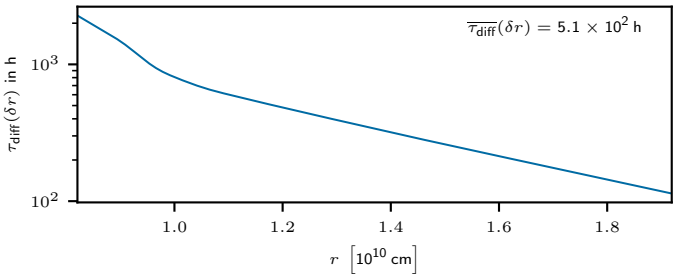

Fig. B.1. Thermal adjustment timescale τ_{diff} according to Eq. (9). The typical length scale is taken to be the radial grid spacing of the 3D simulation run with the highest resolution presented in Section 5.

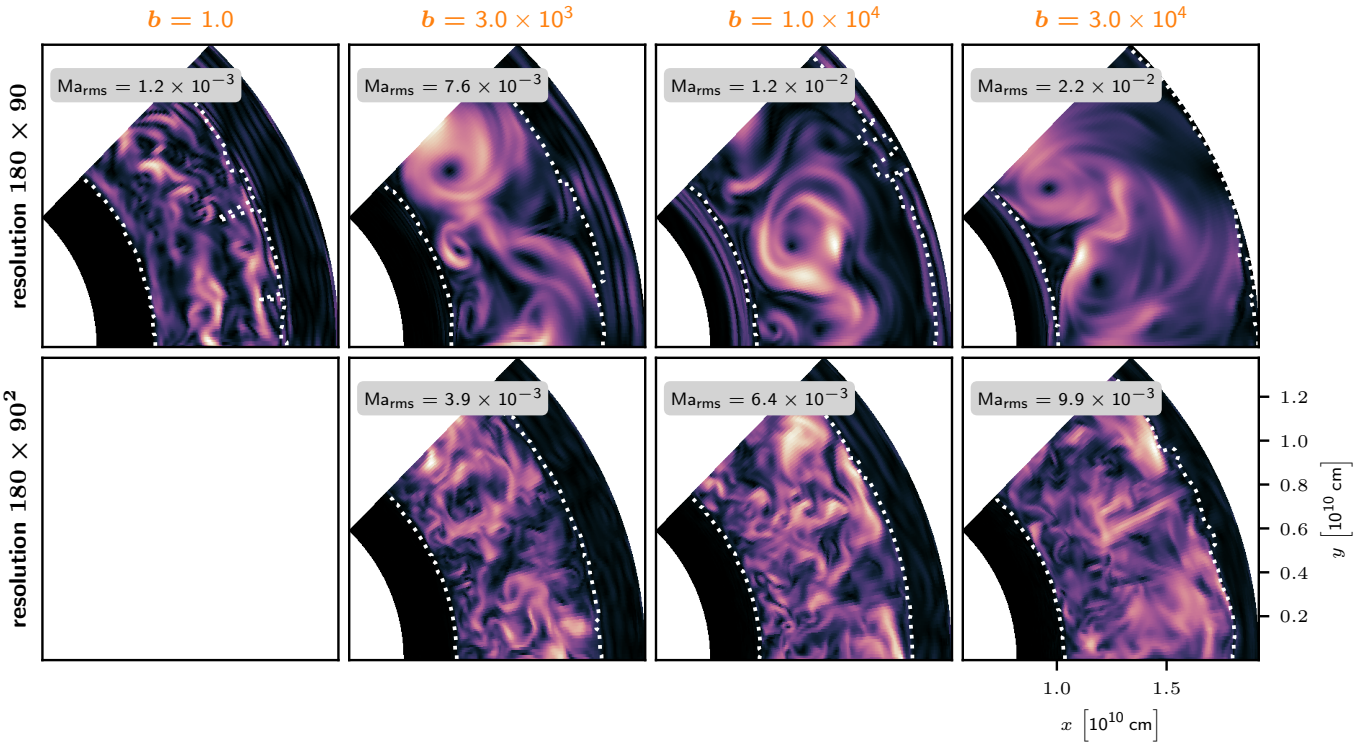

Fig. B.2. Flow patterns for 2D (upper row) and 3D (lower row) simulations at different boosting strengths. The Mach number is color-coded; the color-scale is adjusted to every subplot individually. Plots for the 3D simulations show the equatorial plane. White dashed lines denote the detected boundaries as described in Section 5.1. For all simulations, the AUSM$^+$-up solver was used. No 3D data is available for $b = 1.0$.

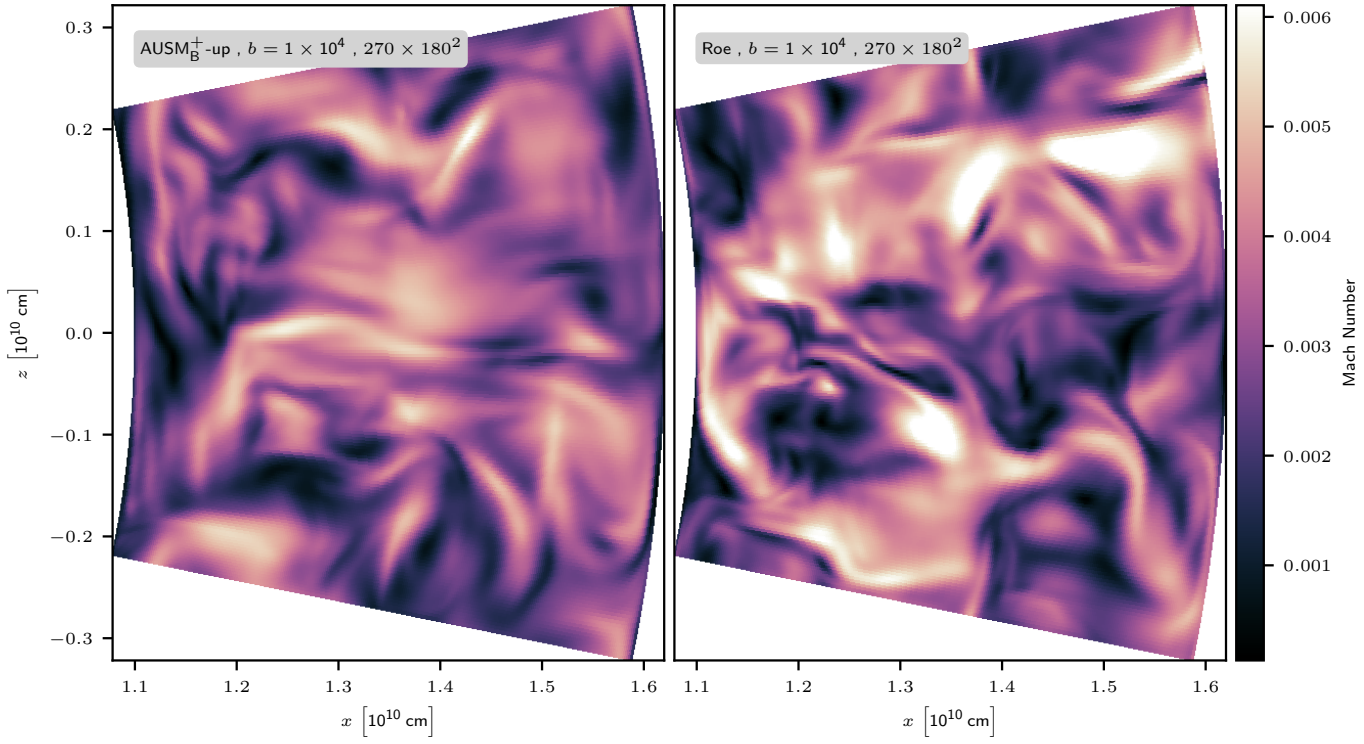

Fig. B.3. Fluid flow in terms of Mach number for the AUSM^+_B-up and Roesolver for a restricted domain that only contains a fraction of the convection zone.

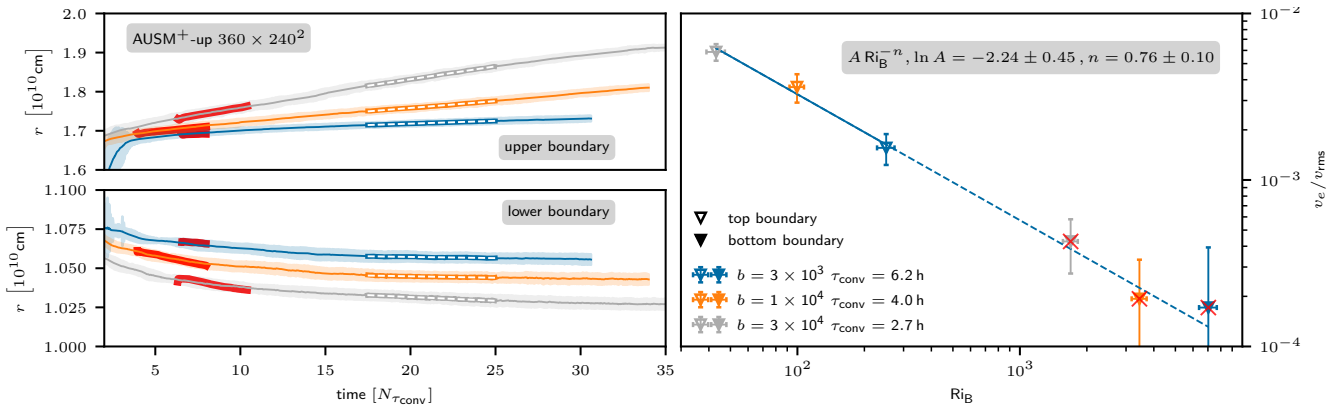

Fig. B.4. Same as Fig. 16 but for the time interval $t \in [t\,(N_{\tau_{\rm conv}} = 17.5)\,, t\,(N_{\tau_{\rm conv}} = 25)]$.

2.3 Publication III: Simulating waves excited by core convection

The publication in this section presents 2D SLH simulations of waves propagating in a simplified test setup and in a realistic stellar model. Different wave properties are extracted from the simulations and compared to expectations from linear theory and observations.

Convection in stars provides a possible source of wave excitation. For solar-like stars it is known that the convective envelope stochastically excites waves which can be observed at the surface (Aerts, 2021). While linear theory provides estimates of eigenfrequencies and their relation to properties of the stellar interior, it is not able to quantitatively predict which frequencies will be excited and what amplitudes can be expected. Furthermore, non-linear effects are difficult to treat in an analytical way.

For example, comparisons to observations of stellar oscillation suggest that additional mixing in radiative zones is required to obtain best fitting models (e.g., Moravveji et al., 2015; Pedersen et al., 2021). However, its parametrization remains unclear. Hydrodynamic simulations of waves propagating inside stars help to assess the importance of waves in this context. Indeed, recent studies for example indicated that IGW can contribute to angular momentum transport and mixing in the radiative zone (e.g., Rogers et al., 2013; Rogers and McElwaine, 2017; McNeill and Müller, 2020; Higl et al., 2021).

However, simulations that address wave excitation in detail are often performed considering the Euler equations in the anelastic approximation which filters out the physics of sound waves. Recently, spectral methods have been used to solve the anelastic equations which required enhanced viscosity and thermal diffusivity (e.g., Rogers et al., 2013; Alvan et al., 2014; Edelmann et al., 2019). The SLH code follows a finite-volume approach to solve the unmodified Euler equation. Although viscosity is not a controllable parameter in the ILES framework, it is thought to be smaller compared to the aforementioned simulations using spectral codes. It can be therefore expected that SLH simulations are closer to actual stellar conditions. While there have been some reports on waves excited in compressible simulations of stellar convection (Meakin and Arnett, 2006, 2007a; Herwig et al., 2006; Gilet et al., 2013), none of them included a larger part of the radiation zone and investigated the wave properties in detail.

The simulations presented in this section are based on a $3\,M_\odot$ MS-star model with a convective core and a radiative envelope. Convective motions in the core excite waves at the interface to the envelope which then propagate toward the surface. Properties of these waves, as for example their dispersion relation, can be extracted from the simulations and compared to predictions from linear theory. The SLH simulations are done in 2D because of the high computational costs of more realistic 3D simulations. The reduced dimensionality changes the eigenfrequencies of the waves and also the turbulent spectrum of convection. Still, 2D simulations can give an at least qualitative picture of the excitation mechanism and the reduced computational costs allow the inclusion of a large part of the radiative envelope and following wave excitation for longer times.

The chosen setup is well suited to assess the quality of simulations with the AUSM$^+$−up flux and, despite its simplicity, enables qualitative comparison to observations of stellar oscillations. Furthermore, the initial setup is the same as in the 3D study of Edelmann et al. (2019) who use a pseudo-spectral code. In this way, some comparison between the different numerical methods is possible.

The publication first describes and analyzes the test setup and compares the results obtained with the AUSM$^+$−up flux to the Roe solver. Because only the Cargo-LeRoux well-balancing scheme was available when the simulations of the $3\,M_\odot$ model were carried out, a

luminosity boosting by a factor of 10^3 was required to reach Mach numbers in the regime of 10^{-3}. The waves excited in the simulation are analyzed in detail regarding fundamental properties. It is found that the AUSM$^+$−up flux is well suited to simulate wave propagation at low Mach numbers and that the results are compatible with theory and observations. Furthermore, the resulting frequency spectra support the hypothesis that the low-frequency excess observed in massive stars is due to IGW excited by core convection.

Title
Fully compressible simulations of waves and core convection in main-sequences stars

Authors
L. Horst, P. V. F. Edelmann, R. Andrassy, F. K. Röpke, D. M. Bowmann, C. Aerts, R. P. Ratnasingam

Publication Status
The manuscript was published on September, 2020.

DOI
10.1051/0004-6361/202037531

Author's contributions
LH is the principal author of this paper. The initial idea developed during discussions with PVFE who also contributed the initial MESA setup and important guidance for the simulations and analysis. LH performed all simulations, analyzed the results, produced all figures and wrote the manuscript. LH also included the changes suggested by the referee. DMB and CA provided guidance regarding the observational interpretation of the results, pointed toward relevant literature, and suggested content and corrections to the manuscript. RA provided substantial guidance during the revision of the manuscript. All authors actively contributed by discussing the results at various stages of the project.

Credit

A&A 641, A18 (2020)
https://doi.org/10.1051/0004-6361/202037531

Astronomy & Astrophysics

Fully compressible simulations of waves and core convection in main-sequence stars

L. Horst[1], P. V. F. Edelmann[2,3], R. Andrássy[1], F. K. Röpke[1,4], D. M. Bowman[5], C. Aerts[5,6,7], and R. P. Ratnasingam[2]

[1] Heidelberger Institut für Theoretische Studien, Schloss-Wolfsbrunnenweg 35, 69118 Heidelberg, Germany
e-mail: leonhard.horst@h-its.org
[2] School of Mathematics, Statistics and Physics, Newcastle University, Newcastle upon Tyne NE1 7RU, UK
[3] X Computational Physics (XCP) Division and Center for Theoretical Astrophysics (CTA), Los Alamos National Laboratory, Los Alamos, NM 87545, USA
[4] Zentrum für Astronomie der Universität Heidelberg, Institut für Theoretische Astrophysik, Philosophenweg 12, 69120 Heidelberg, Germany
[5] Instituut voor Sterrenkunde, KU Leuven, Celestijnenlaan 200D, 3001 Leuven, Belgium
[6] Department of Astrophysics, IMAPP, Radboud University Nijmegen, PO Box 9010, 6500 GL Nijmegen, The Netherlands
[7] Max Planck Institute for Astronomy, Königstuhl 17, 69117 Heidelberg, Germany

Received 20 January 2020 / Accepted 3 July 2020

ABSTRACT

Context. Recent, nonlinear simulations of wave generation and propagation in full-star models have been carried out in the anelastic approximation using spectral methods. Although it makes long time steps possible, this approach excludes the physics of sound waves completely and requires rather high artificial viscosity and thermal diffusivity for numerical stability. A direct comparison with observations is thus limited.
Aims. We explore the capabilities of our compressible multidimensional Seven-League Hydro (SLH) code to simulate stellar oscillations.
Methods. We compare some fundamental properties of internal gravity and pressure waves in 2D SLH simulations to linear wave theory using two test cases: (1) an interval gravity wave packet in the Boussinesq limit and (2) a realistic 3 $M_\odot$ stellar model with a convective core and a radiative envelope. Oscillation properties of the stellar model are also discussed in the context of observations.
Results. Our tests show that specialized low-Mach techniques are necessary when simulating oscillations in stellar interiors. Basic properties of internal gravity and pressure waves in our simulations are in good agreement with linear wave theory. As compared to anelastic simulations of the same stellar model, we can follow internal gravity waves of much lower frequencies. The temporal frequency spectra of velocity and temperature are flat and compatible with the observed spectra of massive stars.
Conclusion. The low-Mach compressible approach to hydrodynamical simulations of stellar oscillations is promising. Our simulations are less dissipative and require less luminosity boosting than comparable spectral simulations. The fully-compressible approach allows for the coupling of gravity and pressure waves in the outer convective envelopes of evolved stars to be studied in the future.

Key words. hydrodynamics – methods: numerical – stars: interiors – convection – waves

1. Introduction

The study of the excitation and propagation of waves within stars has greatly helped to shape stellar structure and evolution theory over the last century. Today, this area of astronomy is called asteroseismology, and it includes the study of oscillations across the Hertzsprung–Russell diagram. For example, pressure modes (p-modes) provide important constraints on the envelopes of stars. Modes of a consecutive radial order (n) and the same angular degree (ℓ) have a characteristic frequency separation known as the large frequency separation, which is sensitive to the average density of a star (Aerts et al. 2010). This application of asteroseismology using p-modes has been extremely successful for low- and intermediate-mass stars (Chaplin & Miglio 2013; Hekker & Christensen-Dalsgaard 2017; García & Ballot 2019). Specifically, the measurement of envelope rotation using rotationally-split pressure modes has facilitated the discovery that stars with masses of about 2 $M_\odot$ have approximately rigid interior rotation profiles (see Kurtz et al. 2014; Saio et al. 2015; Van Reeth et al. 2016, 2018). Hence, current angular momentum theory already needs significant improvement on the main sequence (MS; Aerts et al. 2019).

For later evolutionary stages, including subgiant, red giant, and red clump stars, pulsations that behave as gravity modes (g-modes) near the core and as p-modes near the surface have been detected in thousands of stars (see Beck et al. 2011). These "mixed modes" can be used to distinguish different stages of nuclear burning (Bedding et al. 2011). Hence, understanding pressure modes is not only crucial for measuring interior properties of main sequence stars, but also for post-MS stars (see, e.g., Beck et al. 2012; Mosser et al. 2012).

On the upper main sequence, stars with spectral types O and B ($M > 3\,M_\odot$) observed in μmag precision space photometry show coherent opacity-driven p- or g-modes as well as stochastic variability caused by internal gravity waves. This occurs in slowly pulsating B (SPB) stars with masses between 3 $M_\odot$ and 9 $M_\odot$ (Pápics et al. 2017; Bowman et al. 2019a; Pedersen 2020), in β Cep stars with masses between 8 $M_\odot$ and 25 $M_\odot$ (Briquet et al. 2011; Burssens et al. 2019), and in young and evolved O-type dwarfs and blue supergiants with masses up to

~50 $M_\odot$ (Buysschaert et al. 2015; Bowman et al. 2019b, 2020; Pedersen et al. 2019). This overwhelming observational evidence from CoRoT, *Kepler*/K2, and TESS photometry motivated the development and study of our simulation setup.

The typical numerical approach to model the excitation of waves generated within stars is to solve the Navier–Stokes equations in the anelastic approximation (e.g., Rogers et al. 2013; Alvan et al. 2014; Edelmann et al. 2019). This method allows for large time steps while still being a mostly explicit method and is therefore computationally efficient. While being suitable to simulate internal gravity waves (IGWs) where gravity is the dominant restoring force, some important phenomena, such as the excitation of p-modes, cannot be followed. Furthermore, common numerical methods to solve the equations in the anelastic approximation require to introduce an artificial viscosity to achieve numerical stability. To balance the effect of high viscosity, the stellar luminosity and the thermal diffusivity have to be increased by orders of magnitude. This leads to a damping of the waves, especially in the low frequency regime.

Some of these drawbacks are avoided or reduced by performing compressible simulations of stellar interiors. Here, the full Navier–Stokes equations are solved, most commonly in the finite volume approach. This includes the physics of sound waves and allows the luminosity and the thermal diffusivity to be kept much closer to stellar values. Viscosity is implicitly introduced by the numerical scheme, and is lower than the viscosity typically used by spectral codes (nevertheless still orders of magnitudes higher than the astrophysical value). This is why we commonly speak of solving the Euler equations, which follow from the Navier–Stokes equations without an explicit viscosity term, in this context. On the other hand, this kind of simulations comes with higher computational costs compared to their anelastic counterparts. That compressible simulations show excited IGWs and p-modes has already been reported in the past. For example, Meakin & Arnett (2006, 2007) show a spectrum of the velocity for a simulation of carbon and oxygen burning in a 3D wedge geometry. They compare the form of a wave with predominately g-mode character and a coupled p- and g-mode to the predictions from linear theory and find good agreement for both. Also Herwig et al. (2006) indicate the excitation of p- and g-modes for the case of He-shell burning. They find the frequency of the different modes to be independent of resolution and boosting.

These prior studies focus on the effects of convective boundary mixing rather than the physics of waves. Thus, the computational domains only contain small parts of the radiative zone below and above the convective shells in evolved stars. The frequency spectrum might therefore differ considerably compared to a full star model and comparison to observations is difficult. Also, the analysis of internal waves mainly consists of computing the resulting spectra without further investigations.

Therefore, to further assess the advantages of compressible simulations, we use our finite volume Seven-League Hydro (SLH) code (for a description see Sect. 2) to examine in more detail the properties of excited waves. To ease the validation and comparison of our results, we repeat the simulation of a 3 $M_\odot$ zero-age main-sequence (ZAMS) model by Edelmann et al. (2019, EM19 hereafter). For their simulation, EM19 applied the anelastic approximation and a comparison between these two approaches is therefore possible. We note that many of the diagnostics presented in the main part of this work originate from EM19.

Because 3D simulations of an entire stellar model are costly even on today's supercomputer facilities, we use 2D simulations in this initial verification experiment. The 2D approach allows us to cover almost the entire stellar radius in our simulation domain, excluding only a small part in the core and the outermost layers, and to follow the evolution for an extended period of time. The computational costs are low enough to run the simulations on the local computer cluster of the Heidelberg Institute for Theoretical Studies (HITS), Germany. Convection is known to be only accurately described in three spatial dimensions (see, e.g., Meakin & Arnett 2007 for a comparison of 2D and 3D oxygen burning). However, as pointed out by EM19, the results of their 3D simulation are compatible with those of a 2D simulation by Rogers et al. (2013) for a different, but similar 3 $M_\odot$ model. This indicates that 2D simulations may still serve useful results for excited wave properties despite their reduced dimensionality.

This work is intended as a proof-of-concept: We present and validate in detail the results of simulating IGWs with the compressible hydrodynamics code SLH. The lack of the third dimension may not allow for a full quantitative comparison with observations, but some characteristics of 2D simulations are still expected to match observations of the integrated variability at the surface in a qualitative way. The main questions we aim to answer are therefore: Can the excited waves be identified as pressure waves and IGWs and do they comply with the theoretical expectations? Additionally, we compare the excited wave spectra to previous 2D work by Rogers et al. (2013) and perform qualitative comparisons to observations of frequency spectra of massive stars.

The paper is organized as follows: in Sect. 2 we give a brief overview on the numerical methods that are used in the SLH code. In Sect. 3 we describe and apply a simple test setup to benchmark the capability of SLH to treat IGWs. The 2D results for the 3 $M_\odot$ ZAMS model are discussed in Sect. 4. Section 5 summarizes the most important aspects and gives an outlook for future simulations.

2. The SLH code

We use the SLH code for all simulations presented in this paper. It was developed initially by Miczek (2013) and solves the fully compressible Euler equations in a finite volume framework. It allows us to choose between an ideal gas and a more general equation of state that includes contributions from radiation and electron degeneracy (Timmes & Swesty 2000). The hydro solver is coupled to a nuclear reaction network (Edelmann 2014). Radiation is treated in the diffusion limit, which is appropriate in the optically thick regions of the star covered here. The implemented mapping procedure between the uniform Cartesian computational grid and a general curvilinear physical grid introduces flexibility regarding grid geometry. Our implementation of the mapping is based on Kifonidis & Müller (2012) and Colella et al. (2011), examples for curvilinear grids can be found for example in Calhoun et al. (2008).

The SLH code was developed with a focus on flows at very low Mach numbers. One complication in this regime is the need of specialized flux scheme as common approaches are dominated by artificial dissipation (see, e.g., Miczek et al. 2015; Barsukow et al. 2017). For the simulations presented here, we use the AUSM$^+$-up solver (Liou 2006). It splits the flux function into a pressure and an advective part and has improved low-Mach capabilities. An artificial diffusive component for both parts is introduced for stability. To avoid divergence at very low Mach numbers, the scaling of the diffusion terms is limited by a cutoff Mach number $Mcut$, which is a free parameter. For technical reasons, a separate cutoff number $Mcut_{\mathrm{pdiff}}$ for the pressure diffusion term is used in SLH. In the simulations presented here,

we use $Mcut = 10^{-10}$ and $Mcut_{\mathrm{pdiff}} = 0.1$. For lower values of $Mcut_{\mathrm{pdiff}}$, the convergence rate of the implicit solver decreases considerably.

Due to the large pressure gradient in stars, the AUSM$^+$-up solver quickly destroys the hydrostatic stratification. To resolve this problem, SLH applies a variant of the Cargo–Leroux well-balancing technique. The basic idea is to remove the static background stratification from the conserved variables before they enter the numerical flux function. This considerably reduces the "effective" pressure gradient. The scheme was developed by Cargo & Le Roux (1994) for one-dimensional setups. Edelmann (2014) describes how this approach can be extended to multi-dimensional setups.

The flexible modular design of SLH facilitates the implementation of new developments such that newly published flux functions or reconstruction schemes can be easily implemented and tested. This makes SLH well suited to push hydrodynamical simulations toward low Mach numbers. For the 2D simulation of core hydrogen burning at the ZAMS presented in Sect. 4, mixing-length theory predicts convection at Mach numbers around 10^{-4} which calls for a numerical scheme optimized for slow flows. For a more detailed description of the code we refer the reader to Miczek (2013), Miczek et al. (2015) and Edelmann (2014).

At low Mach numbers, a common drawback of conventional *explicit time stepping* methods is that for stability the maximum possible time step size $\delta t_{\mathrm{CFL_{uc}}}$ is limited to the acoustic Courant–Friedrich–Lewy (CFL) criterion

$$\delta t_{\mathrm{CFL_{uc}}} = \frac{\mathrm{CFL_{uc}}}{N_{\mathrm{dim}}} \min\left(\frac{\Delta x}{|u| + c_{\mathrm{sound}}}\right). \tag{1}$$

Here, N_{dim} is the number of dimensions, Δx is the grid spacing in the different coordinate directions, u is the fluid velocity and c_{sound} is the speed of sound. $\mathrm{CFL_{uc}}$ is a dimensionless number which needs to be smaller than unity. The factor $1/N_{\mathrm{dim}}$ in combination with the minimum over all cells for the cell crossing time in all directions gives a lower limit for the time step. For low-Mach flows, $u \ll c_{\mathrm{sound}}$ and the time step size is dominated by the speed of sound. As a consequence, many small time steps are needed to resolve the fluid flow. Although the computational costs for one explicit time step are low, the large number of necessary steps makes explicit time stepping inefficient in this regime.

The great advantage of *implicit time stepping* is that there is no restriction for the step size required for stability. The main constraint arises from the question of how well the flow is to be resolved in time. This leads to the "advective" $\mathrm{CFL_u}$ criterion which results from Eq. (1) by omitting the speed of sound:

$$\delta t_{\mathrm{CFL_u}} = \frac{\mathrm{CFL_u}}{N_{\mathrm{dim}}} \min\left(\frac{\Delta x}{|u|}\right). \tag{2}$$

For illustration purposes, setting $\mathrm{CFL_u} = 0.5$ corresponds to a time step which does not allow the fluid to cross more than half of a cell per step.

Implicit time integration, however, requires to solve nonlinear systems of equations in each step. This greatly increases the computational costs for one implicit time step compared to explicit time stepping.

In SLH, the family of Explicit first stage, Singly Diagonally Implicit Runge-Kutta (ESDIRK) time steppers is implemented following the description of Hosea & Shampine (1996) and Kennedy & Carpenter (2001). For the simulations in this paper, the ESDIRK23 scheme is applied. It consists of three computing stages and is up to second order accurate in time. This results in two nonlinear systems of equations. SLH applies the Newton-Raphson method which finds their solution in an iterative way. Each iteration itself needs the solution of a linear system of equations. For these, SLH offers a variety of different methods (e.g., Krylov-Subspace schemes and multigrid solvers).

At low Mach numbers, the increased computational costs per time step are overcompensated by the benefit of a larger step size. Numerical tests with SLH imply that implicit time stepping becomes more efficient than explicit time stepping at Mach numbers smaller than about 0.1 to 0.01.

Apart from accuracy requirements, the length of implicit time steps is also limited by the Newton-Raphson solver, which may converge slowly or even diverge if the time step becomes too long. This limit depends on the problem solved and on details of the numerical scheme and needs to be determined experimentally.

The choice of the time step size for the 2D simulation presented in Sect. 4 is discussed in Sect. 4.7 along with an efficiency comparison between implicit and explicit time stepping.

Table 1. Parameters of the Boussinesq IGW simulation.

Temperature	$T_0 = 300\,\mathrm{K}$
Mean mol. weight	$\mu = 1$
Adiabatic index	$\gamma = 5/3$
Density at zero height	$\rho_0 = 1\,\mathrm{g\,cm^{-3}}$
Gravity	$\boldsymbol{g} = -10^3\,\mathrm{cm\,s^{-2}}\,\boldsymbol{e}_y$
Resolution	$288(x) \times 288(y)$
Domain	$[0, (2\pi/\lvert k_x\rvert)] \times [y_1, y_2]$
Boundary conditions	x-direction: periodic y-direction: constant ghost cells
Time stepping	ESDIRK23
Time step size	$\delta t = \frac{1}{20}\frac{2\pi}{N_0}$
Reconstruction	Linear, second order in space

3. Testing internal gravity waves in SLH

In this section, we scrutinize the capability of SLH to correctly reproduce the propagation of IGWs. The base setup is a 2D Cartesian domain containing an isothermal ideal gas in a hydrostatic stratification. A wave packet of small amplitude is evolved for several oscillation periods. The group velocity and the change of the wave shape are then extracted from the simulation and compared to the theoretical prediction which follows from the linear Boussinesq approximation. With this simple but well-defined test setup we verify whether SLH is able to reproduce the prediction accurately enough before applying it to the more complex case of a realistic stellar profile in Sect. 4.

3.1. Boussinesq IGW setup

The theoretical basics of the benchmark test are presented in Appendix A and follow Sutherland (2010). The actual experimental SLH setup closely follows the idea of Miczek (2013) and is extended up to Mach numbers of $\mathrm{Ma} = 10^{-2}$. The basic parameters of the setup are listed in Table 1.

Assuming the ideal gas law $p = \rho\mathcal{R}/\mu T$, where $\mathcal{R}$ is the universal gas constant, the profiles for density, pressure, and potential temperature in hydrostatic equilibrium are given by

$$\rho_{\mathrm{hse}} = \rho_0 \exp\left(-\frac{y}{H_{\mathrm{p}}}\right), \tag{3}$$

$$p_{\rm hse} = \rho_0 \frac{\mathcal{R}}{\mu} T_0 \exp\left(-\frac{y}{H_{\rm p}}\right), \tag{4}$$

$$\vartheta_{\rm hse} = T_0 \exp\left(\frac{y}{H_{\rm p}} \frac{\gamma-1}{\gamma}\right), \tag{5}$$

where the pressure scale height $H_{\rm p}$ is defined as

$$H_{\rm p}^{-1} = -\frac{\partial \ln p}{\partial y} = \frac{g\mu}{\mathcal{R} T_0}. \tag{6}$$

The Brunt–Väisälä frequency (BVF) according to Eq. (A.10) is spatially constant and reads

$$N_0 = \sqrt{\frac{g}{H_{\rm p}} \frac{\gamma-1}{\gamma}}. \tag{7}$$

We perturb this hydrostatic stratification with a monochromatic internal gravity wave packet. The wavelength $\lambda = 2\pi/|\boldsymbol{k}| = \beta H_{\rm p}$ of the packet is set in terms of the fraction β of the pressure scale height and is inclined by -60° with respect to the horizontal direction. We therefore have

$$|\boldsymbol{k}| = \frac{2\pi}{\beta H_{\rm p}}, \quad \theta = -\frac{60^\circ}{180^\circ}\pi \tag{8}$$

and

$$k_x = |\boldsymbol{k}| \cos\theta, \quad k_y = |\boldsymbol{k}| \sin\theta. \tag{9}$$

We set the vertical domain of the Cartesian box such that it corresponds to 13 times the wavelength λ

$$y_1 = -5\beta H_{\rm p}, \quad y_2 = 8\beta H_{\rm p} \tag{10}$$

in order to provide enough space for the wave to move upward in y-direction. The horizontal extent is set to contain one horizontal wavelength $\lambda_x = 2\pi/|k_x|$, which, in combination with periodic boundary conditions, allows for the plane wave approach. At the top and bottom boundary we apply a layer of two cells which are filled with the hydrostatic initial condition but kept constant in time (constant ghost cells). The amplitude for the vertical velocity component A_v is modulated by a Gaussian function according to

$$A_v(\boldsymbol{x}, t=0) = f_{\rm Ma} \underbrace{\sqrt{\gamma \mathcal{R} T_0/\mu}}_{=c_{\rm sound}} \exp\left[-\frac{1}{2}\left(\frac{y}{\beta H_{\rm p}/2}\right)^2\right]. \tag{11}$$

The parameter $f_{\rm Ma}$ therefore sets the peak Mach number in the vertical velocity amplitude. Using the relations Eqs. (A.11)–(A.13) from the theory described in Appendix A one finds for the initial conditions

$$\vartheta(\boldsymbol{x}, t=0) = \vartheta_{\rm hse} + \Re\left\{-\frac{i}{\omega}\frac{{\rm d}\vartheta_{\rm hse}}{{\rm d}y} A_v e^{i\boldsymbol{k}\cdot\boldsymbol{x}}\right\}, \tag{12}$$

$$u(\boldsymbol{x}, t=0) = \Re\left\{-\frac{k_y}{k_x} A_v e^{i\boldsymbol{k}\cdot\boldsymbol{x}}\right\}, \tag{13}$$

$$v(\boldsymbol{x}, t=0) = \Re\left\{A_v e^{i\boldsymbol{k}\cdot\boldsymbol{x}}\right\}, \tag{14}$$

$$p(\boldsymbol{x}, t=0) = p_{\rm hse} + \Re\left\{-\rho_0 \omega \frac{k_y}{k_x^2} A_v e^{i\boldsymbol{k}\cdot\boldsymbol{x}}\right\}, \tag{15}$$

where $\Re\{.\}$ denotes the real part of a complex expression.

In Appendix A, the time evolution of an initial amplitude modulation of the form of Eq. (11) is derived while considering the IGW dispersion relation Eq. (A.9) up to second order in $\boldsymbol{k}$. The result given by Eq. (A.28) shows that the initial profile broadens in time and moves at a vertical velocity of

$$c_{gy} = |\sin\theta \cos\theta| \frac{N_0}{|\boldsymbol{k}|} \tag{16}$$

which corresponds to a vertical Mach number of

$$\mathrm{Ma}_{gy} = |\sin\theta \cos\theta| \frac{\sqrt{\gamma-1}}{\gamma} \frac{\beta}{2\pi} \tag{17}$$

$$\approx 0.034\beta. \tag{18}$$

In Sect. 3.2 we compare the predicted to the simulated evolution of the velocity amplitude to assess the accuracy of our numerical schemes. In order to extract the velocity amplitude function from the simulation, Miczek (2013) suggests the following procedure: It is assumed that the horizontal velocity field can be decomposed as

$$u(x, y) = \hat{u}(y) \sin\left(k_x x + \varphi(y)\right). \tag{19}$$

This is fulfilled for the ansatz Eq. (A.6) and the amplitudes as defined above. Accordingly, also the evolved initial data should at least approximately fulfill this decomposition. However, directly comparing this to the prediction is not straight forward. To simplify the interpretation, the square of Eq. (19) is integrated over the full horizontal width

$$\int_0^{2\pi/k_x} u(x, y)^2 \, {\rm d}x = \frac{\pi}{k_x} \hat{u}(y)^2. \tag{20}$$

The integral can be calculated numerically using the data from the simulation and therefore provides the possibility to recover the vertical profile $\hat{u}(y)$.

The normalized amplitude

$$r_j = \frac{\sqrt{\frac{k_x}{\pi} \sum_i u_{i,j}^2 \Delta x}}{\left|\frac{k_y}{k_x} A_v(y=0)\right|} \tag{21}$$

then measures the change of the evolved data relative to the maximum of the initial data. In Eq. (21), i and j are the indices in horizontal and vertical direction, respectively; Δx refers to the size of the uniform grid spacing. The velocity by which the peak of r_j moves upward is interpreted as the group velocity in Eq. (16).

As discussed in Sect. 4.6, one can define a nonlinearity parameter,

$$\varepsilon = \frac{u}{\omega} k_x, \tag{22}$$

where u and k_x denote the horizontal velocity and wave number, respectively. If $\varepsilon \gtrsim 1$ one expects nonlinear effects to become dominant. Inserting the corresponding expressions into Eq. (22) gives

$$\varepsilon_B = \sin^2\theta \frac{f_{\rm Ma}}{\mathrm{Ma}_{gy}} \tag{23}$$

for the Boussinesq IGWs.

3.2. IGW SLH results

In this section we present simulations of the IGW setup described above for different parameter settings. For comparison, we show the results for the low-Mach solver AUSM$^+$-up and the classical Roe solver (Roe 1981).

The possible parameter space is restricted by two conditions:
(a) We require $\varepsilon_B \ll 1$ to stay within the linear regime;
(b) The Boussinesq approximation requires $\beta \ll 1$.
As free parameters we choose $\varepsilon_B = 10^{-2}$ and vary Ma_{gy}. The values for β and f_{Ma} are then calculated accordingly. This way, we are able to assess the capabilities of both schemes for different Mach numbers. The numerical settings for all of the simulations presented in this section are listed in Table 1. In particular we have chosen the time step size of the implicit time stepping such that the period corresponding to the BVF is resolved by 20 time steps.

We perform simulations for vertical group velocities of $\mathrm{Ma}_{gy} = 10^{-4}$, 10^{-3}, and 10^{-2}. Whereas condition (b) is well fulfilled for $\mathrm{Ma}_{gy} = 10^{-4}$, with $\mathrm{Ma}_{gy} = 10^{-2}$, which is closer to the typical velocity we find in the simulation presented in Sect. 4 (see Fig. 4), we have $\beta = 3 \times 10^{-1}$ and the stratification does not strictly follow the Boussinesq approximation anymore. Press (1981) shows that for the locally Boussinesq but globally anelastic equations the amplitude scales during the propagation with $\sqrt{\rho_0/\rho}$ where ρ_0 is the density at the starting point (cf. Eq. (42)). We therefore multiply equation Eq. (A.28) by the correction factor

$$f_\rho = \sqrt{\frac{\rho\left(y - c_{gy} t\right)}{\rho(y)}} \tag{24}$$

to account for the amplification due to varying density.

The results for the AUSM$^+$-up and Roe solvers are visualized in Figs. 1–3, respectively. The left columns show snapshots of the horizontal velocity u at the end of the simulation. The right columns compare at three points in time the amplitude and shape of the vertical velocity distribution as extracted from the simulation using Eq. (21) with the approximate prediction given by Eq. (24) and (A.28).

In Fig. 1, we have set $\mathrm{Ma}_{gy} = 10^{-4}$, which corresponds to a vertical velocity amplitude of $f_{\mathrm{Ma}} = 10^{-6}$. For the AUSM$^+$-up solver the velocity field in the left column clearly shows the effect of dispersion: waves of longer vertical wavelengths move faster and therefore appear at larger y values compared to smaller vertical wavelengths. The amplitude function broadens over time and is compatible with the prediction in terms of width and peak amplitude. We attribute most of the small deviations from the prediction to our neglect of third order effects in the dispersion relation, which are responsible for the amplitude function's skew. In contrast, the Roe solver heavily damps the initial amplitude within the first few time steps and it becomes impossible to determine a unique peak in the remaining velocity field. This illustrates that the classical Roe solver fails in the very low Mach regime whereas AUSM$^+$-up still gives excellent results.

We continue by increasing the vertical group velocity to $\mathrm{Ma}_{gy} = 10^{-3}$. According to Eq. (17) this can only be achieved by increasing β, which sets the fraction of the pressure scale height covered by one wavelength, to $\beta = 3.0 \times 10^{-2}$. The results are shown in Fig. 2. The relative peak amplitudes and shapes for AUSM$^+$-up do not change considerably compared to Fig. 1. The results of the Roe solver show distinguishable, but still strongly

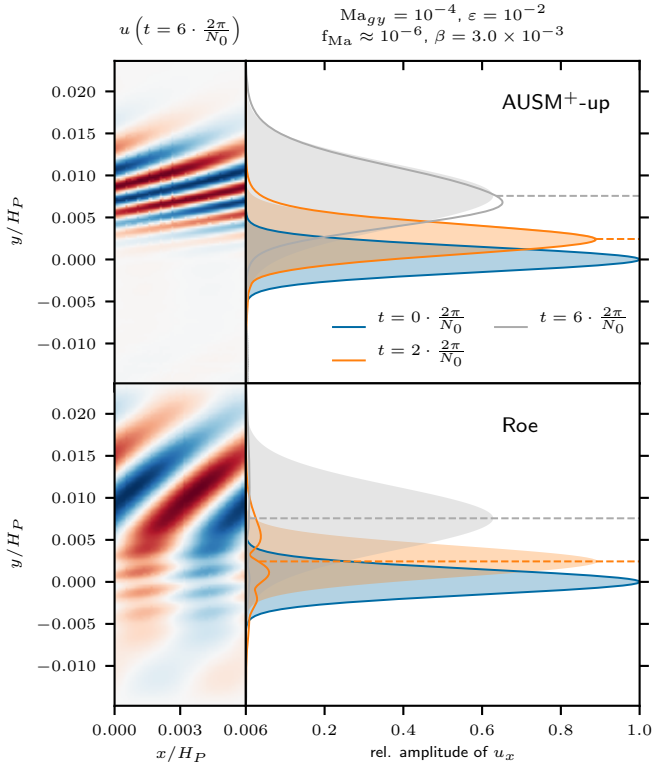

Fig. 1. Results for the IGW test setup as described in Sect. 3 for the AUSM$^+$-up solver (*upper row*) and the classical Roe solver (*lower row*). The parameters for the simulation are shown at the top of the plot and described in the main text. *Left column*: horizontal velocity u in the 2D domain at the end of the simulation at $t = 6\,\frac{2\pi}{N_0}$. Blue color corresponds to a positive value, and red color to a negative value of the velocity. The scale is adjusted to the maximum amplitude for each run. *Right column*: amplitude extracted according to Eq. (21) at the beginning of the simulation and at two later points in time (solid lines). The shaded areas correspond to the predicted shape of the amplitude modulation function according to Eqs. (24) and (A.28). Dashed horizontal lines mark the position of the peak amplitude for the prediction that moves at the group velocity accordingto Eq. (17).

damped, peaks and their vertical group velocity considerably disagrees with the theoretical prediction.

The effect of increasing the vertical group velocity further to $\mathrm{Ma}_{gy} = 10^{-2}$ is depicted in Fig. 3: Again, the shape and peak amplitudes for AUSM$^+$-up are compatible with the prediction. For this setup, $\beta = 3 \times 10^{-1}$ and consequently the density varies noticeably in the simulation volume. This is reflected by the smaller decrease in the expected peak amplitudes in Fig. 3 compared to the amplitudes shown Figs. 1 and 2 for which the amplification according to Eq. (24) is negligible. With the Roe solver, the results are better as compared to those obtained at lower vertical group velocities and the broadening is closer to the prediction. However, significant damping of the velocity amplitude is still evident.

In summary, the results for the classical Roe solver, which we present here solely for comparison, clearly suffer from high damping and show that the wave packages move at the wrong speed. Our tests therefore confirm the need for specialized low-Mach solvers in order to treat IGWs in the regime of velocities below Ma $\sim 10^{-2}$. A variety of such solvers are readily available in SLH. A promising example is the AUSM$^+$-up solver for which our tests demonstrate its capability to treat IGW in the low-Mach regime.

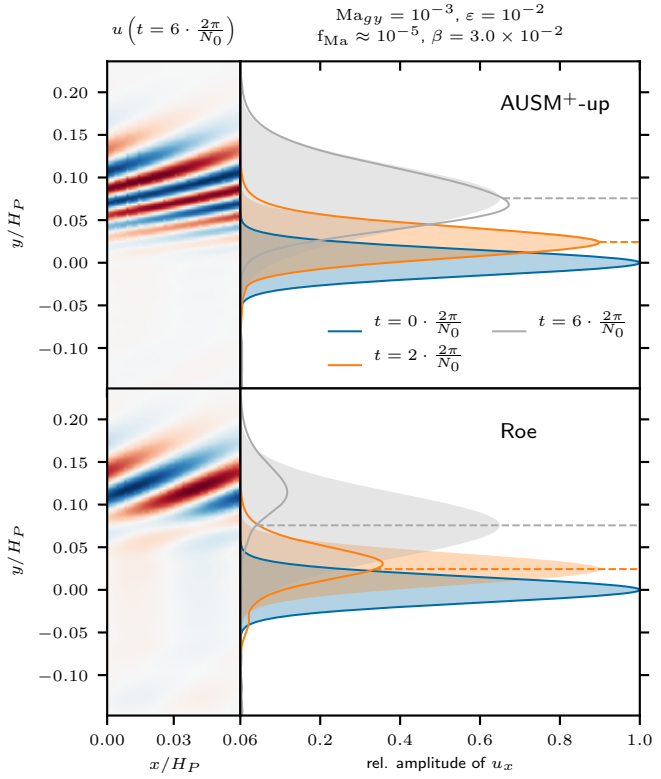

Fig. 2. See Fig. 1 for a description of the quantities shown.

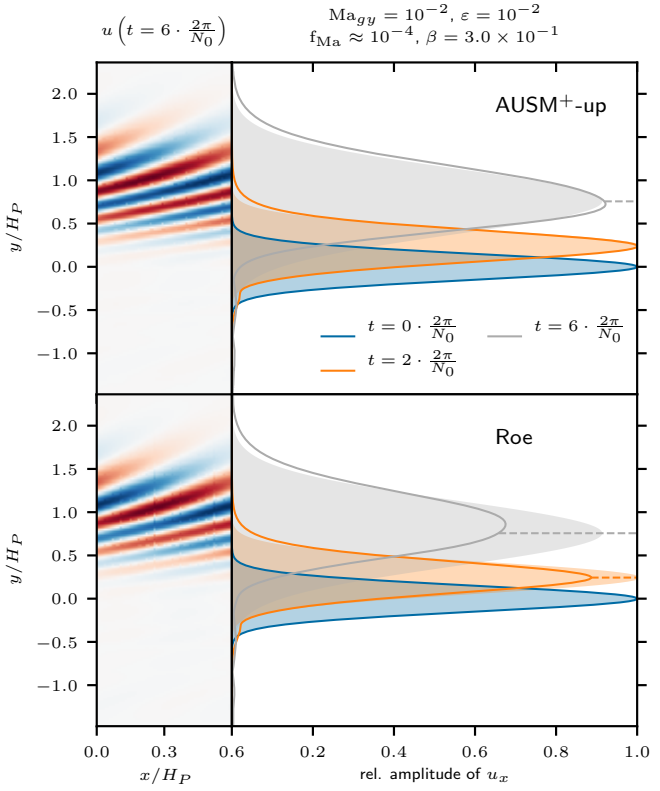

Fig. 3. See Fig. 1 for a description of the quantities shown.

To assess the relevance of this finding we estimate the order of magnitude of the group velocity we expect for the simulation of the real stellar setup presented in Sect. 4. We take the absolute value of Eq. (A.14) and rewrite it in terms of vertical and horizontal components of the wave vector. For the polar coordinates used in the 2D simulation, the horizontal wave number corresponding to the angular degree ℓ is given by

$$k_\mathrm{h} = \frac{\sqrt{\ell(\ell+1)}}{r} \tag{25}$$

and the absolute value of the group velocity is

$$|\boldsymbol{c}_g(r)| = \frac{r\omega^2}{N\sqrt{\ell(\ell+1)}}\sqrt{\frac{N^2}{\omega^2} - 1}, \tag{26}$$

where r denotes the radial position within the model. In Fig. 4 we show the group velocity for $\ell = 4$ when inserting the values from the stellar model used in Sect. 4 into Eq. (26). It illustrates that there are large regions at low frequencies with Mach numbers around and below 10^{-2}. These regions become even more extended at higher ℓ-values. We conclude that low-Mach solvers are needed to correctly describe the wave field in simulations such as that presented in Sect. 4, especially in the low-frequency regime dominated by internal gravity waves.

4. 2D simulation of a 3 $M_\odot$ ZAMS star

The previous section demonstrates the capabilities of the SLH code and the methods implemented therein to propagate IGWs in the low-Mach regime whereas classical approaches fail. In this section, the SLH code is applied to a real stellar setup, which encompasses both the generation and propagation of IGWs and sound waves.

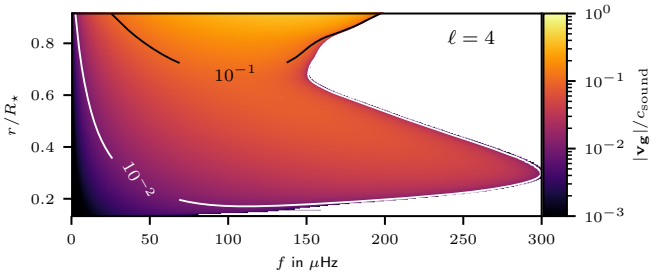

Fig. 4. Expected group velocity according to Eq. (26) expressed in terms of Mach number for values of the stellar model used in Sect. 4. Contour lines mark regions of different typical Mach numbers. There are no IGWs for frequencies above the BVF (white area). Instead, one expects the excitation of sound waves only which have Mach numbers of unity.

4.1. Initial model

For the simulation presented here we use the identical initial 1D model as EM19. It describes a nonrotating 3 $M_\odot$ star at the ZAMS with a metallicity of $Z = 10^{-2}$ and an outer radius of $R_\star = 1.42 \times 10^{11}$ cm. The model has been calculated with the open-source stellar evolution code MESA (see Paxton et al. 2019 for the latest report on code updates).

The 1D data provided by the MESA model needs to be mapped onto the SLH grid while accurately fulfilling the equation of hydrostatic equilibrium

$$\nabla P = \boldsymbol{g}\rho. \tag{27}$$

To do so, we reintegrate Eq. (27) while imposing the radial profile of one thermodynamic quantity from the 1D code (using the 1D density profile for this would be a simple example). All other thermodynamic quantities then follow from the equation of state.

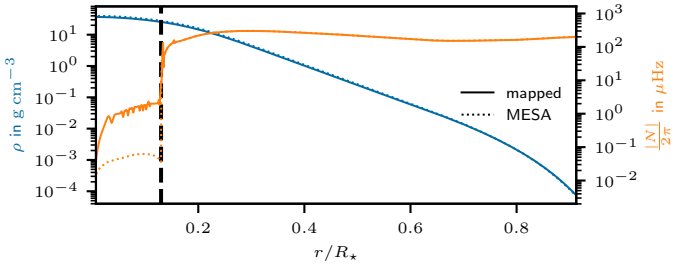

Fig. 5. Density (blue) and absolute value of the BVF (orange). The dotted lines correspond to the profiles of the underlying 1D MESA model. The solid lines result from our mapping to the SLH grid. The vertical dashed line marks the radius below which the BVF has a negative sign and one therefore expects convection to develop. The applied mapping method guarantees that the position of the dashed line is identical for the mapped SLH model and the 1D MESA model.

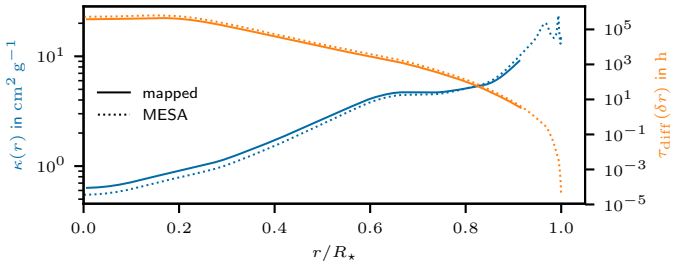

Fig. 6. Blue lines: profiles of the opacity κ for the underlying 1D MESA model (dotted blue line) and the value applied for the mapped 2D SLH model (solid blue line). Orange lines: characteristic diffusion time scale according to Eq. (29) when assuming the radial spacing δr of the SLH grid as typical length scale.

The particular choice of the imposed quantity depends on the specific setup. For the case presented here, it is important to keep the position of the convection zone as close as possible to the 1D input MESA model. Convective instability is characterized by a negative sign of the BVF. In regions without any or with only a small gradient in composition (well fulfilled in ZAMS stars) it is essentially determined by the sign of $\nabla - \nabla_{\rm ad}$. Therefore, we follow the approach of Edelmann et al. (2017) to integrate Eq. (27) while enforcing

$$(\nabla - \nabla_{\rm ad})_{\rm SLH} = (\nabla - \nabla_{\rm ad})_{\rm MESA}. \tag{28}$$

This way the initial spatial extent of the convective zone on the SLH grid exactly matches the 1D input model. Consequently, other quantities might deviate from the 1D model. In Fig. 5 we exemplarily compare the profiles of the SLH model and the 1D input for density and BVF. Both quantities are reproduced reasonably well considering that we cover several orders of magnitudes.There is a deviation of a factor of ten in the convection zone which we attribute to differences in the technical details of the equation of state and the calculations of gradients between MESA and SLH. It is not expected that enforcing $N^2_{\rm SLH} = N^2_{\rm MESA}$ will improve the result as this will only translate the differences into other quantities. However, in the SLH simulation the value of N^2 in the convection zone will self-consistently adjust to a value that corresponds to the equilibrium between energy input, for example due to nuclear burning, and the convective flux. The small initial deviation is therefore not relevant. For the BVF, the mean differences in the radiation zone between the 1D MESA model and the mapped profiles is 0.56% with a maximum value of 1.5% at $r = 0.87\,R_\star$ and we therefore consider the applied method to be sufficiently accurate.

The underlying 1D MESA model is in thermal equilibrium. The reintegration of Eq. (27) for hydrostatic equilibrium changes the 1D stratification only slightly and we expect the mapped SLH stratification in the radiative envelope to be sufficiently close to the equilibrium model. This, however, is not true for the convective core where we have to artificially boost the nuclear energy release (see Sect. 4.2). A stratification that is not in thermal equilibrium will readjust on the thermal-diffusion time scale $\tau_{\rm diff}$. It can be estimated as (e.g., Maeder 2009)

$$\tau_{\rm diff}(\Delta x_{\rm diff}) \sim \frac{(\Delta x_{\rm diff})^2}{K}, \quad K = \frac{4\,a\,c_{\rm light}\,T^3}{3\,\kappa\rho^2\,C_{\rm P}}, \tag{29}$$

where $\Delta x_{\rm diff}$ is a typical length scale. The thermal diffusivity K introduces the radiation constant $a = 7.57 \times 10^{-15}$ erg cm^{-3} K^{-4} and the specific heat at constant pressure $C_{\rm P}$ for the ideal gas. The opacity κ is a function of radius and determined by the physical properties of the gas. However, for the mapped SLH model, we set $\kappa_{\rm SLH}$ such that we achieve $K_{\rm MESA} = K_{\rm SLH}$. Therefore, the value of $\kappa_{\rm SLH}$ is not fully consistent in a physical sense but it allows us to stay closer to the stellar values of thermal diffusion. The blue lines in Fig. 6 show the profiles of $\kappa_{\rm SLH}$ (solid) and $\kappa_{\rm MESA}$ (dashed) and indicate that deviations are reasonably small.

Following Eq. (29), we estimate the thermal-diffusion time scale taking the radial grid spacing δr to be the typical length scale, see Fig. 6. Due to the energy boosting in the convection zone, deviations from thermal equilibrium are expected to be largest there. From Fig. 6 it can be seen that the diffusion time scale is on the order of 10^5 h and thus two orders of magnitude larger than what is covered by our 2D simulation (about 10^3 h, see Sect. 4.2). Furthermore, as the grid spacing δr is already the smallest possible scale, our estimate is a lower limit on the time scale. In the outer parts, the time scale becomes comparable to the simulation time. Thermal flux scales with $1/r$ in the cylindrical geometry of our 2D simulation (see below for more details on the numerical setup) and therefore differs from the MESA model where spherical geometry is assumed. Thus, the thermal flux is not accurately balanced in our simulation. However, we do not recalculate the equilibrium state while considering the correct scaling of the flux in cylindrical geometry as this would lead to large deviations from the 1D MESA input model. For example, this would likely change the profile of the BVF and therefore alter the dynamics of sound and gravity waves. For our simulations, however, we are interested in waves generated in a stratification as close as possible to a realistic stellar stratification.

From Fig. 6 it is clear that slightly imbalanced initial conditions most probably only impact the very outer part of our model during the course of the 2D simulation. To further validate this, we performed two 1D simulations. Although they do not include convection and wave propagation, they reveal the impact of an imbalanced energy flux. The initial conditions and the numerical settings for both simulations are the same as for the 2D simulation (see text below and Table 2) except that the heat input in the convection zone is turned off. The 1D runs only differ in geometry, which is cylindrical and spherical, respectively, and cover the same time span as the 2D simulation.

In the 1D simulations, the maximum change in temperature occurs close to the surface and is only 0.11%. Deviations in the spherical run are slightly smaller but of the same order as in the cylindrical run. Thus, the change is most probably due to the Dirichlet boundary conditions for the temperature which we

Table 2. Parameters of the 2D simulation.

Boosting	$L = 10^3\, L_{\rm MESA}$
Th. diffusivity	$K = K_{\rm MESA}$
EoS	Ideal gas + radiation pressure
Geometry	Polar coordinates
Radial domain	$0.007\, R_\star$ to $0.912\, R_\star$
Resolution	$960(r) \times 720(\varphi)$
Boundary conditions	r-direction: solid-wall
	φ-direction: periodic
Time stepping	ESDIRK23
Time step size	$\overline{\delta t} = 8$ s
Time span	700 h
Reconstruction	Linear, second order in space
Flux function	AUSM$^+$-up

Notes. $R_\star = 1.42 \times 10^{11}$ cm denotes the total radius of the underlying 1D model, $L_{\rm MESA}$ the stellar luminosity, and $K_{\rm MESA}$ the stellar thermal diffusivity as given by MESA.

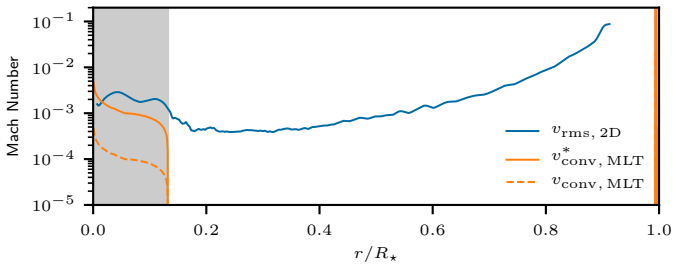

Fig. 7. Predicted and simulated Mach numbers of the 2D model. The orange lines correspond to the MLT prediction: the dashed profile shows the original stellar values, whereas the solid line illustrates the velocities scaled by 10, according to Eq. (30). The blue line shows the 2D results averaged over roughly two convective turnover times, starting at $t = 500$ h. The profile ends at $r \approx 0.9\, R_\star$ as our domain does not contain the entire star model. The gray shaded areas mark the convective core and the small region of surface convection in the 1D model.

have chosen for simplicity and that are used for all radial boundaries in the simulations presented here. To exclude any other cause than radiative diffusion for the slight change in the background state we also ran additional 1D simulations where radiative diffusion was disabled. The stratification remains essentially unchanged in these simulations. For the 1D simulations with enabled radiative diffusion, we show the resulting radial profiles of temperature, temperature gradient, and BVF in Fig. B.1 and list the corresponding maximum values in Table B.1.

While the inconsistent treatment of the thermal flux is certainly not desirable, the 1D tests show that its impact on this particular simulation setup is negligible. Nevertheless, for future 2D simulations, we plan to implement the correct geometrical scaling of the flux and to improve the flux boundary conditions.

EM19 do not need to modify the 1D input MESA model. Therefore, Figs. 5 and 6 serve as a direct comparison between the mapped model on the SLH grid and their initial data.

In Table 2 we list the parameters for the SLH simulation. We use 2D polar geometry which corresponds to an infinite cylinder. SLH currently does not support the geometry of a 3D sphere with azimuthal and longitudinal symmetry. Because of the singularity of polar coordinates at $r = 0$, we cannot include the whole core. The minimum radius of the domain is mainly determined by the decreasing cell sizes in horizontal direction which affects the possible time step size according to the CFL criterion (see Sect. 4.7). We have chosen $r_{\rm min} = 0.007\, R_\star$ which still allows for reasonably large steps. The upper boundary was set to $r_{\rm max} = 0.91\, R_\star$ which is close to the value of EM19 who set the upper boundary to $0.9\, R_\star$. We apply solid-wall boundary conditions at the inner and outer boundaries of the computational domain. They enforce a vanishing velocity perpendicular to the boundary interface. This prohibits mass flux and sound waves from leaving the domain. Periodic boundaries are chosen in the azimuthal direction, which is appropriate since we cover the full azimuthal range of 2π. The number of 960 radial cells ensures that the smallest pressure scale height (close to the outer boundary) is still resolved by 16 grid cells. The number of horizontal grid cells is set such that the cell width at the top of the convection zone $\delta_w = \delta_\varphi r_{\rm top}$ roughly matches the height $\delta_{\rm r}$ of the cells, where $\delta_\varphi = 2\pi/N_\varphi$ and $\delta_{\rm r} = (r_{\rm max} - r_{\rm min})/N_{\rm r}$ denote the angular and radial resolution, respectively.

4.2. 2D SLH results

For the stellar luminosity as given in the 1D MESA input model, mixing-length theory (MLT, e.g., Kippenhahn et al. 2012) predicts Mach numbers for the convective core of around Ma $\sim 10^{-4}$. Simulations in this regime are numerically very challenging and the SLH code has several specialized low-Mach approximate Riemann solvers implemented. However, we have recently noticed that for Mach numbers considerably below 10^{-3} the convective flow seems not to be driven by heating but rather by numerical instabilities. This problem is subject of ongoing investigations but there is no adequate solution available yet. As a workaround, it was decided to artificially boost the energy generation in order to increase the convective velocity. From MLT one finds that the convective velocity $v_{\rm conv}$ scales with the luminosity L as

$$v_{\rm conv} \propto L^{1/3} \tag{30}$$

which has also been confirmed by numerous numerical studies (e.g., Fig. 7 of Cristini et al. 2019 or Fig. 15 of Andrassy et al. 2019). We boost the stellar luminosity by a factor of 10^3 which corresponds to a tenfold increase in velocity compared to the MLT prediction. We note that this boosting is still a factor 10^3 smaller compared to the boosting in the simulations of EM19 and Rogers et al. (2013).

In Fig. 7 we compare the MLT prediction to the results of our 2D simulation. The gray shaded area at small radii marks the region of the core that is convectively unstable according to the Schwarzschild criterion. In the input 1D model, an additional small convection zone near the surface of the star is present but our 2D model already ends at a smaller radius. We find our simulations in good agreement with this "scaled" MLT prediction.

However, outside of the convective core a velocity field of considerable amplitude has developed. These velocities are attributed to the excitation and propagation of IGWs and are of main interest for the work presented here. In stark contrast to that, no velocities are assumed in the input 1D model. This illustrates the shortcomings of 1D stellar evolution, where these dynamical phenomena have to be parametrized (see, e.g., Aerts et al. 2019).

The speed of sound in our model ranges from 7×10^7 cm s^{-1} within the convection zone to 1×10^7 cm s^{-1} at the top of the computational domain. Accordingly, the Mach number shown in Fig. 7 corresponds to typical velocities of 2×10^5 cm s^{-1} (convection zone) to 1.3×10^6 cm s^{-1} (near surface). For the mean

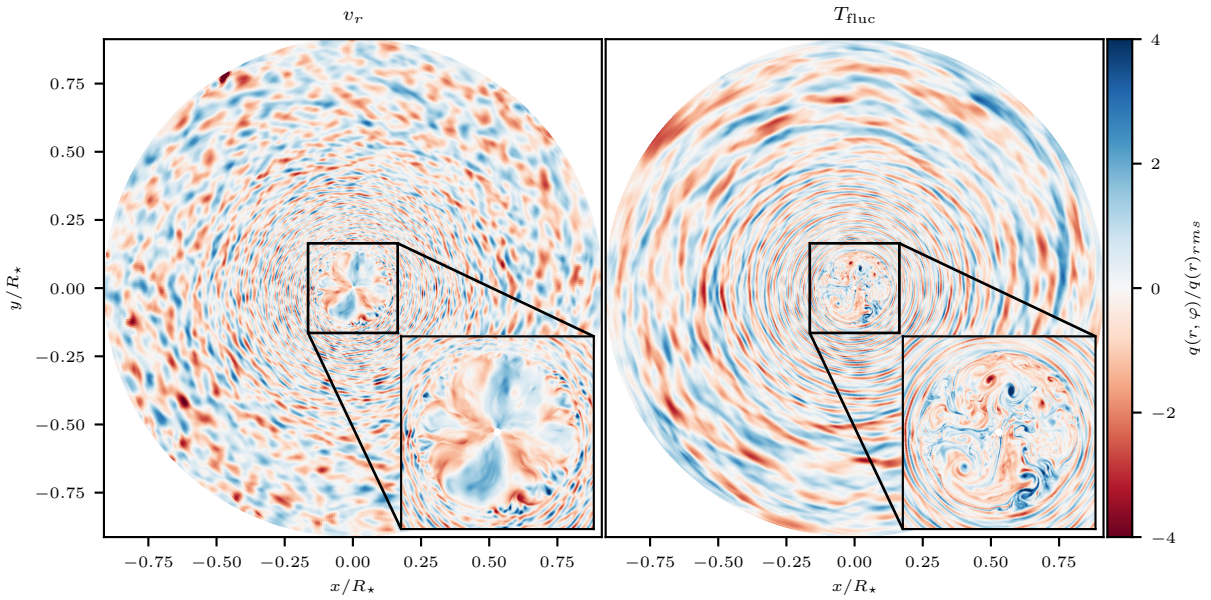

Fig. 8. Radial velocity v_r and temperature fluctuations $T_{\rm fluc}$. As both quantities have larger amplitudes at the outer parts of the model (see further Sect. 4.5) they have been scaled with the corresponding horizontal root-mean-square value at each radius r to ease the visualization. Both panels also show a magnification of the core region. The shown snapshot is taken at $t \sim 580$ h. There is also a movie available on https://zenodo.org/record/3819569.

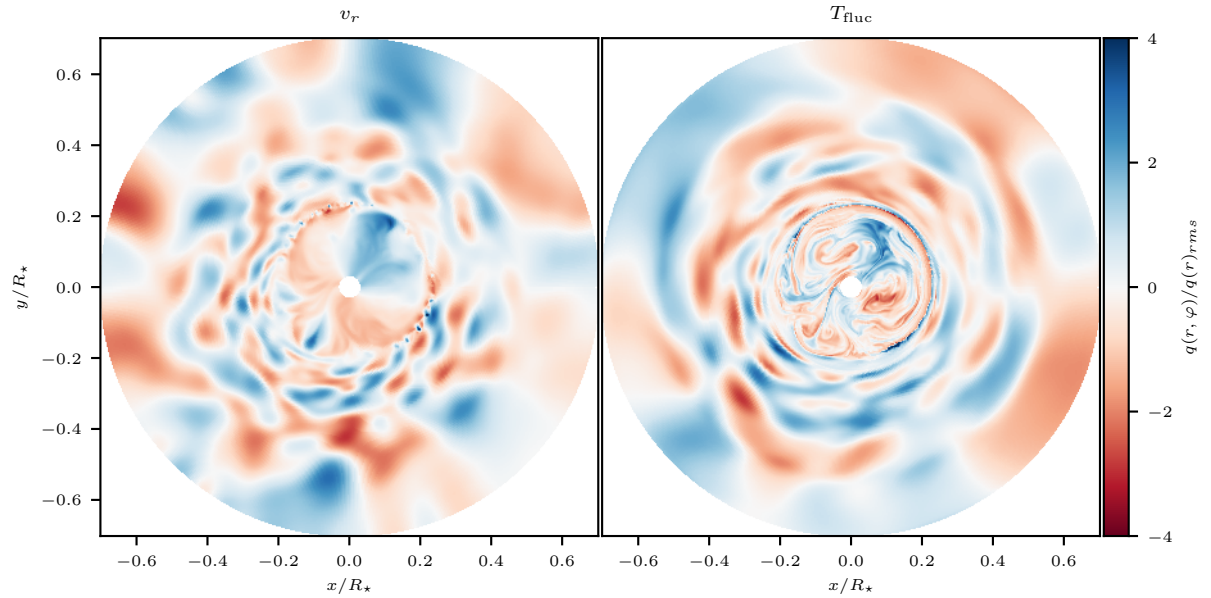

Fig. 9. Same quantities as in Fig. 8 but here for a 2D simulation with a viscosity and thermal diffusivity similar to the values used by EM19. We note that the domain for this simulation is comparable to Fig. 8 but not identical. The radial resolution is slightly higher for the viscous simulation and due to the high viscosity the energy input is boosted by 10^6 in order to get convection starting.

convective turnover time in the convection zone $\overline{\tau}_{\rm conv}$ we find

$$\overline{\tau}_{\rm conv} = \frac{2\Delta r_{\rm cz}}{v_{\rm rms}} \approx 40\,{\rm h} \tag{31}$$

where $\Delta r_{\rm rc} = 1.7 \times 10^{10}$ cm is the depth of the convection zone and $v_{\rm rms}$ the root-mean-square of the absolute velocity. The spatial mean has been taken over the convection zone and the temporal mean includes the entire simulation except for the initial transient phase, where convection has not yet developed (see also Fig. 10). Hence, the 700 h of fully developed convection that we follow in our simulation cover roughly 17 convective turnover times.

The velocity field of the 2D simulation is further illustrated in Fig. 8. It visualizes radial velocity (left panel) and temperature fluctuations from the azimuthal average (right panel). Both quantities are scaled by their horizontal root-mean-square as the amplitudes vary considerably between the outer and inner part of the model. The relative amplitudes have maximum values of four and are approximately equal at all radii for temperature and velocity. In both panels of Fig. 8, the convective core is filled with a few rather coherent structures which correspond to convective eddies that induce wave-like motions. These waves form spiral paths from the point of excitation at the boundary of the convective core as they travel toward the surface. The spatial

structures are smaller than those observed by EM19 (see, e.g., their Fig. 8). This is explained by the much smaller effective viscosity of our simulation and further illustrated in Fig. 9 which shows an SLH simulation of a similar domain and resolution but with explicit viscosity and thermal diffusivity comparable to those used by EM19. It is clearly visible how the enhanced diffusive effects even out small scale structures and only large patterns remain.

Figures 7 and 8 illustrate that the fundamental process of generating internal waves, that is a convective core with plumes that excite waves in the radiative envelope, is present in our 2D simulation. In order to further validate our results in the subsequent sections, we closely follow the methods as presented in EM19.

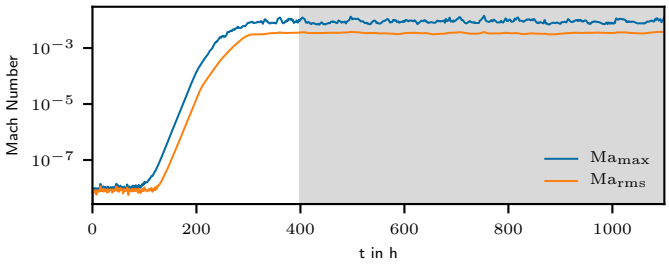

Fig. 10. Maximum (blue) and root-mean-square (orange) Mach number in the convection zone as a function of time. The gray shaded area marks the time frame that has been used to extract the spectra that are presented in this paper.

4.3. Frequency spectra

The fundamental properties of stellar oscillations can be probed by investigating their temporal frequency spectrum. For this, we perform a temporal Fourier transformation (FT) of the entire velocity field in our 2D simulation.

The transformation is done for both the radial and horizontal velocity. In order to select waves corresponding to a specific angular degree ℓ, we apply a filter prior to the temporal FT. For the velocity of each stored snapshot, a spatial FT in the angle φ is taken while using all available data points on the grid. Subsequently, all amplitudes are set to zero, except for the one corresponding to the ℓ value we want to filter for. This manipulated spectrum is brought back to real space via an inverse FT. The resulting time sequence of the grid cells of each radial ray is then multiplied by the Hanning window to reduce leakage effects and serves as input for the temporal FT. To reduce the background noise such that individual modes appear more clearly, the temporal spectra are taken for 100 evenly distributed radial rays. The squares of the amplitudes of the resulting Fourier coefficients are then averaged. In principle, the average could be done for all available angles but we experienced no improvement for a larger number of rays. Keeping the numbers of rays low is desirable regarding memory requirements.

The coefficients of the temporal FT are normalized in the same way as in EM19 (see their Eqs. (12) and (13)), essentially the amplitudes are divided by the number of the input data points. This results in coefficients that are independent of the number of bins and that have the same units as the input quantity. Furthermore, for this normalization, the amplitude of a peak across one single frequency bin corresponds to the actual amplitude of that wave in the time domain which eases the direct interpretation of the spectrum. For our spectra, the frequency bins have a width of $\delta f = 1/(700\,\mathrm{h}) = 0.4\,\mu\mathrm{Hz}$. Spectral lines in our spectra typically (except for a few broad p-modes) span two to four frequency bins and the absolute amplitude is therefore slightly underestimated when directly read off the spectral plots. Finally, the amplitudes are multiplied by a factor of 2 to account for the change in amplitudes in the frequency spectrum due to the application of the Hanning window (see, e.g., Sect. 9.3.9 of Brandt 2011).

We only use the time interval spanning 700 h from 400 h to 1100 h for the spectral analysis (see the gray shaded area in Fig. 10) to avoid the initial development of convection in the core and of the wave field in the envelope.

In Fig. 11 we show the result for the radial velocity, which is the dominant component for p-modes. The upper panel shows the spectrum of the unfiltered velocity, the panels below show the spectra of filtered velocities for some exemplary values of ℓ. This figure is the compressible counterpart of Figs. 24 and 27 in EM19. In Fig. 12, the same quantities are shown for the horizontal velocity which is the dominant component for g-modes. In these plots and in the further course of the paper, a hat denotes quantities that have been obtained using a temporal FT.

The white line in Fig. 11 indicates the profile of the BVF at the start of the simulation, the black dashed line corresponds to the profile averaged over the last 100 h of the simulation. A magnified vision of the top of the domain is given for $\ell = 0$ in the gray box. An oscillatory behavior of the BVF is apparent at the upper boundary of the computational domain which is not removed by the time average. Over time, the oscillations tend to affect a slightly wider range of radii but do not increase their amplitudes considerably. In the 1D simulation (see Sect. 4.1, Fig. B.1, and Table B.1), we find that the change in the BVF is much smaller and does not develop an oscillatory behavior. Thus, the oscillations apparent in the outer parts of the 2D simulation must be due to dynamics that are only captured in multi-dimensional simulations.

While this behavior could be related for example to numerical effects of our boundary conditions, grid resolution, or the transport of angular momentum by propagating IGWs, the exact cause is not fully understood at this point and still subject of ongoing work. However, the deviation is only within a small part of the whole model and we do not expect it to have a significant impact on the general results nor the frequency spectrum of the waves in the envelope below $R = 0.8\,R_\star$. To resolve also the details of the outermost parts more accurately, a more elaborate outer boundary condition is needed as well as a higher resolution to resolve the small scale heights accurately enough.

IGWs can only exist for frequencies below the BVF (see, e.g., Sect. 3.4.2 in Aerts et al. 2010). This property is reflected in the first panel of Fig. 11 by the fact that the whole possible IGW regime (as defined by $f < N/2\pi$) shows a significant amplitude which then suddenly drops for $f > N/2\pi$. This is in qualitative agreement with Fig. 27 of EM19 and a clear indicator of the excitation of IGWs in the 2D SLH simulation. An increasing number of radial nodes (or, equivalently, a decrease in the radial wavelength) for lower frequencies is another general property of IGWs that is confirmed by the spectra in Fig. 11.

These features have already been seen and described in EM19. However, our simulation also shows additional signals. For $\ell = 0$ (second panel in Fig. 11) no IGWs are excited because they cannot be purely radial. Yet, distinct standing modes reaching maximum velocity near the stellar surface are visible at frequencies larger than the BVF. Therefore, they must be signals of excited p-modes.

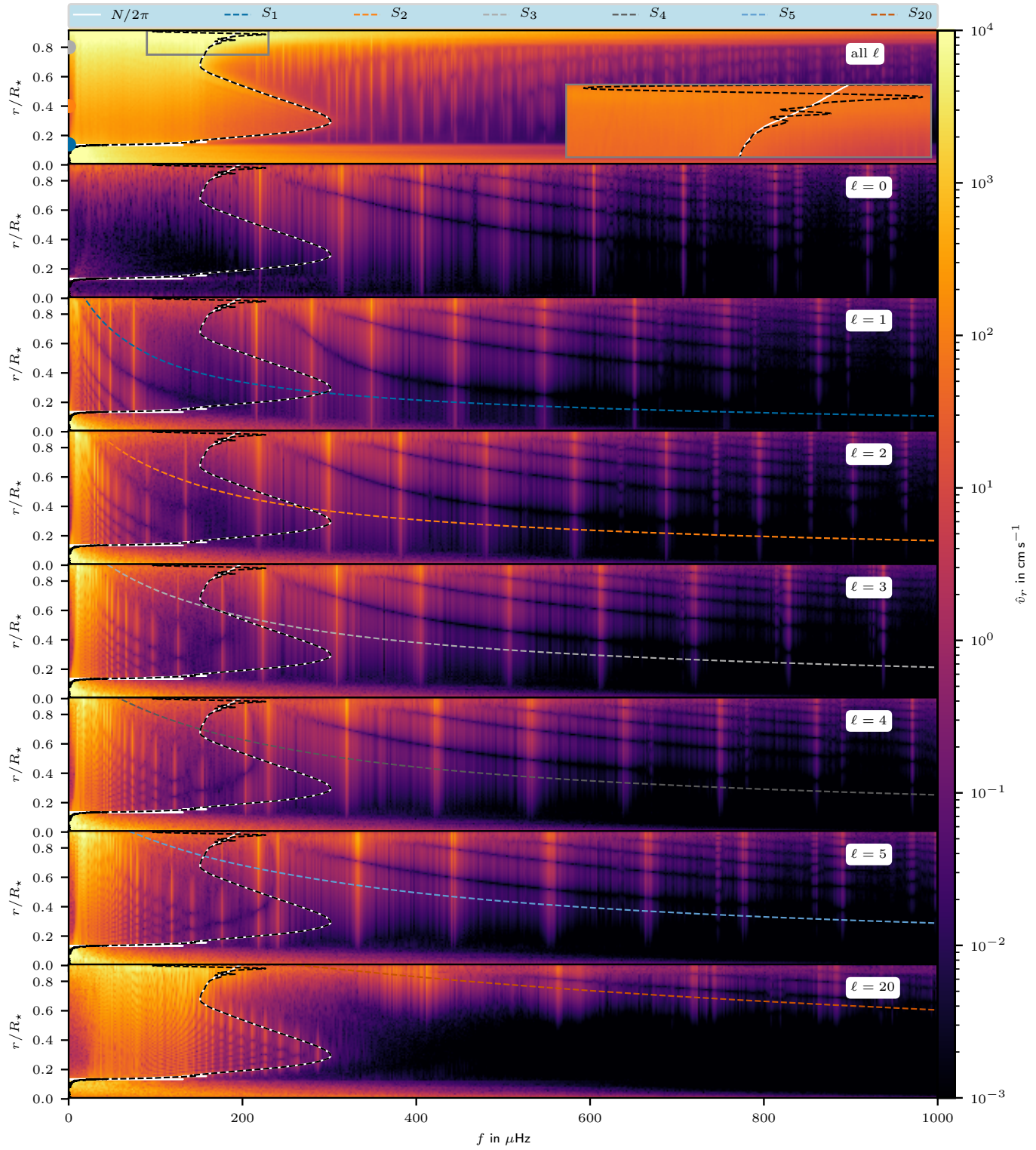

Fig. 11. Frequency spectrum of the radial velocity for a time span of 700 h. The normalization is done in a way that the amplitude of a narrow line of one frequency bin width corresponds to the velocity amplitude of the corresponding wave in the time domain. The data is stored in intervals of 480 s. This allows us to capture frequencies up to $f_{\max} = 10^3\,\mu$Hz with a resolution of $\delta f = 0.4\,\mu$Hz. In order to reduce the background noise, we show the average of the spectrum of 100 individual radial rays. The doublets for the modes with $f \gtrsim 700\,\mu$Hz are due to aliasing, which we verified with a simulation with a very short cadence of outputs. The three colored dots in the uppermost panel mark the radii for which the line profiles are shown in Fig. 16. The white and black lines correspond to the BVF at start and end of the simulation, respectively. Colored dashed lines correspond to the Lamb frequencies of different ℓ values according to Eq. (32). In the *first row*, the uppermost part of the model is magnified (gray box) in order to illustrate the change in the BVF at the end of the simulation. For the magnification, the color scale was adapted to increase the visibility of the lines. We show the spectra for the horizontal velocity in Fig. 12.

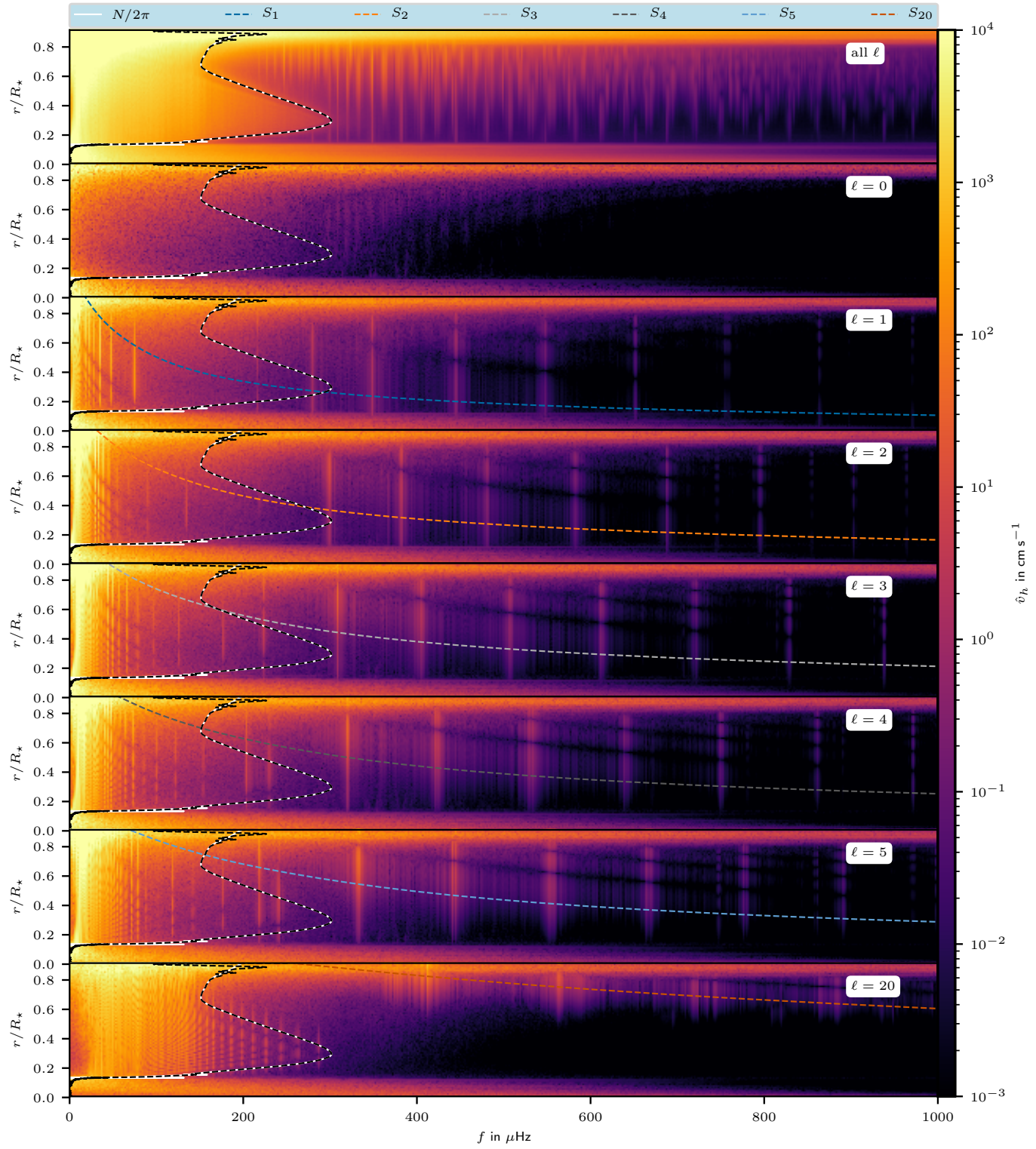

Fig. 12. Frequency spectrum for the horizontal velocity, see Fig. 11 for details. The p-modes are less prominent as their dominant velocity component is radial.

The colored dashed lines in the panels of Fig. 11 for $\ell > 0$ correspond to the respective Lamb frequencies

$$S_\ell = \frac{\ell(\ell+1)\, c_{\rm sound}^2}{r^2}, \tag{32}$$

(e.g., Sect. 3.3.2 of Aerts et al. 2010). They are derived for spherical geometry using spherical harmonics and might not strictly hold in our 2D geometry. However, we still use them here as an estimate to characterize the general behavior of internal waves. A p-mode of angular degree ℓ and frequency f_p can only exist if the frequency fulfills the conditions

$$f_p > \frac{N}{2\pi} \text{ and } f_p > \frac{S_\ell}{2\pi}. \tag{33}$$

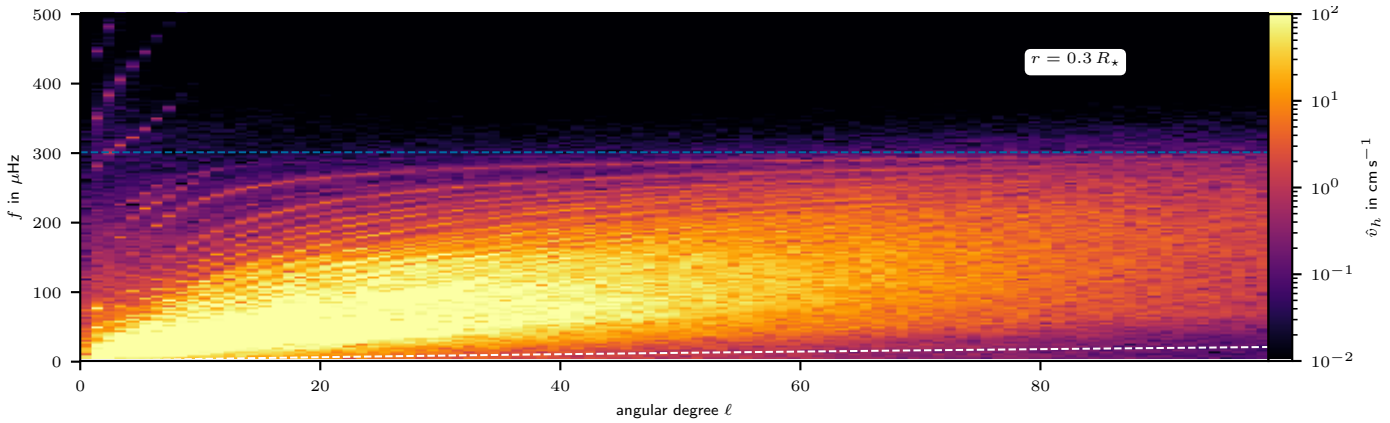

Fig. 13. Color map of amplitudes at different frequencies as a function of the angular degree ℓ at a fixed radius of $R = 0.3\,R_\star$. The blue dashed line corresponds to the BVF at this radius. The white dashed line indicates the cutoff frequency ω_c below which waves are expected to lose too much kinetic energy due to damping to form standing modes.

The corresponding conditions for g-modes are

$$f_g < \frac{N}{2\pi} \text{ and } f_g < \frac{S_\ell}{2\pi}, \tag{34}$$

(see Sect. 3.4 of Aerts et al. 2010 for further details). In regions where the frequency does not fulfill these relations, p- and g-modes are evanescent. This is most easily seen for p-modes in the spectrum for $\ell = 5$ and for g-modes in the spectrum for $\ell = 20$ in Fig. 11.

The occurrence of p-modes is one of the key differences between fully compressible codes and the anelastic approaches. In the latter, p-modes cannot occur because sound waves are not included in the equations. To bring the p-modes of our 2D simulation into context with observations, we compare them to those of the β Cep stars presented in Aerts & De Cat (2003). They find frequencies at low ℓ typically around $f \approx 6\,\mathrm{d}^{-1} \approx 70\,\mu$Hz. For the particular star ω^1 Sco observations indicate $f = 15\,\mathrm{d}^{-1} \approx 174\,\mu$Hz at $\ell = 9$. Of course, the eigenfrequencies of a real star depend on its stellar parameters and excitation mechanism, and β Cep stars have masses typically in the range of 8 $M_\odot$ to 20 $M_\odot$. Thus, the BVFs which set the minimum p-mode frequencies (see Eq. (33)) are smaller compared to our 3 $M_\odot$ model. We find amplitudes associated with p-modes starting at around 300 μHz. Although our model is not directly comparable to the observed β Cep stars, this indicates that the waves, which are excited in our simulations by the convective core, are compatible with those observed in real stars of similar mass. We note, however, that this cannot be seen as a proof for the correctness of the model or the underlying excitation mechanism, especially since p-modes are not typically observed in main-sequence 3 $M_\odot$ stars (Aerts et al. 2010).

For radii deep inside the convection zone ($r \lesssim 0.14\,R_\star$) distinct modes are less pronounced in Figs. 11 and 12 (g-modes generally cannot exist there and in our case the Lamb frequencies prohibit also p-modes) but instead amplitudes in a wide range of frequencies appear, a consequence of the turbulent convection in the core. This is most easily seen for larger ℓ values in the spectrum of the horizontal velocity. On the other hand, also at the largest radii, a band of high amplitudes is visible in the uppermost panel which extends over all frequencies. This is due to the development of a shear flow toward the end of the simulation. As it is located very close to the outer boundary, we cannot determine beyond doubt whether the shear flow is caused by the boundary or by deposition of the IGW's angular momentum due to nonlinear effects. This needs to be examined in more detail in future simulations.

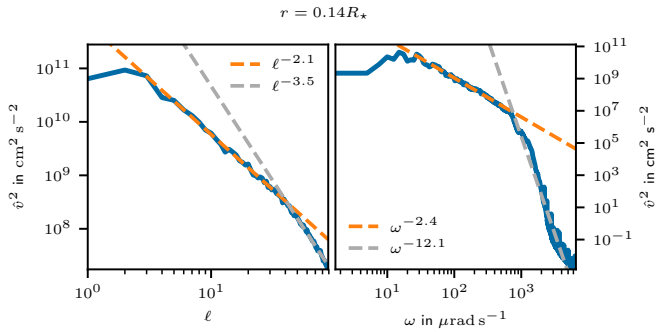

Fig. 14. Kinetic energy as a function of angular degree ℓ (*left panel*) and angular frequency ω (*right panel*) at the top of the convection zone. Dashed lines correspond to power-law fits. This figure is similar to the second and third column in Fig. 6 of Rogers et al. (2013).

Another way of illustrating the emerging spectra of waves is given in Fig. 13 (this is similar to Fig. 22 in Herwig et al. 2006 or Fig. 2 in Alvan et al. 2015). Here, the spectrum at a fixed radius $r = 0.3\,R_\star$ is shown for the first 100 ℓ-values. The horizontal blue line indicates the BVF. One clearly observes distinct modes for small ℓ and decreasing mode spacing for increasing ℓ. The amplitudes drop at the BVF as expected for gravity waves. Alvan et al. (2015) estimate a cutoff frequency ω_c below which waves have lost a considerable amount of the kinetic energy due to radiative diffusion (see their Eq. (26)). The corresponding profile is shown as dashed white line. They argue that a traveling wave without sufficient energy cannot reach the turning point, travel back and interfere with another progressive wave to form a standing mode. Their corresponding cutoff is rather steep and reaches high frequencies, indicating a wide region where they expect progressive waves. This is similar to Fig. 5 of Rogers et al. (2013). In contrast, for the simulation presented here the profile of ω_c is much flatter and stays at much smaller frequencies. It is clear that the excitation of gravity waves from core convection produces an entire spectrum of waves spanning a broad range in frequency.

In Fig. 14 we plot the kinetic energies

$$v^2(\ell) = \sum_{\mathrm{f}} \hat{v}^2_{\ell,f}, \quad v^2(\omega) = \sum_{\ell} \hat{v}^2_{\ell,\omega} \tag{35}$$

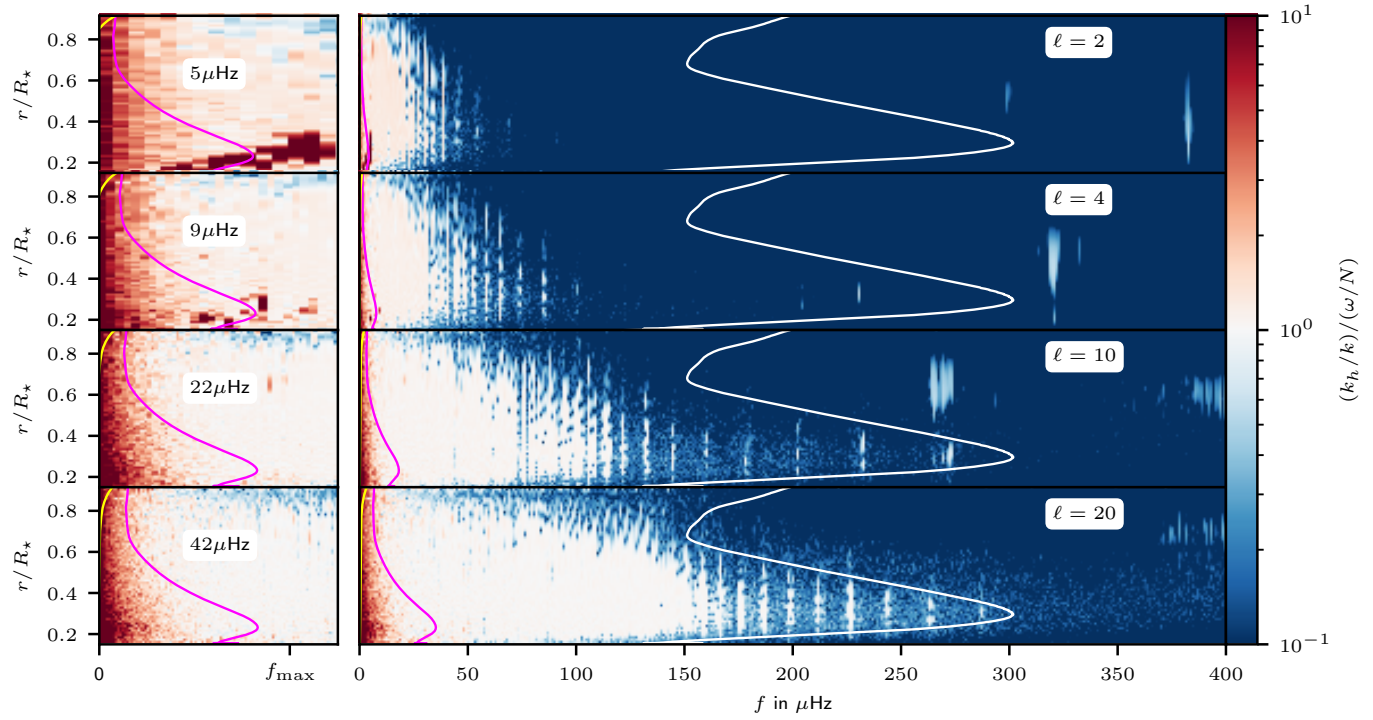

Fig. 15. Ratio of the left and right side of the dispersion relation Eq. (36).The method to extract k_h/k from the simulation is described in the text. A ratio of unity corresponds to a perfect match and is reflected by white regions. A red color indicates a too large value of k_h/k and correspondingly the ratio is too small in blue regions. The white line is the BVF. For frequencies below the yellow line, IGWs are expected to be damped by thermal diffusion. Below the magenta line, the radial wavelength is resolved by less than 10 grid cells. The *left column* zooms into the low frequency region of the corresponding full plane on the right. The frequency given in the white boxes denotes the value of f_{max} which sets the scale of the corresponding x-axis.

at the top of the convection zone. Here, $\hat{v}_{\ell,\omega}$ is the velocity at angular degree ℓ and frequency ω which results from the spatial and temporal FT. The sum over all degrees ℓ is terminated at $\ell = 100$. The spectra are fitted by power-laws, as proposed in Rogers et al. (2013). Their 2D simulation of a nonrotating model gives similar values for $v^2(\ell)$, shown in our left panel. Also the position of the transition between the two regimes is comparable. However, our profiles for $v^2(\omega)$ (right panel) are much steeper (Rogers et al. 2013 find $\omega^{-1.2}$ and $\omega^{-4.8}$). In the 2D simulation presented here the transition between the two regimes is at much higher frequencies.

4.4. Dispersion relations

So far we have presented clear indications of the excitation of IGWs and pressure waves. To further confirm this, we show in the following section that the corresponding dispersion relations are fulfilled for both g- and p-modes.

4.4.1. Dispersion for gravity waves

From theory, one finds a dispersion relation for IGWs of the form (e.g., Sect. 3.1.4 Aerts et al. 2010 or Sect. 3.3.3 Sutherland 2010)

$$\frac{\omega}{N} = \frac{k_h}{|\boldsymbol{k}|} \quad \text{with } |\boldsymbol{k}| = \sqrt{k_h^2 + k_r^2}, \tag{36}$$

where $\omega = 2\pi f$ is the angular frequency of the gravity wave and k_h, k_r are the horizontal and radial wave numbers. We note that this expression is derived under the assumption of a spatially constant value for the BVF. From Fig. 5 it is clear that this is not the case for the stellar model presented here. Therefore, Eq. (36) is expected to hold only for wavelengths that are short compared to the scale height of the BVF.

To estimate how close our simulation follows Eq. (36), we apply the method of EM19 which is briefly summarized in the following:

The angular frequency ω and BVFare readily available quantities. Because of the spatial FT filtering for specific ℓ, we know that $k_h^2 = \ell(\ell+1)/r^2$. The only quantity to determine in Eq. (36) is therefore the vertical wave number $k_r = 2\pi/\lambda_r$ or equivalently the radial wavelength λ_r. To determine the wavelength, the positions of peaks in the amplitude for the FT of the radial velocity are identified for all available frequencies. The distance between adjacent peaks is interpreted as one half of the wavelength at the radial position at the midpoint between the two peaks. We determine the wavelengths starting just above the convection zone until the upper boundary of the model for all frequencies and interpolate in radius afterward. This gives for each frequency f the wavelength $\lambda_{r,f}(r)$. From that, we obtain k_r and are finally able to evaluate Eq. (36) in the entire radius-frequency plane for a specific order ℓ.

To visualize the results, the ratio of the left and right side of Eq. (36) is plotted in Fig. 15 exemplarily for $\ell = 2$, 4, 10, and 20. Regions in which the dispersion relation is fulfilled, that is the ratio is unity, appear white. This reproduces Fig. 28 of EM19. A magenta line denotes the frequency below which one wavelength is resolved by less than 10 grid points: For a given radial grid spacing δ_r, the corresponding wave number is $k_{r,\,n=10} = 2\pi/(10\,\delta r)$ such that this frequency is defined as

$$f_{n=10} = \frac{N}{2\pi} \frac{k_h}{\sqrt{k_h^2 + k_{r,\,n=10}^2}}. \tag{37}$$

The yellow line in Fig. 15 marks the frequency below which one assumes the waves to be dissipated by thermal diffusion. The estimate is based on the equality of the diffusion length and the wavelength at the critical frequency as given by equation[1] (27) of EM19. In comparison to EM19, the effect of dissipation is greatly reduced in the SLH simulation. In our case, we are mainly limited by the radial resolution when going to higher ℓ-values. We see agreement with the dispersion relation of linear internal gravity waves everywhere where such agreement can be expected: for modes that are well resolved in space but with radial wavelengths short enough that N^2 as well as the radius can be considered approximately constant over a single wavelength. This is the case for low-frequency IGW and gets worse for increasing radial wavelengths, corresponding to increasing frequencies. In contrast to EM19, our results are mainly affected by resolution effects rather than damping, yet broad spectra of standing modes are clearly excited in both numerical setups. For a better visibility, the low frequency regions are magnified in the left column of Fig. 15. At frequencies below $5\,\mu$Hz, it is difficult to determine if the dispersion relation is fulfilled because the quality of the FT deteriorates as the number of wave periods that fit into the time window of our analysis decreases. However, we are able to reach much smaller frequencies than the anelastic simulations and provide reliable results for wave frequencies above $5\,\mu$Hz.

Another way of testing the dispersion relation is to measure the inclination of the IGW crests with respect to the radial direction. As the fluid velocity in an internal wave is parallel to the wave crest, we can obtain the inclination by measuring the ratio $v_\mathrm{h}/v_\mathrm{r}$ in our simulation. Because the wave vector $\boldsymbol{k}$ is perpendicular to the crests we have

$$\begin{pmatrix} v_\mathrm{r} \\ v_\mathrm{h} \end{pmatrix} \parallel \begin{pmatrix} -k_\mathrm{h} \\ k_\mathrm{r} \end{pmatrix}, \text{ where } \begin{pmatrix} -k_\mathrm{h} \\ k_\mathrm{r} \end{pmatrix} \cdot \boldsymbol{k} = \boldsymbol{0}. \tag{38}$$

It follows that

$$\left|\frac{v_\mathrm{h}}{v_\mathrm{r}}\right| = \left|\frac{k_\mathrm{r}}{k_\mathrm{h}}\right| \tag{39}$$

and with the aid of Eq. (36) we find the expression

$$\left|\frac{v_\mathrm{h}}{v_\mathrm{r}}\right| = \frac{\sqrt{N^2-\omega^2}}{\omega}, \tag{40}$$

in which the left-hand side can be obtained from the simulation and compared to the theoretical prediction on the right-hand side.

In the top two panels of Fig. 16 we show a line plot representation for the spectra of v_r and v_h at three different radial positions. They are marked by colored dots in the upper panel of Fig. 11. For radii well above the convection zone, the amplitudes rapidly decrease for $f > N/2\pi$. This is expected for a signal mostly made up of IGWs which cannot propagate in this frequency range. Above frequencies of $N/2\pi$ we can see clearly isolated peaks corresponding to p-modes of various angular degrees. The p-mode amplitudes are at least one order of magnitude smaller than the IGW signal across a broad range of frequencies. For the radial velocity, the spectrum is almost flat with a subtle decrease toward higher frequencies. The spectrum for the horizontal velocity shows a decrease already within the IGW regime. Similar to the findings of EM19, these integrated spectra composed of all angular degrees do not show distinct peaks.

[1] Their equation is missing a factor $\sqrt{N^2/\omega^2-1}$. It does not change the result qualitatively but is included here for consistency.

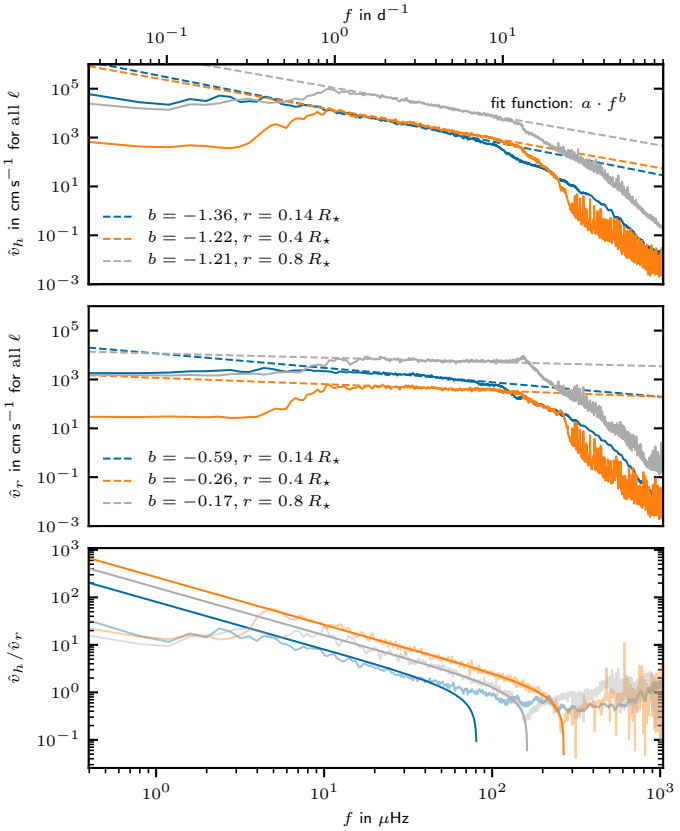

Fig. 16. Line plot representations of the spectra for horizontal and vertical velocity at three different radii $0.14\,R_\star$, $0.4\,R_\star$, and $0.8\,R_\star$ are shown in the *upper two panels*. The dashed lines correspond to the power-law fit as denoted in the labels. The *lowest panel* shows the ratio of the velocity components at each radius (transparent line) and compares them to the prediction according to Eq. (40) (solid lines).

However, our results do not have the steep drop in amplitude at very low frequencies as seen in their Fig. 23, which can be attributed to the lower viscosity and thermal diffusivity in our simulation.

In the lowest panel of Fig. 16 we show the ratio of the velocity components as depicted in the two panels above (semitransparent lines). The solid lines represent the prediction given by Eq. (40). There is an excellent agreement for all three radial positions for frequencies below the BVF. The line for $0.14\,R_\star$ is just beyond the boundary of the convective core and therefore does not follow the steep drop in the ratio as convective motions impact the data. Only for the smallest frequencies the simulation deviates as a result of damping effects and a lack of independent data points for the temporal FT. This result is another strong indication that IGWs are correctly represented in the 2D simulation.

Furthermore, we find the results of our simulations to be comparable to observations of late-B SPB stars. De Cat & Aerts (2002) report the ratio $v_\mathrm{h}/v_\mathrm{r}$ for several SPB stars which are typical g-mode pulsators (this corresponds to the K-value in their Fig. 17). The value ranges from 10 to 100. This observed range is similar to the values shown in the lower panel of Fig. 16 for frequencies to the left of the dip, that is below the BVF. For p-mode pulsators De Cat (2002) (see also Aerts & De Cat 2003) reports K-values for β Cep stars which are typically in the range of 0.01−1. Similar values are found in our 2D simulation at frequencies of standing p-modes which is most easily seen as sharp dips at frequencies above the BVF. Such a simplified comparison

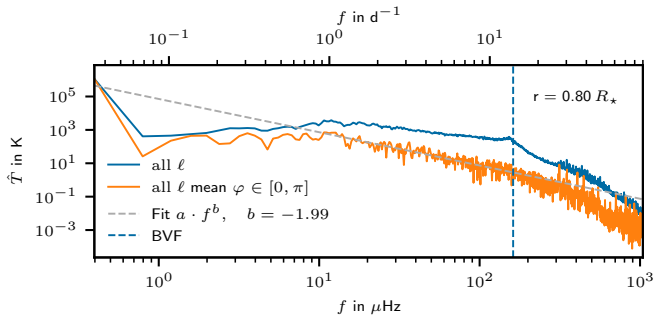

Fig. 17. Spectra for temperature at $r = 0.80\,R_\star$. The orange line shows the spectrum of the temperature fluctuations which have been averaged over half of the circumference of our 2D model. The blue line corresponds to the spectra averaged over 100 radial rays after the FT as it is done for the velocity spectra. The dashed blue vertical line denotes the position of the BVF. The gray line corresponds to a power-law fit for the frequencies ranging from 10 μHz to 200 μHz resulting in an exponent of $b \approx -2$.

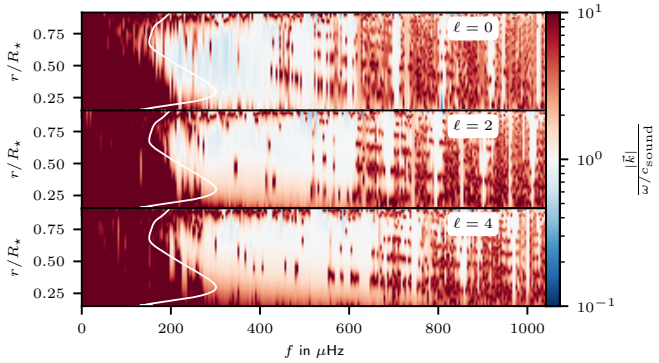

Fig. 18. Same quantities as in Fig. 15 but this time for the dispersion relation of sound waves (Eq. (41)).

of values in the interior of our model to the observations at actual stellar surfaces does not allow for a quantitative comparison or stronger conclusions. However, it shows that the wave spectra that self-consistently arise in our hydrodynamical simulation are compatible with observations of oscillations in real stars of similar mass and evolutionary stage (i.e., SPB stars; De Cat & Aerts 2002).

Besides surface velocities, the variation of the disk-averaged luminosity of stars is another observable. It is supposed that contributions from small-scale fluctuations (high ℓ) are suppressed in this quantity as they cancel out on average whereas large-scale contributions are pronounced (e.g., Aerts et al. 2010, Sect. 6). As a simple estimate of this effect we compute the average temperature over half of the circumference of our 2D model prior to the temporal FT. The result is shown as an orange line in Fig. 17 (for comparison, we show as a blue line the spectra which have been averaged similar to the velocity spectra, i.e., only after the temporal FT). At high frequencies, pressure modes appear clearly as individual peaks. This is, however, not the case in the low frequency regime. We note that our spectrum is like those presented in Bowman et al. (2019a, e.g., see their Fig. 3 for the observables of the O star HD 46150 and the figures in their appendix for additional OB stars). The actual situation for observations is more complex than the diagnostic value of our simulations can be. For example, we do not account for limb darkening while this phenomenon comes into play to determine the net flux variation. The limb darkening has more effect for flux observations but far less for the net velocity variations in the line-of-sight. However, our simple experiment illustrates that the net flux variations do not easily reveal any distinct peaks corresponding to low-ℓ modes in the low-frequency regime despite the expected cancellation of the numerous high-ℓ modes.

4.4.2. Dispersion for pressure waves

For the pressure waves, we perform a similar analysis as described in the previous section except that we now check for the usual dispersion relation of pressure waves

$$\frac{\omega}{c_{\mathrm{sound}}} = |\boldsymbol{k}|\,. \tag{41}$$

The result is shown in Fig. 18 and the colors have the same meaning as in Fig. 15. As expected, the dispersion relation is not fulfilled for $f < N/2\pi$. At frequencies corresponding to a standing mode we get a good agreement with predictions from theory. Furthermore, Fig. 18 indicates that pressure modes are excited in the mixed-mode frequency regime, that is between about 200 μHz and 300 μHz. This suggests that a coupling of p- and g-modes is possible. The deviation between standing modes is probably due to the same reasons as discussed in Sect. 4.4.1. This is further illustrated in Fig. B.2 where we show the amplitudes at two specific frequencies. When the frequency matches a standing mode the wavelength can be detected easily whereas this is not possible for frequencies in-between. These results together with the fact that the modes for a particular angular degree are equidistant in frequency in the regime of high-order p-modes give us confidence that the observed modes are indeed p-modes.

4.5. Wave-amplification

From linear theory, one expects the amplification of IGW toward the surface due to density stratification. As shown in Ratnasingam et al. (2019) for spherical geometry, the prediction for IGW amplification is given by (in the notation[2] of EM19)

$$v_{\mathrm{h}} \propto \left(\frac{r_0}{r}\right)^{3/2} \sqrt{\frac{\rho_0}{\rho}} \left(\frac{N^2 - \omega^2}{N_0^2 - \omega^2}\right)^{1/4} \exp(-\tau/2), \tag{42}$$

where r_0 is the starting point of the wave and ρ_0, N_0 the corresponding density and BVF. The damping factor τ is given by

$$\tau = \int_{r_0}^{r} \mathrm{d}r \frac{\kappa\,(\ell(\ell+1))^{3/2} N^3}{r^3 \omega^4} \sqrt{1 - \frac{\omega^2}{N^2}}. \tag{43}$$

According to Eq. (42), waves are damped by the effects of thermal dissipation and geometry, but amplified by decreasing density. This ignores the damping effect of viscosity. For consistency, Eq. (42) needs to be multiplied by a correction factor $(r_0/r)^{-1/2}$ to account for our 2D polar geometry of an infinite cylinder, which slightly increases the amplification (Ratnasingam et al. 2020). For the radial velocity, Eq. (42) needs to be scaled according to Eq. (40).

In Fig. 19 we compare the result of Eq. (42) for the 3 $M_\odot$ MESA model to the 2D simulation, similar to Fig. 26 of EM19. For both radial and horizontal velocity, the prediction from linear theory and the simulation are in good agreement for

[2] We note that there is an error in the corresponding Eq. (23) of EM19. The expression holds for the horizontal velocity component v_{h} instead of the vertical velocity v_{r} as stated.

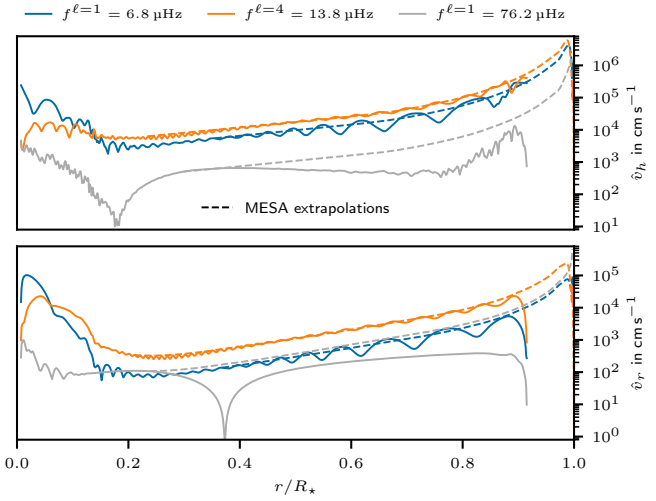

Fig. 19. Velocity amplitude for different frequencies and angular degrees ℓ as function of radius. The amplitudes also include the contribution of the two adjacent frequency bins to account for the fact that peaks typically show a width of two to four bins in our simulation. The expected amplification toward the surface according to Eq. (42) is represented by dashed lines; the 1D MESA profile data serve as input variables whereas the starting points are taken as the simulated amplitudes at the first noticeable local maximum of the respective frequency and angular degree.

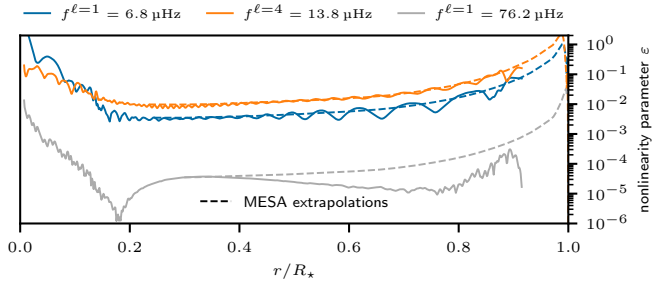

Fig. 20. Nonlinearity parameter ε according to Eq. (44) for the same frequencies and angular degrees as in Fig. 19.

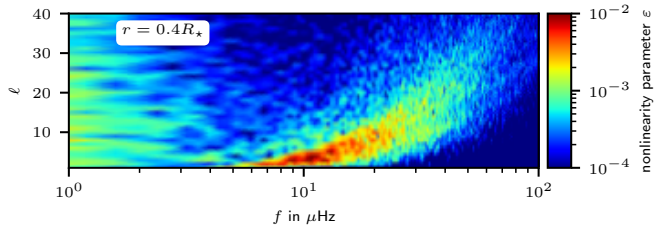

Fig. 21. Nonlinearity parameter at $r = 0.4\,R_\star$ for all available frequencies up to an angular degree of $\ell = 40$.

short radial wavelengths and low frequencies ($f^{\ell=1} = 6.8\,\mu$Hz, $f^{\ell=4} = 13.8\,\mu$Hz), and we assume that the MESA extrapolations toward the surface provide a reasonable estimate of surface velocities. At the highest frequency and longest wavelength ($f^{\ell=1} = 76.2\,\mu$Hz) prediction and simulation clearly differ. However, this is expected as the prediction assumes that wavelengths are short compared to all relevant scale heights in the stratification which is clearly not the case for the highest frequency shown in Fig. 19.

Our extrapolation toward larger radii is a very simplified approach and we do not account for the complex physics at the surface, such as the existence of a subsurface convection zone. Therefore, these numbers should only be seen as an approximation to the order of magnitude of the velocity at the surface due to amplified stellar oscillations. The drop in the simulation data at the very top of the computational domain is an artifact of the numerical solid-wall boundary condition whereas the drop in the prediction is an effect of stronger radiative damping near the surface.

Also for the extrapolated velocities at the stellar surface, the order of magnitude for the ratio of the horizontal velocity over the radial one shown in Fig. 19 is compatible with what is found in time-series spectroscopy of g-mode pulsators (De Cat & Aerts 2002).

4.6. Nonlinearity parameter

If all waves were to remain in the linear regime, a treatment as in Sect. 4.5 would be a sufficient description of the physics involved. Yet it is expected that the amplification toward the surface causes nonlinearities to become relevant at least in certain ranges of frequency and wavenumber. These nonlinearities lead to a redistribution of energy between different wavenumbers and frequencies. Additionally, wave breaking can cause transport of angular momentum from the core, where the waves are excited, to the envelope.

In Ratnasingam et al. (2019) the effect of different input spectra on the expected nonlinearity of IGWs is examined. The nonlinearity can be estimated by

$$\varepsilon = \frac{v_\mathrm{h}}{\omega} k_\mathrm{h} \tag{44}$$

(Press 1981; Barker & Ogilvie 2010). If $\varepsilon \gtrsim 1$, nonlinear effects are dominant. However, as demonstrated in Ratnasingam et al. (2020), already rather small values of ε ($\approx 10^{-3}$) can cause noticeable energy transfer between different frequencies and wavenumbers.

In Fig. 20 we show the result of Eq. (44) for the amplitudes of the horizontal velocity extracted from the simulation and the extrapolation to the surface as illustrated in Fig. 19. The apparent increase in ε with decreasing frequency is caused by the stronger convective wave excitation at lower frequencies. At even lower frequencies, which are not shown here, wave damping becomes dominant and ε decreases further. For the extrapolated amplitudes we find a maximum value for the nonlinearity parameter of $\varepsilon = 2.2$ for $f^{\ell=4} = 13.8\,\mu$Hz.

From this we conclude that nonlinear effects can be expected at the surface in the frequency regime around $10\,\mu$Hz. This is further illustrated in Fig. 21, which shows the value for ε at $r = 0.4\,R_\star$ as a function of frequency f and angular degree ℓ. A narrow range around $10\,\mu$Hz is apparent where the nonlinearity is highest. We note that this looks very similar to *Spectrum K* and *Spectrum LD* in Fig. 5 of Ratnasingam et al. (2019) for convective velocity boosted by a factor of three with respect to the stellar models. The strongest nonlinearity in Fig. 21 is seen in the frequency range in which gravity modes have been detected in a sample of about 30 SPB stars in the *Kepler* data. For all these pulsators, nonlinear behavior has been deduced from the *Kepler* light curves and a low-frequency IGW power excess has been detected after the removal of the coherent g-modes (Pedersen 2020).

We emphasize that the predictive power for the wave amplification and nonlinearity from this SLH simulation is limited. The boosted energy generation in the core and the accompanying increased velocities also impact the amplitudes of the excited

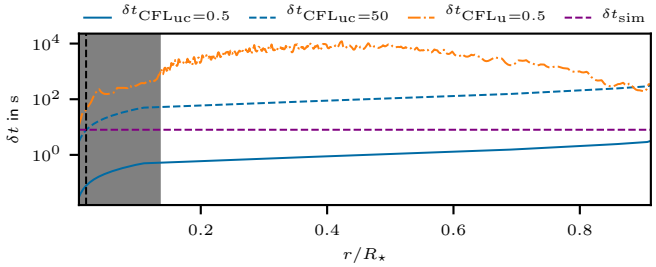

Fig. 22. Time step size as a function of radius for different time step criteria. Because of the polar geometry of the grid, the innermost cells become narrower and thus require shorter time steps. The purple dashed horizontal line denotes the time step size of $\delta t = 8$ s that is used in the 2D simulation. The dashed vertical line marks the radius below which this step size is larger than a time step size according to Eq. (1) with a CFL number of 50. The gray shaded area indicates the convective region.

Table 3. Timings for the SLH code (implicit and explicit) and the pseudo-spectral anelastic code SPIN to perform one time step per cell and core.

Code	Time/cell/step [w−μs]
SLH(impl)	3.3×10^2
SLH(expl)	7.3
SPIN	1.5

waves. Furthermore, convection is known to be faster in 2D simulations and we apply a simple extrapolation from the upper boundary of our 2D model toward the surface. Nevertheless, we believe that the results presented here at least give an idea of what to expect at the stellar surface where we find indication for the existence of nonlinear effects.

4.7. Time stepping and efficiency

After the detailed evaluation of the properties of the excited waves in the previous sections, the paper is concluded with a discussion of the time step sizes and the efficiency of the SLH code.

In Fig. 22, the radial profiles of the time step size $\delta t_{\mathrm{CFL_{uc}=0.5}}(r)$ for explicit time stepping (see Eq. (1)) and the maximum implicit time step size $\delta t_{\mathrm{CFL_{u}=0.5}}(r)$ (see Eq. (2)) are shown for values in the middle of the time span of the 2D simulation. The time step sizes decrease toward the core due to the shrinking azimuthal width of the cells in polar geometry. From the radial profiles, the actual global time step is then given by the minimum over the whole domain. We find $\min[\delta t_{\mathrm{CFL_{uc}=0.5}}(r)] = 0.03$ s and $\min[\delta t_{\mathrm{CFL_{u}=0.5}}(r)] = 21.4$ s. Hence, for implicit time stepping, the possible time step size is roughly 700 times larger than the corresponding explicit time step. This might be counter intuitive as the Mach numbers at the surface are of order unity and one would therefore expect implicit time steps to be closer to the explicit step sizes. In that sense, implicit time stepping helps to overcome the general problem of very small step sizes in polar and spherical geometries for large ratios of the outer to the inner radius of the computational domain.

In Miczek (2013), the propagation of a simple 1D sound wave in SLH is compared to predictions from linear wave theory. The simulations are repeated while successively increasing the implicit time step size. In this test setup, sound waves are resolved without noticeable modification if $\delta t \leq \delta t_{\mathrm{CFL_{uc}=5}}$, whereas they get considerably damped but still propagate at a speed close to the theoretical prediction for $\delta t \approx \delta t_{\mathrm{CFL_{uc}=50}}$. For $\delta t \geq \delta t_{\mathrm{CFL_{uc}=500}}$ sound waves cannot be followed at all anymore.

For the 2D simulation presented here, these findings indicate that choosing a time step size of $\delta t_{\mathrm{CFL_u}} = 0.5$ which corresponds to $\delta t \approx \delta t_{\mathrm{CFL_{uc}=350}}$ at the lower boundary might lead to a strong damping of the sound waves. Although the appropriate time step size clearly depends on the details of the setup and the wavelengths of the considered waves, we follow Miczek (2013) in choosing the time step size in this initial study. As will be shown at the end of this section, this might give a value for the time step size that is too conservative.

For the particular simulation presented here, the time step size is chosen to be $\delta t_{\mathrm{sim}} = 8$ s (dashed purple horizontal line in Fig. 22). For radii smaller than the vertical line, sound waves are expected to suffer from damping as for these cells the time step is larger than $\delta t_{\mathrm{CFL_{uc}=50}}$. This, however, is only a tiny fraction of the whole domain and we do not expect it to have a significant impact on the results. Our choice is a compromise between efficiency and accuracy as will be demonstrated in the following.

To quantify the gain in efficiency when using implicit time stepping, we compare the wall clock time needed to cover a time span of 80 min (2 convective turnover times) when using either implicit or explicit time stepping. For this test, both simulations are restarted at 500 h and all output routines of SLH are disabled in order to minimize possible external effects like a slow file system. We find that the explicit run requires a wall clock time of 37.72 min to perform 15 900 steps on 360 Intel Skylake cores. The implicit run finishes after 6.3 min while performing 600 time steps using the same number of cores. Accordingly, the implicit run is roughly a factor of six faster than the explicit run even though velocities at the top of the computational domain are clearly not in the low-Mach regime, in which implicit time stepping is usually advantageous.

We further compare the efficiency of the SLH code (implicit and explicit) to the pseudo-spectral anelastic SPIN code (EM19). For the comparison, the test runs presented in this section are used for the SLH timings. For the same physical problem, a short test simulation on 300 Ivy Bridge cores for a grid of $1500(r) \times 128(\vartheta) \times 256(\varphi)$ serves as input for the SPIN results.

In Table 3, the timings for the two codes to perform one time step per cell and core are listed. From this measure, the explicit SLH mode is roughly a factor of five slower than the SPIN code, potentially reflecting the fact that SLH has not undergone any substantial optimization effort. The implicit SLH mode is 220 times slower than SPIN with a time step size that is only eight times larger. These numbers illustrates that, while our compressible simulations capture the full set of physics described by the full Euler equations, they come with considerably higher computational costs. Because the SPIN and SLH simulations differ in resolution, computational domain, and the energy boosting, a quantitative comparison considering the wall-clock time needed to evolve a cell by one unit of stellar time is not possible here.

We note that the settings of the SLH implicit mode may not be optimal yet. As stated by Miczek (2013), fine tuning the linear solver for the specific physical problem to be solved and applying a multigrid solver may lead to improved performance. This is subject of ongoing work and the necessary algorithms are readily available in SLH.

To put the computational costs of the SLH runs into context of 3D simulations, we have performed first preliminary low-resolution 3D simulations of the same initial stratification as used for the 2D simulation in this paper on the JUWELS

supercomputer in Jülich, Germany. The domain is discretized in $280(r) \times 90(\vartheta) \times 180(\varphi)$ cells while performing time steps of $\delta t = 8$ s with the ESDIRK23 implicit time stepping scheme. Based on these runs, we estimate that 8×10^5 core-h will be needed to cover 700 h of simulation time. By scaling this number with the number of grid cells, a simulation with $480 \times 180 \times 360$ cells, which corresponds to half of the resolution of the 2D simulation presented here, needs 5.5×10^6 core-h. The reference simulation applies the same time step size as the finer resolved 2D simulation; therefore, a possible change in the step size is not included in the scaling. However, depending on the desired accuracy, a much larger time step can be chosen and the computational costs decrease correspondingly.

This demand of computational resources is a realistic scenario for applications at HPC facilities. A 3D simulation at the same resolution as the 2D simulation requires 44×10^6 core-h which is at the upper limit of common computing time proposals. However, these numbers show that SLH is efficient enough to perform simulations of stellar oscillations also in 3D for sufficiently long time spans.

As demonstrated, the implicit time stepping improves the efficiency of the SLH code. At the same time it is important to confirm that the accuracy at which sound waves are evolved is sufficient. To this end, we restart the simulation from the 2D implicit run at 500 h and evolve it using an explicit, three-stage Runge-Kutta (RK3) scheme (Shu & Osher 1988) which is third-order accurate in time. The time step is set to $\delta t_{\mathrm{CFL_{uc}}=0.5}$, our standard choice for explicit time stepping. The simulation is evolved for 100 h of physical time which corresponds to roughly 80 sound crossing times t_{cross}. We define the sound crossing time to be the time a sound wave needs to travel from the innermost point of the computational domain to the upper boundary,

$$t_{\mathrm{cross}} = \int_{r_0}^{r_1} \frac{1}{c_{\mathrm{sound}}(r)} \,\mathrm{d}r = 1.26\,\mathrm{h}. \tag{45}$$

We expect the time span of $80\,t_{\mathrm{cross}}$ to be sufficient to reveal possible deviations in the spectra.

In Fig. 23, the spectra of the implicit and explicit run are compared at different frequencies corresponding to g- and p-modes. All spectra are based on the same time frame.

Almost no differences between the amplitudes from implicit and explicit time stepping are visible. This result confirms that the propagation of sound waves is treated correctly also in the implicit run. Furthermore, our implicit time step size of 8 s appears to be a rather conservative choice and larger steps sizes might be possible. This could reduce the computational costs considerably and will be investigated in more detail in future simulations.

5. Conclusion

The main goal of this paper has been to verify the capabilities of the time-implicit, compressible SLH code to correctly treat internal gravity waves (IGWs) and p-modes in stars with a convective core. To this end, two test cases have been considered.

The first test is a simple 2D setup where an IGW packet according to the Boussinesq approximation is evolved in time.

We first simulated the propagation of an IGW packet in a weakly-stratified 2D atmosphere. The initial IGW was set up with different expected group velocities. Velocity distributions were extracted from simulations performed using the low-Mach AUSM$^+$-up solver and the classical Roe solver at a few points in time. The ability of the two solvers to follow IGWs was assessed by comparing the numerical solutions with approximate analytic

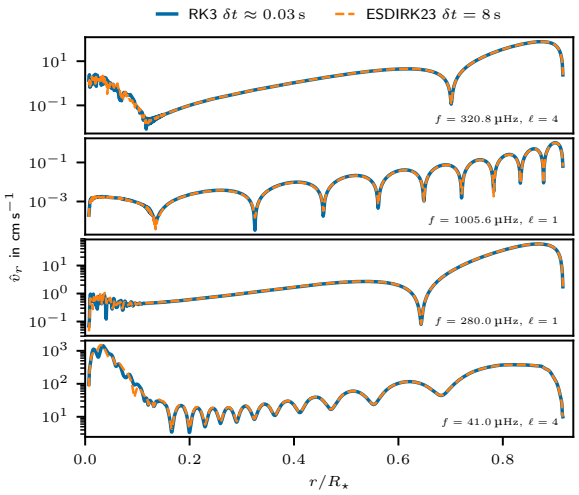

Fig. 23. Amplitudes for the radial velocity spectra at four different frequencies for explicit (blue) and implicit (dashed orange) time stepping. The first two frequencies correspond to p-modes whereas the lower two frequencies match g-modes. For radii above the convection zone, the amplitudes completely overlap each other.

solutions. The Roe solver revealed strong damping and different broadening of the initial wave packet and the packet's group velocity was incorrect. These effects were most pronounced at Mach numbers $\mathrm{Ma}_{gy} = 10^{-3}$. The AUSM$^+$-up scheme showed no significant damping and propagated the packet at a speed close to the prediction. This indicates that a specialized solver is necessary when treating IGWs at low Mach numbers.

Our second test case involving low-Mach-number flows was core hydrogen burning in a $3\,M_\odot$ ZAMS star. We used the same initial 1D model as Edelmann et al. (2019, EM19) to make the simulations comparable. A 2D simulation of this setup was performed using the AUSM$^+$-up solver. The properties of IGW and p-modes were studied following similar methods as in EM19. It was shown that the spectra extracted from the 2D SLH simulations reflect the basic properties of internal waves. A broad spectrum of IGWs is observed for the integrated spectrum whereas individual standing modes can be identified in spectra for single angular degrees ℓ. Modes below the Brunt–Väisälä frequency (BVF) have an increasing radial order with decreasing frequency, a fundamental property of IGWs. Also the dispersion relation extracted from the simulation and the ratios of vertical to horizontal velocities match the theoretical prediction. Furthermore, we find the velocity ratios to be compatible with observational diagnostics from time-series space photometry and high-resolution spectroscopy of slowly pulsating B stars (De Cat & Aerts 2002).

For standing modes above the BVF, the radial order increases with increasing frequency and the dispersion relation matches the one of p-modes. This kind of waves cannot be seen in the anelastic approximation as sound waves are removed from the underlying equations.

Recently, Lecoanet et al. (2019) argued that if the observed variability of stellar surfaces was due to the excitation of IGW from core convection, one would expect to observe distinct peaks in the spectrum which correspond to low ℓ values (see their Fig. 2). We do not see such features in our simulation (see, e.g., Fig. 17). Our explanation for the broad and near-flat profile of IGWs is the same as in EM19: we considered the entire ensemble of waves with large range in radial order and ℓ-values, resulting in small spacings between the resonant frequencies. This "hides"

frequency peaks due to individual low-ℓ modes. We clearly see the individual resonant mode frequencies showing up in the simulations when we limit to particular ℓ-values, as illustrated in Figs. 11 and 12. Moreover, stellar rotation, which is not included in the simulations presented here, would cause spectral line splitting and a further increase in the number of lines in the spectrum.

The amplification of the waves toward the surface agrees with the expectation given in Ratnasingam et al. (2019). In SLH, the treatment of IGWs at very low frequencies is mainly limited by radial resolution. In contrast, anelastic simulations are limited by radiative damping and viscous effects already at larger frequencies. Irrespective of the numerical setup, this work and that of EM19 demonstrate the importance of the excitation and propagation of IGWs as a diagnostic tool for the interior physics of stars burning hydrogen in a convective core.

The simulation of the 3 $M_\odot$ model presented here is intended as a proof of concept and aids in the comparison of the simulations of Rogers et al. (2013) and Edelmann et al. (2019). The chosen 2D geometry reduces computational costs and allows for parameter exploration. A validation of 2D results based on selected 3D models is planned for future work. From the cost of preliminary low-resolution 3D simulations we estimated a need of 44×10^6 core-h to simulate a grid with a size of $960(r) \times 360(\vartheta) \times 720(\varphi)$ for 700 h physical time. Using only half of the number of cells in each dimension reduces the estimated cost to 5.5×10^6 core-h. These estimates are based on a reference run with the same time step size as the higher resolved 2D simulation presented here. Thus, a change in the time step size is not considered in the scaling. Our tests indicate that the implicit time step size could be increased while still resolving sound waves accurately enough. This could considerably reduce the computational costs. Finally, SLH has already proven an excellent scaling up to a large number of cores (e.g., Edelmann & Röpke 2016) such that this kind of 3D simulations are feasible on modern HPC facilities.

After having tested the methods on the 3 $M_\odot$ model, we will extend our study to higher stellar masses and later evolutionary stages for which there are more observational data. Furthermore, we aim to use the velocity and temporal information from our hydrodynamics data to extract synthetic observables by averaging appropriately over the different wavenumber components. Studying the dependence of wave amplitudes on different luminosity boosting will help us to estimate the amplitudes by extrapolating toward stellar values.

Acknowledgements. LH, FKR, and RA acknowledge support by the Klaus Tschira Foundation. PVFE was supported by STFC grant ST/L005549/1 and by the US Department of Energy through the Los Alamos National Laboratory. Los Alamos National Laboratory is operated by Triad National Security, LLC, for the National Nuclear Security Administration of US Department of Energy (Contract No. 89233218CNA000001). This work has been assigned a document release number LA-UR-20-24176. The research leading to these results has received funding from the European Research Council (ERC) under the European Union's Horizon 2020 research and innovation programme (grant agreement No. 670519: MAMSIE). The authors gratefully acknowledge the Gauss Centre for Supercomputing e.V. (www.gauss-centre.eu) for funding this project by providing computing time through the John von Neumann Institute for Computing (NIC) on the GCS Supercomputer JUWELS at Jülich Supercomputing Centre (JSC). LH thanks Johann Higl for insightful comments. We thank Daniel Lecoanet for useful remarks on the paper and the constructive discussion. We also thank the anonymous referee for very helpful and constructive comments that significantly improved this paper.

References

Aerts, C., & De Cat, P. 2003, Space Sci. Rev., 105, 453
Aerts, C., Christensen-Dalsgaard, J., & Kurtz, D. W. 2010, Asteroseismology (Berlin: Springer)
Aerts, C., Mathis, S., & Rogers, T. M. 2019, ARA&A, 57, 35
Alvan, L., Brun, A. S., & Mathis, S. 2014, A&A, 565, A42
Alvan, L., Strugarek, A., Brun, A. S., Mathis, S., & Garcia, R. A. 2015, A&A, 581, A112
Andrassy, R., Herwig, F., Woodward, P., & Ritter, C. 2019, MNRAS, 2556
Barker, A. J., & Ogilvie, G. I. 2010, MNRAS, 404, 1849
Barsukow, W., Edelmann, P. V. F., Klingenberg, C., Miczek, F., & Röpke, F. K. 2017, J. Sci. Comput., 72, 623
Beck, P. G., Bedding, T. R., Mosser, B., et al. 2011, Science, 332, 205
Beck, P. G., Montalban, J., Kallinger, T., et al. 2012, Nature, 481, 55
Bedding, T. R., Mosser, B., Huber, D., et al. 2011, Nature, 471, 608
Bowman, D. M., Aerts, C., Johnston, C., et al. 2019a, A&A, 621, A135
Bowman, D. M., Burssens, S., Pedersen, M. G., et al. 2019b, Nat. Astron., 3, 760
Bowman, D. M., Burssens, S., Símon Díaz, S., et al. 2020, A&A, 640, A36
Brandt, A. 2011, Noise and Vibration Analysis: Signal Analysis and Experimental Procedures, EBL-Schweitzer (Hoboken, NJ, USA: Wiley)
Briquet, M., Aerts, C., Baglin, A., et al. 2011, A&A, 527, A112
Burssens, S., Bowman, D. M., Aerts, C., et al. 2019, MNRAS, 489, 1304
Buysschaert, B., Aerts, C., Bloemen, S., et al. 2015, MNRAS, 453, 89
Calhoun, D. A., Helzel, C., & Leveque, R. J. 2008, SIAM Rev., 50, 723
Cargo, P., & Le Roux, A. 1994, Comptes Rendus de l'Académie des Sciences. Série 1, Mathématique, 318, 73
Chaplin, W. J., & Miglio, A. 2013, ARA&A, 51, 353
Colella, P., Dorr, M. R., Hittinger, J. A., & Martin, D. F. 2011, J. Comput. Phys., 230, 2952
Cristini, A., Hirschi, R., Meakin, C., et al. 2019, MNRAS, 484, 4645
De Cat, P. 2002, in An Observational Overview of Pulsations in β Cep Stars and Slowly Pulsating B Stars (Invited Paper), eds. C. Aerts, T. R. Bedding, & J. Christensen-Dalsgaard, ASP Conf. Ser., 259, 196
De Cat, P., & Aerts, C. 2002, A&A, 393, 965
Edelmann, P. V. F. 2014, Dissertation, Technische Universität München, Germany
Edelmann, P. V. F., & Röpke, F. K. 2016, in JUQUEEN Extreme Scaling Workshop 2016, eds. D. Brömmel, W. Frings, & B. J. N. Wylie, JSC Internal Report No. FZJ-JSC-IB-2016-01, 63
Edelmann, P. V. F., Röpke, F. K., Hirschi, R., Georgy, C., & Jones, S. 2017, A&A, 604, A25
Edelmann, P. V. F., Ratnasingam, R. P., Pedersen, M. G., et al. 2019, ApJ, 876, 4
García, R. A., & Ballot, J. 2019, Liv. Rev. Sol. Phys., 16, 4
Hekker, S., & Christensen-Dalsgaard, J. 2017, A&ARv, 25, 1
Herwig, F., Freytag, B., Hueckstaedt, R. M., & Timmes, F. X. 2006, ApJ, 642, 1057
Hosea, M., & Shampine, L. 1996, Appl. Numer. Math., 20, 21
Kennedy, C. A., & Carpenter, M. H. 2001, Additive Runge-Kutta Schemes for Convection-Diffusion-Reaction Equations, Tech. Rep., NASA Technical Memorandum
Kifonidis, K., & Müller, E. 2012, A&A, 544, A47
Kippenhahn, R., Weigert, A., & Weiss, A. 2012, Stellar Structure and Evolution (Berlin, Heidelberg: Springer-Verlag)
Kurtz, D. W., Saio, H., Takata, M., et al. 2014, MNRAS, 444, 102
Lecoanet, D., Cantiello, M., Quataert, E., et al. 2019, ApJ, 886, L15
Liou, M.-S. 2006, J. Comput. Phys., 214, 137
Maeder, A. 2009, in Physics, Formation and Evolution of Rotating Stars (Berlin, Heidelberg: Springer), Astron. Astrophys. Lib.
Meakin, C. A., & Arnett, D. 2006, ApJ, 637, L53
Meakin, C. A., & Arnett, D. 2007, ApJ, 667, 448
Miczek, F. 2013, Dissertation, Technische Universität München, Germany
Miczek, F., Röpke, F. K., & Edelmann, P. V. F. 2015, A&A, 576, A50
Mosser, B., Goupil, M. J., Belkacem, K., et al. 2012, A&A, 548, A10
Pápics, P. I., Tkachenko, A., Van Reeth, T., et al. 2017, A&A, 598, A74
Paxton, B., Smolec, R., Schwab, J., et al. 2019, ApJS, 243, 10
Pedersen, M. G. 2020, PhD Thesis, KU Leuven, Belgium
Pedersen, M. G., Chowdhury, S., Johnston, C., et al. 2019, ApJ, 872, L9
Press, W. H. 1981, ApJ, 245, 286
Ratnasingam, R. P., Edelmann, P. V. F., & Rogers, T. M. 2019, MNRAS, 482, 5500
Ratnasingam, R. P., Edelmann, P. V. F., & Rogers, T. M. 2020, MNRAS, 497, 4231
Roe, P. L. 1981, J. Comput. Phys., 43, 357
Rogers, T. M., Lin, D. N. C., McElwaine, J. N., & Lau, H. H. B. 2013, ApJ, 772, 21
Saio, H., Kurtz, D. W., Takata, M., et al. 2015, MNRAS, 447, 3264
Shu, C.-W., & Osher, S. 1988, J. Comput. Phys., 77, 439
Sutherland, B. R. 2010, Internal Gravity Waves (Cambridge: Cambridge University Press)
Timmes, F. X., & Swesty, F. D. 2000, ApJS, 126, 501
Van Reeth, T., Tkachenko, A., & Aerts, C. 2016, A&A, 593, A120
Van Reeth, T., Mombarg, J. S. G., Mathis, S., et al. 2018, A&A, 618, A24

Appendix A: Linear theory in Boussinesq approximation

In order to get analytical expressions describing the behavior of IGWs, the fully compressible Euler equations need to be linearized. This can be done in the Boussinesq approximation. It is based on the assumption that pressure and density vary only little in the volume considered. Furthermore, one imposes a time-independent hydrostatic background state and only follows the temporal evolution of deviations from the background state. Additionally, a divergence-free velocity field is assumed. This approach removes the physics of sound waves. For a Boussinesq gas it is convenient to introduce potential temperature ϑ as

$$\vartheta = T\left(\frac{p}{p_0}\right)^{-(\gamma-1)/\gamma}, \tag{A.1}$$

where p_0 is the pressure at a specific reference height in the atmosphere with ϑ_0, ρ_0 (see Sutherland 2010 for a detailed introduction). The two-dimensional equations of motions can then be written as

$$\frac{\mathrm{D}\tilde{\vartheta}}{\mathrm{D}t} + v\frac{\mathrm{d}\vartheta_{\mathrm{hse}}}{\mathrm{d}y} = 0, \tag{A.2}$$

$$\frac{\mathrm{D}u}{\mathrm{D}t} + \frac{1}{\rho_0}\frac{\partial\tilde{p}}{\partial x} = 0, \tag{A.3}$$

$$\frac{\mathrm{D}v}{\mathrm{D}t} + \frac{1}{\rho_0}\frac{\partial\tilde{p}}{\partial y} = -\frac{g}{\vartheta_0}\tilde{\vartheta}, \tag{A.4}$$

$$\frac{\partial u}{\partial x} + \frac{\partial v}{\partial y} = 0, \tag{A.5}$$

where quantities with a tilde denote fluctuations from the hydrostatic background state, for instance $\tilde{p} = p - p_{\mathrm{hse}}$. The letters u, v refer to the horizontal and vertical components of the velocity $\boldsymbol{v} = (v, u)^T$. Further, the notation above makes use of the material derivative $\mathrm{D}q/\mathrm{D}t = \partial q/\partial t + \boldsymbol{v}\nabla q$.

A solution to this set of equations can be found using the ansatz of a 2D plane wave

$$\begin{pmatrix}\tilde{\vartheta}\\ u\\ v\\ \tilde{p}\end{pmatrix} = \begin{pmatrix}A_\vartheta\\ A_u\\ A_v\\ A_p\end{pmatrix}\exp\left[i(\boldsymbol{k}\cdot\boldsymbol{x}) - i\omega t\right], \tag{A.6}$$

which introduces the wave vector $\boldsymbol{k} = (k_x, k_y)^T$, the angular velocity ω, and the complex amplitudes A_i. The absolute values of these amplitudes are assumed to be small, such that terms with products of two or more amplitudes can be neglected. This essentially removes the advection term in the material derivative. Inserting the ansatz into Eqs. (A.2)–(A.5) results in a homogeneous system of linear equations of the form

$$\begin{pmatrix} -i\omega & 0 & \frac{\mathrm{d}\vartheta_{\mathrm{hse}}}{\mathrm{d}y} & 0\\ 0 & -i\omega & 0 & \frac{ik_x}{\rho_0}\\ \frac{g}{\vartheta_0} & 0 & -i\omega & \frac{ik_y}{\rho_0}\\ 0 & ik_x & ik_y & 0\end{pmatrix}\cdot\begin{pmatrix}A_\vartheta\\ A_u\\ A_v\\ A_p\end{pmatrix} = M\cdot\boldsymbol{A} = \boldsymbol{0}. \tag{A.7}$$

Nontrivial solutions exist only if $\det(M) = 0$ which leads to the dispersion relation for Boussinesq IGWs

$$\omega^2 = -\frac{\mathrm{d}\vartheta_{\mathrm{hse}}}{\mathrm{d}y}\frac{g}{\vartheta_0}\frac{k_x^2}{|\boldsymbol{k}|^2} = -\frac{\mathrm{d}\vartheta_{\mathrm{hse}}}{\mathrm{d}y}\frac{g}{\vartheta_0}\cos^2(\theta), \tag{A.8}$$

where we have used $\boldsymbol{k}\cdot\boldsymbol{e}_x = k_x = |\boldsymbol{k}|\cos\theta$ with $\boldsymbol{e}_x$ being the unit vector in horizontal direction and θ the angle between the wave vector $\boldsymbol{k}$ and the horizontal direction. The dispersion relation is usually written in the form

$$\omega = N_0\cos(\theta), \tag{A.9}$$

where

$$N_0 = \sqrt{-\frac{\mathrm{d}\vartheta_{\mathrm{hse}}}{\mathrm{d}y}\frac{g}{\vartheta_{\mathrm{hse}}}} \approx \sqrt{-\frac{\mathrm{d}\vartheta_{\mathrm{hse}}}{\mathrm{d}y}\frac{g}{\vartheta_0}} \tag{A.10}$$

is the BVFin the Boussinesq approximation (see, e.g., Sutherland 2010, Sect. 3.2). This result shows that the angular frequency does not depend on the absolute value of the wave vector $\boldsymbol{k}$ and that IGWs do not propagate isotropically. The maximum frequency is $\omega = N_0$ for $\theta = 0°$ and no purely vertical waves exist as $\omega = 0$ for $\theta = 90°$.

For the specific solution of Eq. (A.7), we set the amplitude of the vertical velocity as free parameter and express the other amplitudes accordingly:

$$A_\vartheta = -\frac{i}{\omega}\frac{\mathrm{d}\vartheta_{\mathrm{hse}}}{\mathrm{d}y}A_v, \tag{A.11}$$

$$A_u = -\frac{k_y}{k_x}A_v, \tag{A.12}$$

$$A_p = -\rho_0\omega\frac{k_y}{k_x^2}A_v. \tag{A.13}$$

As Eq. (A.7) is a linear system, any superposition of solutions remains a solution to the system. The group velocity of such a wave packet is then given by

$$\boldsymbol{c}_g = \nabla_{\boldsymbol{k}}\omega = \frac{N_0}{k_x}\cos\theta\sin\theta\begin{pmatrix}\sin\theta\\ -\cos\theta\end{pmatrix}, \tag{A.14}$$

if one uses $\sin\theta = k_y/|\boldsymbol{k}|$.

In order to describe the time evolution of a wave packet, we follow the methods described in Sutherland (2010, Sect. 1.15) which we generalize to 2D and apply to the specific setup presented in Sect. 3.

In linear theory, a quasi-monochromatic wave packet $\eta(\boldsymbol{x}, t)$ is usually described as

$$\eta(\boldsymbol{x}, t) = \mathcal{A}(\boldsymbol{x}, t)\exp\left[i\left(\boldsymbol{k}_0\cdot\boldsymbol{x} - \omega(\boldsymbol{k}_0)t\right)\right], \tag{A.15}$$

where the amplitude modulation function $\mathcal{A}(\boldsymbol{x}, t)$ changes much slower in space and time than the exponential function in Eq. (A.15). The wave packet $\eta(\boldsymbol{x}, t)$ can be represented via a FT as

$$\eta(\boldsymbol{x}, t) = \int_{-\infty}^{\infty}\hat{\eta}(\boldsymbol{k})\exp\left[i\left(\boldsymbol{k}\cdot\boldsymbol{k} - \omega(\boldsymbol{k})t\right)\right]\mathrm{d}\boldsymbol{k} \tag{A.16}$$

and, by applying the inverse FT, its spectral representation reads

$$\hat{\eta}(\boldsymbol{k}) = \frac{1}{(2\pi)^2}\int_{-\infty}^{\infty}\eta(\boldsymbol{x}, 0)\exp\left[-i\boldsymbol{k}\cdot\boldsymbol{x}\right]\mathrm{d}\boldsymbol{x}. \tag{A.17}$$

From Eqs. (A.15) and (A.17) it further follows that

$$\begin{aligned}\mathcal{A}(\boldsymbol{x}, t) &= \eta(\boldsymbol{x}, t)\exp\left[-i\left(\boldsymbol{k}_0\cdot\boldsymbol{x} - \omega(\boldsymbol{k}_0)t\right)\right]\\ &= \int_{-\infty}^{\infty}\hat{\eta}(\boldsymbol{k})\exp\left[i\Delta\boldsymbol{k}\cdot\boldsymbol{x}\right]\exp\left[-i\Delta\omega t\right]\mathrm{d}\boldsymbol{k},\end{aligned} \tag{A.18}$$

where $\Delta\boldsymbol{k} = \boldsymbol{k} - \boldsymbol{k}_0$ and $\Delta\omega = \omega(\boldsymbol{k}) - \omega(\boldsymbol{k}_0)$. For $t = 0$, Eq. (A.18) illustrates that an initial amplitude modulation $\mathcal{A}(\boldsymbol{x}, 0)$ introduces waves with $\boldsymbol{k} \neq \boldsymbol{k}_0$. Because the wave packet is quasi-monochromatic with a typical wavenumber of $\boldsymbol{k}_0$, the amplitude

$\hat{\eta}(\boldsymbol{k})$ must decrease quickly for $\boldsymbol{k} \neq \boldsymbol{k}_0$. However, in the presence of a nontrivial dispersion relation $\omega = \omega(\boldsymbol{k})$, any superposition of waves with different wavenumbers will lead to a broadening of the initial wave packet over time. This will be explicitly shown for the setup presented in Sect. 3.

Here, the initial vertical velocity modulation is a Gaussian as given by Eq. (11):

$$\eta(\boldsymbol{x}, 0) = \underbrace{\mathcal{A}_0 \exp\left[-\frac{y^2}{2\sigma^2}\right]}_{\mathcal{A}(\boldsymbol{x},0)} \exp\left[i\boldsymbol{k}_0 \cdot \boldsymbol{x}\right] \tag{A.19}$$

with

$$\mathcal{A}_0 = f_{\mathrm{Ma}} \sqrt{\gamma \mathcal{R} T_0/\mu}; \quad \sigma = \beta H_{\mathrm{p}}/2. \tag{A.20}$$

Evaluating the FT in Eq. (A.16) leads to

$$\hat{\eta}(\boldsymbol{k}) = \delta(k_x - k_{x,0}) \sqrt{2\pi}\sigma \mathcal{A}_0 \exp\left[-\frac{1}{2}\sigma^2 \Delta k_y^2\right], \tag{A.21}$$

where δ denotes the Dirac delta function. This specific form of $\eta(\boldsymbol{k})$ illustrates that a narrower Gaussian modulation in real space leads to a broader distribution in wavenumber space and consequently to a larger dispersion.

From Eqs. (A.18) and (A.21) the time evolution of $\mathcal{A}$ is determined. To evaluate the FT in Eq. (A.18), we expand the dispersion relation in a Taylor series up to second order

$$\begin{aligned}\omega(\boldsymbol{k}) =& \omega(k_0) + \nabla_{\boldsymbol{k}}\omega|_{\boldsymbol{k}_0}\Delta\boldsymbol{k} + \frac{1}{2}\left(\partial^2_{k_x,k_x}\omega|_{\boldsymbol{k}_0}\Delta k_x^2 + \partial^2_{k_y,k_y}\omega|_{\boldsymbol{k}_0}\Delta k_y^2\right) \\ &+ \partial^2_{k_x,k_y}\omega|_{\boldsymbol{k}_0}\Delta k_x \Delta k_y + O\left(k^3\right)\end{aligned} \tag{A.22}$$

where we have introduced the abbreviations $\partial_q = \frac{\partial}{\partial q}$, $\partial^2_{p,q} = \frac{\partial^2}{\partial p \partial q}$ for convenience. Inserting Eqs. (A.21) and (A.22) into Eq. (A.18) gives

$$\begin{aligned}\mathcal{A}(\boldsymbol{x}, t) = \sqrt{2\pi}\sigma\mathcal{A}_0 \int_{-\infty}^{\infty} &\exp\left[i\Delta k_y y\right] \\ &\times \exp\left[-\frac{1}{2}\sigma^2\Delta k_y^2 - i\left(\nabla_{\boldsymbol{k}}\omega|_{\boldsymbol{k}_0} + \partial^2_{k_y,k_y}\omega|_{\boldsymbol{k}_0}\Delta k_y^2\right)t\right] \mathrm{d}k_y.\end{aligned} \tag{A.23}$$

This can be simplified to

$$\mathcal{A}(\boldsymbol{X}, t) = \sqrt{2\pi}\sigma\mathcal{A}_0 \int_{-\infty}^{\infty} \exp\left[-\frac{\tilde{\sigma}^2}{2}\Delta k_y^2\right] \exp\left[i\Delta k_y Y\right] \mathrm{d}k_y, \tag{A.24}$$

by transforming into a moving frame via

$$\boldsymbol{X} = (X, Y)^T = \boldsymbol{x} - \nabla_{\boldsymbol{k}}\omega|_{\boldsymbol{k}_0} t \tag{A.25}$$

and setting

$$\tilde{\sigma} = \sqrt{\sigma^2 + i\partial^2_{k_y,k_y}\omega|_{\boldsymbol{k}_0} t}. \tag{A.26}$$

The integral in Eq. (A.24) is again the FT of a Gaussian and leads to the final expression

$$\mathcal{A}(\boldsymbol{X}, t) = \mathcal{A}_0 \frac{\sigma}{\tilde{\sigma}} \exp\left[\frac{-Y^2}{2\tilde{\sigma}^2}\right] \tag{A.27}$$

where the absolute value of $\mathcal{A}$ is given by

$$|\mathcal{A}(\boldsymbol{X}, t)| = \frac{\mathcal{A}_0\sigma}{\left(\sigma^4 + \left(\partial^2_{k_y,k_y}\omega|_{\boldsymbol{k}_0} t\right)^2\right)^{1/4}} \cdot \exp\left[-\frac{Y^2}{2}\frac{1}{\sigma^2 + \left(\frac{\partial^2_{k_y,k_y}\omega|_{\boldsymbol{k}_0} t}{\sigma}\right)^2}\right]. \tag{A.28}$$

Equations (A.27) and (A.28) describe the broadening and decrease in amplitude of an initial Gaussian profile over time when considering the dispersion relation up to second order in $\boldsymbol{k}$ in a system of coordinates moving with the wave packet at its group velocity $\nabla_{\boldsymbol{k}}\omega|_{\boldsymbol{k}_0}$. For the dispersion relation of a Boussinesq IGW according to Eq. (A.9), the group velocity is given by Eq. (A.14) and

$$\partial^2_{k_y,k_y}\omega|_{\boldsymbol{k}_0} = N_0 k_{0,x} \frac{2k_{0,y}^2 - k_{0,x}^2}{\left(k_{0,x}^2 + k_{0,y}^2\right)^{5/2}}. \tag{A.29}$$

Appendix B: Supplementary plots and tables

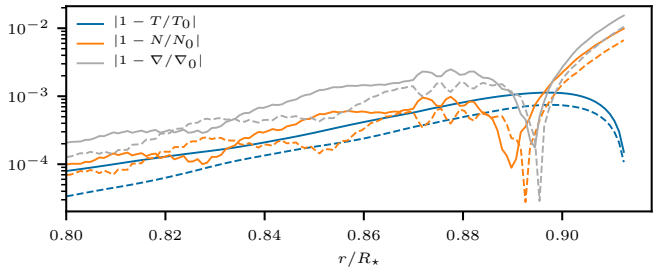

Fig. B.1. Relative deviation from the initial profile for the 1D simulations described in Sect. 4.1 at $t \sim 1100$ h. Shown are results for the temperature T, the BVF N, and the temperature gradient $\nabla = \partial \log T/\partial \log P$, respectively. Solid lines correspond to cylindrical geometry whereas dashed lines denote the results for spherical geometry. Only the surface of the computational domain is shown to emphasize the change at the outer radial boundary. The deviations are even smaller in the inner part which is not shown here.

Table B.1. Maximum deviations for the quantities shown in Fig. B.1.

Quantity	Maximum
$\lvert 1 - T/T_0\rvert_{\mathrm{cyl}}$	1.1×10^{-3}
$\lvert 1 - T/T_0\rvert_{\mathrm{sph}}$	7.5×10^{-4}
$\lvert 1 - N/N_0\rvert_{\mathrm{cyl}}$	9.9×10^{-2}
$\lvert 1 - N/N_0\rvert_{\mathrm{sph}}$	6.7×10^{-3}
$\lvert 1 - \nabla/\nabla_0\rvert_{\mathrm{cyl}}$	1.5×10^{-2}
$\lvert 1 - \nabla/\nabla_0\rvert_{\mathrm{sph}}$	1.1×10^{-2}

Notes. The subscripts denote cylindrical and spherical geometry, respectively.

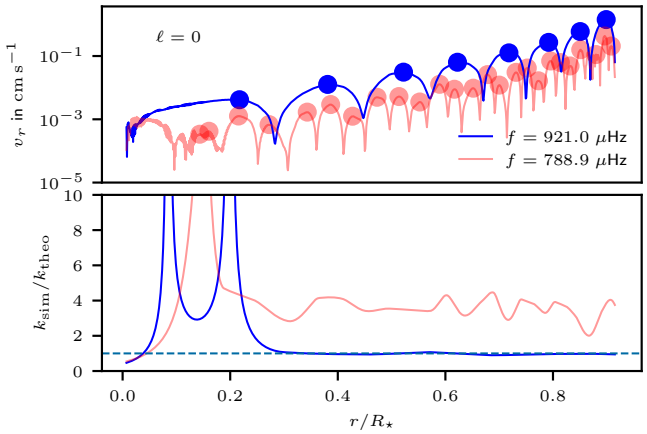

Fig. B.2. Check for the dispersion relation of sound waves. *Upper panel*: amplitudes of the radial velocity at two different frequencies for $\ell = 0$. Circles mark radii where our routine detects peaks in the amplitude. The radial wavelengths are then estimated from the distance of neighboring peaks. For the blue line, the frequency matches a standing mode and it shows well defined, distinct peaks. The red line corresponds to a frequency which is between standing modes and shows small-scale incoherent oscillations with many peaks. *Lower panel*: resulting wave numbers from the simulation are compared to the expectation for sound waves $k_{\rm theo} = 2\pi f/c_{\rm sound}$. We find the blue line in good agreement with theory for radii above the convection zone while the red line considerably differs.

CHAPTER 3

Conclusion

In this thesis, the finite-volume SLH code was used to simulate different hydrodynamic phenomena regarding the stellar interior, with a focus on low-Mach flows. As discussed in Chapter 1, such simulations are important in order to resolve the current difficulties of 1D parametrization in conventional stellar evolution codes, but at the same time they are numerically challenging. The results presented in Chapter 2 demonstrate that the combination of elaborate numerical methods used in the SLH code alleviates some of these challenges. The approach taken with the SLH code is therefore promising regarding more realistic, multidimensional simulations. In the following Section 3.1, each of the publications in Chapter 2 is separately summarized in a simplified fashion. The publications are then brought into context and discussed in the light of current research in the field of stellar hydrodynamics in Section 3.2. The thesis ends with a brief outlook on possible next steps in Section 3.3.

3.1 Summary of the individual publications

Well-balancing [Section 2.1]

Numerical codes for hydrodynamic simulations need to be able to maintain the hydrostatic background stratification of stars accurately in order to evolve small dynamical perturbations of the equilibrium, such as convection. However, due to the different discretization of the hydrodynamic equations and the gravity source term in finite-volume schemes, spurious velocities may deteriorate the physical flow. Well-balancing techniques enhance the accuracy at which the equilibria are maintained. In Section 2.1, three well-balancing schemes were tested in simulations with the SLH code. The Cargo-LeRoux well-balancing method (Edelmann, 2014; Edelmann et al., 2021) modifies the EoS such that only deviations from the initial hydrostatic pressure and density profiles enter the numerical flux function. The α-β well-balancing method (Berberich et al., 2018, 2019) scales the set of thermodynamic variables that is reconstructed at the cell interfaces with their a priori calculated profiles in hydrostatic equilibrium. For hydrostatic initial conditions, the left and right reconstructed states at the cell interface are then identical and the numerical flux vanishes. Using the Deviation well-balancing method (Berberich et al., 2021), only the difference between a stationary target solution and the grid state are evolved in time. If the grid state is identical to the target solution, the numerical flux vanishes. The target solution may be a hydrostatic solution, but also stationary solutions that involve non-zero velocities are possible.

The three well-balancing schemes in combination with the AUSM$^+$−up flux were benchmarked for a suite of 1D and 2D test problems: (i) different hydrostatic atmospheres, (ii) a slowly rising bubble in an isentropic hydrostatic atmosphere, (iii) a toy-model convection zone, and (iv) a density perturbation orbiting a central mass.

Test case (i) demonstrates that without well-balancing, simulations of hydrostatic atmospheres quickly develop spurious velocities. Applying well-balancing significantly improves

the stability, while results obtained with α-β and Deviation well-balancing are generally superior compared to Cargo-LeRoux well-balancing. However, the tests also reveal that instabilities develop in all simulations that use the low-Mach AUSM$^+$−up flux and, over long timescales, some simulations eventually reach Mach numbers in the range of 10^{-4} to 10^{-2}, depending on the applied well-balancing scheme and type of the model atmosphere. It is suspected that the instabilities are checkerboard modes due to a reduced pressure-velocity coupling in combination with unresolved IGW. In simulations using a non low-Mach flux, the atmospheres remain stable. Whether the instabilities are problematic in real astrophysical applications depends on many factors, as, for example, the strength of the stratification, the spatial dimensions and resolution, or the covered timescales. It is therefore important to critically inspect the results obtained with the AUSM$^+$−up flux when it is used to address scientific questions.

Test cases (ii) and (iii) demonstrate that combining the AUSM$^+$−up flux with α-β or Deviation well-balancing enables simulations of dynamical phenomena at low-Mach numbers also in strongly stratified setups. It was further noticed that a prerequisite for this is the inclusion of the potential energy into the energy budget, such that it does not enter as energy source term (e.g., see Miczek, 2013, Sect. 2.3). In this way, the sum of the internal, kinetic, and potential energy is conserved and no source term appears in the energy equation. In particular, test case (iii) validates that convection could be followed down to Mach numbers of Ma $\sim 10^{-4}$, reaching the expected regime for convection in actual stars.[9] For the Cargo-LeRoux well-balancing scheme, however, the flows in test cases (ii) and (iii) show an unphysical behavior below Mach numbers of about 10^{-3}.

Test case (iv) demonstrates the ability of the Deviation well-balancing scheme to balance also non-static setups. In the non well-balanced simulation, mass quickly accumulates at the inner boundary of the domain while the angular average of the initial perturbation is maintained even after many orbits when Deviation well-balancing is used.

Overall, the results in the different test scenarios indicate that the most promising scheme is the Deviation well-balancing method. It is the most flexible approach and produces reasonable results for all test problems. This represents important progress toward realistic simulations of stars. Without well-balancing, numerical instabilities generally prevent the simulated flow from reaching Mach numbers below Ma $\sim 10^{-3}$.

Helium shell burning [Section 2.2]

In Section 2.2, the AUSM$^+$−up flux was applied in combination with Cargo-LeRoux well-balancing to the case of convective helium shell burning. At the time when the simulations for this project were carried out, no other well-balancing method was readily available in the SLH code. Because of the known deficiencies of Cargo-LeRoux well-balancing, the energy generation was boosted by factors of 3×10^3, 1×10^4, and 3×10^4, leading to Mach numbers between 10^{-3} and 10^{-2}. The simulations were used to verify the results obtained with the applied low-Mach methods and to obtain fitting values (A, n) for the Bulk-Richardson entrainment law (Eq. (1.22)).

In the simulated flows, no signs of instabilities are apparent and the obtained convective velocities scale with the input energy as expected. Comparing fundamental properties of the turbulent convective flow between the AUSM$^+$−up solver and its non low-Mach variant AUSM$^+_{\mathrm{B}}$−up shows the superiority of AUSM$^+$−up already at intermediate Mach numbers: At the same resolution, it resolves the turbulent Kolmogorov-like spectrum toward scales roughly two times smaller. Or, equivalently, it requires one eighth of the cells to resolve similar

[9] Further, unpublished results indicate that even lower Mach numbers can be achieved.

scales as the $\mathrm{AUSM}_{\mathrm{B}}^{+}-$up flux. Furthermore, the kinetic energy dissipation as obtained from the RA-ILES equations and the width of the upper and lower transition from convective to radiative regions seem to be converged already at smaller resolutions compared to the $\mathrm{AUSM}_{\mathrm{B}}^{+}-$up flux.

The simulations further confirm the findings of other publications, namely that the stiffness of a boundary has a significant influence on the entrainment of material into the convection zones. By measuring the entrainment rates for different energy boostings, the parameters (A, n) of the Bulk-Richardson scaling (Eq. (1.22)) are determined. They are compatible with values reported for carbon shell burning, but differ, for example, from values reported for oxygen shell burning. The origin of the discrepancy, numerical or physical, has yet to be addressed in detail. Furthermore, it was estimated that the increase of the mean entropy in the convective region and the associated successively destabilization at the upper boundary constitutes up to 50 % of the measured entrainment rate. This effect is already captured in 1D evolution calculations and should therefore be subtracted from the measured mass entrainment that is used to determine the Bulk-Richardson scaling for turbulent mixing.

An important phenomenon which has not been considered in these simulations are waves. These are excited by convection, travel throughout the star and possibly contribute to mixing and redistribution of angular momentum. Asteroseismology deduces information on properties of stellar interior from observations of their surface signatures. Therefore, they are interesting phenomena to be followed in hydrodynamic simulations. Their detailed analysis is prohibited by the restricted computational domain of the simulation presented.

Excitation of waves by core convection [Section 2.3]

The ability of the SLH code to evolve waves inside stars was specifically addressed in Section 2.3 for a test scenario and a realistic stellar setup. The test consists of a 2D setup in which an IGW packet is evolved on top of a weakly stratified atmosphere. For such a simplified setup, linear theory predicts the evolution of the amplitude function and group velocity of the wave packet. The results obtained with the $\mathrm{AUSM}^{+}-$up flux are fully compatible with the analytical solution, even at very low Mach numbers. In contrast, the standard Roe solver evolves the wave packet at the wrong group velocities and the amplitude quickly decreases due to high dissipation. This indicates that low-Mach methods are also of importance for the proper propagation of waves insides stars.

In addition to the test setup, the excitation of waves by core convection in a $3\,\mathrm{M}_{\odot}$ star has been studied by means of 2D simulations. The reduced computational costs compared to 3D simulations allowed the inclusion of more than 90 % of the star's envelope and to follow the propagation of the waves starting from their point of excitation near the core up to the surface for roughly one month of physical time. The luminosity had to be boosted by a factor of 10^3 in order to use Cargo-LeRoux well-balancing (the only well-balancing method available at the time) with the $\mathrm{AUSM}^{+}-$up flux. This is, however, much smaller compared to the required boosting in the simulations of the same initial model by Edelmann et al. (2019). With their anelastic, pseudo-spectral approach to model fluid dynamics, artificial viscosity and thermal diffusivity are required for numerical stability. To reach Reynolds numbers in the turbulent regime, Edelmann et al. (2019) therefore boosted the luminosity by a factor of 10^6.

The analysis of the frequency spectrum of the simulated waves in the envelope of the star reveals that they can be identified as standing IGW (g-modes), sound waves (p-modes), and propagating waves. Various properties measured from the simulation are in good agreement with linear theory and it can be concluded that they are represented in a physically correct way in the simulation. Furthermore, the results show that mild nonlinear effects can be

expected at the stellar surface, constituting a possible mechanism for transport of angular momentum.

As the impact of viscosity and thermal diffusivity increases with decreasing frequency, the SLH code is able to resolve waves at much smaller frequencies in addition to the inclusion of p-modes compared to similar anelastic simulations. Furthermore, some qualitative agreements between the surface spectra in the simulations and observations are found. For example, the ratio of vertical to horizontal velocity components is in agreement with observations of SPB stars. The flat shape of the frequency spectrum is also compatible with recent observations of OB stars.

The implicit time stepping used in these simulations constitutes a major benefit when using standard polar/spherical grids: The curvature of the grid leads to cells in the core region which are much smaller compared to cells at the surface. For explicit time stepping, the short sound crossing time for the small cells dictates a correspondingly small global time step. The applied implicit time stepping enabled a step size that is about 260 times larger. This reduces the computational cost by a factor of 6 compared to the explicit mode of the SLH code.

3.2 Discussion

This thesis represents an important step toward more realistic simulations of astrophysical flows at low Mach numbers. The foundation for this was already laid by the work of Miczek (2013) and Edelmann (2014) who developed the main part of the SLH code, identified the fundamental problems when simulating low-Mach flows, and suggested different methods to tackle these problems, including the AUSM$^+$−up flux function and the Cargo-LeRoux well-balancing method. The value of the present thesis consists in finding working combinations of the different components and the critical assessment of their performance. This way, several problems, as for example implementation details or conceptional issues, could be identified that prevented earlier SLH simulations from reaching low Mach numbers. Their manifestation in the resulting flows are often subtle and hidden underneath a seemingly correct main flow. In particular, it was recognized that the Cargo-LeRoux method is not suitable for low-Mach simulations.

Regarding the numerical and technical aspects, the work presented in this thesis illustrates that the SLH code has reached a solid, well-tested basis upon which further improvements and more complex simulations are possible. Section 2.1 shows that the novel well-balancing methods developed by Berberich et al. (2018, 2019, 2021) significantly improve the simulations regarding stability and representation of convection. The detailed analysis of the properties of the turbulent convective flow based on a realistic helium shell burning model in Section 2.2 validates that physically sound results can be obtained with the low-Mach AUSM$^+$−up flux also in astrophysical applications. The results are on par with current state-of-the-art finite-volume codes developed by other groups. It further proves the ability of the SLH code to perform simulations on large 3D grids using current high-performance computing facilities. The simulation of waves in massive stars presented in Section 2.3 demonstrates the promising prospects of fully compressible, finite-volume simulations.

In a recent study, Andrassy et al. (2021) compare the flow characteristics between 3D simulations with five different hydrodynamic codes (including the SLH code using the AUSM$^+$−up flux), each of which follows a slightly different numerical approach. All codes are used to simulate the same simplified convective setup which involves convective flows with a mean Mach number of Ma ~ 0.04. The authors show that fundamental properties, as for instance mass entrainment rates or time averages of the kinetic energy, are consistent with each other

already at the smallest considered grid size of 128^3 cells. The good agreement for a turbulent setup, for which no analytical solution exists, strengthens the general credibility of results obtained from hydrodynamic simulations. This direct comparison also further demonstrates the validity of the results obtained with the SLH code in the moderate Mach number regime. In light of the results obtained in this thesis, this also illustrates the prospects of the "all-Mach" approach followed by the SLH code.

After this summary of the thesis in a common context, each publication presented in Chapter 2 will be reflected regarding its contribution to current research and remaining challenges in the following.

Well-balancing

The methods presented in Section 2.1 ensure that the numerical flux vanishes for the initial time steps of a hydrostatic atmosphere without source terms. The tests indicate that they diminish the growth of checkerboard-like modes, probably because the driving by the gravity source term is reduced. However, it is evident that they do not completely resolve the problem. A possible solution could be to apply a staggered grid, where scalar quantities are stored as cell averages but vector quantities are stored at the respective cell interfaces. This lifts the pressure-velocity decoupling of conventional colocated grids and improves the representation of hydrostatic balance. Goffrey et al. (2017) report for the MUSIC code, which uses a staggered grid formalism, that they are able to keep a static atmosphere stable at Ma $\sim 10^{-11}$. However, introducing a staggered grid into an already existing code requires some coding effort. For the SLH code in particular, the formulation of the equation in general coordinates (see publication in Section 2.1) and the enormous effort that is required to adapt the Jacobian matrix of the Newton-Raphson scheme makes such an adaption very time-consuming.

Moreover, an advantage of Deviation well-balancing is its ability to stabilize stationary but non-static equilibria, including non-zero velocities. This can be particularly helpful if simulations of rotating stars are of interest. Here, gravity is balanced by a pressure gradient and centrifugal forces. Rotation impacts a star's evolution as it leads to a wealth of possible new mixing mechanisms, for instance dynamical and secular shear instabilities, meridional circulation, or angular momentum transport (Maeder, 2009).

Convective boundary mixing in convective helium shell burning

The results presented in Section 2.2 complement recent studies of CBM in different convection zones (e.g., Meakin and Arnett, 2007b; Viallet et al., 2013b; Gilet et al., 2013; Cristini et al., 2017; Jones et al., 2017; Pratt et al., 2017). Extending these studies over a range of evolutionary stages helps to find possible dependencies of mixing on stellar parameters. For oxygen burning, the dependence of mass entrainment $\dot{m}_e$ on the driving luminosity L found by Meakin and Arnett (2007b), Jones et al. (2017), and Andrassy et al. (2020) corresponds to $\dot{m}_e \propto L$ which is equivalent to $n = 1$ for the Bulk-Richardson scaling.[10] Gilet et al. (2013) reports agreement within a factor of a few in 3D simulations of core hydrogen burning with the entrainment predicted by Eq. (1.22) using the best fit values of Meakin and Arnett (2007b). These findings are in line with the theoretical prediction of Spruit (2015) who argues that the buoyancy of the entrained material sets an upper limit for the entrainment rate which scales with the driving luminosity. In contrast, Cristini et al. (2019) find $n = 0.74 \pm 0.04$ for carbon burning and the present thesis $n = 0.76 \pm 0.10$ for helium burning (Section 2.1) while

[10] According to Eq. (1.22), $v_e \propto v_{\mathrm{rms}}^{1+2n}$. Typically, v_{rms} scales with the driving luminosity L as $v_{\mathrm{rms}} \propto L^{1/3}$ (see, for example, Section 2.2). Hence, $v_e \propto L^{(1+2n)/3}$ and $\dot{m}_e = 4\pi r^2 \rho v_e \propto L$ for $n = 1$.

the simulations of core hydrogen burning by Higl et al. (2021) suggest $n = 1.32 \pm 0.79$ (based on 2D simulations).

Different values for n are found also in laboratory experiments, mostly ranging from $1 \leq n \leq 3/2$ (see, e.g., the review by Fernando, 1991). However, some studies mentioned by Fernando (1991) find values of $n = 1/2$, depending on the mechanism that drives turbulence. A recent DNS simulation also finds $n = 1/2$ for shear-driven entrainment (Jonker et al., 2013). Furthermore, some results indicate that n changes for different regimes of $\mathrm{Ri_B}$ (Strang and Fernando, 2001; Guyez et al., 2007).

It is therefore of interest to further investigate the origin of the different values found in hydrodynamic simulations, especially to exclude a numerical cause. One problem is the current lack of a standard definition of the different terms in Eq. (1.22) which makes a direct comparison between results from different groups difficult. For instance, the integral length scale l required to calculate $\mathrm{Ri_B}$ (see Section 2.2) is sometimes assumed to be some fraction of the pressure scale height (e.g., Cristini et al., 2017; Salaris and Cassisi, 2017), the horizontal integral scale of turbulence near the interface (Meakin and Arnett, 2007b), the depth of the convection zone (Collins et al., 2018), or an autocorrelation function of the average radial velocity (Higl et al., 2021). The definition also differs for the other components involved. For example, Müller et al. (2016) find that their value of A changes by a factor of 3 if the convective velocity is taken to be the spatial average over the entire convection zone compared to considering the convective velocity only near the radiative-convective boundary.

Analyzing the entrainment rate for the already published simulations in a standardized way could help to validate a possible setup-dependence of the entrainment law in the astrophysical context. This is important for the application of Eq. (1.22) in stellar evolution simulations. Furthermore, at nominal luminosity, $\mathrm{Ri_B}$ reaches values which are much larger (for example $\mathrm{Ri_B} \sim 10^5$ for the setup presented in Section 2.2) than what has been addressed in hydrodynamic simulations and laboratory experiments so far (typically $\mathrm{Ri_B} \leq 10^3$).[11] With numerical tools like the SLH code it may be possible to explore the regime of very high $\mathrm{Ri_B}$ in future simulations. This will be a crucial step in order to validate the applicability of the simple entrainment law Eq. (1.22) over a broad parameter range. First studies present stellar evolution calculations using the entrainment law (Staritsin, 2013; Scott et al., 2021). These indicate that the values extracted from hydrodynamic simulations result in too efficient mixing if it is used as a general prescription for convective entrainment and that the current calibration of Eq. (1.22) needs further refinement. Also, other parametrizations of CBM (Section 1.2.3) should be tested on a single data set in order to reveal possible differences to the Bulk-Richardson entrainment at different evolutionary stages.

The impact of rotation has not been included in these studies to keep the setup as simple as possible. However, rotation may alter the efficiency of mixing by convection (Rogers et al., 2013; Brun et al., 2017; Constantino et al., 2021) and the dependence of convective mixing on rotation is also suggested by the observed lithium depletion in solar-like stars (e.g., Constantino et al., 2021; Dumont et al., 2021). Furthermore, the inclusion of rotationally induced instabilities into 1D evolution codes is even more complex due to the deviation from spherical symmetry and typically, they are parametrized by diffusion coefficients with large uncertainties (e.g., Heger et al., 2000; Maeder et al., 2013). The application of the Deviation well-balancing method combined with the low-Mach methods of SLH opens the possibility to simulate slowly progressing rotational phenomena and to contribute to recent simulations of rotationally induced instabilities (e.g., Ballot et al., 2007; Matt et al., 2011; Edelmann et al., 2017). A possible pathway could be to map 1D models of rotating stars that are assumed

[11] An exception is the simulation of core hydrogen burning by Gilet et al. (2013) where $\mathrm{Ri_B} \sim 4 \times 10^5$. However, Gilet et al. (2013) do not derive their own values for n and A.

to be in shellular rotation (Meynet and Maeder, 1997) into 3D space, for example using the method of Roxburgh (2006) in order to follow the dynamical evolution in hydrodynamic simulations.

The recent study of Varma and Müller (2021) shows that also magnetic fields could influence the dynamics of convection in the stellar interior. While they find only a modest impact on the bulk convective flow, magnetic fields seem to suppress rare but strong entrainment events which appear in their pure hydrodynamic simulation. This could explain the lower entrainment rate they find in their simulations with magnetic fields. Magneto hydrodynamic simulations at low-Mach numbers are, however, even more complicated than pure hydrodynamic simulations and beyond the scope of this thesis.

Excitation of waves by core convection

The results presented in Section 2.3 contribute to the recent studies of stellar oscillations in stars by hydrodynamic simulations. It provides insight into the formation and propagation of sound waves and IGW in the context of wave excitation by core convection in a massive star. The fully compressible approach includes pressure and gravity modes while the low-Mach, finite-volume approach has reduced artificial viscosity compared to recent studies that commonly use an anelastic formulation of the underlying equation of hydrodynamics (Alvan et al., 2015; Rogers and McElwaine, 2017; Edelmann et al., 2019). The inclusion of sound waves enables the self-consistent formation of mixed modes where p-modes and g-modes couple. Interpretation of observed mixed mode frequencies allow probing the deep stellar interior and can, for example, be used to distinguish different evolutionary phases in red giants (Bedding et al., 2011), or to constrain rotation profiles in giant stars (Deheuvels et al., 2014). While the proper representation of p-modes was verified in Section 2.3, a more detailed analysis of the possible formation of mixed modes in the simulations remains to be done.

The simulations presented in Section 2.3 support the conjecture of Bowman et al. (2019a,b, 2020) that the low-frequency excess observed in massive stars is due to IGW excited by core convection. However, also the SLH simulations required some artificial boosting, although the boosting used in Section 2.3 is a factor of 10^3 smaller than in the comparable simulation of Edelmann et al. (2019). The required boosting is one of the criticisms of Cantiello et al. (2021) and Lecoanet et al. (2021) who suggest that surface convection is responsible for the low-frequency excess. Without boosting, the convective turnover frequency and hence the frequency of the predominately excited IGW will be lower than in the boosted case. IGW at smaller frequencies have smaller spatial scales and smaller group velocities. This changes the way these waves propagate through the stellar surface, for example because of the increased relative impact of thermal diffusion. Furthermore, the more vigorous convection in boosted simulations leads to larger wave amplitudes, which may enable non-linear effects that would not occur otherwise.

With the improvements presented in Section 2.1, simulations of IGW excitation through core convection at nominal luminosity have come into reach. However, the waves need to be resolved spatially by at least a few grid cells. Taking the values from the $3\,\mathrm{M}_\odot$ model of Section 2.3, the typical frequency f_typ at which IGW will be excited can be estimated by the turnover frequency of the largest eddies in the convection zone as

$$f_\mathrm{typ} = \frac{v_\mathrm{conv}}{2\Delta r_\mathrm{CZ}} \approx 0.2\,\mu\mathrm{Hz}, \tag{3.1}$$

where $\Delta r_\mathrm{CZ} = 1.7 \times 10^{10}\,\mathrm{cm}$ is the radial extent of the convection zone and $v_\mathrm{conv} = 7 \times 10^3\,\mathrm{cm\,s^{-1}}$ ($\mathrm{Ma} \sim 10^{-4}$) the expected convective velocity from MLT. The typical

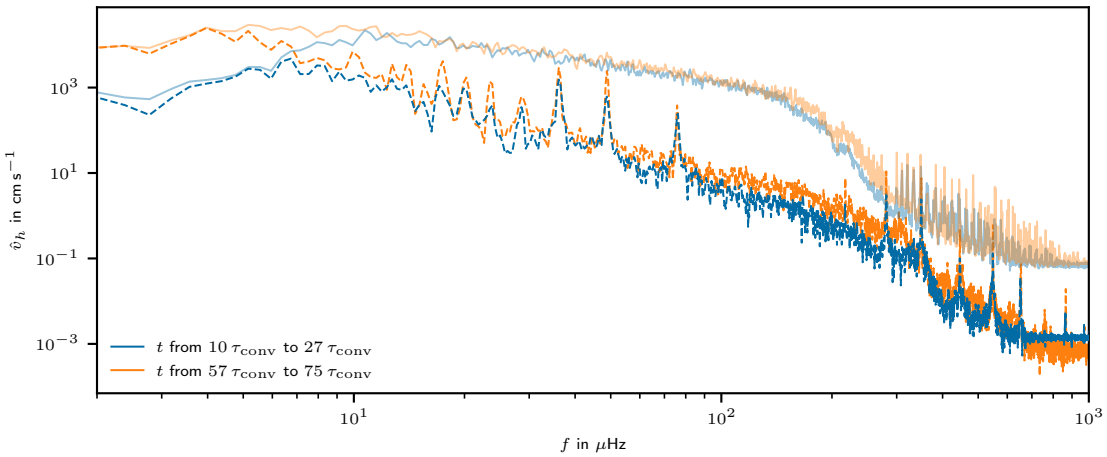

Figure 3.1: Frequency-spectra of the horizontal velocity for the stellar model presented in Section 2.3 for all ℓ (solid, semi-transparent lines) and $\ell = 1$ (dashed, opaque lines). The profiles are obtained at different times but for the same size of the time interval of about $17\,\tau_{\rm conv}$. The velocity data is extracted at half of the stellar radius. The spectra change only slightly for frequencies above $10\,\mu$Hz while amplitudes increase visibly at lower frequencies.

radial wavelength λ_r is then given by

$$\lambda_r = \frac{2\pi}{k_h \sqrt{(N/(2\pi\, f_{\rm typ}))^2 - 1}}, \tag{3.2}$$

where N is the BVF and $k_h = \sqrt{\ell\,(\ell+1)}/r$ the horizontal wave number of angular degree ℓ at radius r (see Section 2.3). For the $3\,\mathrm{M}_\odot$ model of Section 2.3 this yields for example $\lambda_r = 3 \times 10^8\,$cm (if $\ell = 1$ and evaluated at 30 % of the total stellar radius). Therefore, a minimum of 8×10^3 radial grid cells are required if the wave is to be resolved by a minimum of 10 radial cells and 90 % of the total stellar radius should be included in the simulation. For comparison, boosting the luminosity by a factor of 10^3 shifts the characteristic frequency such that the corresponding $\ell = 1$ mode is resolved already with 0.8×10^3 radial cells. This illustrates the high computational demands imposed by the physical properties of IGW which can not be circumvented. It is therefore important to assess the impact of unresolved waves on the resulting spectra as the required resolutions are hardly feasible in full 3D simulations.

Furthermore, sufficiently large time frames need to be covered by the simulations in order to obtain realistic results for the spectra: In the simplified simulations of Lecoanet et al. (2021), peaks from resonant modes only become distinguishable from the background signal if the simulations cover more than 100 convective turnover times. The presence of distinct, individual peaks is an important diagnostic as it is directly comparable to observations. The simulations presented in Section 2.3 cover about 27 convective turnover times (700 h) and the cumulative spectrum does not reveal any obvious peaks.

These simulations have now been extended to cover 75 turnover times (2600 h). The spectrum for all ℓ does mainly change at very low frequencies, as apparent from Fig. 3.1. In the IGW regime ($10\,\mu$Hz to $200\,\mu$Hz), the spectrum does not change considerably. However, individual resonant modes are best visible for filtered velocity and the spectra for $\ell = 1$ in Fig. 3.1 show that the amplitude of resonant peaks (e.g., at $50\,\mu$Hz) indeed slightly increases over time. These peaks are buried underneath the background signal but it is possible that they will grow sufficiently to eventually stand out. However, because of the applied boosting,

the background stratification slightly changes over time, and a strong shear flow develops at the top of the domain.[12] It is therefore not meaningful to continue the simulations presented in Fig. 3.1 even longer.

The wave amplitudes saturate if the energy injected by convection (independent of the wave's amplitude) equals the energy loss by radiative damping (proportional to the wave's amplitude), provided that the waves remain in the linear regime. Whether the final amplitude of a resonant mode will protrude above the background therefore depends on the interplay between the excitation mechanism, amplification, and damping. Simulations with parameters as close as possible to actual stellar values will thus be a step forward to reveal the underlying mechanism behind the low-frequency excess.

3.3 Outlook

Hydrodynamic simulations are an important tool for further understanding the details of dynamical phenomena in stellar interiors. Their results can be interpreted to support or challenge current theories and prescriptions that are applied in 1D evolution codes. The present thesis demonstrated that the SLH code is suitable to address simulations of stars which typically show highly turbulent, low-Mach flows on large spatial scales, including orders of magnitude changes in density and pressure. The results of Chapter 2 constitute a step forward toward the ultimate goal to simulate low-Mach phenomena in stellar interiors without an artificially enhanced energy input.

In upcoming simulations the combination with the recently implemented Deviation well-balancing scheme should be tested in real astrophysical applications. Already the comparison between boosted and unboosted 2D simulations of the helium burning setup of Section 2.2 will be helpful to identify differences induced by boosting and to improve current CBM prescriptions. Furthermore, the simulation of IGW excitation needs to be extended into 3D as only then frequencies of standing waves will become directly comparable to real stars. Preliminary 3D simulations with the SLH code show that the emerging p- and g-modes are in good agreement with linear theory.

Furthermore, it will be crucial to explore scenarios and scientific questions which can be addressed in such simulations with feasible computational resources. Of particular importance is the efficiency of the implicit time stepping schemes applied in the SLH code. As described by Miczek (2013), the solution requires a combination of specialized linear solver and matrix-preconditioning to achieve acceptable efficiency. Optimizing the parameter set of the available iteration schemes has not yet been done with respect to individual applications. Substantial improvements regarding efficiency of time stepping may therefore be achieved.

In future simulations, more complicated setups are possible with SLH. In particular, the inclusion of rotational effects for convective mixing and IGW propagation will be beneficial: The majority of stars rotate and current 1D modeling still struggles to reproduce observed rotation rates and surface abundances, indicating that the current theory is incomplete. It was shown in this thesis that simulations with the SLH code have the potential to include the relevant processes, in particular convection and wave excitation, at improved accuracy. To include also the evolution of magnetic fields is subject of a current PhD project.

[12] Some further numerical experiments indicate that this is a physical effect from angular-momentum deposition of waves and not a numerical artifact of the boundaries: The shear flow does not occur in simulations with smaller radial domains, and it also does not occur for lower resolution. Therefore, it seems possible that better resolved waves lead to high enough amplitudes at the outer domain boundary. This may enable mild non-linear effects which can cause the development of a shear flow over time. However, further tests, especially with lower artificial boosting, are needed for confirmation.

Glossary

1D one-dimensional.

2D two-dimensional.

3D three-dimensional.

BVF Brunt-Väisälä frequency.

CBM convective boundary mixing.

CFL Courant-Friedrichs-Lewy.

DNS direct numerical simulations.

EoS equation of state.

HR diagram Hertzsprung-Russel diagram.

IGW internal gravity waves.

ILES implicit large eddy simulations.

LES large eddy simulations.

MLT mixing-length theory.

MS main-sequence.

RA-ILES Reynolds-averaged implicit large eddy simulations.

SLH Seven-League Hydro.

SPB stars slowly pulsating B stars.

List of Publications

L. Horst, P. V. F. Edelmann, R. Andrássy, F. K. Röpke, D. M. Bowman, C. Aerts, and R. P Ratnasingam.
Fully compressible simulations of waves and core convection in main-sequence stars.
A&A, 641:A18, Sept. 2020.
(Used in Section 2.3)

D. M. Bowman, S. Burssens, S. Simón-Díaz, P. V. F. Edelmann, T. M Rogers, **L. Horst**, F. K. Röpke, and C. Aerts.
Photometric detection of internal gravity waves in upper main-sequence stars. II. Combined TESS photometry and high-resolution spectroscopy.
A&A, 640:A36, Aug. 2020.
(Not used in this thesis)

P. V. F. Edelmann, **L. Horst**, J. P. Berberich, R. Andrassy, J. Higl, C. Klingenberg, and F. K. Röpke.
Well-balanced treatment of gravity in astrophysical fluid dynamics simulations at low Mach numbers.
A&A, 652:A53, Aug. 2021.
(Used in Section 2.1)

L. Horst, R. Hirschi, P. V. F. Edelmann, R. Andrassy, and F. K. Röpke.
Multidimensional low-Mach number time-implicit hydrodynamic simulations of convective helium shell burning in a massive star.
A&A, 653:A55, Sep. 2021.
(Used in Section 2.2)

R. Andrassy, J. Higl, H. Mao, M. Mocák, D. G. Vlaykov, W. D. Arnett, I. Baraffe, S. W. Campbell, T. Constantino, P. V. F. Edelmann, T. Goffrey, T. Guillet, F. Herwig, R. Hirschi, **L. Horst**, G. Leidi, C. Meakin, J. Pratt, F. Rizzuti, F. K. R. Röpke, and P. Woodward.
Dynamics in a stellar convective layer and at its boundary: Comparison of five 3D hydrodynamics codes.
In preparation, 2021.
(Not used in this thesis)

Bibliography

C. Aerts. Probing the interior physics of stars through asteroseismology. *Reviews of Modern Physics*, 93(1):015001, Jan. 2021.

C. Aerts, J. Christensen-Dalsgaard, and D. W. Kurtz. *Asteroseismology*. 2010.

C. Aerts, G. Molenberghs, M. G. Kenward, and C. Neiner. The Surface Nitrogen Abundance of a Massive Star in Relation to its Oscillations, Rotation, and Magnetic Field. *ApJ*, 781 (2):88, Feb. 2014.

C. Aerts, S. Mathis, and T. M. Rogers. Angular Momentum Transport in Stellar Interiors. *ARA&A*, 57:35–78, Aug. 2019.

A. S. Almgren, J. B. Bell, and M. Zingale. MAESTRO: A Low Mach Number Stellar Hydrodynamics Code. *Journal of Physics Conference Series*, 78(1):012085, July 2007.

L. Alvan, A. S. Brun, and S. Mathis. Theoretical seismology in 3D: nonlinear simulations of internal gravity waves in solar-like stars. *A&A*, 565:A42, May 2014.

L. Alvan, A. Strugarek, A. S. Brun, S. Mathis, et al. Characterizing the propagation of gravity waves in 3D nonlinear simulations of solar-like stars. *A&A*, 581:A112, Sep 2015.

E. H. Anders and B. P. Brown. Convective heat transport in stratified atmospheres at low and high Mach number. *Physical Review Fluids*, 2(8):083501, Aug. 2017.

R. Andrassy, F. Herwig, P. Woodward, and C. Ritter. 3D hydrodynamic simulations of C ingestion into a convective O shell. *MNRAS*, 491(1):972–992, Jan. 2020.

R. Andrassy, J. Higl, H. Mao, M. Mocák, et al. Dynamics in a stellar convective layer and at its boundary: Comparison of five 3D hydrodynamics codes. 2021. in preparation.

W. D. Arnett, C. Meakin, M. Viallet, S. W. Campbell, et al. Beyond Mixing-length Theory: A Step Toward 321D. *ApJ*, 809(1):30, Aug. 2015.

W. D. Arnett, C. Meakin, R. Hirschi, A. Cristini, et al. 3D Simulations and MLT. I. Renzini's Critique. *ApJ*, 882(1):18, Sept. 2019.

K. C. Augustson, B. P. Brown, A. S. Brun, M. S. Miesch, et al. Convection and Differential Rotation in F-type Stars. *ApJ*, 756(2):169, Sept. 2012.

W. H. Ball, B. Beeck, R. H. Cameron, and L. Gizon. MESA meets MURaM. Surface effects in main-sequence solar-like oscillators computed using three-dimensional radiation hydrodynamics simulations. *A&A*, 592:A159, Aug. 2016.

J. Ballot, A. S. Brun, and S. Turck-Chièze. Simulations of Turbulent Convection in Rotating Young Solarlike Stars: Differential Rotation and Meridional Circulation. *ApJ*, 669(2): 1190–1208, Nov. 2007.

I. Baraffe, J. Pratt, T. Goffrey, T. Constantino, et al. Lithium Depletion in Solar-like Stars: Effect of Overshooting Based on Realistic Multi-dimensional Simulations. *ApJ*, 845(1):L6, Aug. 2017.

I. Baraffe, J. Pratt, D. G. Vlaykov, T. Guillet, et al. Two-dimensional simulations of solar-like models with artificially enhanced luminosity - I. Impact on convective penetration. *arXiv e-prints*, art. arXiv:2109.00943, Sept. 2021.

T. R. Bedding, B. Mosser, D. Huber, J. Montalbán, et al. Gravity modes as a way to distinguish between hydrogen- and helium-burning red giant stars. *Nature*, 471(7340): 608–611, Mar. 2011.

E. P. Bellinger, S. Basu, S. Hekker, and J. Christensen-Dalsgaard. Testing Stellar Evolution with Asteroseismic Inversions of a Main-sequence Star Harboring a Small Convective Core. *ApJ*, 885(2):143, Nov. 2019.

J. P. Berberich. Numerical Representation of Turbulent Flows in the "Seven-League Hydro" Code. Bachelor's thesis, Universität Würzburg, 2014.

J. P. Berberich, P. Chandrashekar, and C. Klingenberg. A general well-balanced finite volume scheme for Euler equations with gravity. In C. Klingenberg and M. Westdickenberg, editors, *Theory, Numerics and Applications of Hyperbolic Problems I, Springer Proceedings in Mathematics & Statistics 236*, 2018.

J. P. Berberich, P. Chandrashekar, C. Klingenberg, and F. K. Röpke. Second order finite volume scheme for Euler equations with gravity which is well-balanced for general equations of state and grid systems. *accepted for publication in Communications in Computational Physics*, 2019.

J. P. Berberich, P. Chandrashekar, and C. Klingenberg. High order well-balanced finite volume methods for multi-dimensional systems of hyperbolic balance laws. *Computers & Fluids*, page 104858, 2021. ISSN 0045-7930.

E. Böhm-Vitense. Über die Wasserstoffkonvektionszone in Sternen verschiedener Effektivtemperaturen und Leuchtkräfte. Mit 5 Textabbildungen. *ZAp*, 46:108, 1958.

A. Bolaños Rosales. *Low Mach Number Simulations of Convective Boundary Mixing in Classical Novae*. Dissertation, Julius-Maximilians-Universität Würzburg, July 2016.

A. Bonaca, J. D. Tanner, S. Basu, W. J. Chaplin, et al. Calibrating Convective Properties of Solar-like Stars in the Kepler Field of View. *ApJ*, 755(1):L12, Aug. 2012.

J. P. Boris. *More for LES: A Brief Historical Perspective of MILES*, page 9–38. Cambridge University Press, 2007.

D. M. Bowman. Asteroseismology of high-mass stars: new insights of stellar interiors with space telescopes. *Frontiers in Astronomy and Space Sciences*, 7:70, Oct. 2020.

D. M. Bowman, C. Aerts, C. Johnston, M. G. Pedersen, et al. Photometric detection of internal gravity waves in upper main-sequence stars. I. Methodology and application to CoRoT targets. *A&A*, 621:A135, Jan. 2019a.

D. M. Bowman, S. Burssens, M. G. Pedersen, C. Johnston, et al. Low-frequency gravity waves in blue supergiants revealed by high-precision space photometry. *Nature Astronomy*, 3:760–765, May 2019b.

D. M. Bowman, S. Burssens, S. Simón-Díaz, P. V. F. Edelmann, et al. Photometric detection of internal gravity waves in upper main-sequence stars. II. Combined TESS photometry and high-resolution spectroscopy. *A&A*, 640:A36, Aug. 2020.

T. M. Brown. Solar p-Mode Eigenfrequencies are Decreased by Turbulent Convection. *Science*, 226(4675):687–689, Nov. 1984.

M. K. Browning, A. S. Brun, and J. Toomre. Simulations of Core Convection in Rotating A-Type Stars: Differential Rotation and Overshooting. *ApJ*, 601(1):512–529, Jan. 2004.

A. S. Brun, A. Strugarek, J. Varela, S. P. Matt, et al. On Differential Rotation and Overshooting in Solar-like Stars. *ApJ*, 836(2):192, Feb. 2017.

G. Buldgen. Current problems in stellar evolution. *arXiv e-prints*, art. arXiv:1902.10399, Feb. 2019.

K. J. Burns, G. M. Vasil, J. S. Oishi, D. Lecoanet, et al. Dedalus: A flexible framework for numerical simulations with spectral methods. *Physical Review Research*, 2(2):023068, Apr. 2020.

S. Burssens, S. Simón-Díaz, D. M. Bowman, G. Holgado, et al. Variability of OB stars from TESS southern Sectors 1-13 and high-resolution IACOB and OWN spectroscopy. *A&A*, 639:A81, July 2020.

B. Buysschaert, C. Aerts, D. M. Bowman, C. Johnston, et al. Forward seismic modeling of the pulsating magnetic B-type star HD 43317. *A&A*, 616:A148, Aug. 2018.

M. Cantiello and J. Braithwaite. Envelope Convection, Surface Magnetism, and Spots in A and Late B-type Stars. *ApJ*, 883(1):106, Sept. 2019.

M. Cantiello, D. Lecoanet, A. S. Jermyn, and L. Grassitelli. On the Origin of Stochastic, Low-Frequency Photometric Variability in Massive Stars. *ApJ*, 915(2):112, July 2021.

V. M. Canuto. Stellar mixing. I. Formalism. *A&A*, 528:A76, Apr. 2011.

V. M. Canuto and I. Mazzitelli. Stellar turbulent convection - A new model and applications. *ApJ*, 370:295–311, Mar. 1991.

V. M. Canuto, I. Goldman, and I. Mazzitelli. Stellar Turbulent Convection: A Self-consistent Model. *ApJ*, 473:550, Dec. 1996.

N. Castro, L. Fossati, N. Langer, S. Simón-Díaz, et al. The spectroscopic Hertzsprung-Russell diagram of Galactic massive stars. *A&A*, 570:L13, Oct. 2014.

O. Clarkson and F. Herwig. Convective H-He interactions in massive population III stellar evolution models. *MNRAS*, 500(2):2685–2703, Jan. 2021.

C. Collins, B. Müller, and A. Heger. Properties of convective oxygen and silicon burning shells in supernova progenitors. *MNRAS*, 473(2):1695–1704, Jan. 2018.

T. Constantino, I. Baraffe, T. Goffrey, J. Pratt, et al. Suppression of lithium depletion in young low-mass stars from fast rotation. *arXiv e-prints*, art. arXiv:2108.10361, Aug. 2021.

A. Cristini, C. Meakin, R. Hirschi, D. Arnett, et al. 3D hydrodynamic simulations of carbon burning in massive stars. *MNRAS*, 471:279–300, Oct. 2017.

A. Cristini, R. Hirschi, C. Meakin, D. Arnett, et al. Dependence of convective boundary mixing on boundary properties and turbulence strength. *MNRAS*, 484(4):4645–4664, Apr 2019.

A. Davis, S. Jones, and F. Herwig. Convective boundary mixing in a post-He core burning massive star model. *MNRAS*, 484(3):3921–3934, Apr. 2019.

S. Deheuvels, G. Doğan, M. J. Goupil, T. Appourchaux, et al. Seismic constraints on the radial dependence of the internal rotation profiles of six Kepler subgiants and young red giants. *A&A*, 564:A27, Apr. 2014.

S. Deheuvels, I. Brandão, V. Silva Aguirre, J. Ballot, et al. Measuring the extent of convective cores in low-mass stars using Kepler data: toward a calibration of core overshooting. *A&A*, 589:A93, May 2016.

J. W. den Hartogh, P. Eggenberger, and S. Deheuvels. Asteroseismology of evolved stars to constrain the internal transport of angular momentum. III. Using the rotation rates of intermediate-mass stars to test the Fuller-formalism. *A&A*, 634:L16, Feb. 2020.

T. Z. Dorn-Wallenstein, E. M. Levesque, K. F. Neugent, J. R. A. Davenport, et al. Short-term Variability of Evolved Massive Stars with TESS. II. A New Class of Cool, Pulsating Supergiants. *ApJ*, 902(1):24, Oct. 2020.

D. Drikakis, C. Fureby, F. F. Grinstein, and D. Youngs. Simulation of transition and turbulence decay in the Taylor–Green vortex. *Journal of Turbulence*, 8:N20, 2007.

T. Dumont, A. Palacios, C. Charbonnel, O. Richard, et al. Lithium depletion and angular momentum transport in solar-type stars. *A&A*, 646:A48, Feb. 2021.

P. V. F. Edelmann. *Coupling of Nuclear Reaction Networks and Hydrodynamics for Application in Stellar Astrophysics*. Dissertation, Technische Universität München, 2014.

P. V. F. Edelmann, F. K. Röpke, R. Hirschi, C. Georgy, et al. Testing a one-dimensional prescription of dynamical shear mixing with a two-dimensional hydrodynamic simulation. *A&A*, 604:A25, July 2017.

P. V. F. Edelmann, R. P. Ratnasingam, M. G. Pedersen, D. M. Bowman, et al. Three-dimensional Simulations of Massive Stars. I. Wave Generation and Propagation. *ApJ*, 876 (1):4, May 2019.

P. V. F. Edelmann, L. Horst, J. P. Berberich, R. Andrassy, et al. Well-balanced treatment of gravity in astrophysical fluid dynamics simulations at low Mach numbers. *A&A*, 652:A53, Aug. 2021.

P. Eggenberger, G. Meynet, A. Maeder, R. Hirschi, et al. The Geneva stellar evolution code. *Ap&SS*, 316:43–54, Aug. 2008.

P. Eggenberger, N. Lagarde, A. Miglio, J. Montalbán, et al. Constraining the efficiency of angular momentum transport with asteroseismology of red giants: the effect of stellar mass. *A&A*, 599:A18, Mar. 2017.

S. Ekström, C. Georgy, P. Eggenberger, G. Meynet, et al. Grids of stellar models with rotation. I. Models from 0.8 to 120 M at solar metallicity (Z = 0.014). *A&A*, 537:A146, Jan. 2012.

D. Fan, A. Nonaka, A. S. Almgren, A. Harpole, et al. MAESTROeX: A Massively Parallel Low Mach Number Astrophysical Solver. *ApJ*, 887(2):212, Dec. 2019.

H. J. S. Fernando. Turbulent mixing in stratified fluids. *Annual Review of Fluid Mechanics*, 23:455–493, Jan. 1991.

B. Freytag, H. G. Ludwig, and M. Steffen. Hydrodynamical models of stellar convection. The role of overshoot in DA white dwarfs, A-type stars, and the Sun. *A&A*, 313:497–516, Sept. 1996.

U. Frisch. *Turbulence. The legacy of A.N. Kolmogorov*. 1995.

M. Gabriel, A. Noels, J. Montalbán, and A. Miglio. Proper use of Schwarzschild Ledoux criteria in stellar evolution computations. *A&A*, 569:A63, Sept. 2014.

C. Georgy, H. Saio, and G. Meynet. The puzzle of the CNO abundances of α Cygni variables resolved by the Ledoux criterion. *MNRAS*, 439:L6–L10, Mar. 2014.

C. Georgy, H. Saio, and G. Meynet. Blue supergiants as tests for stellar physics. *A&A*, 650: A128, June 2021.

C. Gilet, A. S. Almgren, J. B. Bell, A. Nonaka, et al. Low Mach Number Modeling of Core Convection in Massive Stars. *ApJ*, 773:137, Aug. 2013.

T. Goffrey, J. Pratt, M. Viallet, I. Baraffe, et al. Benchmarking the Multidimensional Stellar Implicit Code MUSIC. *A&A*, 600:A7, Apr. 2017.

N. J. Grin, O. H. Ramírez-Agudelo, A. de Koter, H. Sana, et al. The VLT-FLAMES Tarantula Survey. XXV. Surface nitrogen abundances of O-type giants and supergiants. *A&A*, 600: A82, Apr. 2017.

F. F. Grinstein, L. G. Margolin, and W. J. Rider. *A Rationale for Implicit LES*, page 39–58. Cambridge University Press, 2007.

E. Guyez, J. B. Flor, and E. J. Hopfinger. Turbulent mixing at a stable density interface: the variation of the buoyancy flux gradient relation. *journal of fluid mechanics*, 577:127, Apr. 2007.

S. Hanasoge, L. Gizon, and K. R. Sreenivasan. Seismic Sounding of Convection in the Sun. *Annual Review of Fluid Mechanics*, 48(1):191–217, Jan. 2016.

A. Heger, N. Langer, and S. E. Woosley. Presupernova Evolution of Rotating Massive Stars. I. Numerical Method and Evolution of the Internal Stellar Structure. *ApJ*, 528:368–396, Jan. 2000.

F. Herwig. The evolution of AGB stars with convective overshoot. *A&A*, 360:952–968, Aug. 2000.

F. Herwig, B. Freytag, R. M. Hueckstaedt, and F. X. Timmes. Hydrodynamic Simulations of He Shell Flash Convection. *ApJ*, 642:1057–1074, May 2006.

J. Higl, E. Müller, and A. Weiss. Calibrating core overshooting parameters with two-dimensional hydrodynamical simulations. *A&A*, 646:A133, Feb. 2021.

M. Hosea and L. Shampine. Analysis and implementation of TR-BDF2. *Applied Numerical Mathematics*, 20(1-2):21 – 37, 1996. ISSN 0168-9274. Method of Lines for Time-Dependent Problems.

I. Hunter, I. Brott, D. J. Lennon, N. Langer, et al. The VLT FLAMES Survey of Massive Stars: Rotation and Nitrogen Enrichment as the Key to Understanding Massive Star Evolution. *ApJ*, 676(1):L29, Mar. 2008.

C. Johnston. One size does not fit all: Evidence for a range of mixing efficiencies in stellar evolution calculations. *arXiv e-prints*, art. arXiv:2107.09075, July 2021.

S. Jones, R. Hirschi, M. Pignatari, A. Heger, et al. Code dependencies of pre-supernova evolution and nucleosynthesis in massive stars: evolution to the end of core helium burning. *MNRAS*, 447(4):3115–3129, Mar. 2015.

S. Jones, R. Andrassy, S. Sandalski, A. Davis, et al. Idealized hydrodynamic simulations of turbulent oxygen-burning shell convection in 4π geometry. *MNRAS*, 465:2991–3010, Mar. 2017.

H. J. J. Jonker, M. van Reeuwijk, P. P. Sullivan, and E. G. Patton. On the scaling of shear-driven entrainment: a DNS study. *Journal of Fluid Mechanics*, 732:150–165, Oct. 2013.

A. C. S. Jørgensen and A. Weiss. Addressing the acoustic tachocline anomaly and the lithium depletion problem at the same time. *MNRAS*, 481(4):4389–4396, Dec. 2018.

A. C. S. Jørgensen, J. R. Mosumgaard, A. Weiss, V. Silva Aguirre, et al. Coupling 1D stellar evolution with 3D-hydrodynamical simulations on the fly - I. A new standard solar model. *MNRAS*, 481(1):L35–L39, Nov. 2018.

A. C. S. Jørgensen, J. Montalbán, G. C. Angelou, A. Miglio, et al. On the impact of the structural surface effect on global stellar properties and asteroseismic analyses. *MNRAS*, 500(4):4277–4295, Jan. 2021.

M. Joyce and B. Chaboyer. Not All Stars Are the Sun: Empirical Calibration of the Mixing Length for Metal-poor Stars Using One-dimensional Stellar Evolution Models. *ApJ*, 856 (1):10, Mar. 2018.

E. A. Kaiser, R. Hirschi, W. D. Arnett, C. Georgy, et al. Relative importance of convective uncertainties in massive stars. *MNRAS*, 496(2):1967–1989, June 2020.

P. J. Käpylä. Overshooting in simulations of compressible convection. *A&A*, 631:A122, Nov. 2019.

P. J. Käpylä. Star-in-a-box simulations of fully convective stars. *A&A*, 651:A66, July 2021a.

P. J. Käpylä. Prandtl number dependence of compressible convection: Flow statistics and convective energy transport. *arXiv e-prints*, art. arXiv:2105.08453, May 2021b.

C. A. Kennedy and M. H. Carpenter. Additive Runge-Kutta Schemes for Convection-Diffusion-Reaction Equations. Technical report, NASA Technical Memorandum, 2001.

R. Kippenhahn, A. Weigert, and A. Weiss. *Stellar Structure and Evolution*. Springer-Verlag, Berlin Heidelberg, 2012. ISBN 978-3-642-30255-8.

L. Korre, P. Garaud, and N. H. Brummell. Convective overshooting and penetration in a Boussinesq spherical shell. *MNRAS*, 484(1):1220–1237, Mar. 2019.

F. Kupka and H. J. Muthsam. Modelling of stellar convection. *Living Reviews in Computational Astrophysics*, 3(1):1, July 2017.

L. D. Landau and E. M. Lifshitz. *Fluid Mechanics (Course of Theoretical Physics: Volume 6)*. Butterworth-Heinemann, Oxford, 2 edition, January 1987. ISBN 0750627670.

N. Langer. Presupernova Evolution of Massive Single and Binary Stars. *ARA&A*, 50:107–164, Sept. 2012.

N. Langer, K. J. Fricke, and D. Sugimoto. Semiconvective diffusion and energy transport. *A&A*, 126(1):207, Sept. 1983.

D. Lecoanet, M. McCourt, E. Quataert, K. J. Burns, et al. A validated non-linear Kelvin-Helmholtz benchmark for numerical hydrodynamics. *MNRAS*, 455(4):4274–4288, Feb. 2016.

D. Lecoanet, M. Cantiello, E. Quataert, L.-A. Couston, et al. Low-frequency Variability in Massive Stars: Core Generation or Surface Phenomenon? *ApJ*, 886(1):L15, Nov. 2019.

D. Lecoanet, M. Cantiello, E. H. Anders, E. Quataert, et al. Surface manifestation of stochastically excited internal gravity waves. *MNRAS*, Sept. 2021.

R. J. LeVeque. *Finite volume methods for hyperbolic problems*, volume 31. Cambridge university press, Cambridge, 2002.

T. Li, T. R. Bedding, D. Huber, W. H. Ball, et al. Modelling Kepler red giants in eclipsing binaries: calibrating the mixing-length parameter with asteroseismology. *MNRAS*, 475(1): 981–998, Mar. 2018.

M.-S. Liou. A sequel to AUSM, Part II: AUSM< sup>+</sup>-up for all speeds. *Journal of Computational Physics*, 214(1):137–170, 2006.

C. C. Lovekin. Challenges in 2D Stellar Modelling. *Frontiers in Astronomy and Space Sciences*, 6:77, Jan. 2020.

A. Maeder. *Physics, Formation and Evolution of Rotating Stars*. Astronomy and Astrophysics Library. Springer Berlin Heidelberg, 2009. ISBN 978-3-540-76949-4.

A. Maeder and G. Meynet. The Evolution of Rotating Stars. *ARA&A*, 38:143–190, 2000.

A. Maeder and G. Meynet. Rotating massive stars: From first stars to gamma ray bursts. *Reviews of Modern Physics*, 84(1):25–63, Jan. 2012.

A. Maeder and G. Meynet. Physics of rotation: problems and challenges. In G. Meynet, C. Georgy, J. Groh, and P. Stee, editors, *New Windows on Massive Stars*, volume 307, pages 9–19, Jan. 2015.

A. Maeder, G. Meynet, N. Lagarde, and C. Charbonnel. The thermohaline, Richardson, Rayleigh-Taylor, Solberg-Høiland, and GSF criteria in rotating stars. *A&A*, 553:A1, May 2013.

Z. Magic, A. Serenelli, A. Weiss, and B. Chaboyer. On Using the Color-Magnitude Diagram Morphology of M67 to Test Solar Abundances. *ApJ*, 718(2):1378–1387, Aug. 2010.

Z. Magic, A. Chiavassa, R. Collet, and M. Asplund. The Stagger-grid: A grid of 3D stellar atmosphere models. IV. Limb darkening coefficients. *A&A*, 573:A90, Jan. 2015.

N. Markova, J. Puls, and N. Langer. Spectroscopic and physical parameters of Galactic O-type stars. III. Mass discrepancy and rotational mixing. *A&A*, 613:A12, May 2018.

S. Martinet, G. Meynet, S. Ekström, S. Simón-Díaz, et al. Convective core sizes in rotating massive stars. I. Constraints from solar metallicity OB field stars. *A&A*, 648:A126, Apr. 2021.

F. Martins and A. Palacios. A comparison of evolutionary tracks for single Galactic massive stars. *A&A*, 560:A16, Dec. 2013.

S. Mathis, T. Decressin, P. Eggenberger, and C. Charbonnel. Diagnoses to unravel secular hydrodynamical processes in rotating main sequence stars. II. The actions of internal gravity waves. *A&A*, 558:A11, Oct. 2013.

S. P. Matt, O. Do Cao, B. P. Brown, and A. S. Brun. Convection and differential rotation properties of G and K stars computed with the ASH code. *Astronomische Nachrichten*, 332:897, Dec. 2011.

L. O. McNeill and B. Müller. Stochastic core spin-up in massive stars - implications of 3D simulations of oxygen shell burning. *MNRAS*, 497(4):4644–4653, Oct. 2020.

C. A. Meakin and D. Arnett. Active Carbon and Oxygen Shell Burning Hydrodynamics. *ApJ*, 637:L53–L56, Jan. 2006.

C. A. Meakin and D. Arnett. Anelastic and Compressible Simulations of Stellar Oxygen Burning. *ApJ*, 665(1):690–697, Aug 2007a.

C. A. Meakin and D. Arnett. Turbulent Convection in Stellar Interiors. I. Hydrodynamic Simulation. *ApJ*, 667(1):448–475, Sep 2007b.

G. Meynet and A. Maeder. Stellar evolution with rotation. I. The computational method and the inhibiting effect of the μ-gradient. *A&A*, 321:465–476, May 1997.

G. Meynet, S. Ekstrom, A. Maeder, P. Eggenberger, et al. *Models of Rotating Massive Stars: Impacts of Various Prescriptions*, volume 865, page 3. 2013.

G. Meynet, A. Maeder, C. Georgy, S. Ekström, et al. Massive stars, successes and challenges. In J. J. Eldridge, J. C. Bray, L. A. S. McClelland, and L. Xiao, editors, *The Lives and Death-Throes of Massive Stars*, volume 329, pages 3–14, Nov. 2017.

A. Michel. *Modeling of silicon burning during late stages of stellar evolution.* Dissertation, Ruprecht-Karls-Universität Heidelberg, January 2019.

F. Miczek. *Simulation of low Mach number astrophysical flows.* Dissertation, Technische Universität München, 2013.

F. Miczek, F. K. Röpke, and P. V. F. Edelmann. New numerical solver for flows at various Mach numbers. *A&A*, 576:A50, Apr. 2015.

M. Mocák, C. Meakin, M. Viallet, and D. Arnett. Compressible Hydrodynamic Mean-Field Equations in Spherical Geometry and their Application to Turbulent Stellar Convection Data. *arXiv e-prints*, art. arXiv:1401.5176, Jan. 2014.

M. Mocák, C. Meakin, S. W. Campbell, and W. D. Arnett. Turbulent mixing and nuclear burning in stellar interiors. *MNRAS*, 481(3):2918–2932, Dec. 2018.

E. Moravveji, C. Aerts, P. I. Pápics, S. A. Triana, et al. Tight asteroseismic constraints on core overshooting and diffusive mixing in the slowly rotating pulsating B8.3V star KIC 10526294. *A&A*, 580:A27, Aug. 2015.

E. Moravveji, R. H. D. Townsend, C. Aerts, and S. Mathis. Sub-inertial Gravity Modes in the B8V Star KIC 7760680 Reveal Moderate Core Overshooting and Low Vertical Diffusive Mixing. *ApJ*, 823(2):130, June 2016.

T. Morel, S. Hubrig, and M. Briquet. Nitrogen enrichment, boron depletion and magnetic fields in slowly-rotating B-type dwarfs. *A&A*, 481(2):453–463, Apr. 2008.

J. R. Mosumgaard, A. C. S. Jørgensen, A. Weiss, V. Silva Aguirre, et al. Coupling 1D stellar evolution with 3D-hydrodynamical simulations on-the-fly II: stellar evolution and asteroseismic applications. *MNRAS*, 491(1):1160–1173, Jan. 2020.

B. Müller. Hydrodynamics of core-collapse supernovae and their progenitors. *Living Reviews in Computational Astrophysics*, 6(1):3, June 2020.

B. Müller, M. Viallet, A. Heger, and H.-T. Janka. The Last Minutes of Oxygen Shell Burning in a Massive Star. *ApJ*, 833:124, Dec. 2016.

A. Nonaka, A. S. Almgren, J. B. Bell, M. J. Lijewski, et al. MAESTRO: An Adaptive Low Mach Number Hydrodynamics Algorithm for Stellar Flows. *ApJS*, 188:358–383, June 2010.

B. Paxton, M. Cantiello, P. Arras, L. Bildsten, et al. Modules for Experiments in Stellar Astrophysics (MESA): Planets, Oscillations, Rotation, and Massive Stars. *ApJS*, 208:4, Sept. 2013.

B. Paxton, J. Schwab, E. B. Bauer, L. Bildsten, et al. Modules for Experiments in Stellar Astrophysics (MESA): Convective Boundaries, Element Diffusion, and Massive Star Explosions. *ApJS*, 234(2):34, Feb 2018.

B. Paxton, R. Smolec, J. Schwab, A. Gautschy, et al. Modules for Experiments in Stellar Astrophysics (MESA): Pulsating Variable Stars, Rotation, Convective Boundaries, and Energy Conservation. *ApJS*, 243(1):10, Jul 2019.

M. G. Pedersen. *Interior rotation, mixing and ages of a sample of Slowly Pulsating B stars from gravity-mode asteroseismology.* Phd thesis, KU Leuven in Belgium, 2020.

M. G. Pedersen, C. Aerts, P. I. Pápics, M. Michielsen, et al. Internal mixing of rotating stars inferred from dipole gravity modes. *Nature Astronomy*, May 2021.

S. B. Pope. *Turbulent Flows.* Cambridge University Press, Cambridge, 2000.

M. V. Popov, R. Walder, D. Folini, T. Goffrey, et al. A well-balanced scheme for the simulation tool-kit A-MaZe: implementation, tests, and first applications to stellar structure. *A&A*, 630:A129, Oct. 2019.

J. Pratt, I. Baraffe, T. Goffrey, C. Geroux, et al. Spherical-shell boundaries for two-dimensional compressible convection in a star. *A&A*, 593:A121, Oct. 2016.

J. Pratt, I. Baraffe, T. Goffrey, T. Constantino, et al. Extreme value statistics for two-dimensional convective penetration in a pre-main sequence star. *A&A*, 604:A125, Aug. 2017.

J. Pratt, I. Baraffe, T. Goffrey, C. Geroux, et al. Comparison of 2D and 3D compressible convection in a pre-main sequence star. *A&A*, 638:A15, June 2020.

D. Prialnik. *An Introduction to the Theory of Stellar Structure and Evolution*. Cambridge University Press, Cambridge, UK, July 2000.

R. P. Ratnasingam, P. V. F. Edelmann, and T. M. Rogers. Two-dimensional simulations of internal gravity waves in the radiation zones of intermediate-mass stars. *MNRAS*, 497(4): 4231–4245, Oct. 2020.

A. Renzini. Some embarrassments in current treatments of convective overshooting. *A&A*, 188(1):49–54, Dec. 1987.

P. L. Roe. Approximate Riemann solvers, parameter vectors, and difference schemes. *Journal of Computational Physics*, 43(2):357 – 372, 1981.

T. M. Rogers and G. A. Glatzmaier. Gravity waves in the Sun. *MNRAS*, 364(4):1135–1146, Dec. 2005.

T. M. Rogers and J. N. McElwaine. On the Chemical Mixing Induced by Internal Gravity Waves. *ApJ*, 848(1):L1, Oct. 2017.

T. M. Rogers, D. N. C. Lin, J. N. McElwaine, and H. H. B. Lau. Internal Gravity Waves in Massive Stars: Angular Momentum Transport. *ApJ*, 772(1):21, Jul 2013.

C. S. Rosenthal, J. Christensen-Dalsgaard, Å. Nordlund, R. F. Stein, et al. Convective contributions to the frequencies of solar oscillations. *A&A*, 351:689–700, Nov. 1999.

I. W. Roxburgh. 2-dimensional models of rapidly rotating stars. II. Hydrostatic and acoustic models with Ω=Ω(r,θ). *A&A*, 454:883–888, Aug. 2006.

M. Salaris and S. Cassisi. *Evolution of Stars and Stellar Populations*. 2005.

M. Salaris and S. Cassisi. Stellar models with the ML2 theory of convection. *A&A*, 487(3): 1075–1080, Sept. 2008.

M. Salaris and S. Cassisi. Chemical element transport in stellar evolution models. *Royal Society Open Science*, 4(8):170192, Aug. 2017.

A. Schootemeijer, N. Langer, N. J. Grin, and C. Wang. Constraining mixing in massive stars in the Small Magellanic Cloud. *A&A*, 625:A132, May 2019.

L. J. A. Scott, R. Hirschi, C. Georgy, W. D. Arnett, et al. Convective core entrainment in 1D main-sequence stellar models. *MNRAS*, 503(3):4208–4220, May 2021.

A. Serenelli, A. Weiss, C. Aerts, G. C. Angelou, et al. Weighing stars from birth to death: mass determination methods across the HRD. *A&A Rev.*, 29(1):4, Dec. 2021.

C.-W. Shu and S. Osher. Efficient implementation of essentially non-oscillatory shock-capturing schemes. *Journal of Computational Physics*, 77(2):439 – 471, 1988. ISSN 0021-9991.

N. Smith. Mass Loss: Its Effect on the Evolution and Fate of High-Mass Stars. *ARA&A*, 52: 487–528, Aug. 2014.

F. Spada, M. Gellert, R. Arlt, and S. Deheuvels. Angular momentum transport efficiency in post-main sequence low-mass stars. *A&A*, 589:A23, May 2016.

F. Spada, P. Demarque, and F. Kupka. Stellar evolution models with entropy-calibrated mixing-length parameter: application to red giants. *MNRAS*, 504(3):3128–3138, July 2021.

H. C. Spruit. The growth of helium-burning cores. *A&A*, 582:L2, Oct. 2015.

R. J. Stancliffe, L. Fossati, J. C. Passy, and F. R. N. Schneider. Confronting uncertainties in stellar physics. II. Exploring differences in main-sequence stellar evolution tracks. *A&A*, 586:A119, Feb. 2016.

E. I. Staritsin. Turbulent entrainment at the boundaries of the convective cores of main-sequence stars. *Astronomy Reports*, 57(5):380–390, May 2013.

J. M. Stone, T. A. Gardiner, P. Teuben, J. F. Hawley, et al. Athena: A New Code for Astrophysical MHD. *ApJS*, 178:137–177, Sept. 2008.

E. J. Strang and H. J. S. Fernando. Entrainment and mixing in stratified shear flows. *journal of fluid mechanics*, 428:349–386, 2001.

W. Szewczuk and J. Daszyńska-Daszkiewicz. Domains of pulsational instability of low-frequency modes in rotating upper main sequence stars. *MNRAS*, 469(1):13–46, July 2017.

W. Szewczuk and J. Daszyńska-Daszkiewicz. KIC 3240411 - the hottest known SPB star with the asymptotic g-mode period spacing. *MNRAS*, 478(2):2243–2256, Aug. 2018.

S. Talon. Transport Processes in Stars: Diffusion, Rotation, Magnetic fields and Internal Waves. In C. Charbonnel and J. P. Zahn, editors, *EAS Publications Series*, volume 32 of *EAS Publications Series*, pages 81–130, Nov. 2008.

M. Tassoul, G. Fontaine, and D. E. Winget. Evolutionary Models for Pulsation Studies of White Dwarfs. *ApJS*, 72:335, Feb. 1990.

A. Tkachenko, K. Pavlovski, C. Johnston, M. G. Pedersen, et al. The mass discrepancy in intermediate- and high-mass eclipsing binaries: The need for higher convective core masses. *A&A*, 637:A60, May 2020.

E. F. Toro. *Riemann Solvers and Numerical Methods for Fluid Dynamics: A Practical Introduction*. Springer, Berlin Heidelberg, 2009. ISBN 9783540498346.

G. Torres, J. Andersen, and A. Giménez. Accurate masses and radii of normal stars: modern results and applications. *A&A Rev.*, 18(1-2):67–126, Feb. 2010.

R. Trampedach, R. F. Stein, J. Christensen-Dalsgaard, Å. Nordlund, et al. Improvements to stellar structure models, based on a grid of 3D convection simulations - II. Calibrating the mixing-length formulation. *MNRAS*, 445(4):4366–4384, Dec. 2014.

G. Valle, M. Dell'Omodarme, P. G. Prada Moroni, and S. Degl'Innocenti. Statistical errors and systematic biases in the calibration of the convective core overshooting with eclipsing binaries. A case study: TZ Fornacis. *A&A*, 600:A41, Apr. 2017.

G. Valle, M. Dell'Omodarme, P. G. Prada Moroni, and S. Degl'Innocenti. Mixing-length calibration from field stars. An investigation on statistical errors, systematic biases, and spurious metallicity trends. *A&A*, 623:A59, Mar. 2019.

V. Varma and B. Müller. 3D simulations of oxygen shell burning with and without magnetic fields. *MNRAS*, 504(1):636–647, June 2021.

M. Viallet, I. Baraffe, and R. Walder. Comparison of different nonlinear solvers for 2D time-implicit stellar hydrodynamics. *A&A*, 555:A81, July 2013a.

M. Viallet, C. Meakin, D. Arnett, and M. Mocák. Turbulent Convection in Stellar Interiors. III. Mean-field Analysis and Stratification Effects. *ApJ*, 769:1, May 2013b.

M. Viallet, C. Meakin, V. Prat, and D. Arnett. Toward a consistent use of overshooting parametrizations in 1D stellar evolution codes. *A&A*, 580:A61, Aug. 2015.

M. Viallet, T. Goffrey, I. Baraffe, D. Folini, et al. A Jacobian-free Newton-Krylov method for time-implicit multidimensional hydrodynamics. Physics-based preconditioning for sound waves and thermal diffusion. *A&A*, 586:A153, Feb. 2016.

L. S. Viani and S. Basu. Examining the Relationship Between Convective Core Overshoot and Stellar Properties Using Asteroseismology. *ApJ*, 904(1):22, Nov. 2020.

L. S. Viani, S. Basu, M. J. Ong J., A. Bonaca, et al. Investigating the Metallicity-Mixing-length Relation. *ApJ*, 858(1):28, May 2018.

A. Weiss, W. Hillebrandt, H.-C. Thomas, and H. Ritter. *Cox & Giuli's Principles of Stellar Structure*. Cambridge Scientific Publishers, Cambridge, 2004.

P. R. Woodward, F. Herwig, and P.-H. Lin. Hydrodynamic Simulations of H Entrainment at the Top of He-shell Flash Convection. *ApJ*, 798(1):49, Jan. 2015.

T. Wu, Y. Li, Z.-m. Deng, G.-f. Lin, et al. Asteroseismic Analyses of Slowly Pulsating B Star KIC 8324482: Ultraweak Element Mixing beyond the Central Convective Core. *ApJ*, 899 (1):38, Aug. 2020.

Acknowledgements

I want to thank my supervisor Fritz Röpke for the interesting topic and for giving me the opportunity to do my doctoral thesis in his group at HITS and for the, without any exception, always open and friendly atmosphere. I also want to acknowledge the Klaus Tschira Foundation for their financial support through the HITS Scholarship.

The work presented in this thesis has further greatly benefited from numerous other people: From Philipp who aided me for many years now with computational and scientific questions. The same holds for Raphael who always found some encouraging words and who invited me to an STSM in his working group at the Keele University. Robert for sharing his valuable physical knowledge that certainly improved the work presented here. Also many thanks to those who helped proof-reading the thesis, which further includes Fabian and Sabrina.

Thanks also to the many "PSO beer meetings", with all the different PSO members and other HITS fellows that joined or left along the years. I will in particular miss the many hours I spent with Florian, with whom I share the same academic path since the second semester, ranting about everything we could think of.

And, of course, I have to thank my family and Viviana who always had my back and who had to endure for many years my grumbling about studying.